# MEASUREMENT OF THE INCLUSIVE $b$-QUARK PRODUCTION CROSS SECTION AND $b\bar{b}$ AZIMUTHAL ANGLE CORRELATIONS IN $p\bar{p}$ COLLISIONS AT $\sqrt{s} = 1.8$ TeV

by

David Lee Vititoe

---

A Dissertation Submitted to the Faculty of the

DEPARTMENT OF PHYSICS

In Partial Fulfillment of the Requirements
For the Degree of

DOCTOR OF PHILOSOPHY

In the Graduate College

THE UNIVERSITY OF ARIZONA

1 9 9 6

# STATEMENT BY AUTHOR

This dissertation has been submitted in partial fulfillment of requirements for an advanced degree at The University of Arizona and is deposited in the University Library to be made available to borrowers under rules of the Library.

Brief quotations from this dissertation are allowable without special permission, provided that accurate acknowledgment of source is made. Requests for permission for extended quotation from or reproduction of this manuscript in whole or in part may be granted by the head of the major department or the Dean of the Graduate College when in his or her judgment the proposed use of the material is in the interests of scholarship. In all other instances, however, permission must be obtained from the author.

SIGNED: _____

# ACKNOWLEDGMENTS

There are several people who I would like to take the time to thank. First and foremost is my wife, Janet, who has always been supportive of my dreams and ambitions no matter how impossible they may seem. Along the way, she has made many sacrifices which helped insure that I finish this work. I only hope that someday I am able to return the favor. I would also like to thank my advisor, Ken Johns. Ken always managed to make time for me regardless of how busy he became with his work. Without his aid and advice, I doubt that I would have been able to finish this work within the four year deadline imposed upon me by the Air Force.

I'd especially like to thank my officemate, Ajay Narayanan, for his friendship over the past couple of years. I am also grateful for all of his work on the Level 1.5 muon system while I was busy studying for my preliminary exams. Also, I'd like to thank the 'Arizona Boys': Dave Fein, Alex Smith, and Eric James. They were especially helpful when I first joined the group, because they were always willing to answer my 'silly' questions. I am also grateful to Kevin Davis for his help in editing this document.

I would like to thank all of the faculty members and staff at the University of Arizona. A special thanks goes to Iris Wright, the physics department's Graduate Secretary, who was my lifeline back to the university while I was away at FNAL. I would also like to thank all of my fellow collaborators at DØ. In particular, I am grateful to Ken Johns, Andrzej and Daria Zieminski, Dave Hedin, Marc Baarmand, and Arthur Maciel for all of their advice and guidance over the past few years. Finally, I'd like to thank GUS, Q, Noz, Tense, and Lymie for your continued friendship. The 'Box' may be dead, but the boxers live on .....

This Thesis is dedicated to:

The memory of my Grandfather, William Rankin,
who, in his own way, helped me get started.

My wife, Janet,
who, in her many ways, helped me finish.

# TABLE OF CONTENTS

# LIST OF FIGURES

# LIST OF TABLES

# ABSTRACT

Using dimuon events produced in proton-antiproton collisions at $\sqrt{s} = 1.8$ TeV at the DØ detector, the integrated inclusive $b$-quark production cross section has been extracted. The inclusive $b$-quark production cross section for $P_T^b > 9$ GeV/$c$ is $2.61 \pm 0.07(\text{Stat}) \pm 1.13(\text{Syst})$ nb. The cross section, $d\sigma/d\Delta\varphi_{\mu\mu}$, where $\Delta\varphi_{\mu\mu}$ is the azimuthal angle difference between the dimuons, has also been measured. Both measurements are in good agreement with next-to-leading order QCD predictions.

# Chapter 1

# Introduction

The primary objective of particle physics is to study nature at its most basic level. This involves studying the properties of the most fundamental particles and the interactions between them. Our present understanding of the strong, weak, and electromagnetic interactions are embodied in the Standard Model. This model has been extremely successful at describing all high energy phenomenon. However, the Standard Model is esthetically unsatisfactory in that it contains many parameters that are not predicted by the theory. Further, the gauge theories used in this model must employ an ad hoc method, the Higgs mechanism [1], to describe why particles have mass. It is generally felt that a more fundamental theory is waiting to be discovered. Thus, physicists are constantly searching for an observation that violates the Standard Model. It is hoped that such an observation will point the way toward a deeper understanding of the underlying physics. In any case, future extensions to

the Standard Model are likely, because the model does not yet describe gravitational interactions.

In addition to searching for experimental results which contradict the Standard Model, physicists are also trying to improve our understanding of the various components of the model. This is especially true for the theory of the strong interaction which is the least understood of the three forces described by the model. The present theory describing the strong interaction is Quantum Chromodynamics (QCD). It describes 'colored' quarks, gluons, and the interactions between them. The difficulty with this theory is that the coupling constant, $\alpha_s$, becomes large at small energy scales[1] making perturbative techniques impractical.

There are several reasons why the $b$-quark is useful for studying QCD. First, the heavy flavor production theories can be treated perturbatively meaning that cross sections can be expressed as a convergent power series in $\alpha_s$. Second, the bottom quark can be identified experimentally and has a relatively large cross section at Tevatron energies, $\sqrt{s} = 1.8$ TeV. The branching ratio of $b$-quarks into muons is approximately 10%. An additional 10% of the time, the $b$-quark decays sequentially, $b \to c \to \mu$. In both cases the $b$-quark is identified by a lepton plus an accompanying hadronic jet. In this thesis, the lepton used to tag the $b$-quarks are muons, because the DØ experiment can readily identify muons in the presence of hadronic jets.

[1] The useful renormalization scale, $\mu$, has a lower bound which is given approximately by the mass of the heavy quark. Therefore, cross sections calculated for the bottom and top quarks are considered reliable, but perturbative calculations for lighter quarks should be considered approximations at best. The renormalization scales required for these lighter masses, $m_c = 1.5$ GeV, forces $\alpha_s$ to become large making it difficult to use perturbative techniques [2].

There exist theoretical calculations to order $\alpha_s^3$ for the production of $b$-quarks [2, 3, 4]. These predictions are for the inclusive $b$-quark cross section and the fully exclusive $b\overline{b}$ cross section. The aim of this thesis is to test both predictions. The integrated inclusive $b$-quark cross section is extracted from a measurement of the inclusive dimuon cross section, $b\overline{b} \rightarrow \mu\mu X$. The fully exclusive cross section prediction is tested by measuring $b\overline{b}$ correlations. Specifically, the differential cross section for $b\overline{b} \rightarrow \mu\mu X$ as a function of the difference in azimuthal angle between the two muons is measured. This measurement allows for a more subtle test of the theory, because it attempts to distinguish between the various production mechanisms for the bottom quark. This can be accomplished because each of the production mechanisms is topologically different in this variable.

These measurements are important for several reasons:

- Test the machinery of QCD. Is the current theory adequate enough to describe heavy flavor production? What processes, if any, must be added?
- Give insight into other processes such as charm or top production.
- Determine accurate cross sections which can be used to predict $b$-quark production at LHC energies.

The first measurement of the $b$-quark cross section at Tevatron energies was made at Fermi National Laboratory by the CDF collaboration [5] and was found to be a factor of three above $\mathcal{O}(\alpha_s^3)$ theoretical predictions. This motivated theoretical efforts

to explain the differences, as well as experimental efforts to measure the cross section with other independent data samples. Early in 1996, a low statistics measurement of the $b$-quark cross section was made at DØ [6]. Here, it was found that the $b$-quark cross section was approximately a factor of two above theory but agreed within experimental and theoretical uncertainties. This thesis describes the continuation and improvement upon this early DØ measurement by using improved analysis techniques to study a higher statistics and better understood data sample.

The outline of this thesis is as follows. Chapter 2 gives a brief introduction to the Standard Model and describes some of the details of heavy flavor production. Chapter 3 contains an abridged description of the DØ detector. Next, Chapter 4 describes the criteria used in selecting the events for this study. The Monte Carlo samples used in this analysis are documented in Chapter 5. The efficiencies for the analysis cuts are detailed in Chapter 6. Chapter 7 describes the methods used to separate $b\overline{b} \rightarrow \mu\mu X$ events from the various backgrounds contained in the data sample. The muon momentum resolutions are unfolded in Chapter 8. The actual cross section and correlation measurements are produced in Chapter 9, and this is followed by a discussion of these results in Chapter 10.

Two appendices are given at the end. Appendix A discusses the models used to determine the statistical uncertainties associated with the various measurements made in this thesis. Appendix B lists the results of all of the cross section measurements. This appendix also lists all of the inputs that went into calculating these results.

# Chapter 2

# Theory

## 2.1 The Standard Model

The fundamental building block of matter are the fermions known as quarks and leptons. There are six quarks (and leptons), each having an associated antiparticle. These particles can be subdivided into three separate families:

$$\text{Leptons} \quad \begin{pmatrix} \text{e} \\ \nu_{\text{e}} \end{pmatrix} \quad \begin{pmatrix} \mu \\ \nu_{\mu} \end{pmatrix} \quad \begin{pmatrix} \tau \\ \nu_{\tau} \end{pmatrix}$$

$$\text{Quarks} \quad \begin{pmatrix} \text{u} \\ \text{d} \end{pmatrix} \quad \begin{pmatrix} \text{c} \\ \text{s} \end{pmatrix} \quad \begin{pmatrix} \text{t} \\ \text{b} \end{pmatrix}$$

Only the first family (u, d, e, $\nu_e$) contributes to everyday matter. For example, protons and neutrons consist of combinations of the up and down quarks; electrons can be found in all atoms and molecules. The other families contain particles which

| Name | Symbol | Charge | Mass ($GeV/c^2$) |
|---|---|---|---|
| Electron | $e$ | -1 | $5.1 \times 10^{-4}$ |
| $e$-neutrino | $\nu_e$ | 0 | $\sim 0$ |
| Muon | $\mu$ | -1 | 0.106 |
| $\mu$-neutrino | $\nu_\mu$ | 0 | $< 1.7 \times 10^{-4}$ (90% CL) |
| Tau | $\tau$ | -1 | 1.78 |
| $\tau$-neutrino | $\nu_\tau$ | 0 | $< 2.4 \times 10^{-2}$ (90% CL) |

Table 2-1: Lepton Properties. Charge is given in units of proton charge, mass in units of $GeV/c^2$.

| Name | Symbol | Charge | Mass ($GeV/c^2$) |
|---|---|---|---|
| Up | u | $\frac{2}{3}$ | $\sim 0.3$ |
| Down | d | $-\frac{1}{3}$ | $\sim 0.3$ |
| Strange | s | $-\frac{1}{3}$ | $\sim 0.5$ |
| Charmed | c | $\frac{2}{3}$ | 1.6 |
| Bottom (Beauty) | b | $-\frac{1}{3}$ | 4.3 |
| Top (Truth) | t | $\frac{2}{3}$ | 180 |

Table 2-2: Quark Properties. Units are identical to Table 2-1.

do not naturally exist. Instead, each of these particles must be created in a high energy collision and tend to decay shortly afterwards into one of the lighter partons; u, d, and e.

A few of the lepton properties can be found in Table 2-1, while the corresponding properties for quarks can be found in Table 2-2. There is evidence to suggest that this list is complete [7] and that no further families will be found. The final member of the quark family, the top quark, was only recently discovered. This discovery was made in 1995 at Fermi National Laboratory [8, 9].

With the exception of mass, all leptons have nearly the same properties. Each of the leptons (e, $\mu$, and $\tau$) has a corresponding neutrino ($\nu_e$, $\nu_\mu$, and $nu_\tau$) which is assumed massless. Neutrinos are difficult to detect experimentally because they interact solely through the weak force; whereas electrons, muons, and taus interact via both the weak and electromagnetic forces. Interactions through the weak force typically produce cross sections $10^{-8}$ times smaller than those produced by the electroweak force. Thus, neutrinos are much more difficult to detect than the other leptons.

Quarks are massive spin 1/2 fermions. They are unique in that they interact via all four of the fundamental forces: strong, weak, electromagnetic, and gravity. However, quark properties are difficult to measure directly, because quarks apparently do not exist as free entities. Instead, they are found only in bound states known as hadrons. At large distances, individual quarks do not directly interact with other quarks. Instead, hadrons interact with other hadrons through the exchange of pions. In higher energy interactions, individual quarks *can* interact with each other through the exchange of gluons.

In all hadrons, the ($q\overline{q}$) and (qqq) configuration of the quarks completely determine the quantum numbers of the hadron. These quarks are known as the valence quarks. In addition to the valence quarks, hadrons contain a fluctuating cloud (or *sea*) of virtual quarks and gluons. These virtual particles are continually created and annihilated within the hadron under the constraint of the Heisenberg uncertainty principle. The particle sea can play a role in high energy collisions, because partons

| Force | Boson Name | Symbol | Charge | Spin | Mass ($GeV/c^2$) |
|---|---|---|---|---|---|
| Strong | gluon | $g$ | 0 | 1 | 0 |
| Electromagnetic | photon | $\gamma$ | 0 | 1 | 0 |
| Weak | W-boson | $W^{\pm}$ | $\pm 1$ | 1 | 81 |
| | Z-boson | $Z^0$ | 0 | 1 | 92 |
| Gravitational | graviton | $G$ | 0 | 2 | 0 |

Table 2-3: Gauge Boson Properties. Units are the same as Table 2-1

in the sea of one hadron can interact with the partons within another hadron.

All of the quarks and leptons interact with each other through the exchange of integer spin gauge bosons. These bosons are the mediators of the the four fundamental forces. Each of these four forces and their respective bosons are listed in Table 2-3.

A mathematical tool which can be used to describe these forces is quantum field theory. In quantum field theory, particles are associated with functions of space-time coordinates known as fields. A standard technique in field theory is to use a perturbative approach to describe physical processes. This approach involves expressing cross sections as power series expansions in the coupling constant. This technique, however, introduces new difficulties as it is possible for terms in the expansion to diverge. Often these singularities are difficult to deal with mathematically.

An example of a very successful quantum field theory is quantum electrodynamics (QED). QED has the property that all unphysical infinite contributions can be consistently eliminated through a cancelation procedure. Theories with this property are said to be renormalizable. This property can be traced back to the fact the QED is a local gauge theory. In particular, the Lagrangian is unchanged by the local gauge

transformations of the electron field $\psi(x)$ and the photon field $A_\mu(x)$ at all space-time points $x$

$$\begin{aligned} \psi(\mathrm{x}) &\rightarrow \mathrm{e}^{\mathrm{ie}\Lambda(\mathrm{x})}\psi(\mathrm{x}), \\ \mathrm{A}_\mu(\mathrm{x}) &\rightarrow \mathrm{A}_\mu(\mathrm{x}) + \delta_\mu\Lambda(\mathrm{x}), \end{aligned} \tag{2.1}$$

where $\Lambda(x)$ is arbitrary and $e$ is the electron-photon coupling strength. Exact gauge invariance is possible only if the gauge bosons are massless. Since we require that electroweak and strong interaction theories be renormalizable, it is required that their Lagrangians be locally gauge invariant.

The phase factor $e^{i\Lambda(x)}$ belongs to the symmetry group U(1). In this case, the group is Abelian since the generator of the group commutes with itself. In less trivial groups, such as SU(2) and SU(3), this is not true. Here the generators follow the relation

$$[\mathrm{T}^\mathrm{a}, \mathrm{T}^\mathrm{b}] = \mathrm{f}^{\mathrm{abc}}\ \mathrm{T}^\mathrm{c}, \tag{2.2}$$

where $f^{abc}$ are non-vanishing. A consequence of using nonabelian groups is that the resulting gauge bosons will be self-coupling. Self-coupling gauge bosons exist in both electroweak and QCD theories.

The combination of the theory of electroweak interactions (Glashow, Salam, and Weinburg) [10, 11, 12, 13, 14] with the theory of strong interactions [15, 16, 17] is collectively known as the Standard Model. Both theories are nonabelian implying that the theory contains self-coupling gauge bosons. Currently, gravity is not included

in the model. Developing a self-consistent field theory for gravity is a formidable task fraught with many mathematical difficulties; however, string theories provide an example of how this unification may be possible [18, 19].

The Standard Model has been phenomenologically successful in that it is calculable and explains a vast body of high energy data. To date, no experiment has been able to seriously contradict it.

### 2.1.1 Theory of Electroweak Interactions

Electroweak theory unifies Quantum Electrodynamics (QED) and the V-A theory of weak interactions. This combined theory is formulated such that it is invariant under the quantities:

- **Isospin (I)** requires that left handed quarks and leptons form doublets. Right handed members form singlets. The (assumed) right handed neutrinos do not take part in weak interactions and have never been observed. The asymmetry between left and right handed particles violates parity in the weak interaction.

- **Hypercharge (Y)** is related to both the electric charge and the isospin projection ($I_3$) by the Gell-Mann-Nishijima relation $Q = I_3 + Y/2$.

Electroweak theory is based upon the direct product of the groups generated by the local gauge invariance of $I$ and $Y$, $SU(2)_L \otimes U(1)_Y$. In order to obtain local gauge invariance of the Lagrangian, gauge covariant derivatives, which contain

gauge bosons, must be introduced. This produces four massless bosons: three for $SU(2)_L$ $(W^1_\mu, W^2_\mu, W^3_\mu)$ and one for $U(1)_Y$ $(B_\mu)$. However, the finite range of the weak interaction implies that in reality there are three massive bosons $(W^\pm, Z^0)$, and one massless boson $(\gamma)$. The Higgs mechanism was developed to reconcile this difference. This mechanism involves introducing four real scalar fields, $\varphi_i$, into the electroweak Lagrangian. It is convenient to arrange these four scalar fields into an isospin doublet with hypercharge, $Y = 1$,

$$\varphi = \begin{pmatrix} \varphi^+ \\ \varphi^0 \end{pmatrix} \quad \text{with} \quad \begin{aligned} \varphi^+ &= (\varphi_1 + i\varphi_2)/\sqrt{(2)} \\ \varphi^0 &= (\varphi_3 + i\varphi_4)/\sqrt{(2)} \end{aligned} \tag{2.3}$$

and a nonzero vacuum expectation value

$$\varphi_0 = \sqrt{\frac{1}{2}} \begin{pmatrix} 0 \\ v \end{pmatrix}. \tag{2.4}$$

The interaction of this field with the other fields in the theory gives mass to the gauge bosons and fermions. The resulting massive bosons and their masses are given by

$$\begin{aligned} W^\pm_\mu &= \tfrac{W^1_\mu \mp i W^2_\mu}{\sqrt{2}} & M^2_W &= \left(\tfrac{g\nu}{2}\right)^2 \\ Z_\mu &= -B_\mu \sin\theta_W + W^3_\mu \cos\theta_W & M^2_Z &= \left(\tfrac{M_W}{\cos\theta_W}\right)^2 \\ A_\mu &= B_\mu \cos\theta_W + W^3_\mu \sin\theta_W & M^2_A &= 0, \end{aligned} \tag{2.5}$$

where $\theta_W$ is the weak mixing angle $(\sin^2\theta_W = 0.23)$.

In addition to providing mass to the partons that need it, the Higgs mechanism also leaves us with a massive scalar particle, the Higgs boson. This particle has

yet to be discovered, and its mass is a free parameter in the theory. This is not unprecedented as the masses of leptons and quarks are also free parameters which must be determined through experiment.

An added complication is that the weak isospin eigenstates of the quarks, $q'$, are not equal to their mass eigenstates, $q$. These states are connected by a unitary matrix, $V$, known as the Cabibo-Kobayashi-Maskawa (CKM) matrix [20, 21]. By convention, this matrix acts only on the (d,s,b) quarks.

$$\begin{pmatrix} d' \\ s' \\ b' \end{pmatrix} = \begin{pmatrix} V_{ud} & V_{us} & V_{ub} \\ V_{cd} & V_{cs} & V_{cb} \\ V_{td} & V_{ts} & V_{tb} \end{pmatrix} \begin{pmatrix} d \\ s \\ b \end{pmatrix} \tag{2.6}$$

Matrix elements for leptons are not given, because the neutrinos are assumed to be massless.

The terms in the matrix are not independent of one another. It is possible to rewrite the CKM matrix in terms of 4 real parameters [22]

$$\mathrm{V} = \begin{pmatrix} c_{12}c_{13} & s_{12}c_{13} & s_{13}e^{-i\delta} \\ -s_{12}c_{23} - c_{12}s_{13}s_{23}e^{i\delta} & c_{12}c_{23} - s_{12}s_{13}s_{23}e^{i\delta} & c_{13}s_{23} \\ s_{12}s_{23} - c_{12}s_{13}c_{23}e^{i\delta} & -c_{12}s_{23} - s_{12}s_{13}c_{23}e^{i\delta} & c_{13}c_{23} \end{pmatrix} \tag{2.7}$$

where $s_{ij} = \sin(\theta_{ij})$, $c_{ij} = \cos(\theta_{ij})$, and $\delta$ is a real phase. For $\delta \neq 0$ or $\pi$, the theory is not invariant under charge $\otimes$ parity (CP) conjugation. This CP violation has been observed in the decay of the neutral kaon particles, $K_L \rightarrow \pi^-\pi^+$ and $K_L \rightarrow \pi^0\pi^0$ which was observed in 1964 [23] with a branching fraction on the order of $10^{-3}$.

### 2.1.2 Quantum Chromodynamics (QCD)

Quantum Chromodynamics is based upon the SU(3) color group. 'Color' can be thought of as the strong force equivalent of electric charge. In Quantum Chromodynamics, the strongly interacting particles which carry color charge are the quarks. The quarks can assume one of three color states (or anti-color states). Further, local gauge invariance under $SU(3)_c$ requires eight massless gauge bosons (which themselves also carry color charge).

It is important to note that quarks and gluons have never been observed as free particles. Instead, they are confined within colorless bound states. This confinement is a feature of QCD that occurs because the coupling strength between quarks and gluons *increases* with increasing distance between the partons. Thus, an infinite amount of energy would be required for a quark (or gluon) to become a free particle. Instead, it is energetically more feasible for the parton to fragment forming additional $q\overline{q}$ pairs. The resulting quarks then form into hadrons which all move in the general direction of the original parton. This process is known as hadronization, and collectively these hadrons are referred to as *jets*. The observation of these jets is perhaps the closest that we can come experimentally to observing individual gluons and quarks.

Another important feature of the strong force is that the coupling strength approaches zero at very small interaction distances. At these short distances quarks behave as free particles. This condition is referred to as *asymptotic freedom*.

## 2.2 Theory of Heavy Flavor Production

The general expression for the cross section between two colliding hadrons is given by

$$d\sigma_{H1H2} = \sum_{i,j} \int dx_1 dx_2 d\hat{\sigma}_{ij}(x_1 P_1, x_2, P_2, k_1, k_2, m, \mu) f_i^{H_1}(x_1, \mu) f_j^{H_2}(x_2, \mu), \qquad (2.8)$$

where $k_{1,2}$ are the momenta of the quark and antiquark, $f_i^{H_k}$ are the structure functions for the $i_{th}$ parton of the incoming hadron $H_k$ with momentum $P_k$, $d\hat{\sigma}_{ij}$ is the short distance parton-parton cross section, $m$ is the mass of the heavy quark, and $\mu$ is the subtraction scale for ultraviolet and collinear divergences. Unfortunately, the terms of this equation can not be calculated directly. Instead, the expression must be expanded as a power series in increasing powers of the strong coupling constant, $\alpha_s$.

### 2.2.1 The Strong Coupling Constant

In Quantum Chromodynamics the behavior of the coupling constant is very different than in Quantum Electrodynamics. In QED the running coupling constant increases (decreases) with decreasing (increasing) interaction distances. The opposite is true in QCD. The primary reason for this behavior in QCD is that gluons carry color charge and can couple with other gluons. Some of the details of this behavior are illustrated in this section.

Following the discussion by Field [24], we begin by looking at the lowest order contribution to the propagating gluon, the bubble diagram, $B_{QCD}(Q^2)$. These con-

tributions consist of gluon propogators that contain internal quark and gluon loops (Fig. 2-1). Choosing the Coulomb gauge, this contribution, can be written as

$$\alpha_0 B_{QCD}(Q^2) = -\alpha_0 \tilde{a} \log(\lambda^2/Q^2), \tag{2.9}$$

where $\lambda$ is the ultraviolet cutoff, $\alpha_0$ is the bare quark-gluon coupling constant, $q^2 = -Q^2$ is the 4-momentum squared of the gluon propogator,

$$\tilde{a} = \frac{1}{4\pi}(\frac{2}{3}n_f + 5 - 16), \tag{2.10}$$

and $n_f$ is the number of quark flavors. In this expression, the terms $+\frac{2}{3}n_f$ and $+5$ come from quark loop and gluon loop graphs respectively. The -16 comes from a virtual graph containing a ghost loop that is needed to eliminate extraneous gluon polarization states. These extra states are introduced by our choice of a covariant gauge.

If $\frac{2}{3}n_f < 11$ then $\tilde{a}$ is negative implying that contributions from the bubble graphs increase as $Q \to 0$ (increasing distance). This behavior is strikingly different than in QED in which the opposite is true. This effect is illustrated in Fig. 2-2.

In QED, the ultraviolet divergences are handled through a renormalization scheme that takes the experimental electric charge to be $e \equiv \lim_{Q^2 \to 0} \alpha_{QED}(Q^2)$. This can not be done in QCD because the contributions from Eq. 2.9 grow infinitely large as $Q^2 \to 0$. Taking such a limit would require one to resort to nonperturbative techniques. An alternative approach defines some value of $Q^2$ at which the coupling strength, $\mu^2 \equiv Q^2$, is defined. The coupling at all other $Q^2$ is then found with respect

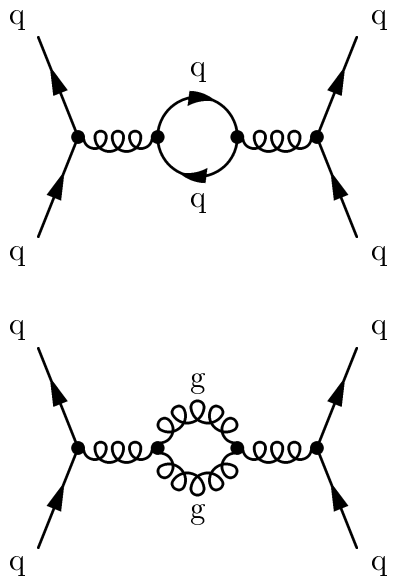


Figure 2-1: The lowest order corrections to the strong coupling are due to virtual quark-antiquark and gluon-gluon virtual loops.

to $\mu^2$ which is referred to as the renormalization or subtraction point.

The bubble corrections to $\alpha_s(Q^2)$ form a geometric series

$$\alpha_s(Q^2) = \alpha_0[1 + \alpha_0 B_{QCD}(Q^2) + \alpha_0 B_{QCD}(Q^2)\alpha_0 B_{QCD}(Q^2) + \cdots]. \tag{2.11}$$

Instead of arbitrarily truncating this expression at a finite order, it is more convenient to keep all the terms of the expression writing it as

$$\alpha_s(Q^2) = \frac{\alpha_0}{1 - \alpha_0 B_{QCD}(Q^2)}, \tag{2.12}$$

so that

$$\frac{1}{\alpha_s(Q^2)} = \frac{1}{\alpha_0} - B_{QCD}(Q^2). \tag{2.13}$$

The bare charge, $\alpha_0$, is unobservable and must be eliminated from the expression.

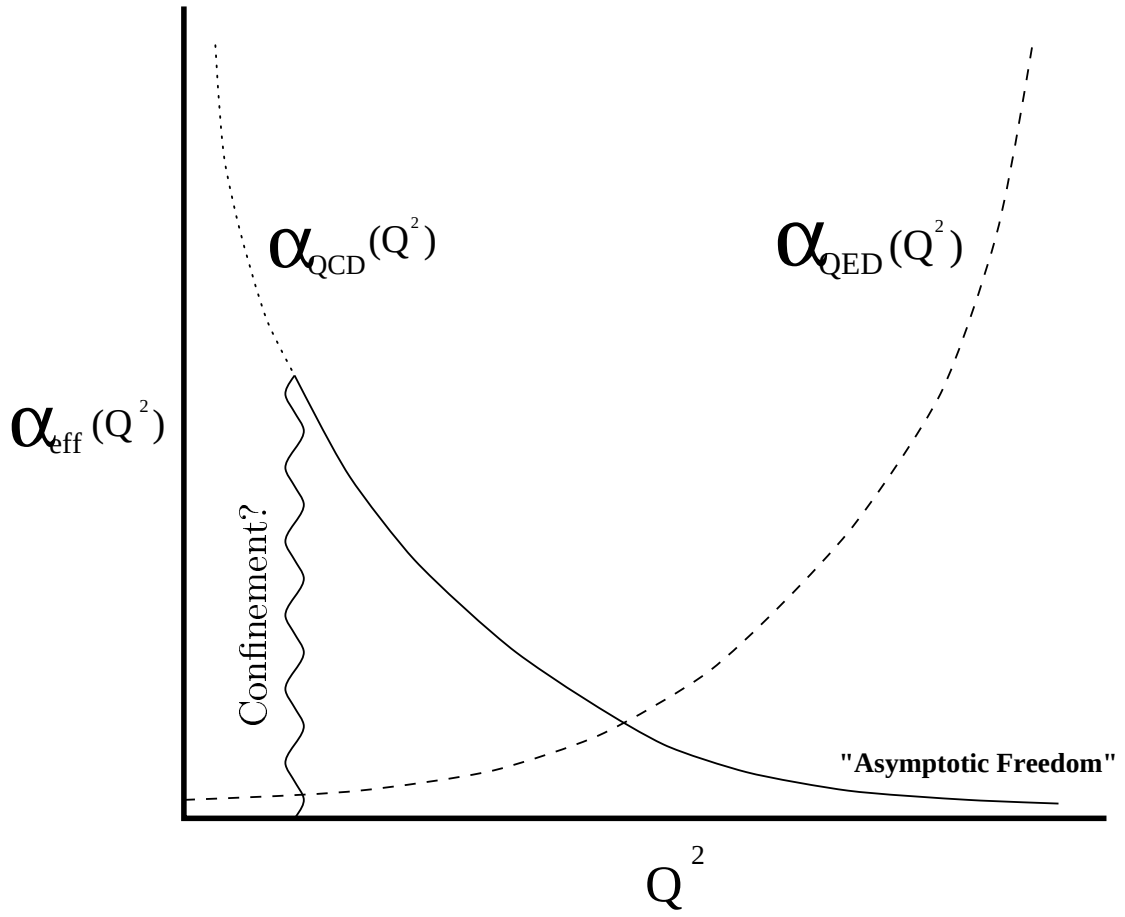


Figure 2-2: An illustration of the behavior of the QED and QCD effective coupling strengths as a function of the energy scale, $Q^2$. In QED, the effective coupling strength, $\alpha_{QED}(Q^2)$, is small with small $Q^2$, but grows large with large $Q^2$ (short distances). With QCD, the effective coupling strength, $\alpha_{QCD}(Q^2)$, grows large with decreasing $Q^2$ where quark confinement occurs but decreases with increasing $Q^2$ (asymptotic freedom).

Defining

$$\alpha_s \equiv \alpha_s(\mu^2), \tag{2.14}$$

and subtracting $\frac{1}{\alpha_s}$ from $\frac{1}{\alpha_s(Q^2)}$ leads to

$$\frac{1}{\alpha_s} = \frac{1}{\alpha_s(Q^2)} - (B_{QCD}(Q^2) - B_{QCD}(\mu^2)). \tag{2.15}$$

Substituting Eq. 2.9 into Eq. 2.15 gives

$$\alpha_s(Q^2) = \frac{\alpha_s(\mu^2)}{1 + \alpha_s(\mu^2)\frac{\beta_0}{4\pi}\log(Q^2/\mu^2)}. \tag{2.16}$$

It is important to note that the renormalization point, $\mu$, was arbitrarily chosen. Had another point, $\overline{\mu}$, been chosen then the two expressions would be related through

$$\frac{1}{\alpha_s(\overline{\mu}^2)} = \frac{1}{\alpha_s(\mu^2)} + \frac{\beta_0}{4\pi}\log(\overline{\mu}^2/\mu^2). \tag{2.17}$$

This means that $\alpha_s(Q^2)$ is not a function of $\alpha_s(\mu^2)$ and $\mu^2$ separately. Instead, $\alpha_s(Q^2)$ has a dependence upon a new function, $\Lambda$, which is independent of $\mu$.

$$\log(\Lambda^2) = -\frac{4\pi}{\beta_0\alpha_s(\mu^2)} + \log(\mu^2). \tag{2.18}$$

Inserting this expression into Eq. 2.16 yields

$$\alpha_s(Q^2) = \frac{4\pi}{\beta_0\log(Q^2/\Lambda^2)}, \tag{2.19}$$

where $\Lambda$ is a parameter not predicted by the theory. This expression gives $\alpha_s(Q^2)$ through $\mathcal{O}(\alpha_s^2)$.

For completeness, the next-to-leading order expression for $\alpha_s(Q^2)$ is given. This expression keeps terms out to $\mathcal{O}(\alpha_s^3)$.

$$\alpha_s(Q^2) = \frac{4\pi}{\beta_0 \log(Q^2/\Lambda^2)} \left[1 - \frac{(306 - 38n_f)}{3\beta_0^2} \frac{\log\log(Q^2/\Lambda^2)}{\log(Q^2/\Lambda^2)}\right]. \tag{2.20}$$

There is some freedom as to how one chooses $\Lambda$. Formally $\Lambda$ is defined as

$$\Lambda = \mu \cdot \exp\left\{\frac{1}{2}\int_{\alpha_s(\mu^2)}^{A} \frac{d\alpha}{\beta(\alpha)}\right\}, \tag{2.21}$$

where $A$ is an arbitrary constant which is chosen by convention. Unless otherwise stated, the renormalization scheme used in this thesis will be the "modified minimal subtraction" ($\overline{\text{MS}}$) scheme [25] to next-to-leading order when defining $\Lambda$.

### 2.2.2 Parton-Parton Cross section

#### Leading Order Contributions

The lowest order contribution to the single heavy quark cross section ($\mathcal{O}(\alpha_s^2)$) consists of quark-antiquark annihilation and gluon-gluon fusion terms.

$$\begin{aligned} q(p_1) + \overline{q}(p_2) &\rightarrow Q(k_3) + \overline{Q}(k_4) \\ g(p_1) + g(p_2) &\rightarrow Q(k_3) + \overline{Q}(k_4) \end{aligned} \tag{2.22}$$

The Feynman diagrams used to calculate the matrix elements for these processes are shown in Fig. 2-3 [26]. The details of this calculation can be found in many standard QCD texts [27, 28]. The resulting squared matrix elements are averaged (summed) over the initial (final) color and spin states and are written in terms of the following

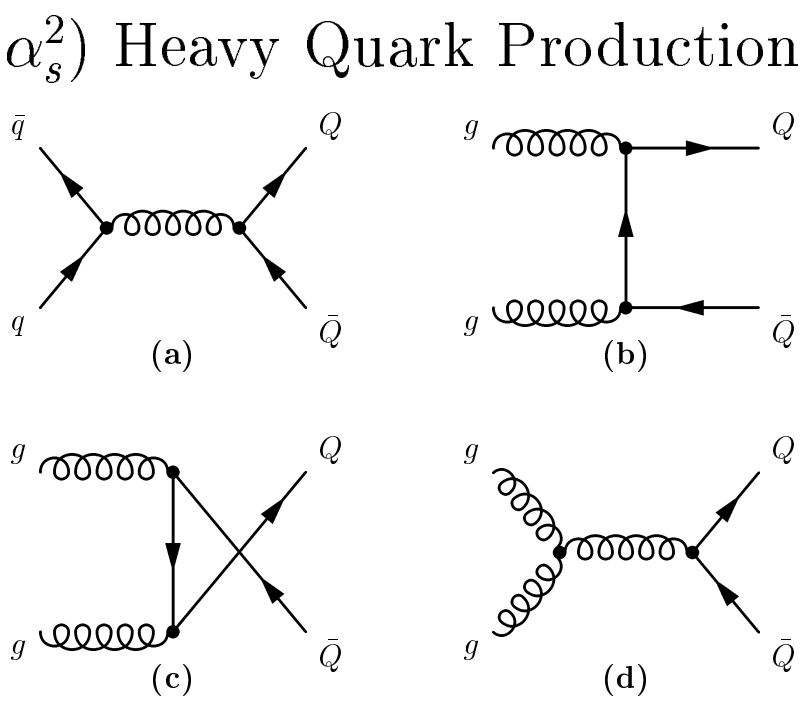


Figure 2-3: The lowest order heavy quark production graphs. The dominate contribution to the leading order cross section are from initial $gg$ states (graphs b, c, and d).

4-vectors

$$\tau_1 = \frac{2p_1 \cdot k_3}{\hat{s}} = \frac{m_Q^2 - \hat{t}}{\hat{s}},\ \tau_2 = \frac{2p_1 \cdot k_4}{\hat{s}} = \frac{m_Q^2 - \hat{u}}{\hat{s}},\ \rho = \frac{4m_Q^2}{\hat{s}}, \tag{2.23}$$

where $\hat{s}$, $\hat{t}$, and $\hat{u}$ are the Mandelstam variables describing $2 \rightarrow 2$ parton-parton scattering processes. The resulting matrix elements are listed in Table 2-4.

These matrix elements can be used to calculate cross sections. In the center of momentum coordinate system, the following equation can be used to calculate the single heavy quark production cross section [4, 29, 30]

$$\frac{d\hat{\sigma}_{ij}}{dyd^2k_t} = \frac{1}{\hat{s}^2}\delta(1 - \tau_1 - \tau_2) \sum \mid \overline{M_{ij}}\mid^2. \tag{2.24}$$

| Process | $\sum \mid \overline{M_{ij}} \mid^2$ |
|---|---|
| $q\overline{q} \rightarrow Q\overline{Q}$ | $\frac{2C_f^2}{D_A}\alpha_s^2(\tau_1^2 + \tau_2^2 + \rho/2)$ |
| $gg \rightarrow Q\overline{Q}$ | $\frac{2T_f}{D_A}\left(\frac{C_f}{\tau_1\tau_2} C_A\right)\alpha_s^2\left(\tau_1^2 + \tau_2^2 + \rho - \frac{\rho^2}{4\tau_1\tau_2}\right)$ |

Table 2-4: The squared matrix elements for the leading order contributions to heavy flavor production. The constants, $C_A$, $C_f$, $D_A$, and $T_f$ depend upon the group representation being used. For SU(3) they are $C_A = 3$, $C_f = 4/3$, $D_A = 8$, and $T_f = 1/2$.

The useful normalization scales, $\mu$, have a lower bound which is given approximately by the mass of the heavy quark. Therefore, cross sections calculated for the bottom and top quarks can be considered reliable, but perturbative calculations for lighter quarks can be considered approximations at best. The renormalization scales required for these lighter masses, $m_c = 1.5$ GeV, forces $\alpha_s$ to become large making it difficult to use perturbative techniques [2].

### Higher Order Contributions

The naive expectation is that higher order processes will contribute less than leading order processes to the overall heavy quark cross section, since the next-to-leading order (NLO) terms are suppressed by an additional order of $\alpha_s(Q^2)$. Unlike many other QCD processes, heavy flavor production is an exception, because the QCD process $gg \rightarrow gg$ is heavily favored over $gg \rightarrow Q\overline{Q}$. In fact, the cross section for $gg \rightarrow gg$ is roughly 100 times larger.

$$\frac{\sigma(gg \rightarrow gg)}{\sigma(gg \rightarrow Q\overline{Q})} \sim 100. \tag{2.25}$$

The subsequent splitting of a gluon into a $Q\overline{Q}$ pair suppresses the $2 \rightarrow 2$ diagram, $gg \rightarrow gg$, by an additional order of $\alpha_s(Q^2)$.

$$\begin{array}{rcl} gg & \rightarrow & g^* g \\ & & \downarrow \\ & & \hookrightarrow Q\overline{Q} \end{array} \tag{2.26}$$

The Feynman diagram showing this process can be seen in Fig. 2-5(a) (gluon splitting). Eq. 2.25 is strictly true only for on-mass-shell gluons. In processes such as those in Eq. 2.26, the virtual gluon is off-mass-shell by an amount that is of the order of the heavy quark mass. This gives an additional reduction in the gluon splitting cross section. However, large contributions to the overall cross section are still expected from $\mathcal{O}(\alpha_s^3)$ processes.

### 2.2.3 Structure Functions

The final component in the calculation of the heavy quark cross section are the structure functions. The structure functions are parameterizations describing the probability that a specific parton of a certain momentum will be found within a given hadron. These functions depend upon the energy scale at which they are evaluated. For convenience, this energy scale (factorization scale) is usually set equal to the renormalization scale used in evaluating $\alpha_s(Q^2)$.

The scale dependence is described by the Altarelli-Parisi equations [31]. In general, these equations are $2n_f+1$ dimensional matrix equations. The simplest case describes

one quark flavor and can be written as

$$\mu^2 \frac{\delta}{\delta \mu^2} \begin{pmatrix} q(x,\mu) \\ G(x,\mu) \end{pmatrix} = \frac{\alpha_s(\mu)}{2\pi} \int_x^1 \frac{dz}{z} \begin{pmatrix} P_{qq}(\frac{x}{z}, \alpha_s(\mu)) & P_{qg}(\frac{x}{z}, \alpha_s(\mu)) \\ P_{gq}(\frac{x}{z}, \alpha_s(\mu)) & P_{gg}(\frac{x}{z}, \alpha_s(\mu)) \end{pmatrix} \times \begin{pmatrix} q(z,\mu) \\ G(z,\mu) \end{pmatrix} \tag{2.27}$$

where $q(x,\mu)$ ($G(z,\mu)$) are the quark (gluon) distribution functions in the hadron being considered. The $P_{ij}$ are the Altarelli-Parisi kernels that, to lowest order, can be considered the probability that a parton of type $i$ radiates from a parton of type $j$ with $i$ carrying a fraction, $x$, of $j$'s momentum. This expression has been evaluated to both LO [31] and NLO [32]. To leading order, $\mathcal{O}(\alpha_s^2)$, the quarks contained within hadrons can emit gluons, and gluons can split into $q\overline{q}$ pairs. This behavior is described by Eq. 2.27 and consequently makes the structure functions scale dependent.

In practice, the structure functions are obtained by parameterizing them at some scale $\mu_0$. The functions are then evolved to the other $\mu$, through the use of QCD scale $\Lambda$ (Eq. 2.18), at which experimental results on $x$ and $Q$ dependence are available. Information from experiments at different $\mu$ can be used to perform fits to find the best values for the structure function parameters.

Many different parameterizations have been developed to describe the structure functions. This thesis uses functions obtained from Eichten, Hinchliffe, Lane, and Quigg (EHLQ) [33, 34]; the CTEQ collaboration [35]; and Martin, Roberts, and Sterling (MRS) [36]. A recent compilation of all available sets can be found in reference [37]. The Monte Carlo in this thesis uses the CTEQ2L structure functions

almost exclusively, while the EHLQ set is used in a small fraction. Both CTEQ2L and EHLQ use LO QCD evolutions. This is appropriate as ISAJET [38] is a LO event generator. The MRS set is evaluated to NLO and is used in the NLO theoretical predictions of heavy quark production. The gluon structure functions for each of the sets used in this thesis are shown in Fig. 2-4.

## 2.3 Heavy Flavor Production at $p\overline{p}$ colliders

With all of the components of the heavy quark cross section assembled, Eq. 2.8 can be used to make predictions for heavy flavor production at the Tevatron. Nason, Dawson, and Ellis [3] were the first to calculate the total heavy quark production cross section through order $\alpha_s^3$. Later, [4] they extended this work producing a single particle inclusive differential cross section for heavy quarks. In doing this, they considered the following production mechanisms:

$$\begin{array}{llll} gg \to Q\overline{Q}X & q\overline{q} \to Q\overline{Q}X & gq \to Q\overline{Q}X & g\overline{q} \to Q\overline{Q}X \\ gg \to \overline{Q}Q X & \overline{q}q \to \overline{Q}QX & g\overline{q} \to \overline{Q}QX & gq \to \overline{Q}QX \end{array} \tag{2.28}$$

There are many difficulties involved in performing the above calculations including problems with collinear and infrared divergences in the phase-space integrals. These singularities make it difficult to perform the necessary numerical integrations. Nason *et al.* circumvented this problem by integrating over the recoil partons in the system. Doing so allowed them to isolate the divergences and integrate with cut-off values. They were then able to cancel the singularities in a proper manner. The disadvantage

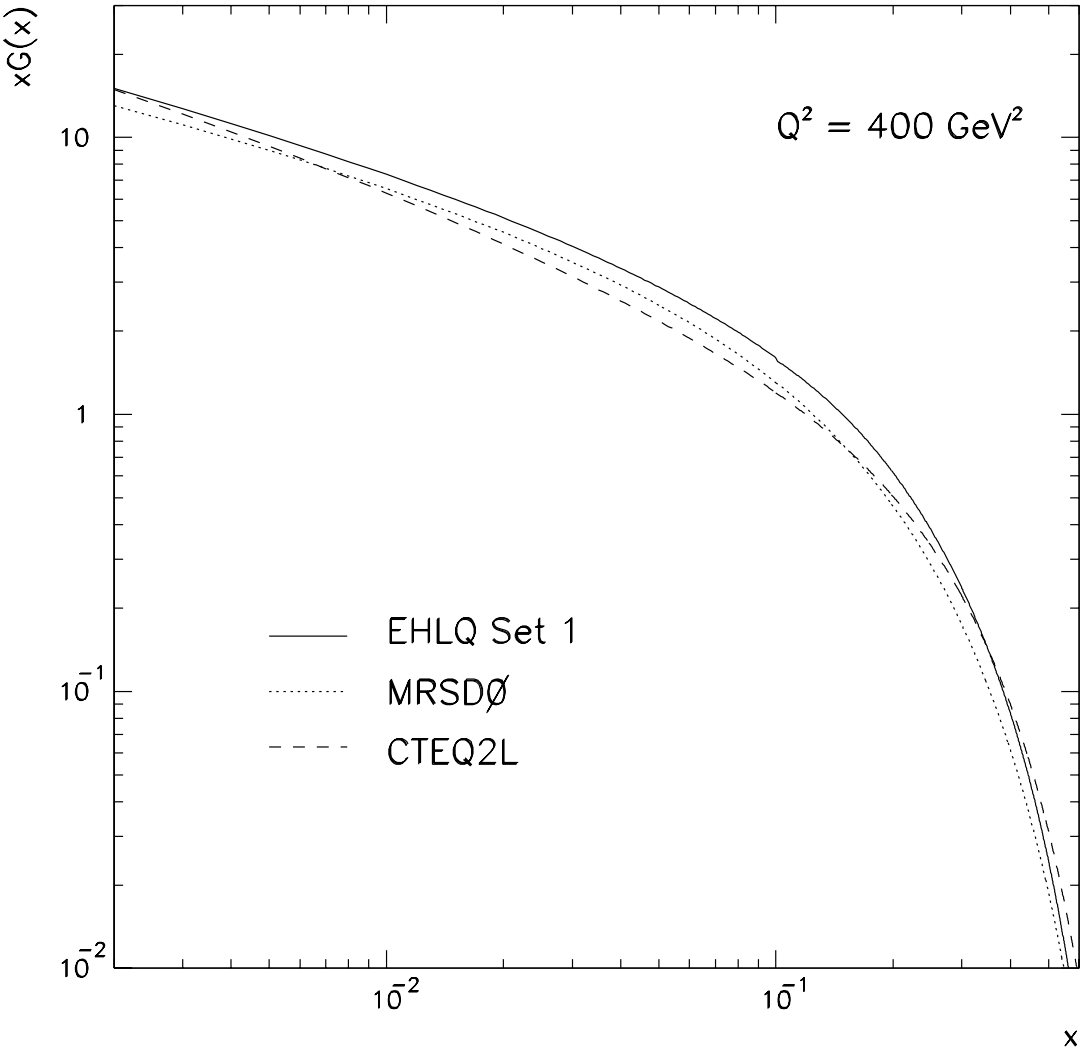


Figure 2-4: The gluon structure functions used in this thesis.

to this approach is that only a single quark cross section is obtained. All information about the recoil partons is lost. However, this cross section prediction can be used as a comparison to the measured $b$-quark production cross section.

Later, Mangano, Nason, and Ridolfi (MNR) were able to extend this into a fully exclusive $\mathrm{Q\overline{Q}}$ theory [2] for correlated heavy quark production. Here, they circumvented the difficulties encountered by Nason *et al.* by arranging the various contributions so that the cancelations are performed under the phase-space integrals. This calculation considers the processes:

$$\begin{array}{c} gg \rightarrow Q\bar{Q}g \\ q\bar{q} \rightarrow Q\bar{Q}g \\ gq \rightarrow Q\bar{Q}q \\ g\bar{q} \rightarrow Q\bar{Q}\bar{q} \\ q\bar{q} \rightarrow Q\bar{Q} \\ gg \rightarrow Q\bar{Q} \end{array} \tag{2.29}$$

Representative Feynman diagrams for the first four of these processes can be seen in Fig. 2-5(a)-(c). A by-product of these higher order processes is an additional light parton. The topology of these diagrams is much more complicated than the back-to-back topology of the leading order processes. As an example, gluon splitting can produce nearly collinear $Q\overline{Q}$ pairs along with light parton jet recoiling in the opposite direction.

In the full $\mathcal{O}(\alpha_s^3)$ cross section calculation, the last two processes in Eq. 2.29 (see Fig. 2-3) must be supplemented with virtual graphs. These virtual terms interfere

with the leading order terms (see Fig. 2-5(d)) and are needed in order to cancel infrared and collinear singularities in the real diagrams [4].

It is not possible to compare the results of MNR directly to data. Such a comparison requires that the $b$-quarks produced by MNR to be fragmented, hadronized, and allowed to decay into muons. A Monte Carlo package has been developed, HVQJET [39], which does this. The details of this will be given below. HVQJET will be used when comparing theory with the $\Delta\varphi_{\mu\mu}$ correlation measurements.

### 2.3.1 Inclusive Single Heavy Quark Production

The following parameters are used in the NDE[3, 4] calculation of the single inclusive heavy quark cross section.

- $b$-quark mass, $m_b = 4.75$ GeV/c$^2$.
- renormalization/factorization scale, $\mu_1 = \mu_2 = \sqrt{m_b^2 + p_t^2}$.
- MRSD0 structure function with $\Lambda_4^{QCD} = 215$ MeV.

In order to compare the theoretical prediction with the experimental data, the cross section must be written in a form that can be more directly related to the data. Generally, experimental data is sensitive to $b$-quark production within certain $P_T$ and $\eta$ regions that are defined by detector acceptances. Therefore, the theoretical prediction is written in the form

$$\sigma(p\overline{p} \rightarrow bX; p_t^b > p_t^{min}, \mid y_b \mid < y_{max}) = \int_{-y_max}^{y_max} dy_b \int_{p_t^{min}}^{\infty} dp_t^b \frac{d^2\sigma(p\overline{p} \rightarrow bX)}{dy_b dp_t^b}. \quad (2.30)$$

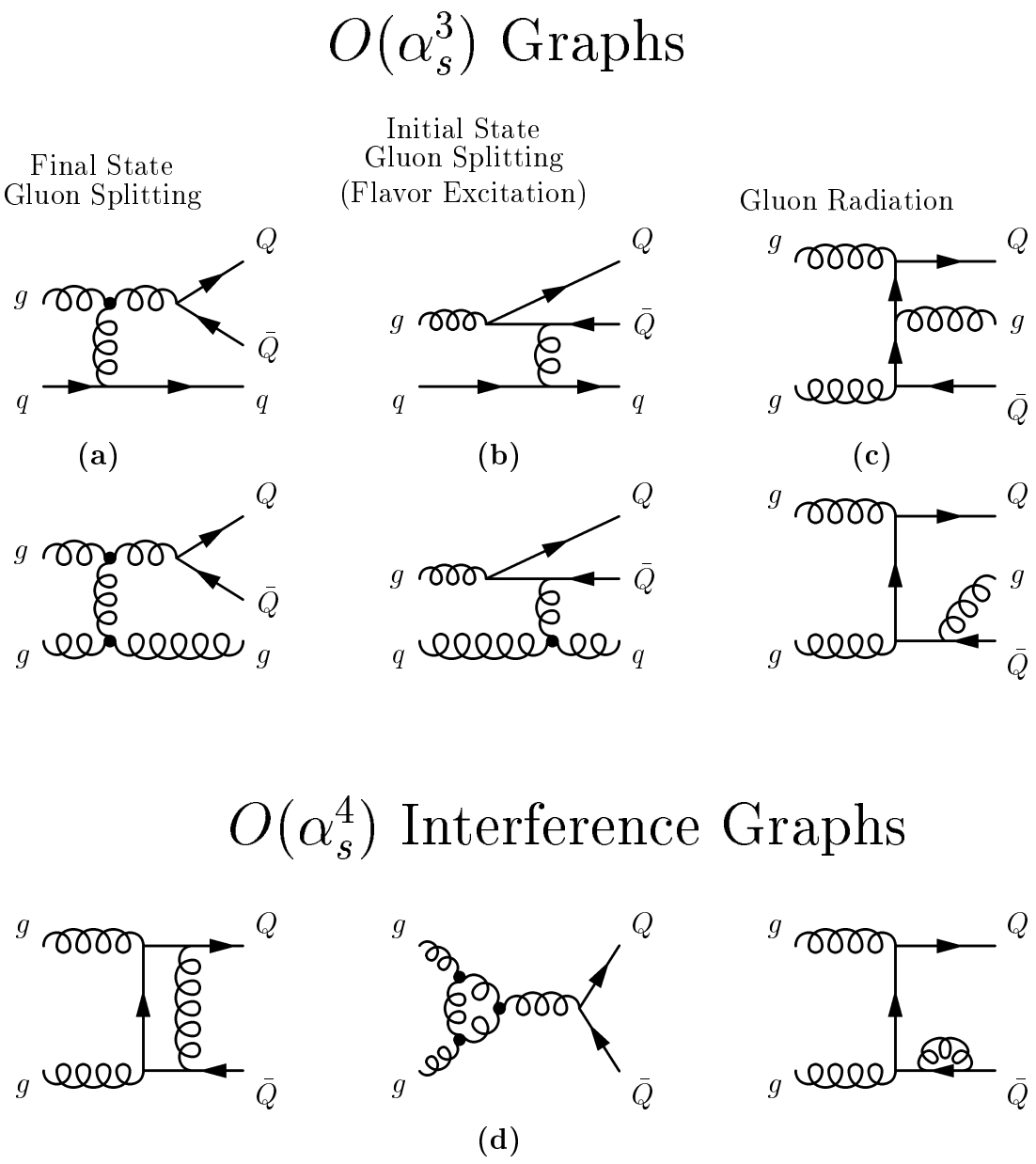


Figure 2-5: Some examples of the next-to-leading order heavy quark production graphs. Both final (a) and initial (b) state gluons can split into $Q\bar{Q}$ pairs. $O(\alpha_s^2)$ graphs can radiate gluons (c). Additional $O(\alpha_s^4)$ graphs (d) interfere with the lowest order production graphs shown in Fig. 2-3.

The resulting prediction can be seen in Fig. 2-6 for $\sqrt{s} = 1.8$ TeV and $y_{max} = 1$.

### 2.3.2 Correlated $b\overline{b}$ Production

A Monte Carlo event generator (HVQJET [39]) has been developed which is a direct implementation of the $\mathcal{O}(\alpha_s^3)$ calculation given by Mangano *et al.* [2]. MNR produces events with both positive and negative weights, and at times the negative weights are quite large. Cancelations of these weights is achieved by matching events with similar topologies. For example, a soft virtual event may be matched with a topologically similar real gluon event. ISAJET is then used to simulate initial and final state gluon radiations. ISAJET is also used for the modeling of the fragmentation, hadronization, and eventual decay of the $b$-quarks into muons (see Sections 5.1.1 and 5.1.2).

The HVQJET (MNR) uses the parameters:

- $b$-quark mass, $m_b = 5.0$ GeV/c$^2$.
- renormalization/factorization scale, $\mu_1 = \mu_2 = \sqrt{m_b^2 + [(P_T^1)^2 + (P_T^2)^2]/2}$.
- MRSA' structure function with $\Lambda_4^{QCD} = 215$ MeV.

Note that the renormalization and factorization scales have been modified to include knowledge of the second quark. The results of this calculation are shown in Fig. 2-7.

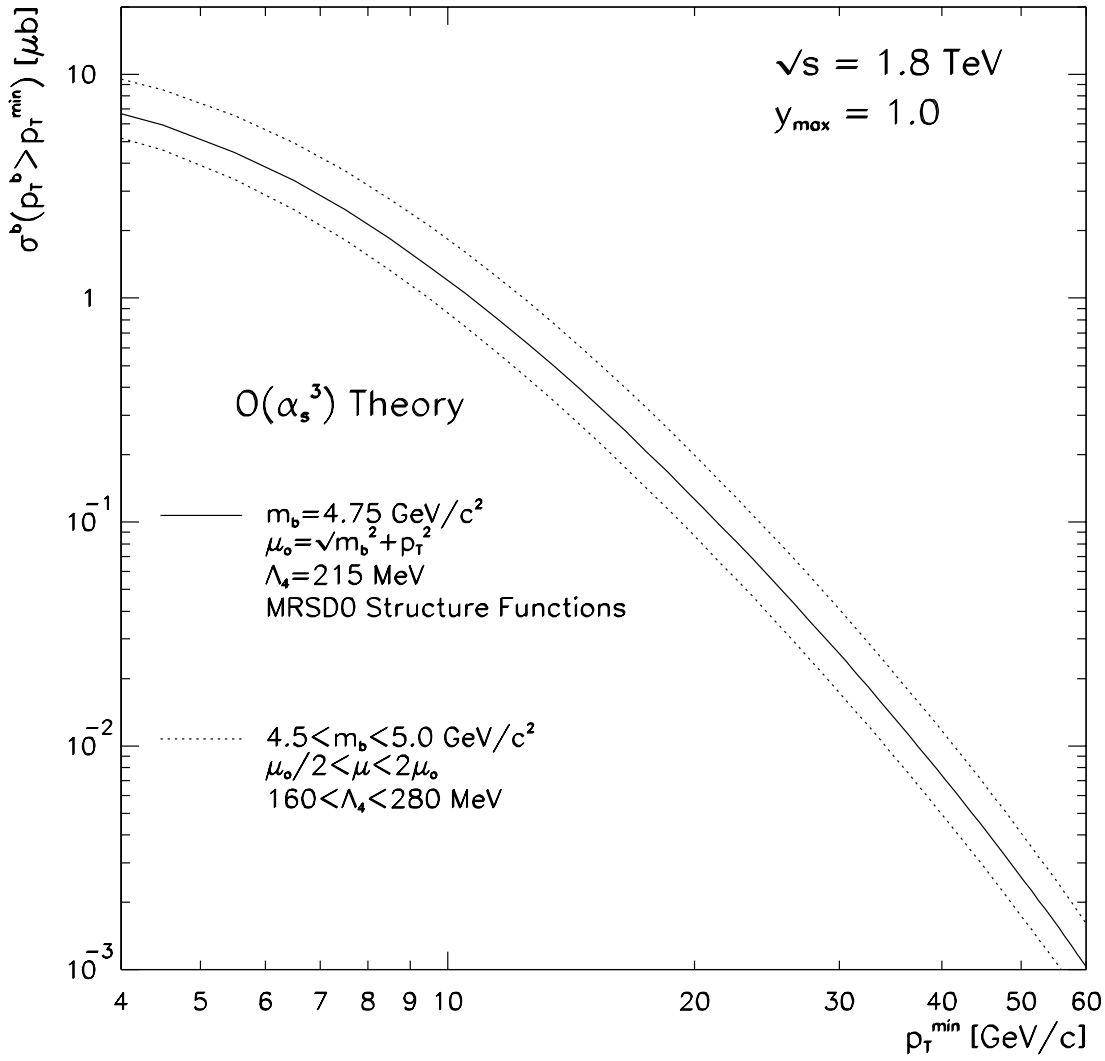


Figure 2-6: The NLO QCD prediction for the $b$-quark production cross section as given by Nason *et al.*.

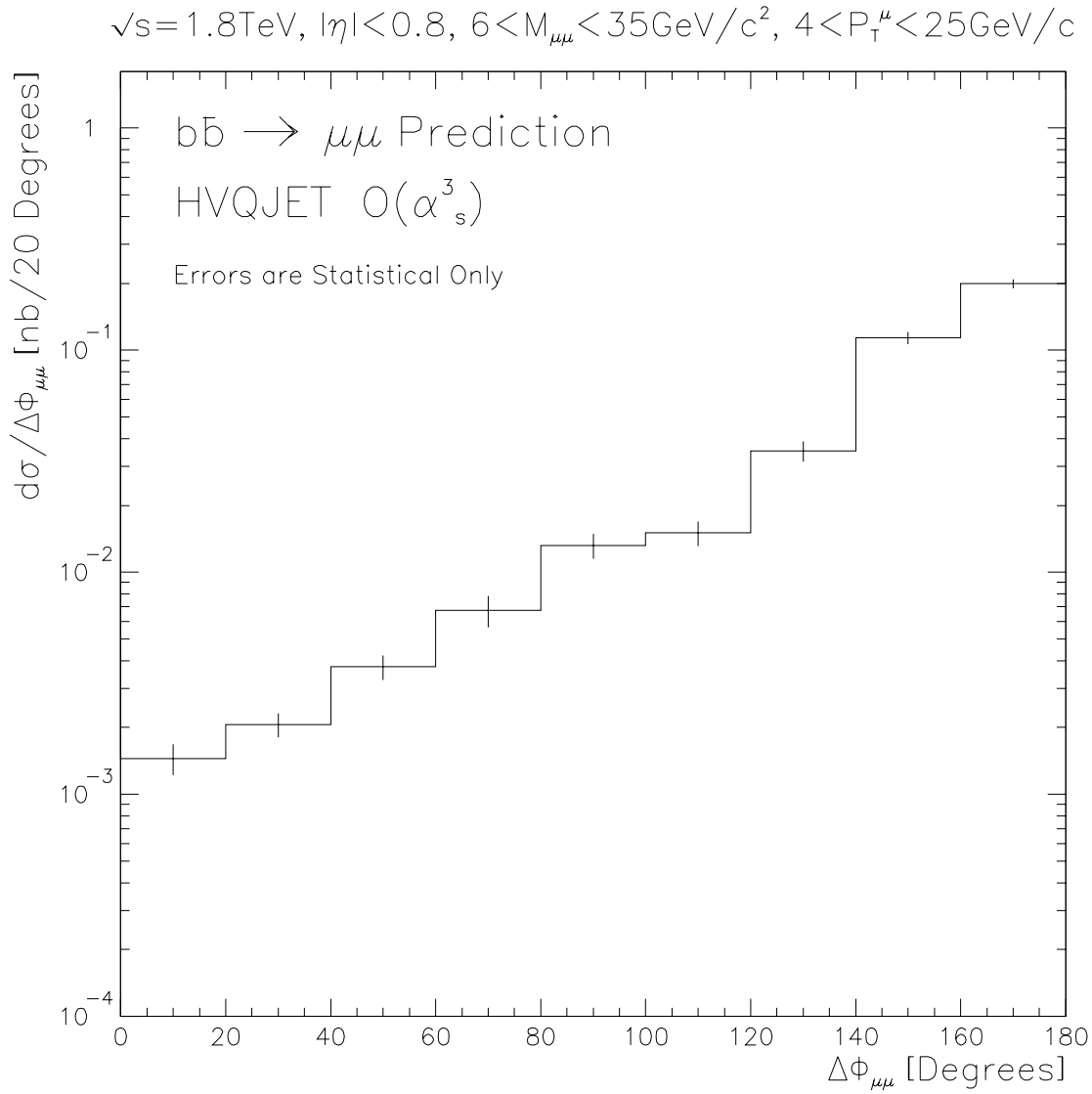


Figure 2-7: The differential $\Delta\varphi_{\mu\mu}$ distribution as predicted by HVQJET. The error bars are statistical only.

# Chapter 3

# The DØ Experiment

Fermi National Accelerator Laboratory (FNAL) currently holds the distinction of operating the world's highest energy particle accelerator. The Tevatron can be operated in a fixed target mode delivering 900 GeV particle beams to fixed target experiments, or it can be operated in collider mode producing counter-rotating proton and anti-proton beams with a combined center-of-momentum energy of $\sqrt{s} = 1.8$ TeV. In this mode, the beams are 'squeezed' into two luminous regions along the ring which are referred to as BØ(CDF) and DØ.

It is here that the DØ collaboration studies the high $P_T$ physics and high mass states that are produced by the colliding beams. Of particular note is the discovery of the elusive top quark which was simultaneously discovered by both DØ and CDF. [8, 9]. DØ has also focused on making precision measurements of the W mass, searching for new particles, and constraining perturbative QCD theory through the study of

hadronic jets and heavy quark production.

## 3.1 The Tevatron

The DØ experiment depends entirely upon the performance of Tevatron for both the quality and quantity of the data taken. The Tevatron is actually the final stage in a series of seven accelerators which are needed to create stable high energy colliding beams. These accelerators are the Cockroft-Walton pre-accelerator, the linac, the booster synchrotron, The Main Ring accelerator, the $\overline{p}$ debuncher and accumulator complex, and finally the Tevatron ring [40]. Fig. 3-1 shows the general layout of the machines.

Both the proton and the anti-proton beams actually begin their lives in a relatively small tank of hydrogen gas. A magnetron surface-plasma source is used to ionize the hydrogen gas. Electrons are added producing $H^-$ ions with an energy of 18 keV. These ions are then injected into the pre-accelerator where a Cockroft-Walton generator creates an electrostatic accelerating column boosting the hydrogen ions to 750 keV.

At this point, transport lines direct the beam into a two stage linear accelerator (linac). The first stage is an Alvarez drift-tube accelerator which boosts the ions up to 116 MeV. Then, a side-coupled linac continues to boost the ions up to 400 MeV. Throughout this process, quadrupole magnets act to focus the beam. These magnets are analogous to a focusing lens in optics. At the end of the linac is a carbon foil

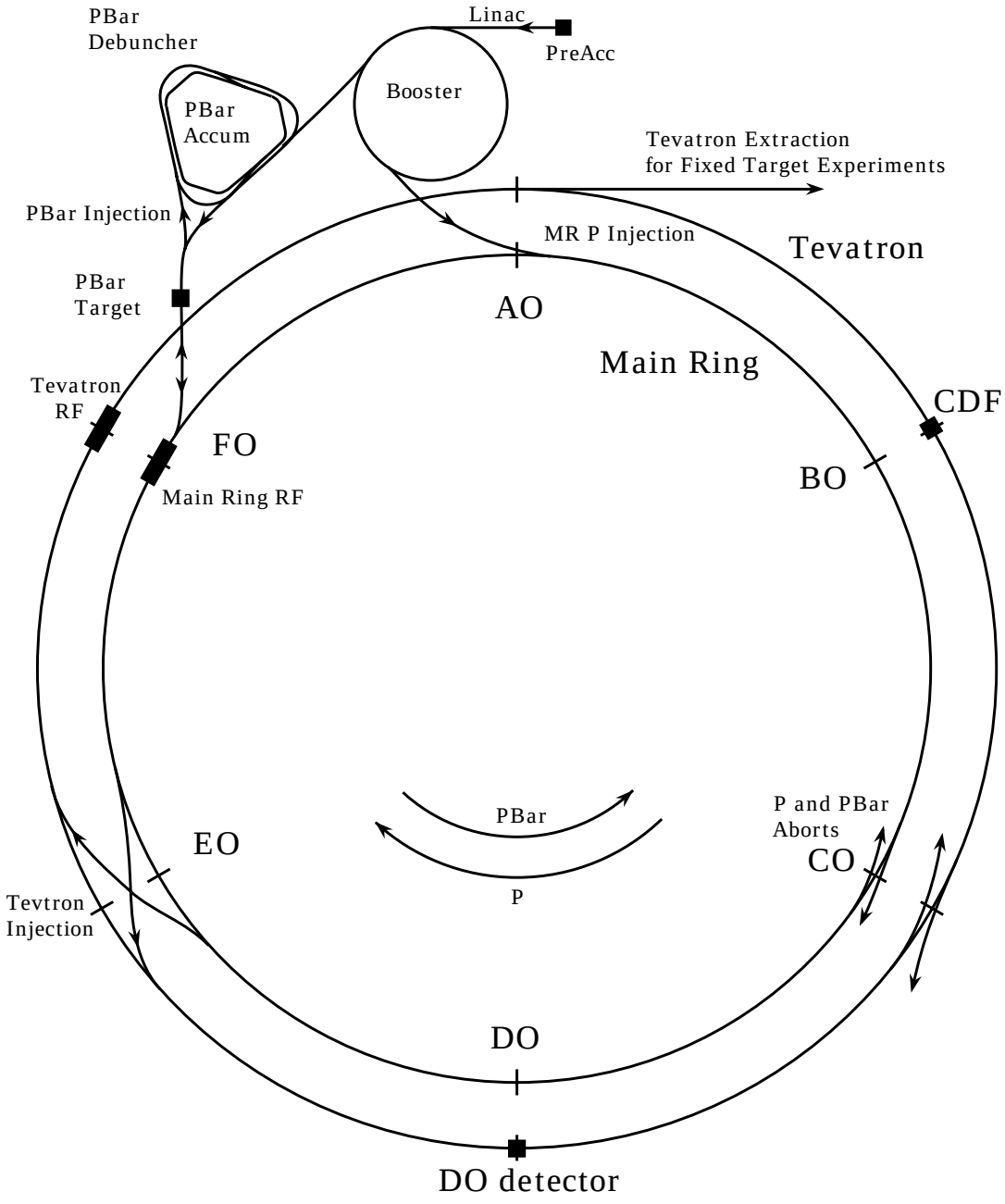


Figure 3-1: The Fermilab $p\overline{p}$ collider (not to scale). The Main Ring and the Tevatron actually have the same radius. Here, they are shown offset to clarify the figure.

target which strips the electrons from the hydrogen ions producing a proton beam.

The proton beam is injected into the booster accelerator, a synchrotron with a circular diameter of 151 meters. A total of 96 dual function dipole/quadrupole magnets focus and bend the beam to the required circular orbit. RF electromagnetic fields are used to further accelerate the protons. The frequency of this field is raised synchronously with the strength of the magnetic field. In this way, the increasingly energetic protons are kept in their circular orbit. The final energy of the protons before injection into the Main Ring is 8 GeV.

The Main Ring is a synchrotron with a diameter of 2 kilometers. One hundred copper coil bending and focusing magnets are used to control the beam. The Main Ring serves two purposes. The first is to feed the anti-proton source with protons. Proton bunches are accelerated up to 120 GeV and are directed at a nickel/copper target which produces anti-protons. Immediately after this target is a cylindrical lithium focusing lens. This lens works by sending a pulsed 0.5 MA current down its length producing an azimuthal magnetic field that collimates the anti-protons. This lens selects anti-protons that have energies near 8 GeV. Approximately $10^7$ anti-protons are produced for every $10^{12}$ incident protons. The second purpose of the Main Ring is to accelerate the proton and anti-proton beams to 150 GeV before separately injecting the two opposite moving beams into the Tevatron.

The initially incoherent anti-protons are injected into the $\overline{p}$ debuncher. The purpose of the debuncher is to reduce the phase space occupied by the initially incoherent

anti-protons. The debuncher uses a method known as stochastic cooling [41] to reduce the variations in momentum exhibited by the anti-protons. After the cooling process, approximately $2 \times 10^{10}$ anti-protons are sent into the accumulator. The accumulator further 'cools' the anti-protons and stores them until the accumulator contains approximately $2 \times 10^{11}$ anti-protons. At this point, there are enough anti-protons for a 'shot'. It usually takes 4 to 6 hours to gather enough anti-protons in the accumulator for a shot.

After enough antiprotons have been collected, the protons and anti-protons are ready for injection in the Tevatron. The Tevatron is located 2 feet below the main ring. It has approximately one hundred magnets which are used for focusing and steering the beam. These magnets are superconducting magnets that are cooled to 4.6 K by a liquid helium cooling system. Six proton bunches are injected into the the Tevatron from the Main Ring followed by the injection of six anti-proton bunches. Each proton bunch contains about $150 \times 10^9$ particles per bunch, while the anti-proton bunches usually contain $50 \times 10^9$ particles per bunch. The Tevatron then accelerates the proton and anti-proton bunches to 900 GeV producing collisions with a center-of-mass energy of 1.8 TeV and a bunch crossing time of around 3.5 $\mu$s. Throughout run 1B (see Fig. 3-2), the Tevatron was able to produce a wide range of instantaneous luminosities. The peak was $\sim 25 \times 10^{30} \mathrm{s}^{-1}$ cm$^2$, while the lower value was less than $1 \times 10^{30} \mathrm{s}^{-1}$ cm$^2$.

The final stage in producing collisions is to 'squeeze' the beam at the two luminous

| Running Period | Dates | Delivered Lum. | Recorded Lum. |
|---|---|---|---|
| 1a | 1992-1993 | $23.0\text{pb}^{-1}$ | $15\text{pb}^{-1}$ |
| 1b | 1994-1995 | $121.5\text{pb}^{-1}$ | $87.6\text{pb}^{-1}$ |
| 1c | 1995-1996 | $16.9\text{pb}^{-1}$ | $12.7\text{pb}^{-1}$ |

Table 3-1: The total integrated luminosity for the three running periods during run 1b. These number are estimated to be correct to within 5%.

regions at the Tevatron, BØ and DØ. This is accomplished through the use of special focusing magnets called the low beta quadrupoles. When finished, each beam has a cross sectional area of approximately 1 $\text{mm}^2$. Each 'store' generally lasts between 12 and 14 hours. While the protons and anti-protons continue to collide at DØ and CDF, the Main Ring continues to produce anti-protons. Thus, when the current store is terminated, enough anti-protons will have accumulated for the next 'shot'.

Fig. 3-2 shows the integrated luminosity produced at the Tevatron during run 1. The delivered and recorded integrated luminosities for each of the three running periods of run 1 are listed in Table 3-1. For this thesis, only the data taken during run 1b is used.

## 3.2 Introduction to the DØ Detector

In order to best study the physics produced at the Tevatron, the DØ experiment was designed with the following goals in mind:

- Excellent electron and muon identification.

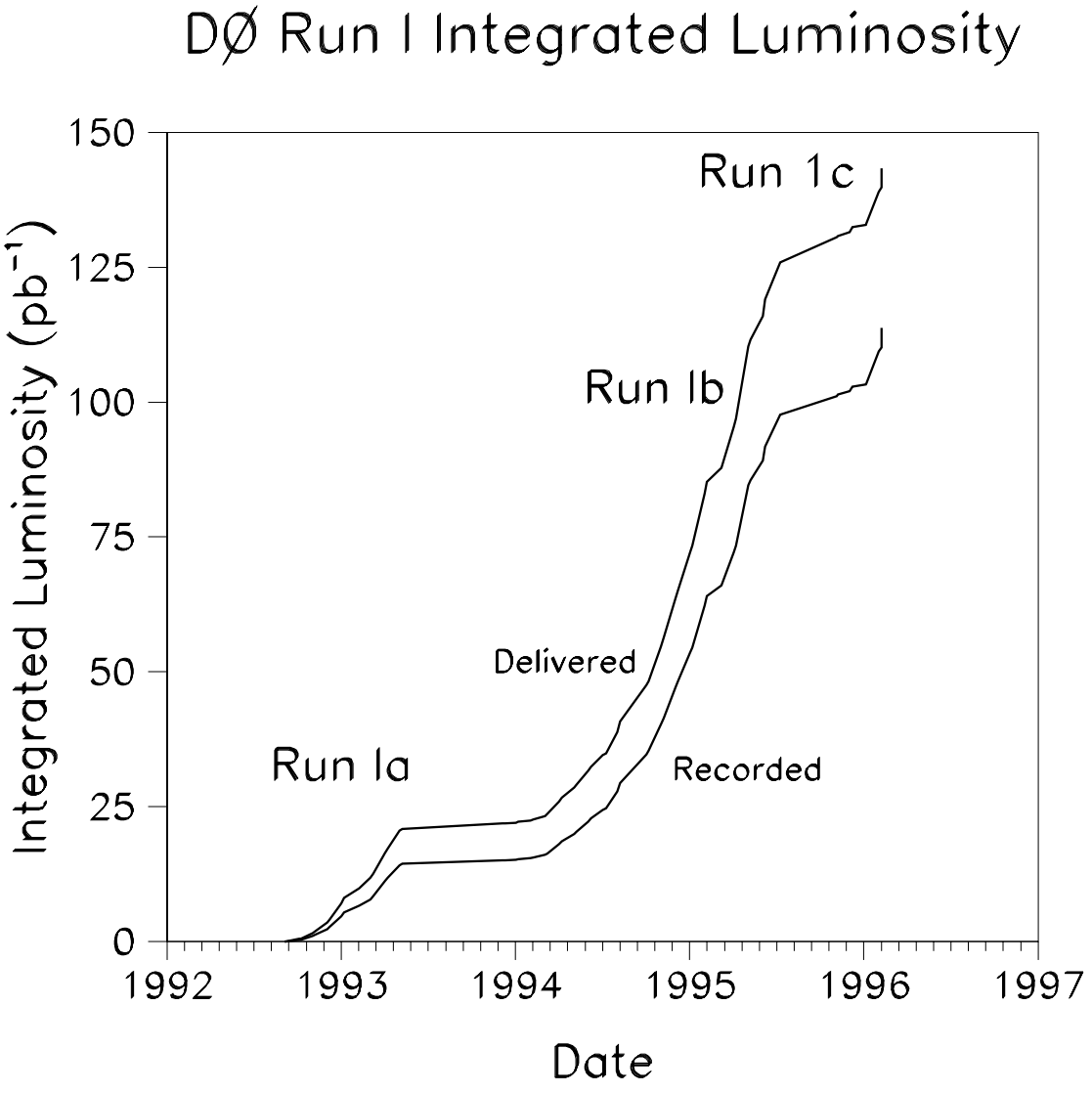


Figure 3-2: The upper curve represents the Integrated Luminosity produced by the Tevatron. The lower curve shows the amount of data written to permanent media by DØ.

- Good measurement of parton jets at large transverse energy ($E_T$) with good energy resolution.

- Good measurement of missing $E_T$ ($\not\!\!E_T$) which signals the presence of neutrinos or other non-interacting particles. [42]

These goals were chosen because many of the phenomena of interest, such as the top quark or W boson physics, have appreciable branching ratios into leptonic channels. Further, the accompanying QCD backgrounds have much smaller branching fractions. A particular emphasis on high $P_T$ phenomenon was made so that measurements of short distance interactions could be made.

The resulting detector has:

- A stable, hermetic, finely segmented, thick, and radiation-hard liquid argon calorimeter.

- A muon detector with thick magnetic iron toroids to provide sufficient momentum resolution and to minimize backgrounds from hadronic punchthrough.

- A compact non-magnetic tracking volume with adequate spatial resolution. Particular emphasis was placed on electron background suppression. [42]

Fig. 3-3 shows a cut away view of the detector. The DØ detector consists of three primary subsystems: inner tracking, calorimeter, and the muon system. A detailed description of the detector is given in reference [42].

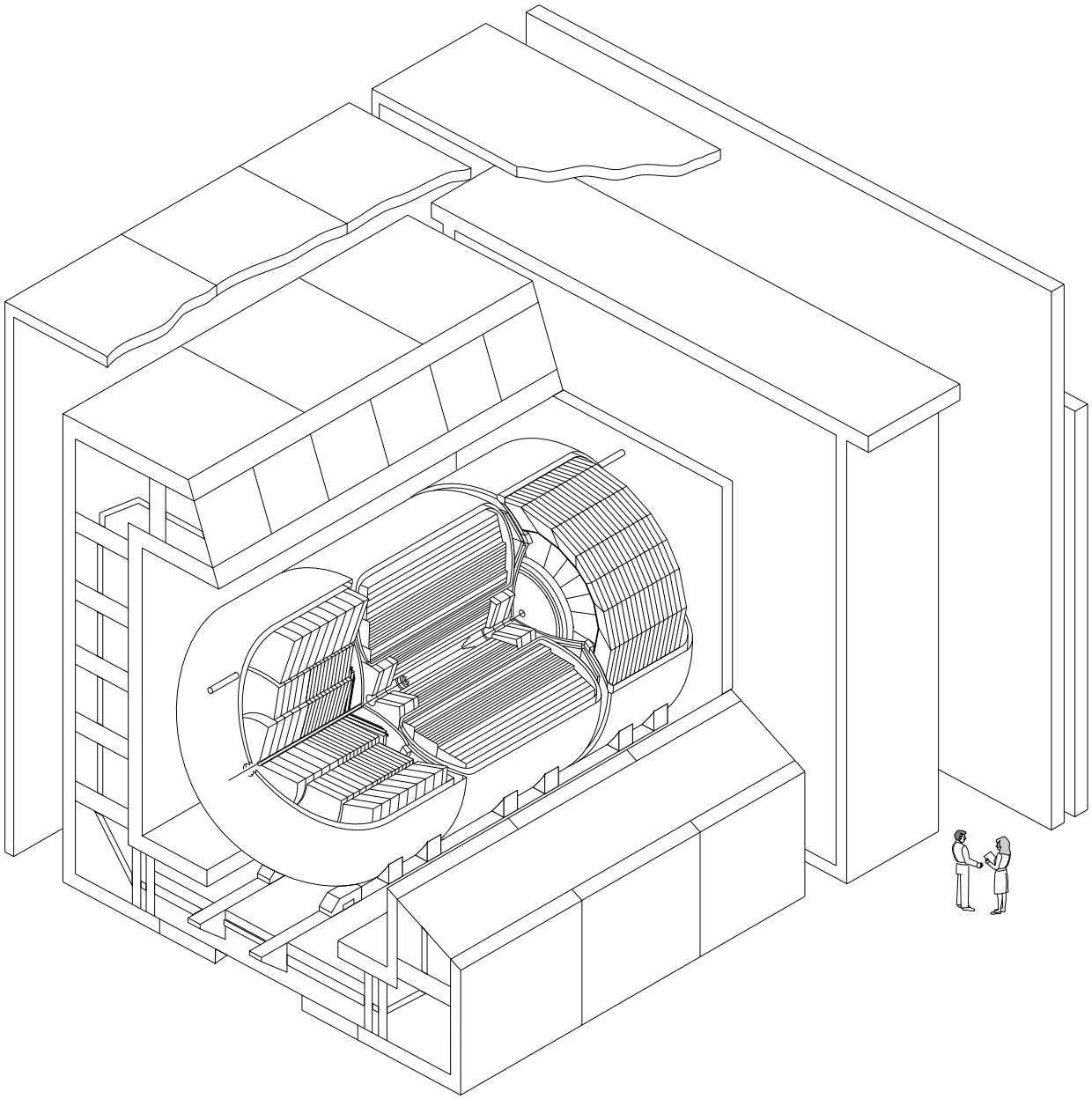


Figure 3-3: Cut away view of the DØ detector showing the three main subsystems: central detector, calorimeter, and muon detector.

Nestled within a cylindrical volume with a radius of 78 cm is the inner tracking system. This system consists of the vertex detector (VTX), the transition radiation detector (TRD), and the central drift chamber (CDC). On the ends of this cylindrical volume are the forward drift chambers (FDC). Surrounding the central detector is a uranium/liquid argon calorimeter. Outermost is the muon detector consisting of three layers of proportional drift chambers and an system of iron toroids.

The entire detector rests on a support platform that can be rolled out of the collision hall when necessary. Most of the front end electronics is on this platform. Connected to the detector through an articulating bridge is the movable counting house (MCH). The MCH contains the additional electronics needed to digitize signals and trigger on events. The MCH is located in a radiation safe environment outside the detector's concrete shielding wall. The digitized signals produced by the MCH are sent over high-speed data highways to one of several data acquisition (DAQ) processor nodes located near the DØ control room. Here, software filtering code selects out the interesting events for later analysis.

Throughout this thesis, the polar angle, $\theta$, with respect to the proton beam, will not be used. Instead, pseudorapidity, $\eta = -\ln(\tan(\frac{\theta}{2}))$, will be used for angular measurement. Pseudorapidity approximates true rapidity,

$$y = \frac{1}{2} \ln \left( \frac{E + P_Z}{E - P_Z} \right), \tag{3.1}$$

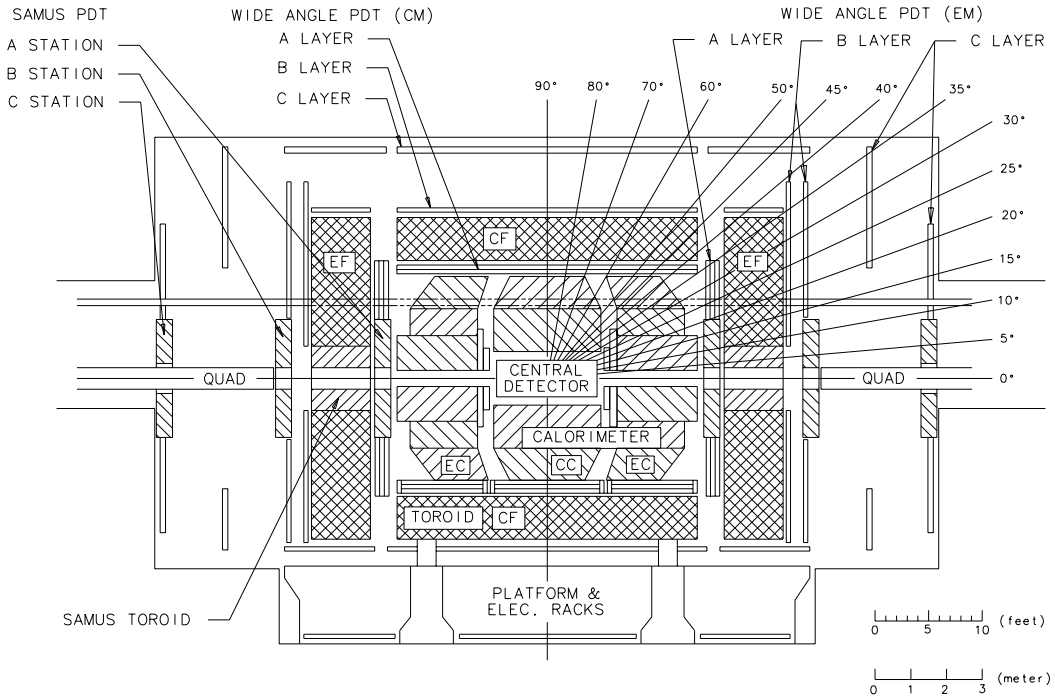


Figure 3-4: Elevation view of the DØ Detector showing the relative positions of the calorimeter, iron toroids, and the three layers of the muon system.

for finite angles and in the limit that $(m/E) \rightarrow 0$. Pseudorapidity is the preferred unit of measurement due to the relativistic nature of the particles produced at the Tevatron.

## 3.3 The Central Detector

The inner tracking system is composed of four detectors, *i*) The vertex detector (VTX), *ii*) the transition radiation detector (TRD), *iii*) the central drift chambers (CDC), and *iv*) the forward drift chambers (FDC). Each of these is contained within a cylindrical volume with $r = 78$ cm and $z = \pm 135$ cm. The VTX, TRD, and the CDC each form concentric shells about the beam pipe and cover out to $\mid \eta \mid < 1.2$. On either end lie the FDC which cover the region $1.4 < \mid \eta \mid < 3.1$.

Without a central field, the central detector (CD) did not need to have the ability to resolve particle momenta. Thus, the main design criteria was that it have good two track resolving power, high efficiency, and good ionization energy measurement. The TRD was added to give an additional factor of 50 rejection of isolated pions beyond what the calorimeter can do alone. The transition between the central and forward drift chambers was designed to match the corresponding transition between the central and forward calorimeters.

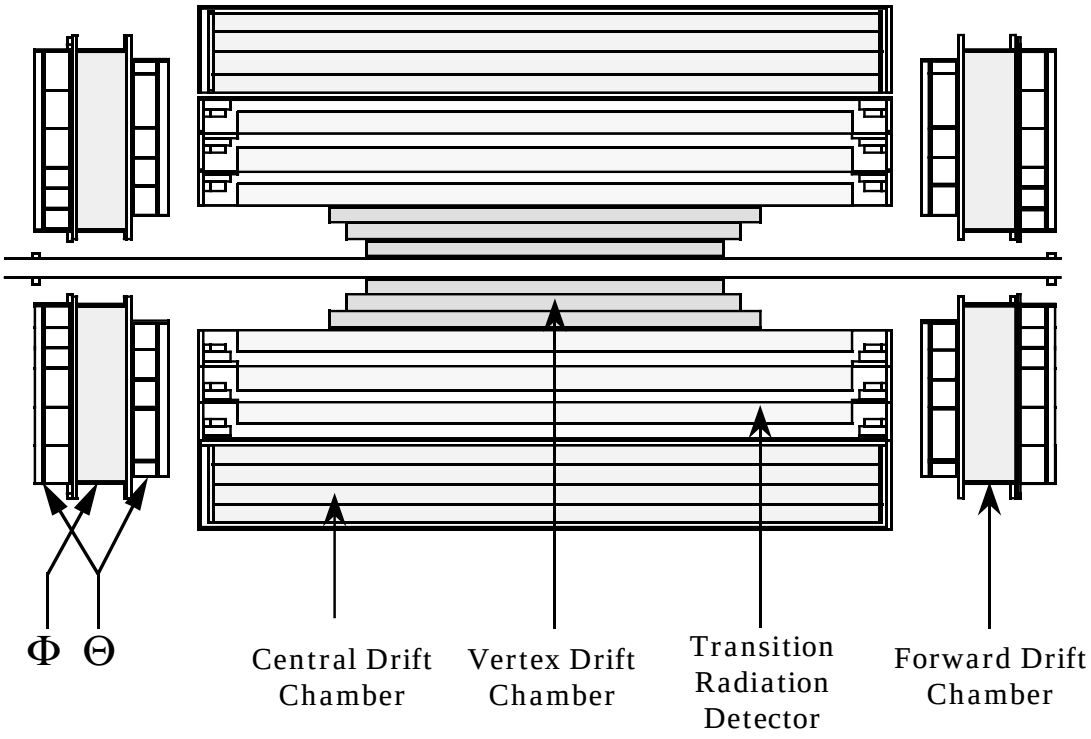


Figure 3-5: Side view of the central detector showing the relative positions of the VTX, TRD, CDC, and FDC.

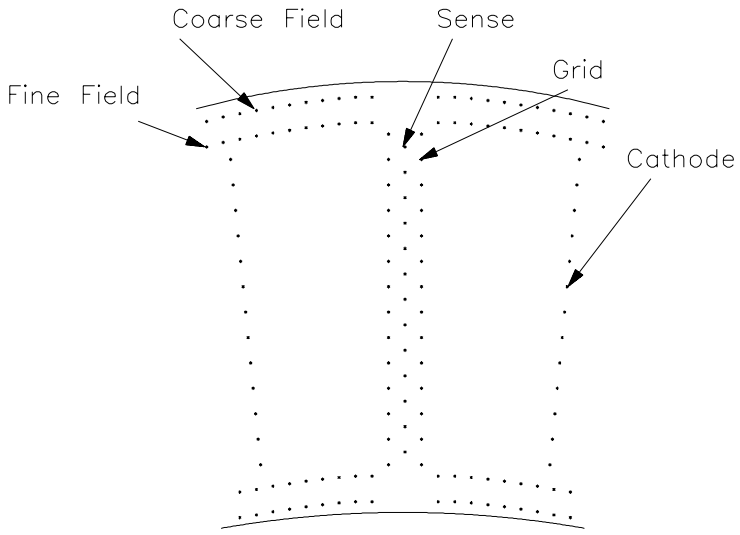


Figure 3-6: End view of the VTX showing the positions of the field, sense, and grid wires.

### 3.3.1 Vertex Detector

The VTX is the innermost detector with an inner radius of 3.7 cm (just outside the beryllium beam pipe) and an outer active radius of 16.2 cm. The VTX consists of three mechanically independent concentric layers. The walls between each of the cells are made of a low density material (carbon fiber) in order to minimize photon production of $e^+e^-$ pairs. Each cell consists of eight sense wires which provide measurements of the $r-\varphi$ coordinate. Adjacent sense wires are staggered by $\pm 100$ $\mu$m to resolve left-right ambiguities. The three layers of cells are staggered in $\varphi$ to aid in pattern recognition. The VTX provides position resolution of approximately 50-60 $\mu$m for charged particle tracks.

### 3.3.2 The Transition Radiation Detector

The TRD supplies a means of electron identification independent of the calorimeter. The TRD works by taking advantage of transition radiation X-ray production that occurs whenever highly relativistic particles traverse the boundary between two media with different dielectric constants. The TRD is composed of a radiation chamber which is followed by an X-ray detection section. The radiation chamber consists of alternating materials of high and low dielectric constants, polypropylene, and nitrogen gas respectively. The TRD was operating such that X-rays were produced with a peak energy of approximately 8 keV. The X-rays produced in the radiation chamber are measured by proportional wire chambers (PWC).

### 3.3.3 Central Drift Chambers

Outside of the TRD is the CDC. It has a length of 184 cm and a radius ranging from 49.5 cm to 74.5 cm. The design of the CDC is similar to the TRD except that it consists of four layers with each containing 32 cells. Each cell has seven 30 $\mu$m gold-plated tungsten sense wires which are read out at one end. Two delay lines lie on either side of the sense wires and are read out at both ends. The operating gas in the CDC is Ar(92.5%)$CH_4$(4%)$CO_2$(3%) with 0.5% $H_2O$. The signals induced by the anode wires propagate to the delay lines. Measuring the arrival times of the signal at the two ends of the delay lines produces a positional measurement along the wire. The position resolution of the CDC is 150-200 $\mu$m.

### 3.3.4 Forward Drift Chambers

The FDC covers the forward region of the central detector down to approximately 5 degrees. The FDC consists of three layers of chambers. The two $\Theta$ layers consist of modules in which the wires are perpendicular to the beam axis. Further, each of the $\Theta$ layers is rotated 45 degrees with respect to each other. The third layer, $\varphi$, has wires which are oriented radially outward from the beam. Test beam results show the FDC has a spatial resolution of 200 $\mu$m perpendicular to the beam axis.

## 3.4 Calorimeter

Since the detector does not have a central magnetic field, it must rely on the calorimeter for measurements of electrons, photons, and jets energies. The calorimeter also plays a key role in particle identification. Muons, for example, are expected to deposit the energy of a minimum ionizing particle (approximately 2 GeV) in the calorimeter. This energy is also expected to lie along the muon track.

The DØ calorimeter is a 'sampling' calorimeter; as particles traverse the calorimeter, only a portion of the particle's energy is measured by the active medium. The general design is to alternate cells with dense absorbing material (uranium) with an active medium (LAr). The active medium samples the ionization of the hadronic and electromagnetic showers.

A hermetic calorimeter was needed in order for $\not\!\!E_T$ to be well measured. This

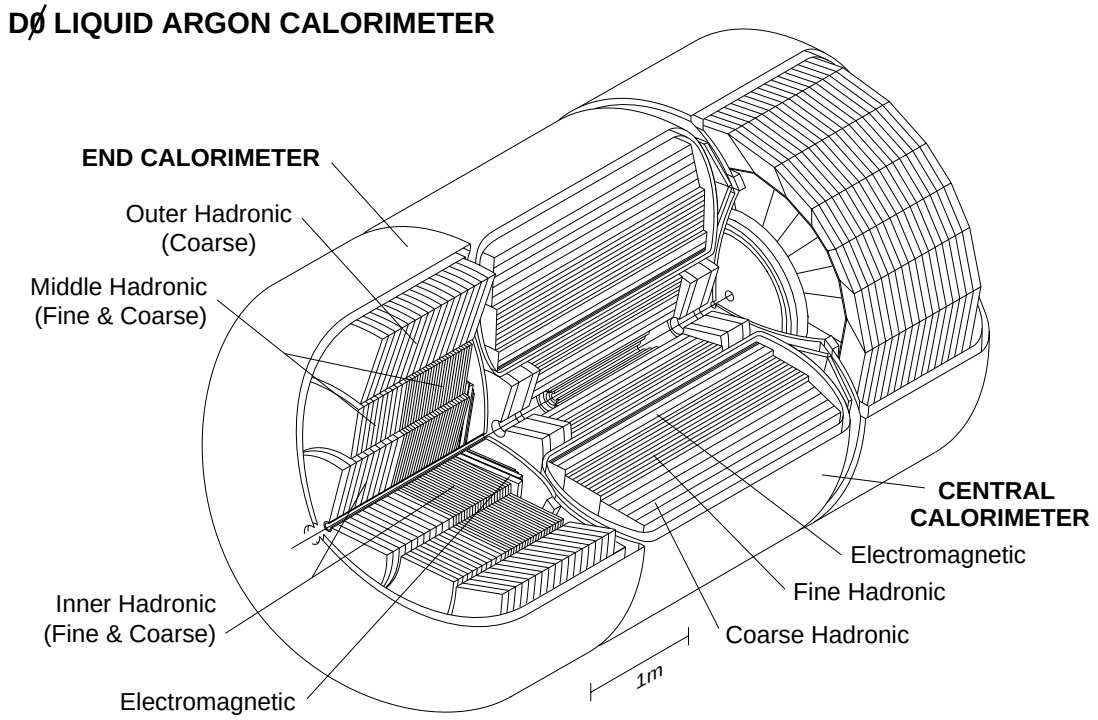


Figure 3-7: Cut Away view of the calorimeter illustrating the fine and coarse segmentation. The relative position of the CC and EC is shown.

requirement had to be balanced with the need to have a serviceable central detector. The resulting design is shown in Fig. 3-7. The calorimeter is divided into the central calorimeter (CC) and the two end calorimeters (EC). An array of scintillators known as the inter-cryostat detector (ICD) was placed in the dead space between the central and end calorimeters along with a collection of single celled readout structures called massless gaps. The crack between the central and end calorimeters is nearly perpendicular to the beam axis as this was found to minimize the degradation of the $\not\!\!E_T$ resolution.

The calorimeter is built so that the readout towers form pseudo-projective readout towers, Fig. 3-8. Each readout tower is further subdivided into a series of cells. The centers of these cells lie along constant rays of pseudorapidity originating at the center of the interaction region. A typical calorimeter cell is pictured in Fig. 3-9 depicting the relative positioning of the signal boards. These boards consist of two laminated 0.5 mm thick G-10 boards [43]. One side of each signal board is coated with a high resistivity carbon-loaded epoxy while the other side is left bare. One of the inner surfaces of the board contains copper that was milled into the pattern needed for the segmented readout. Liquid argon fills the gaps between the signal boards and the dense absorbing plates. An electric field of approximately 8.7 kV/cm is placed between the plates.

Incident particles hit the dense absorbers producing secondary hadronic showers. Ionization from these showers is collected on the outer surfaces of the signal boards, and the induced charge on the copper pads is pre-amplified and read out by the calorimeter electronics. The average size of a readout cell is that of a typical parton jet, $\Delta R = \sqrt{\Delta\eta^2 + \Delta\varphi^2} \sim 0.5$.

### 3.4.1 The Central Calorimeter (CC)

The CC is designed to cover the region $\mid \eta \mid < 1.2$ and consists of three concentric shells. The innermost shell contains 32 electromagnetic modules (CCEM). Surrounding this is a shell of 16 fine hadronic modules (CCFH); outermost is a ring of 16 coarse hadronic

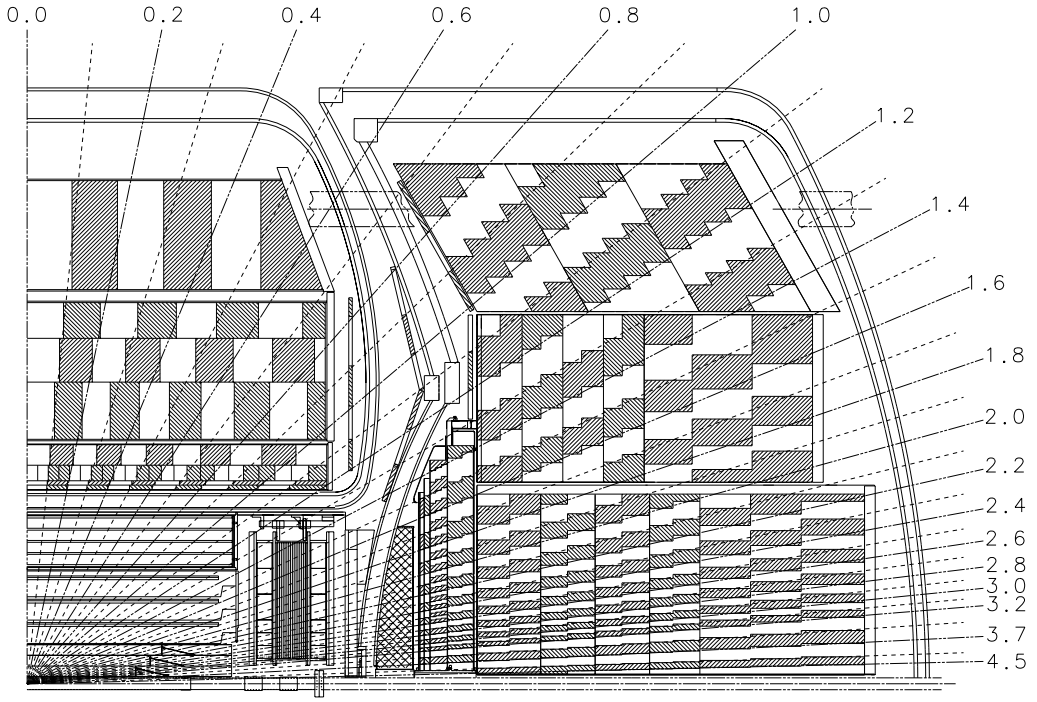


Figure 3-8: Side view of the calorimeter showing the pseudo-projective trigger towers denoted by light and dark shades in the calorimeter.

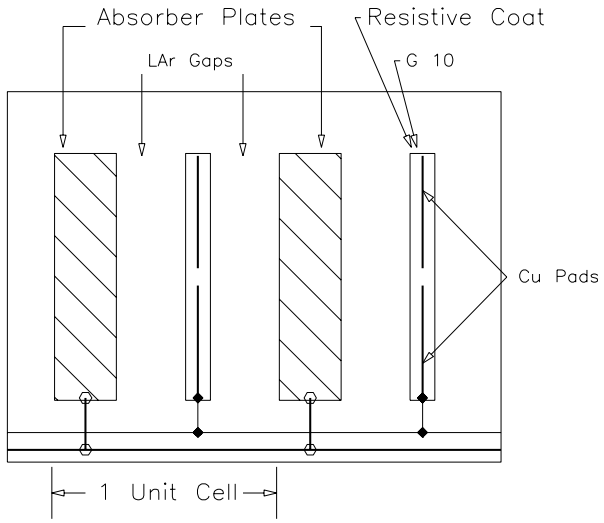


Figure 3-9: Unit Cell of the DØ calorimeter.

modules (CCCH), Fig. 3-7. The CC uses depleted uranium for its absorbing material.

The CCEM is made of 4 separate layers. The first two layers are 2.0 radiation lengths ($X_0$) thick. Their purpose is to sample early longitudinal shower development. Photons and $\pi^0$'s differ statistically in how their showers develop in this region. The third layer, where most of the electromagnetic energy is deposited, is 6.8 $X_0$ thick. This layer is more finely segmented in both $\eta$ and $\varphi$ allowing for a precise determination of electromagnetic shower centroids. The fourth layer is 9.8 $X_0$ thick. The CCEM contains 32 modules. Within each are 24 $\Delta\eta = 0.1$ towers for a total length of 260 cm. A full module is 20.5 $X_0$ and 0.76 $\lambda_A$ (nuclear absorption lengths) and weighs 0.6 metric tons.

The CCFH has three layers with 1.3, 1.0, and 0.9 $\lambda_A$ respectively and a weight of 8.3 metric tons each. The CCCH contains just one layer with a depth of 3.2 $\lambda_A$. Each CCCH module weighs 7.2 metric tons. The total weight of all the CC modules along with their support structure is 305 metric tons, with an additional 26 metric tons added by the LAr.

### 3.4.2 The End Calorimeters (EC)

The two end calorimeters each contain 4 sub-detectors. The electromagnetic (ECEM) and inner hadronic module (ECIH) have similar constructions as they contain only one module. This arrangement is designed to eliminate dead space in the detectors. Finally, there are the middle hadronic (ECMH) and the outer hadronic (EMOH)

calorimeters which consist of 16 modules each. The boundaries between the modules in the ECMH and ECOH are rotated so that rays projected from the interaction vertex will encounter no more then one crack.

The ECEM consists of only one module with many readout plates, Fig. 3-10. The total thickness of the ECEM is 24.1 cm with diameter of 2 m. It is located 1.7 m away from the nominal interaction point and gives complete coverage down to the beam pipe ($1.4 <| \eta |< 4.0$). Depleted uranium is used as the absorber with LAr as the active medium. The module weighs 5 metric tons.

The hadronic modules are cylindrical in structure. The ECIH has an inner radius of 3.92 cm and an outer radius of 86.4 cm. The ECIH covers the pseudorapidity range $1.6 <| \eta |< 4.5$ and weighs 28.4 metric tons. Surrounding the ECIH is the ECMH which consists of four fine hadronic modules. Each module weighs 4.3 metric tons. Together they cover the pseudorapidity range of $1.1 <| \eta |< 2.0$. Finally, the ECOH contains 16 modules that weigh 5.5 metric tons each. The ECOH covers the range $0.7 <| \eta |< 1.4$. The ECIH, ECMH, and ECOH use various materials for absorbers: uranium, uranium-niobium alloys, and stainless steal. LAr is used as the active medium in all. The complete EC weighs a total of 238 metric tons.

### 3.4.3 Massless Gaps and the ICD

The region in the calorimeter between $0.8 <| \eta |< 1.4$ has a lot of uninstrumented space. This space consists mostly of support structures, module end plates, and the

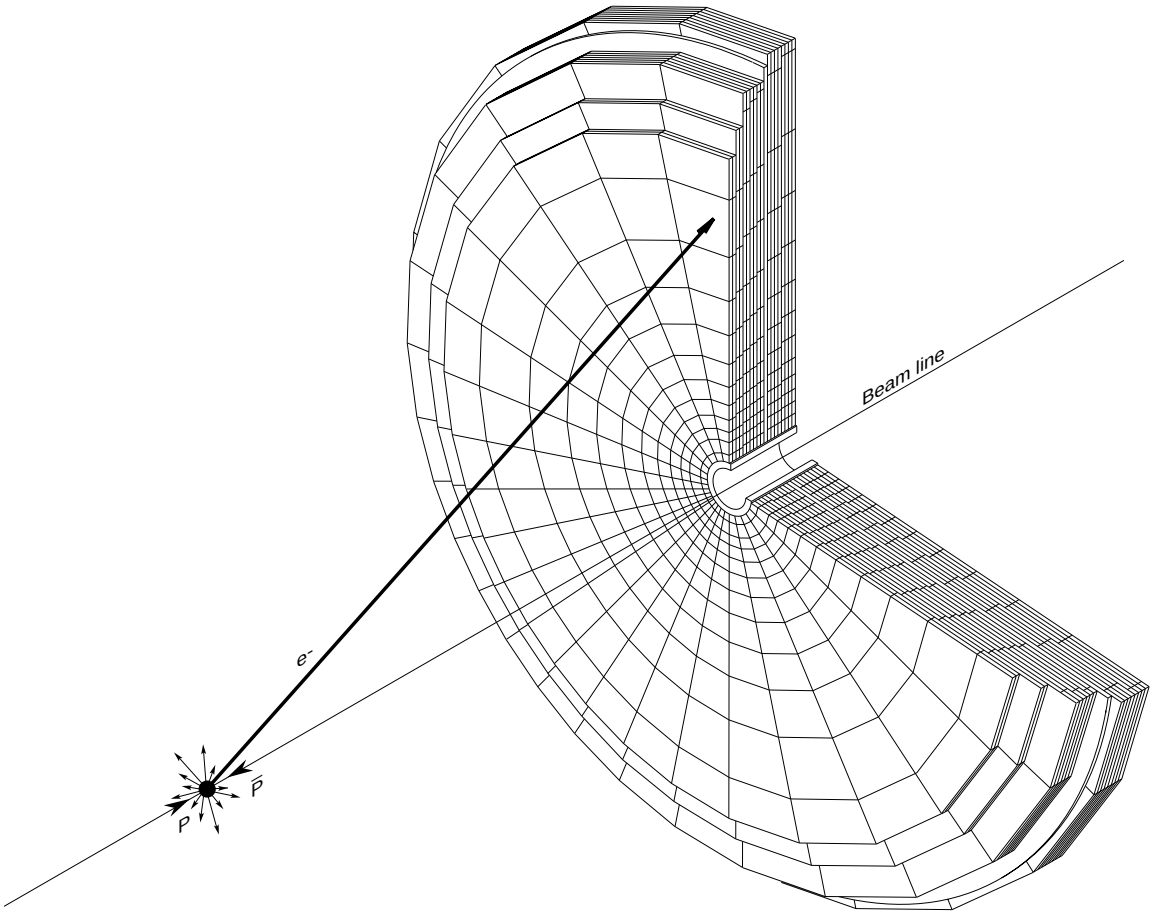


Figure 3-10: View of the ECEM. The readout boards form disks that contain no azimuthal cracks. The ICEM has a similar construction.

cryogenic walls of the CC and EC calorimeters. To combat this, two scintillator arrays were built and placed on the faces of each EC. These arrays, known as the intercryostat detector (ICD), consist of a collection of 384 scintillators of the size $\Delta\eta = \Delta\varphi = 0.1$. This size is designed to match the size of the calorimeters LAr cells.

In addition, single-cell structures known as massless gaps (MG) were installed on the faces of the CCFH, ECMH, and ECOH. These cells consist of two signal boards surrounded by three LAr gaps. The size of the massless gaps matches the size of the ICD and calorimeter cells. The MG and the ICD allow us to estimate the energy flow through through this region of the detector.

## 3.5 Muon Detector

The DØ muon detector is composed of five separate iron toroid magnets, and a system of proportional drift chambers (PDT's). The muons system has been subdivided into two subsystems: the wide angle muon system (WAMUS) and the small angle muon system (SAMUS). The SAMUS system has been specially designed to handle the high rate region near the beam pipe. In both systems the muon chambers have been placed into three layers (A, B, and C), with the muon toroids positioned between the A and B layers.

A total of five toroids are used by the muon system. The central toroid (CF) covers a pseudorapidity range of $|\eta| < 1.0$ and produces an average field of 1.9 T. The two end toroids (EF) cover the region $1.0 < |\eta| < 2.5$ producing a 2.0 T field.

The SAMUS toroids actually fit inside the end toroids covering $2.5 <| \eta | < 3.6$. The magnetic field produced by the SAMUS toroids ranges from 1.5–2.1 T.

The toroids serve two primary purposes. First, the sign and momentum of muon tracks are found by measuring the bend angle of the muon track through the toroid. Second, the longitudinal depth of the calorimeter plus toroid greatly reduces hadronic punchthrough. Hadronic punchthrough refers to hadrons that are incident on the calorimeter which later produce hits in the muon chambers. The punchthrough rate varies as a function of pseudorapidity, but in the central region this rate is less than 2% of all tracks [44]. This makes the identification of muons within hadronic jets relatively easy.

At $\eta = 0$ a muon must have momentum greater than 3 GeV/c in order to make in through the central toroid. This value increases to around 5 GeV/c at larger $\eta$ where it must traverse 13-20 $\lambda_A$. The thickness in nuclear interaction lengths as a function of polar angle is shown in Fig. 3-11. Some problems with detector acceptances exist at the bottom of the detector due to holes created by the calorimeter support structure.

### 3.5.1 The Wide Angle Muon System

WAMUS consists of 164 PDT's that collectively cover the pseudorapidity range $| \eta | < 2.5$. The PDT's are oriented so that their anode wires are perpendicular to the bend direction of the muons passing through the toroid. The measured drift times and

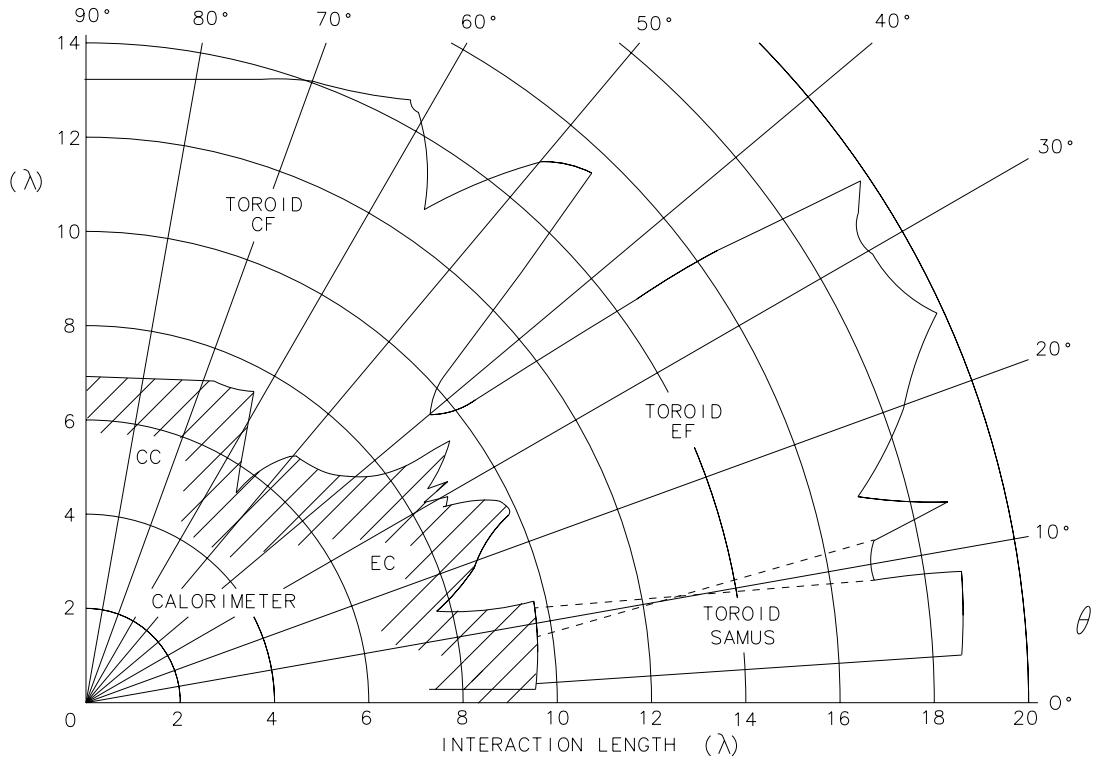


Figure 3-11: Thickness of the calorimeter and muon system in nuclear interaction lengths.

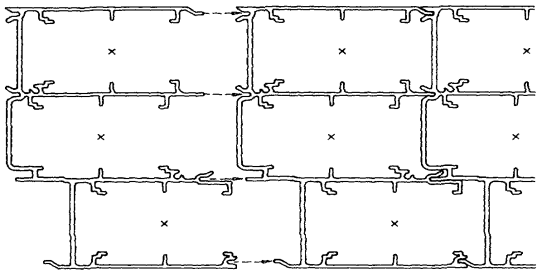

Figure 3-12: Example of the aluminum extrusions which make up the B and C layer PDT chambers. The A Layer is similar except that it has four decks instead of three.

known drift velocities of electrons through the active medium make it possible to determine the position of the muon tracks in the cells relative to the anode wires. The active medium used during run 1B was $Ar(90\%)/CO_2(10\%)$.

The A layer of chambers consists of four planes, called 'decks', of 10 cm wide drift cells. The B and C layers have three decks each (Fig. 3-12). This multi-deck structure increases the muon detection efficiency by forcing the muons to traverse several muon chambers instead of just one per layer. The decks are offset relative to neighboring decks so as to eliminate left-right ambiguities. The drift time information along with the known position of the anode wires gives the information needed to determine muon track momentum and rapidity.

Each PDT cell has a 50 $\mu$m gold-plated tungsten anode wire in the center of the cell. Vernier cathode pads are placed above and below this. The cathode pads are formed from electrically isolated diamond shaped structures which repeat every 60.96 cm as in Fig. 3-13. The pads are held in place by an aluminum extrusion that make up the body of the cell. The anode and cathodes are maintained at 4.56 kV,

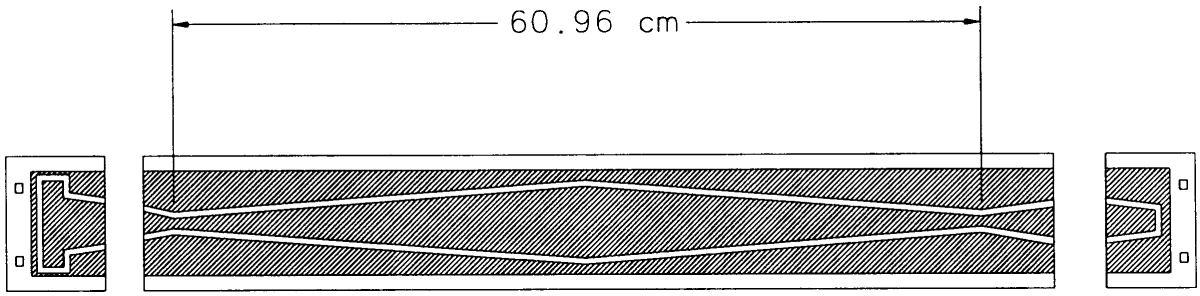


Figure 3-13: WAMUS PDT cathode pad structure.

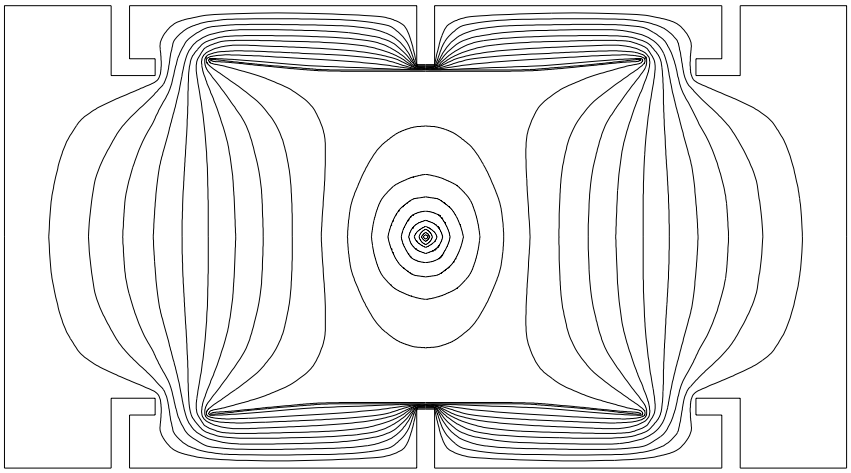

Figure 3-14: Electrostatic potential lines of a muon proportional drift chamber.

and 2.3 kV respectively (Fig. 3-14).

The WAMUS PDT's also have the ability to determine the azimuthal coordinate by the measurement of the track position along the wire. This measurement is performed in two steps. First, a coarse measurement is found by measuring the difference in the arrival times of the signals at each end of the anode wires. This measurement yields the position to within 10-20 cm and is good enough to pinpoint the location to a particular cathode diamond. The cathodes are then used to refine the measurement

by taking the ratio of the sum of the charge signals and the difference of the charge signals. This ratio is related to the distance between the cathode wires. The diamond shaped cathode allows a measurement of the track position along the wires to within $\pm 3$ mm.

### 3.5.2 The Small Angle Muon System

The position of the small angle muon system (SAMUS) is shown in Fig. 3-4. In SAMUS, the low beta quads lie just outside of the C layer of the muon system. Each layer covers $312 \times 312$ cm$^2$ perpendicular to the beam pipe and consists of three doublet planes of cylindrical proportional drift tubes (PDT's). The three planes in each layer are oriented in the x, y, and u directions. The u direction is tilted 45 degrees with respect to both the x and y planes, (see Fig. 3-15). This is necessary to resolve the ambiguities presented by multiple hits in the layer.

The SAMUS PDT's have an outer diameter of 3 cm and are made from stainless steel tubes. The ends are capped but allow for electrical connections and gas input. In each doublet plane the tubes are offset by 1/2 a tube diameter. The anode wire is a 50 $\mu$m gold-plated tungsten wire. The gas used is $CF_4(90\%)/CH_4(10\%)$ and has an average drift velocity of 9.7 cm/$\mu$s giving a maximum drift time of 150 ns and resolution of approximately 350 $\mu$m. In all, SAMUS contains 5308 PDT tubes.

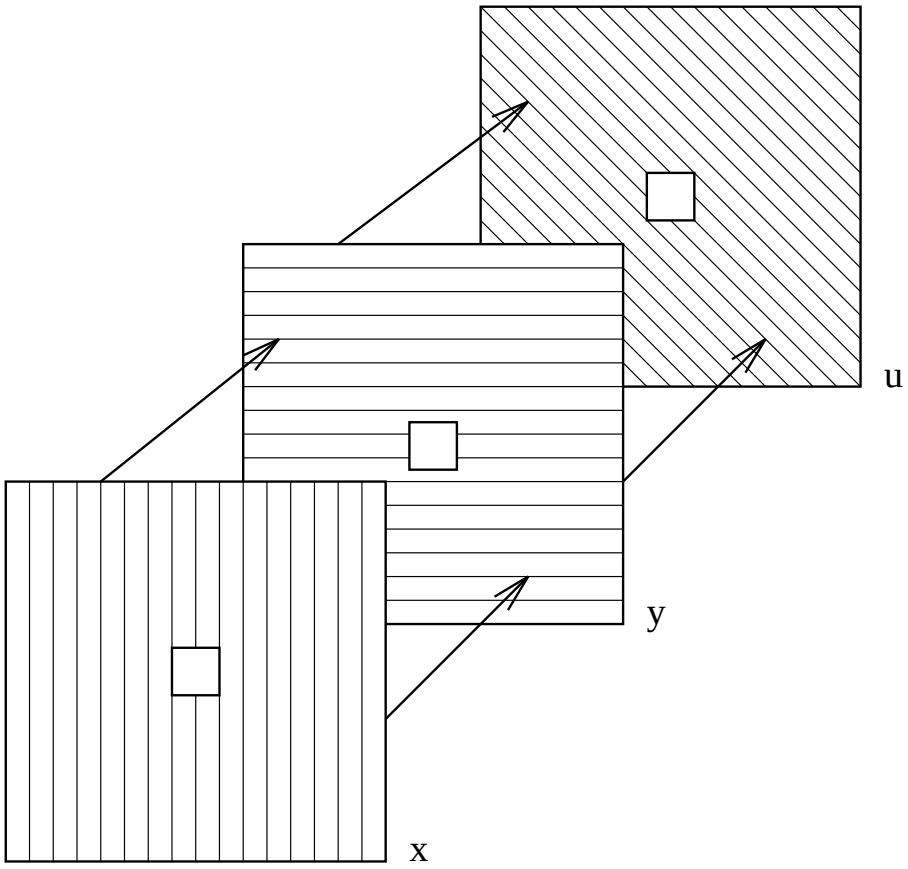


Figure 3-15: A model (not to scale) showing an exploded view of a SAMUS layer. Each of the three layers consists of three planes: x, y, and u. The u plane is rotated 45° with respect to the x and y planes.

### 3.5.3 Scintillators

A major background to beam-produced muons are events due to cosmics rays. Because of this, the muon scintillators [45] were installed during run 1B on the outside of the C layer of the muon system. The scintillators are made from Bicron 404A 1/2" thick scintillator [46] material. Each is 25" wide with lengths varying from 81.5" to 113" depending upon the size of the PDT to which it is attached. The scintillators are mounted in a nested configuration which is designed to reduce geometrical inefficiencies.

A muon passing through the scintillator deposits approximately 2 MeV of energy. Approximately 10 photons are produced for each keV of deposited energy. Therefore, muons cause $\sim 2 \times 10^4$ photons to be created in the scintillator. Photomultiplier tubes amplify this signal by a factor of approximately $10^7$.

For the data used in this analysis, the scintillators are active during a 50 ns gate centered around the beam crossing time. If a muon hits the scintillator within this gate, a signal is produced and is read by the attached photomultiplier tube. The current triggering scheme relies on the manual scintillation modules (MSM) which use NIM logic to make their trigger decisions. The high voltage supply for the scintillators are produced by Fluke supplies located in the MCH cable bridge.

## 3.6 Data Acquisition

The DØ trigger and data acquisition system is used to collect interesting events for later analysis. The trigger system has three levels of increasing sophistication. The first is the Level 0 trigger which is a hardware based system using scintillators to indicate the presence of inelastic collisions. The trigger rate out of Level 0 is around 150 kHZ at a luminosity of $5 \times 10^{30}$ cm$^{-2}$s$^{-1}$. The Level 1 trigger is also a system composed of hardware trigger elements. Most of the Level 1 triggers operate within the 3.5 $\mu$s beam crossing time. Such triggers are able to operate without incurring dead time in the trigger system. Other Level 1 triggers require several beam crossings to make their decisions. These triggers are referred to as the Level 1.5 triggers. The rate out of Level 1 is approximately 200 Hz; while the rate out of Level 1.5 is approximately 100 Hz. The final trigger, Level 2, consists of a farm of microprocessors which form a software triggering system that further reduce the rate to approximately 2 Hz. Events passing the Level 2 trigger are sent to host computers for monitoring and recording on 8 mm tape.

### 3.6.1 Level 0

The Level 0 trigger detects inelastic collisions, monitors luminosity, provides a relative zero-time for other triggers, and provides a fast measurement of the z-coordinate of the collision vertex. The Level 0 detector consists of two hodoscopes with a checker board-like array of scintillating counters covering $1.9 <\mid \eta \mid < 4.3$. The time resolution

for each counter is 100-150 ps. By measuring the relative arrival times of the signals in each hodoscope, a fast measurement of the interaction vertex can be made to within 8 cm. This information is determined quickly enough to be used by the $\not\!\!E_T$ triggers at Level 2. Use of the full detector information later improves the vertex position measurement to within $\pm 3$ cm. Often high luminosity runs will have multiple interactions during each beam crossing. When a multiple interaction occurs, the Level 0 vertex measurement is ambiguous and a flag is set in the data marking this occurrence.

### 3.6.2 Level 1 Trigger Framework

The Level 1 trigger system must function within the 3.5 $\mu$s bunch crossing time. Because of this time limitation, the Level 1 trigger is composed of hardware logic devices that find objects such as muons, electrons, and jets. The Level 1 framework collects the decisions from each of these hardware triggers. The trigger framework uses a two dimensional AND/OR network array which collects 256 input bits. The output from the network is 32 preselected trigger conditions. Each of the trigger conditions is formed from the 256 inputs by requiring that each input be asserted, negated, or ignored. The trigger conditions are selected from a trigger menu that is downloaded from the host VAX cluster. If one of the 32 conditions is met, then the detector electronics are read out and sent on to the Level 2 trigger for further processing. The Level 1 framework also handles the prescaling of the Level 1 triggers.

Prescaling becomes necessary if the rates into Level 2 become too large.

### 3.6.3 Level 1 Muon Trigger

Each of the 16694 muon drift cells has a corresponding pad latch bit in the chamber electronics. This bit is set whenever the accumulated charge in the chamber cathode pads exceeds a preset threshold. This information is made available to the Level 1 trigger via the Module Address Cards (MAC's). The MAC's take the hit information and form an address (centroid). These centroids correspond to the z-coordinate of the half-cell of the PDT that was most likely hit. The granularity of the centroids is 5 cm (1.5 cm) in WAMUS (SAMUS). The MAC's are located in custom VME crates in the movable counting house (MCH) along with analog-to-digital (ADC) cards. For Level 1, the MAC's take the logical OR of 3 (4) centroids producing 'coarse' centroids for WAMUS (SAMUS). The Level 1.5 trigger makes use of the full centroid resolution ('fine' centroids) and will be described in detail later.

The coarse centroid information is sent to the Coarse Centroid Trigger (CCT) cards where they are further OR'ed by another factor of four. This produces a hodoscopic pattern with 'cells' that are 12 centroids wide (60 cm). Fig. 3-16 shows an example of this pattern. WAMUS muon tracks can be formed whenever 2 or 3 layers have been hit and align themselves properly. This pattern recognition is performed by the CCT's through the logic contained on their ELPD's. Each octant of the muon system has a CCT. A summing CCT is used to collect the tracks found

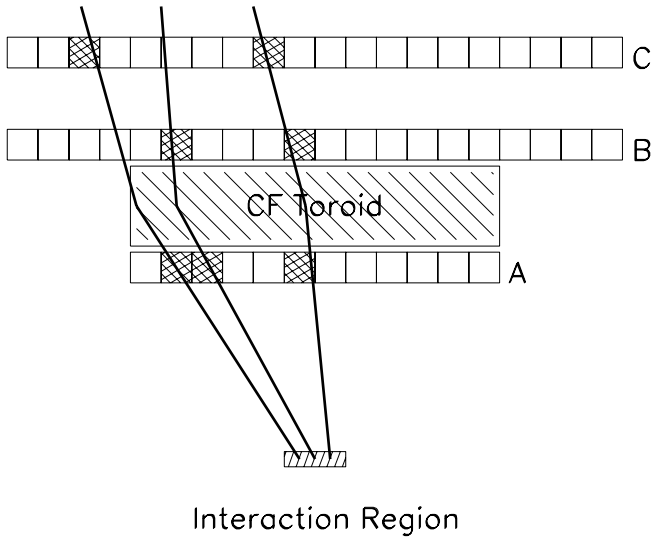


Figure 3-16: An example showing how Level 1 coarse centroids can form a muon track. Note that only two layers of the muon system are needed to form a track.

by each octant.

The trigger decision from the summing CCT's is sent to the trigger monitor (TRGMON) card which is located in the muon supervisor crate in the MCH. The TRGMON maps the CCT trigger information onto the 16 trigger states which are then sent on to the Level 1 trigger framework. This mapping is given to TRGMON by the muon trigger control computer (MUTCC). The MUTCC receives the mapping from the host VAX cluster. The supervisor crate is also responsible for handling the distribution of the timing signals from the trigger framework to the MAC, Level 1, and Level 1.5 trigger crates.

### 3.6.4 Level 1.5 Muon Trigger

The Level 1.5 muon trigger is a hardware based system that utilizes the full centroid resolution of the MAC's. This allows for sharper momentum cuts on the tracks as well as better rejection of bad tracks. Upon receipt of a Level 1 trigger, the MAC's strobe their information to the Octant Trigger Cards (OTC's). The OTC's use combinations of the A, B, and C layer centroids to form addresses that are used to access their static random access memories (SRAM's). The SRAM's contain patterns relating to trigger conditions. The details of this depend upon the detector region and will be discussed in detail later. The OTC's contain a $4 \times 4$ array of SRAM's allowing the OTC's to process up to 16 ABC centroid combinations simultaneously.

Common to all detector regions are the kinematic OTC's. These OTC's use centroid information to form addresses for memory lookups in the SRAM's. The resulting lookups to the SRAM's indicates whether a legitimate muon track has been found. The triggering information contained in the SRAM's is actually determined first on the VAX cluster before being downloaded into the SRAM's. On the VAX cluster, this information is determined by calculating the momentum range of each triplet ABC centroid. All centroid combinations producing tracks with momenta above a set threshold are included in the tables. The SRAM tables for run 1B had a $P_T^{\mu}$ threshold at around 4 GeV. The resulting tables are then transferred from the VAX cluster to four 4 Mb battery backed up memory modules located in the MCH. The tables can then be downloaded from the memory modules to the OTC's. This

intermediate step allows for quick downloads from the memory modules to the OTC's in the event that power to the VME crates is lost.

After the SRAM lookup, further processing is done by the OTC's. The centroids associated with good Level 1.5 triggers are used to form another address for an additional set of memories. This lookup produces two 24-bit user defined trigger words. In run 1B, these words contain the centroids of the good track passing the initial SRAM lookup. These trigger words are placed into FIFO's for later readout by the Octant Trigger Manager (OTCMGR). The OTCMGR then uses the centroids in these trigger words to apply a second $P_T^\mu$ cut. This second cut has a threshold of approximately $P_T^\mu = 7$ GeV. This design allows the Level 1.5 muon trigger the flexibility of applying different $P_T^\mu$ thresholds. The OTCMGR produces trigger decision data for each $\eta$ region and sends this information to the TRGMON. Here the TRGMON translates the trigger decision information into 16 muon trigger states which are used by the trigger framework in the global physics trigger decision. Should an event also pass Level 2, all Level 1.5 trigger decisions and the centroid patterns associated with good triggers are written to tape.

**WAMUS L1.5 Trigger**

The WAMUS Level 1.5 trigger system uses 16 kinematic OTC's to make trigger decisions. These OTC's are placed into three of the five VME crates containing OTC's in the MCH. Each of the three crates contain one OTCMGR. These OTC's

process centroids that fall within $\mid \eta \mid < 2$. The kinematic OTC's used in WAMUS use the centroid information from all three layers. These centroids form the address for the SRAM lookup described above.

The kinematic OTC's require that all three layers of the muon system be hit before registering a trigger. Midway through run 1B, this requirement was relaxed in the central region by allowing two layer tracks for low $P_T^\mu$ tracks. Since the Level 1 CCT's require only two layers tracks to trigger, the OTCMGR's were modified so that they would overwrite the CF kinematic OTC's low $P_T^\mu$ trigger counter with that which was found by the CF CCT's. This hardware change was implemented on October 31, 1995 (run 85277).

**SAMUS L1.5 Trigger**

The particles produced at the small angles near the beampipe often produce secondary interactions with the detector edges and beamline elements found in the muons system. Thus, a different triggering scheme was employed in this region. In addition to the kinematic OTC's, additional types of OTC's were used. These include the 'x-road', 'y-road', and 'pair-find' OTC's. Before continuing with the description of the SAMUS Level 1.5 trigger, a description of these OTC's is given.

The x-road OTC's use the centroids only from the x-planes in each of the three layers (see Fig. 3-15). The centroids from the x-plane PDT's are used to form an address which is used to look up trigger information contained in their SRAM's. This

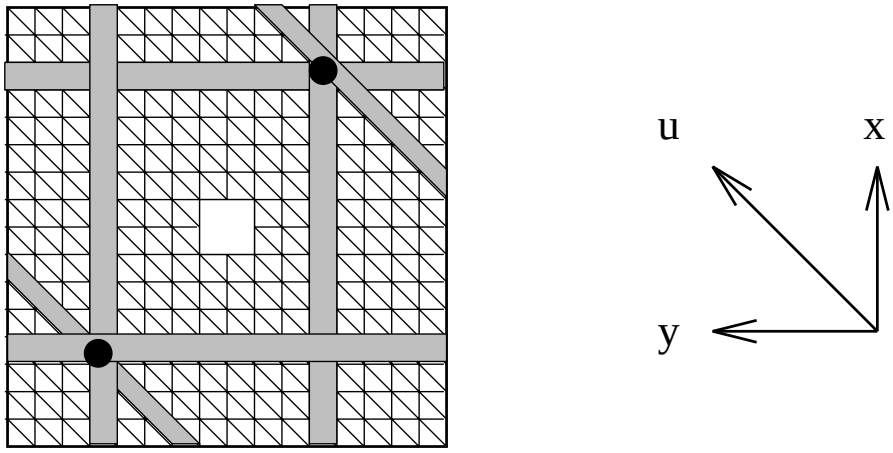


Figure 3-17: In SAMUS centroids from the x, y, and u planes are used to locate where charged particles hit the layer.

process is very similar to that which was described for the kinematic WAMUS OTC's. Entries in the SRAM tables forming tracks with momenta below a set threshold (approximately 4 GeV) are rejected. The y-road OTC's are exactly the same as the x-road OTC's except that they use the centroids from the y-plane in each of the layers. The user defined trigger information in this case consists of the x(y) centroids in the B layer associated with the x(y) road.

The pair find OTC's differ from the road OTC's in two ways. First, they use centroid information only from the B layer in SAMUS. Second, they use centroids from the x, y, and u planes. The purpose of the pair find OTC's is use all three planes to determine where a charged particle struck the B layer (Fig. 3-17). Note that the term 'pair-find' is retained for historical purposes only. A more precise term would perhaps be 'triplet-find' OTC.

Unlike WAMUS, the centroid information does not flow directly from the MAC's

to the OTC's. Instead, the centroids go to an intermediate card called the SAMUS centroid card (SAMCEN). SAMUS has a rather complicated system of OTC's that require input from many different MAC's. One of the main purposes of the SAMCEN's was to send the necessary centroids to the appropriate OTC's. This reduced the number of centroids input into the OTC's. The second purpose of the SAMCEN's was to eliminate consecutive centroids. Low energy particles or spray from the beam-pipe can often cause large sections of the SAMUS PDT's to fire. The SAMCEN's define adjacent centroids to be those that are less than 2 centroids apart. If two centroids are found to be adjacent then only the second of the pair is sent out. Eliminating consecutive centroids helps to reduce the rates into the OTC's.

When a Level 1 trigger is found, the TIMER cards cause the MAC's to strobe their centroid information into the SAMCEN's. The SAMCEN's prepare the data by eliminating the unnecessary consecutive centroids. The SAMCEN's then send the centroids on to the appropriate OTC's. The road find OTC's form roads in both the x and y planes. If roads are found, then these OTC's send their trigger information on to the SAMUS kinematic OTC's. Simultaneously, the pair find OTC's look for good triplet matches in the B layer. If triplets are found, then the pair find OTC's send the associated centroids on to the kinematic OTC's.

At this point, the kinematic OTC compare the B layer centroids from the x-road, y-road, and pair find OTC's. If the x and y centroids from the road find OTC's match those from the pair find OTC, a SAMUS trigger has been found. At this

point, the kinematic OTC performs the additional memory lookup forming the user defined trigger words. These words are then stored in the FIFO's as described before.

#### Overlap L1.5 Trigger

The overlap region is made up of muon tracks having hits in both the SAMUS A and WAMUS B and C layers (or SAMUS A and B and WAMUS C layer). In this region, pair find OTC's are used in the SAMUS A and, if necessary, SAMUS B layers. The appropriate x or y coordinate of the pair find OTC's are sent to the kinematic OTC's. The kinematic OTC's also collect the centroid information from the WAMUS kinematic OTC's.

### 3.6.5 Level 2

During run 1B the Level 2 trigger system consists of 32 micro-VAX 4000-M60 and 16 micro-VAX 4000-M90 worker nodes. Four additional micro-VAX 4000-M60's were used as control nodes that managed the operations of the worker nodes. The Level 2 trigger collects digitized data from events satisfying Level 1 and Level 1.5 triggers at a rate of approximately 100 Hz and reduces this rate to approximately 2 Hz. In order to keep dead-time at less than 5%, each node must be able to process an event within 350 ms.

The Level 2 software is built around a collection of algorithms known as 'tools'. Each tool is designed to recognize a specific object or condition within the event.

There are tools to recognize muons, electrons, photons, jets, taus, scalar $E_T$, and $\not\!\!E_T$ . These tools are typically developed offline in a VMS environment which uses a Level 1 trigger simulator to mimic the behavior of the Level 1 hardware. Both Monte Carlo and data are used to test these tools before using them online. Further tests can be performed online through the use of a 'shadow run'. In a shadow run, one of the nodes is loaded with a test version of the Level 2 code. Data is then sent to this node for the testing of the new tools. During a shadow run, however, the node is not allowed to participate in trigger decisions.

The triggers and tools are specified by a script file. This file contains the description of the 32 Level 1 triggers. Each Level 1 trigger has attached to it at least one Level 2 filter. Up to 128 Level 2 filters can be included in each script. Each filter is composed of various combinations of the tools described above. If an event passes any of the Level 2 filters, then the event is transferred to the host computer for the logging and recording of the event.

# Chapter 4

# Data Selection

This chapter describes the criteria used to select the data for this analysis. In particular, the trigger requirements, event reconstruction, and offline selection cuts are described. Each of these requirements ultimately affects the number of events seen in the final sample. Therefore, it is important to understand both the efficiencies and the history (run dependence) of these cuts.

The data used for this analysis was taken from the 1B collider run, 1994–1995. Only a subset of the available runs are used in this analysis, 85277 through 931150. The total integrated luminosity for these runs is 46.2 $pb^{-1}$ which was calculated by using the DØ offline luminosity utilities [47]. This subset represents 53% of the total 87.6 $pb^{-1}$ of data written to tape by DØ during run 1B.

## 4.1 Trigger Requirements

For this analysis, two different triggers were used: MU_2_LOW and MU_2_CENT. The primary difference between these triggers is that MU_2_LOW selected dimuon candidates in the range $|\eta| < 2$, while MU_2_CENT only searched in $|\eta| < 1$. Many other subtle differences between the two triggers exist and are listed below.

### 4.1.1 Level 1

The similarities and differences between MU_2_LOW and MU_2_CENT can best be seen by studying the various Level 1 tools used by the two triggers. The use of these tools varied throughout run 1B. Thus, it is necessary to understand their history when selecting a trigger for data analysis. The hardware tools listed below are summarized in Table 4-1.

- **Level 1.5 Confirmation**

  Both triggers required Level 1.5 confirmation of each Level 1 muon CCT trigger. As discussed in Section 3.6.4, however, the Level 1.5 trigger system changed in the CF on October 31, 1995 (run 85277). Prior to this run, Level 1.5 confirmation was required for Level 1 muon triggers. After run 85277, the Level 1.5 confirmation was effectively turned off in the central region. Both MU_2_LOW and MU_2_CENT used the Level 1.5 confirmation tool throughout run 1B, so both triggers were affected by this change.

- **Scintillator Veto Tool**

  The scintillators 'trigger' whenever a discriminated pulse is found within the 50 ns gate that the scintillators are active. Whenever a Level 1 muon CCT trigger is found, this tool checks to see if a scintillator has triggered in the same octant. If such a match is found, then the event is confirmed. However, if no match was found and at least one 'scintillator covered' CCT triggered, then the event is rejected. Muons passing through octants 5 and 6 do not participate in the decision, because these octants do not have scintillator coverage. The Level 1 scintillator tool does not confirm or reject individual CCT triggers. Instead, it confirms or rejects entire events based upon the above logic. This tool became operational in octants 0–3 for run 79055. Later (run 90477), octants 4 and 7 were also used by this tool.

- **Multiple Interaction Veto Tool**

  The multiple interaction veto tool uses information from the Level 0 trigger to determine the likelihood that an event contains a single interaction. This tool returns four states which range from 'most probably a single interaction' to 'most probably a multiple interaction'. The dimuon triggers used this tool intermittently throughout run 1B (see Table 4-1). When in use, however, the most stringent condition, 'most probably a single interaction', was required. This tool was originally introduced as a way of reducing the Level 1 trigger rate and was used as an alternative to applying Level 1 prescales.

| Run Number | Level 1.5 | Level 1 Scintillator | Multiple Interaction Veto (MU_2_LOW) | (MU_2_CENT) |
|---|---|---|---|---|
| 73296 | CF Confirmed | - - | On | - - |
| 77825 | CF Confirmed | - - | Off | - - |
| 79055 | CF Confirmed | 0–3 | On | - - |
| 79983 | CF Confirmed | 0–3 | Off | - - |
| 85277 | CF Not Confirmed | 0–3 | Off | - - |
| 87804 | CF Not Confirmed | 0–3 | Off | Off |
| 91923 | CF Not Confirmed | 0–4,7 | On | Off |

Table 4-1: A listing of the Level 1 changes to MU_2_LOW and MU_2_CENT. Note that while the changes to the Level 1.5 confirmation and scintillator tools were the same for both triggers, the multiple interaction veto tool changed differently for the two. The symbol - - is used to indicate whenever a tool was unavailable, or a trigger did not yet exist. The Level 1 scintillator column lists the octants in which the Level 1 scintillator veto tool was active.

### 4.1.2 Level 2

Three different Level 2 tools were used by the MU_2_LOW and MU_2_CENT filters. As with the Level 1 tools, these tools changed frequently during run 1B. Each of these tools are described below and are summarized in Table 4-2.

- **Muon Tracking Tool**

  MU_2_LOW (MU_2_CENT) required that muon tracks be found within $|\eta| < 2$ ($|\eta| < 1$). The track-finding algorithms used in the Level 2 software are essentially the same as those used in the full offline reconstruction code. The Level 2 code uses information from the Level 1 and Level 1.5 triggers to form seeds that are used to begin the track-finding algorithm. During all of run 1B, the tracking tool had the ability to use Level 1 CCT roads as its seed. Late in run 1B, the additional ability of using Level 1.5 tracks as seeds was added. This

capability was added so that the quality of the seeds sent to the tracking code would increase thus decreasing the computation time needed to perform the Level 2 tracking. Unfortunately, early versions of this code improperly implemented the change causing an approximately 30% inefficiency in the tracking of dimuon events. This problem was later fixed (run 91676). MU_2_CENT always used the Level 1 seeds, so it was never subject to this tracking bug.

- **Calorimeter Confirmation Tool**

  This tool uses the energy deposited in the calorimeter to reject bad or fake muons. It sums the energy from the cells along the muon track, as well as the energy in the nearest neighbor cells. The tool requires that the sum of the energies exceed 0.5 GeV. During the first two-thirds of the collider run, a bug in this tool caused it to fail all muons with $\varphi \sim 0$. This caused the calorimeter confirmation tool to be less efficient for these earlier runs. This bug was fixed for run 89247.

- **Scintillator Rejection Tool**

  Midway though run 1B, the Level 2 scintillator tool became available. This tool looks at all the muon tracks passing the Level 2 muon tracking tool. These tracks are projected out to the scintillators. If a muon track points at a scintillator, the tool requires that a discriminated pulse be found within the 50 ns gate that the scintillator is active. If the track does not point at a scintillator, then no requirement is made and the track is accepted. Both MU_2_LOW and

| Run Number | Calorimeter Confirmation | Level 2 Scintillator | Multiple Interaction Veto (MU_2_LOW) | (MU_2_CENT) |
|---|---|---|---|---|
| 73296 | On* | - - | Level 1 Seeds | - - |
| 85277 | On* | 0–3 | Level 1 Seeds | - - |
| 87804 | On* | 0–3 | Level 1 Seeds | Level 1 Seeds |
| 89247 | On | 0–4,7 | Level 1 Seeds | Level 1 Seeds |
| 89518 | On | 0–4,7 | Level 1 Seeds* | Level 1 Seeds |
| 91676 | On | 0–4,7 | Level 1 Seeds | Level 1 Seeds |

Table 4-2: A listing of the Level 2 tools used by MU_2_LOW and MU_2_CENT. The changes to the calorimeter confirmation and scintillator tools affected both triggers equally. However, the two triggers differed in how they used the muon tracking tool. Table entries marked (*) signify tools that had bugs causing extra inefficiencies in the data taking. The Level 2 scintillator column lists the octants in which the scintillator veto tool was active.

MU_2_CENT used this tool as soon as it became available (run 85277). At that time, the tool was used only in octants 0–3. Later, in run 89247, this tool became available for octants 4 and 7.

### 4.1.3 Selected Triggers

The triggers and runs selected for this analysis were chosen to make the best use of all the Level 1 and Level 2 tools. The scintillator veto tool is very effective at eliminating cosmic ray events; therefore, it is desirable to choose runs and triggers that use this tool. The multiple interaction veto tool is less desirable, because this tool lowers the statistics of the data sample. Furthermore, it adds an additional 'inefficiency' to the data sample which must be determined.

It was found that a particular combination of the two triggers, MU_2_LOW and

| Bad Runs | Reason |
|---|---|
| [73296, 75179) | Level 2 muon tracking code is unstable in WAMUS |
| (88674, 89299) | Experimental Level 1.5 trigger tables |
| [91676, 91854) | Defective Level 1.5 confirmation tool |

Table 4-3: List of bad runs which can not be used in data analysis. In each case, temporary problems with the Level 2 code corrupted the data.

MU_2_CENT, allows one to take advantage of the scintillator tool, avoid the multiple interaction veto tool, and avoid the Level 2 tracking bug. Before run 85277, MU_2_LOW used the multiple interaction veto, so events occurring prior to this were rejected. Also, the Level 2 scintillator tool was not available for these early runs. The trigger MU_2_CENT was created on run 87804. Since this trigger looked only for central dimuons, it was easier to keep the prescales low. Further, this trigger always used Level 1 seeds for the Level 2 muon tracking, so MU_2_CENT was not affected by the inefficient Level 2 tracking code. Therefore, runs after 87804, only the MU_2_CENT trigger was used (see Table 4-4).

### 4.1.4 Bad Runs

During various time periods of the run the trigger system corrupted the data that was being recorded. These runs had to be eliminated from the data sample. The bad running periods for central muons are given in Table 4-3. Further details of these runs can be found in reference [48]. In addition to this, various individual runs were occasionally bad due to temporary hardware or data acquisition problems. These

| Runs | Dates | Trigger |
|---|---|---|
| [85277, 87804) | 10/94 – 01/95 | MU_2_LOW |
| [87804, 93115] | 01/95 – 07/96 | MU_2_CENT |

Table 4-4: Triggers selected for this analysis. Note that different triggers were selected for different running periods.

runs are listed in reference [49] and were also eliminated from the data sample. The integrated luminosity for the runs listed in Table 4-4 after the removal of bad runs is 46.2 $pb^{-1}$.

## 4.2 Data Reconstruction

Once the data has been selected by the Level 1 and Level 2 triggers, it is written to tape. After it is on tape, the data must be processed with the DØ reconstruction program. 'Reconstruction' simply refers to the process of turning raw information such as muon hits and calorimeter cell ADC values into physics objects like muons, electrons, and jets. This data set was processed with versions 12.14–12.20 of the DØ reconstruction code. As part of the reconstruction process, the data was separated into various streams, which were then used in each of the analysis performed at DØ.

## 4.3 The B2M Stream

The ALL stream consists of all the data that has been collected by DØ for physics analysis. The B2M stream is a subset of this stream, representing about 4% of the

ALL stream. The events contained in the B2M stream are selected by imposing a set of relatively loose selection cuts on the ALL stream events. These cuts are designed to select dimuon events of reasonable quality while maintaining a high overall efficiency. The following cuts were applied for this stream:

- At least two, but less than seven, reconstructed muons. Each of the muons must make it through the iron toroid.
- The muon track quality flag, IFW4, must be $< 2$ for both muons.
- Each muon must have deposited a minimum amount of energy in the calorimeter. The energy in the calorimeter cells along the muon track plus the energy in the nearest neighbor cells must exceed 1 GeV, or the energy in the hadronic calorimeter cells must exceed 0.5 GeV.
- The event must contain two muons that are not rejected by the scintillator. A muon candidate is rejected by the scintillator if the muon track points to a scintillator but the scintillator did not trigger.

## 4.4 Offline Muon Identification

Before using the data in the analysis, two additional DØ package were used to process the data. The CAFIX [50] package is designed to correct the energy scale of the reconstructed jets in each of the events. In addition, CAFIX recalculated the muon corrected $\not\!\!E_T$ variable. CAFIX v5.0 was used for this data set. MUFIX [51] improves

upon the muon reconstruction code and in some cases fixes problems in the data set caused by bugs in the older versions of the reconstruction code. MUFIX improves the muon momentum resolution and fixes the scintillator timing information. MUFIX is also designed to recalculate the global fitting parameter, but, unfortunately, this portion of the code was turned off during the processing of this data set. This processing error occurred only in the data and not the Monte Carlo sample. Consequently, there are expected to be small differences between the momentum resolutions found in the data and the Monte Carlo. The errors associated with this discrepancy are discussed in Chapter 8.

Offline cuts in addition to those imposed by the B2M stream were imposed. These cuts are designed to select quality muons and reject cosmic ray and poor quality muons. Below is a list describing each of these cuts (see Table 4-5).

- **A-Stubs**

  An A-Stub is a muon candidate which hits only the A layer of the muon system. These candidates are low energy muons that fail to make it through the toroid. Because DØ does not have a central magnetic field, it is not possible to determine the momentum or sign of such muons. Therefore, these muon candidates are eliminated from the sample.

- **Muon Track Quality**

  The muon reconstruction program assigns a quality flag, IFW4, to each muon track. 'Golden' muons are denoted by IFW4 = 0. This flag takes into account

the fit of the track in the bend and non-bend view, whether it hits the A layer of the muon system, the impact parameter of the extrapolated track, and the number of muon cells hit. In this analysis, each track is required to have IFW4 $\leq 1$. A further requirement is that at least one the two muons must have IFW4 $= 0$.

- **Calorimeter Confirmation**

  A minimum ionizing particle is expected to deposit a characteristic amount of energy in the calorimeter along the particle's path. Therefore, it is required that the fraction of hadronic layers in the calorimeter hit by the muon (HFRACT) must be greater than 0.6. In the central region, the calorimeter has between three and five layers, so this cut ensures that, at most, only one layer of the calorimeter is missed. A second requirement is that at least 0.5 GeV of energy must be deposited in the calorimeter along the muon track (ETRACK).

- **Layers Hits**

  Information such as impact parameter and muon momentum can best be determined when all three layers of the muon system are hit. In an attempt to increase the efficiency of track finding, however, this requirement is relaxed allowing two or three layer tracks to be used.

- **Scintillator** $\Delta tof$

  The scintillator $\Delta tof$ is defined as the difference in time between when the muon

| | |
|---|---|
| Muon Track Quality | IFW4 = (0,1), (1,0), or (1,1) |
| Fraction of Hadronic Calorimeter Layers | HFRACT $> 0.6$ |
| Calorimeter Energy along Muon Track | ETRACK $> 0.5$ GeV |
| Layers Hit in Muon System | 2 or 3 |
| No A-Stubs | IFW1 $\neq 5$ |
| Fiducial Cut | $\varphi_\mu < 80^\circ$ or $\varphi_\mu > 110^\circ$ |
| Scintillator Timing | $\lvert\Delta tof\rvert < 10$ ns |

Table 4-5: Single muon quality cuts used for CF muon identification.

hits an active scintillator (with respect to the beam crossing time) and the time it would take for a particle traveling at the speed of light to traverse the same distance. Beam produced muons have $\Delta tof$ values near zero. Cosmic ray muons produce times which are uncorrelated with the beam crossing time. Each of the muons pointing to a scintillator is required to satisfy $-10 < \Delta tof < 10$ ns.

- **$\varphi$ Fiducial Cut**

  The Main Ring of the Tevatron passes through the top portion of the DØ detector. Particle flux associated with the Main Ring have caused radiation damage to many of the nearby muon chambers. Because of this damage, the efficiency of these chambers is very low. Since the Monte Carlo does not accurately reproduce these inefficiencies, all muon tracks within $80^\circ < \varphi < 110^\circ$ are removed from the data sample. This fiducial cut is also useful in that it removes muon tracks which originate from within the Main Ring.

## 4.5 Offline Jet Identification

### 4.5.1 Jet Finding Algorithm

The reconstructed jets used in this analysis were found with the 0.7 cone reconstruction algorithm [48]. Jets are defined by the sum of their measured $E_T$ within a cone radius $\Delta R = \sqrt{\Delta\varphi^2 + \Delta\eta^2}$ about the jet axis. Jet reconstruction begins with a list of measured $E_T$ values found in each of the calorimeter trigger towers. The transverse size of these towers in the central regions is $0.1\eta \times 0.1\varphi$ with somewhat larger towers in the forward regions near the beampipe. The $E_T$ for each of the towers is corrected for the position of the vertex as measured by the central detector.

The reconstruction code begins by finding localized energy deposits (pre-clusters), which are used as seeds for the iterative reconstruction process. Adjacent towers with energies exceeding the $E_T = 1$ GeV threshold form the pre-clusters. The $E_T$ weighted average $(\eta, \varphi)$ coordinate is calculated and used as the starting point for the jet axis. The weighted average of the cells within a $\Delta R = 0.7$ cone about this axis is then calculated to form a new jet axis. If the new average is equal to the pre-cluster average then the jet is considered to be stable. If the jet is not stable, the new axis is used to form a new $\Delta R = 0.7$ cone, and the process is repeated until a stable jet is found. After all jets stabilize, an $E_T$ cut at 8 GeV is applied.

Finally, the reconstruction code checks to see if it is necessary to split or merge the jets. It does this by checking the $E_T$ shared between the jets. If two jets share more

than 50% of their transverse energy, they are merged. Otherwise, the jets are split with the shared cells being awarded to the jet with the closest axis. If two different pre-clusters produce jets that lie within $\Delta R \leq 0.1$ of each other, then the jets are assumed to be identical. In this case, the pre-cluster with the smallest $E_T$ is removed.

### 4.5.2 Jet Quality Cuts

The jet reconstruction code is sensitive to non-beam related events. A set of standard jet quality cuts have been developed to help reduce the number of fake jets in the sample. The sources for fake jets include energy deposition from the Main Ring, hot cells in the calorimeter, and bremsstrahlung from cosmic ray muons.

- **Electromagnetic Fraction**

  A cut on the fraction of jet $E_T$ found in the electromagnetic portion of the calorimeter, EMFRAC, is made. It is required that $0.05 <$ EMFRAC $< 0.95$. It has been shown that this cut is 90% effective at removing fake jets due to calorimeter 'hot cells' [52]. Monte Carlo studies have shown that his cut is 99% efficient with real jets except in the region between the central and end calorimeters ($\eta \sim 1.4$) where this efficiency decreases slightly.

- **Coarse Hadronic Fraction**

  The fraction of the jet $E_T$ contained in the coarse hadronic portion of the calorimeter is required to be less than 0.4. This cut helps eliminate fake jets caused by energy deposition from the Main Ring. The Main Ring passes through

the coarse hadronic portion of the calorimeter and is expected to deposit energy into this region. This cut is 95% effective at removing these types of fake jets, and 99% effective at removing fake jets caused by hot cells in the coarse hadronic calorimeter [53]. Monte Carlo studies show that this cut is 99% efficient except in the crack between the CC and EC where this efficiency decreases to 95%.

- **Hot Cell Ratio**

  The hot cell ratio is defined as the ratio between the $E_T$ of the highest energy cell in a jet to the $E_T$ of the second most energetic cell. Real jets are not expected to produce large variations in the energy deposited in the calorimeter cells within a jet. It is required that the hot cell ratio be less than 10. This cut is effective at removing fake jets caused by noise in the calorimeter [52, 54].

The efficiencies of these cuts have been studied extensively. They have been found to range from 96% for a jet with $E_T = 11$ GeV to 91% at $E_T = 400$ GeV. The rejection rate for fake jets is greater than 95% [52].

## 4.6 $b\bar{b}$ Event Selection

Additional selection cuts were applied to the data that were designed to enhance the $b\bar{b}$ signal and reduce the dimuon contribution from background processes. These selection cuts are listed below and are sumarized in Table 4-6.

- **Muon Pseudorapidity**

| | |
|---|---|
| Muon Pseudorapidity | $\|\eta_\mu\| \leq 0.8$ |
| Muon Transverse Momentum | $4 \leq P_T^\mu \leq 25$ GeV/c |
| Invariant Mass | $6 < M_{\mu\mu} < 35$ GeV/c$^2$ |
| Associated Jet | Jet and muon within $\Delta R = 0.7$ |
| Jet Transverse Energy | $E_T > 12$ GeV |
| Jet Electromagnetic Fraction | $0.5 <$ EMFRAC $< 0.95$ |
| Jet Coarse Hadronic Fraction | HADFRAC $> 0.4$ |
| Jet Hot Cell Ratio | HOTCELL $< 10$ |

Table 4-6: Additional selection cuts used to enhance the $b\overline{b} \rightarrow \mu\mu X$ signal.

A kinematic cut of $|\eta_\mu| < 0.8$ is made on both muons. This cut takes advantage of the higher efficiency and better performance of the central muon system. The efficiency of the muon systems falls off near the border of the CF and EF muon chambers. Thus, this cut restricts us to the region of the detector which contains the better understood efficiencies.

- **Muon Transverse Momentum**

  Muons in the central region must have an energy of 3.0 GeV to pass through the iron toroid. Thus, the requirement of $P_T^\mu > 4.0$ GeV/c helps to ensure that the muon's momentum is measurable. Further, it is difficult to determine the trigger efficiencies for muons with $P_T^\mu < 4.0$ GeV/c, because muon trigger efficiencies fall off sharply below this value. When $P_T^\mu > 25$ GeV/c, muon momentum and sign resolution become increasingly difficult to measure. This upper bound also helps reduce backgrounds from the decay of W and Z bosons.

- **Associated Jets**

  Each muon track is required to have an 'associated' reconstructed jet. The jets

used in this analysis have a cone size of $\Delta R = \sqrt{\eta^2 + \varphi^2} = 0.7$ about the jet axis. Each jet is required to have a transverse energy greater than 12 GeV. It is possible to reconstruct jets with $E_T$'s less than this, but the jet reconstruction efficiencies for these jets are not well understood. An associated jet is one in which a muon track lies within $\Delta R = 0.7$ of the jet axis. In the semileptonic decay of B hadrons, jets arising from the hadronization of the $b$-quark are expected to be produced along with a lepton (muon). The associated jet requirement reduces backgrounds from $\Upsilon$ and Drell-Yan events since dileptons from these processes are, in general, isolated. Due to the associated jet requirement, less than 0.01% of the events in the data sample are expected from $\Upsilon$ or Drell-Yan production. In addition, each muon is required to have a unique associated jet. This requirement suppresses sequential decays of the $b$-quark:

$$\begin{array}{rcl} b & \rightarrow & c\mu^{-}\overline{\nu} \\ & & \downarrow \\ & & \hookrightarrow \mu X \end{array} \tag{4.1}$$

- **Dimuon Invariant Mass**

  The invariant mass of the dimuons, $M_{\mu\mu}$, is required to fall within the range $6 \leq M_{\mu\mu} \leq 35$ GeV/c$^2$. The lower cut is made in order to eliminate background contributions from the J/$\psi$, other low mass mesons, and the sequential decay of the $b$-quark to lighter quarks. The upper cut is made to suppress the $Z \rightarrow \mu\mu$ background.

# Chapter 5

# Monte Carlo

## 5.1 ISAJET Monte Carlo

The Monte Carlo used for this analysis was produced by the ISAJET event generator [38], version 7.13. ISAJET produces events in the following manner:

1. Primary $2 \rightarrow 2$ hard scattering events are generated according to the appropriate QCD cross sections.

2. Initial and final state QCD radiative corrections are added.

3. Partons are independently fragmented into hadrons, and particles with lifetimes less than approximately $10^{-12}$ s are decayed.

4. Minimum bias beam jets are added to the event in the assumption that they account for the remainder of the event energy.

A general schematic of this process is shown in Fig. 5-1. First, an initial parton-parton hard scatter is generated according to the lowest order matrix elements. For this analysis, the TWOJET option in ISAJET was used. This option forces ISAJET to produce all $\alpha_s^2$ QCD processes. Some of these $2 \rightarrow 2$ matrix elements are shown in Fig. 5-2. The cross sections from the hard scattering processes are then convolved with the proton structure functions

$$\sigma = \sigma_0 \cdot F(x_1, Q^2) \cdot F(x_2, Q^2), \tag{5.1}$$

where $\sigma_0$ is the parton-parton cross section calculated from perturbative QCD, $F(x, Q^2)$ are the structure functions, $x_1$ and $x_2$ are the parton momentum fractions, and $Q^2$ is the momentum transfer scale.

Approximate QCD radiative corrections are included by allowing initial and final state partons to emit gluons which can in turn decay into $q\overline{q}$ quark pairs. This process is governed by the Altarelli-Parisi splitting functions (2.27) which describe the probability that a given parton will split. The Altarelli-Parisi functions are modeled in ISAJET through the use of the branching approximations of Fox and Wolfram [55].

In order to avoid infrared and collinear singularities, each of the partons that radiate gluons is required to have a mass above a set threshold, $t_c$. It is assumed that gluon radiations below this scale are non-perturbative and are handled by the hadronization model. In ISAJET, this mass threshold is set at $t_c = 6$ GeV/c$^2$. Fortunately, the minimum energy transfer, $Q$, required to produce a $b\overline{b}$ pair is $2m_b \approx$

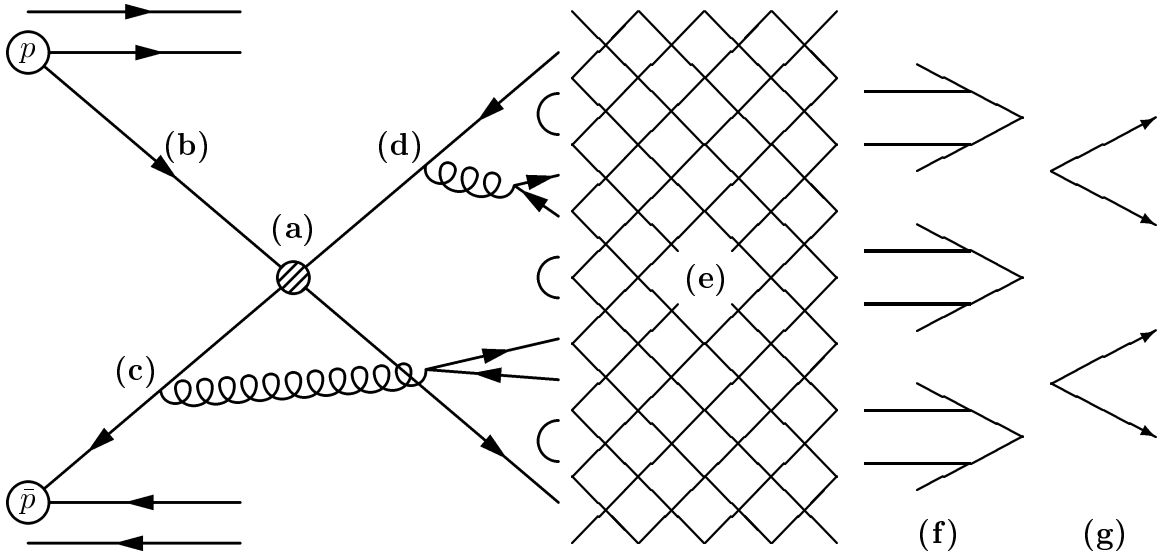


Figure 5-1: A model illustrating how ISAJET produces $p\overline{p}$ inelastic scattering events: generation of a $2 \rightarrow 2$ matrix element (a), evolution of the hard scatter partons of the event back to the $p\overline{p}$ (b), addition of initial (c), and final state gluon radiations (d), quark fragmentation (e), hadronization (f), and the decay of the short lived hadrons (g).

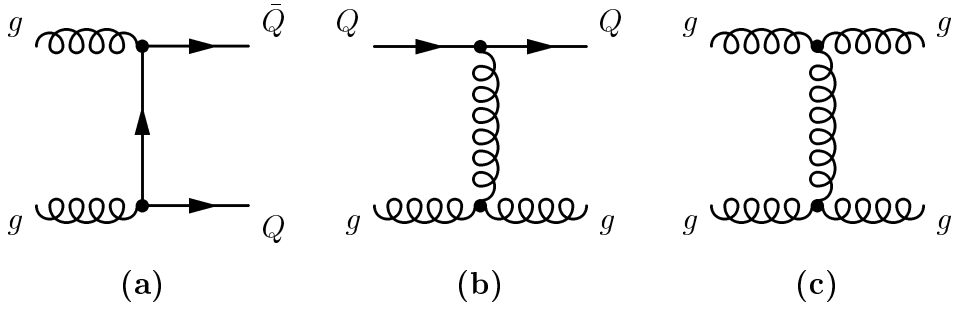


Figure 5-2: Feynman diagrams representing the three lowest order matrix elements used by ISAJET. Higher order terms are simulated by adding initial and final state gluon radiation.

10 GeV/c$^2$.

ISAJET is a phenomenological model that approximates NLO perturbative QCD. In ISAJET, heavy flavor production can occur via the following mechanisms:

- All lowest order graphs ending with the production of a $Q\overline{Q}$ pair, Fig. 5-2(a), are called *flavor creation*. Approximately 20% of the time, gluon radiation corrections are added to these flavor creation terms. Collectively these graphs are referred to as 'ISAJET lowest order'.

- States in which the hard scatter involves one heavy flavor $Q$ or $\overline{Q}$ (Fig. 5-1(b)) are referred to as *flavor excitation*. These processes are considered higher order because of the presence of an initial state gluon which splits into a $Q\overline{Q}$ pair.

- All graphs in which the hard scatter does not involve heavy quarks are called *gluon splitting* (Fig. 5-1(c)). In this case, a $Q\overline{Q}$ pair is produced by a final state gluon decaying into a $Q\overline{Q}$ pair. This process is also higher order.

- Initial and final state gluon radiations are not classified separately. Interference terms, Fig. 2-5(d) are ignored.

These classifications are strictly true only in the theoretical limit $m_b \to 0$. However, it is a useful phenomenological model as it allows one to use the different topologies of the production mechanisms to tag the $b\overline{b} \to \mu\mu X$ events.

### 5.1.1 Quark Fragmentation and Hadronization

The next step in the production of ISAJET Monte Carlo is to form hadrons from the produced quarks and gluons. The fragmentation model used by ISAJET is the independent fragmentation ansatz first proposed by Field and Feynman [56]. In this model, a quark, $q$, with momentum, $p$, is formed into a hadron by pairing the $q$ with a $\overline{q}'$ from a $q'\overline{q}'$ pair generated from the q's color field. The hadron is given a fraction of $q$'s momentum, $z$, and the $q'$ are created with an average $P_T$ of 0.35 GeV/c under the constraint u:d:s = 0.43:0.43:0.14. These ratios are necessary as the strange quark is the heaviest of the three quarks and is less likely to be produced. This process is repeated in an iterative fashion with the new $q'$ which has a momentum $(1-z)p$.

The momentum fraction for the resulting hadron is defined as

$$z = \frac{E^{had} + p_{||}^{had}}{E^q + p^q} \tag{5.2}$$

where $p_{||}^{had}$ is the momentum of the hadron in the direction of quark $q$. These fractions are generated according to the distribution for heavy quarks given by Peterson *et al.* [57]

$$f(z) = \frac{1}{z[1 - \frac{1}{z} - \frac{\epsilon}{(1-z)}]^2} \tag{5.3}$$

There is only one parameter in this expression, $\epsilon$, which is expected to scale with quark mass

$$\epsilon = \frac{k_q}{m_q^2}. \tag{5.4}$$

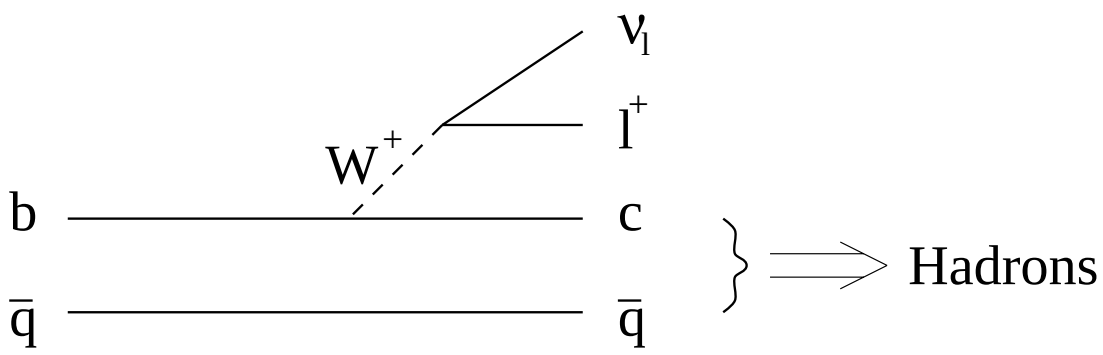


Figure 5-3: A B-meson semileptonic spectator decay.

The default values given by ISAJET are $k_c = 0.80$ and $k_b = 0.50$.

### 5.1.2 B Hadron Decays

ISAJET uses the simplified V-A spectator model to decay unstable hadrons. In this model the heavy quark within a meson is considered independent of the lighter (spectator) quark. Thus, the heavy quark is allowed to decay as a free particle (Fig. 5-3). This model is only an approximation as it ignores gluon radiation, binding effects, and other perturbative and nonperturbative QCD corrections. For large quark masses, however, these effects are expected to be small making this a reasonable model to use for B meson decays.

In addition to the direct decay of B mesons into muons, it is also possible for the B to decay sequentially. In this case, the meson follows the decay chain $B \to DX$, $D \to l\nu X$. The spectator model is expected to be less accurate for these decays because of the lighter $c$-quark mass.

Measurements at LEP [58] show that the inclusive semileptonic branching ratio

for B hadrons into muons is

$$BR(B \to \mu^{\pm}\nu_{\mu}X) = 11.0 \pm 0.3 \pm 0.4\% \tag{5.5}$$

This is different from the 12% used by ISAJET. In order to insure that the ISAJET predictions are accurate, a correction factor must be applied to the $b\overline{b} \to \mu\mu X$ events. A correction of $(\frac{11.0}{12.0})$ is applied for every muon that is produced by the direct decay of a $b$-quark; therefore, events in which both the $q$ and $\overline{q}$-quarks directly decay into muons require a correction of $(\frac{11.0}{12.0})^2 = 0.840$. In sequential decays, $B \to D \to \mu$, only one muon decays directly from a $b$-quark. In this case, a correction of $(\frac{11.0}{12.0}) = 0.917$ is applied. No corrections are made for the $c$-quarks as the branching ratios used by ISAJET for this decay agree with experimental measurements.

## 5.2 Monte Carlo Samples

### 5.2.1 $b\bar{b}$ and $c\bar{c}$ Monte Carlo

The ISAJET Monte Carlo generator was used to simultaneously produce both the $b\overline{b}$ and $c\overline{c}$ samples. As previously mentioned, ISAJET is a LO event generator that adds radiative terms to simulate NLO processes. Thus, $2 \to 2$ scattering processes are at the core of every event. For the $b\overline{b}$ and $c\overline{c}$ Monte Carlo samples, the range of transverse momenta of the hard scatter was chosen to be between 4 and 80 GeV/c. This limited kinematic range can be used to generate an accurate dimuon sample, because quarks

with $P_T^q < 4$ GeV/c do not generally produce muons with $P_T^\mu > 3$ GeV/c. The CTEQ2L structure function was used in the generation of these events.

This simulation process is time consuming and CPU intensive, because the fraction of hard scatters producing heavy quark flavors is small. To overcome this, a routine known as ISALEP was used to speed up the event generation. The first technique used by ISALEP is to perform multiple evolutions of the QCD radiative corrections for each of the $2 \rightarrow 2$ hard scatters. Multiple evolutions are useful because the NLO $Q\overline{Q}$ production relies on radiative processes that occur infrequently; thus, this method is useful for speeding up the production of NLO heavy flavor events. The second technique involves the multiple evolution of the quark fragmentation and hadron decays for events that contain $Q\overline{Q}$ pairs. Since hadrons produced from heavy quark fragmentation have $\sim 20\%$ chance of decaying into a muon, the probability that a single evolution will produce dimuons is smaller than 5%. Multiple evolutions of the quark fragmentation and decays make the production of dimuon events more likely. The parameters used to set the number of evolutions for each of these techniques are NEVOLVE and NHADRON respectively. For this Monte Carlo sample, both parameters were set to 10.

While generating the $b\bar{b}$ and $c\bar{c}$ Monte Carlo sample, it was noticed that the inclusive heavy quark cross section calculated in ISALEP varied as a function of the values NHADRON and NEVOLVE. Fig. 5-4 shows examples of how the $b$-quark cross section given by ISALEP compares with the NLO QCD theory given by Nason *et al.*

for different values of NEVOLVE and NHADRON. It was also found that the inclusive muon cross section calculated with ISALEP is also dependent upon NHADRON and NEVOLVE, but in a manner different than was found for the heavy quark cross sections.

A two step correction was applied to the Monte Carlo so that the heavy quark cross sections would be consistent with NDE. In the first step, a normalization factor was applied to translate the heavy quark cross section for single muon events generated with NEVOLVE and NHADRON equal to 10 to the cross section for muon events generated with these parameters set equal to 1. Next, the total heavy quark cross section (ISALEP parameters equal to 1) is normalized to the total heavy quark cross section as predicted by NDE. Both of these correction factors are calculated as a function of the average heavy quark $P_T$ (Fig. 5-5). Corrections for $b\overline{b}$ and $c\overline{c}$ events are calculated independently. Note that it is assumed that the correction factors determined using inclusive single muons are identical to those for dimuons.

### 5.2.2 Decay Background Monte Carlo

A significant contribution from the decay of pions and kaons into muons is expected. The decay lengths of pions and kaons are boosted in the lab frame, so that the fraction of charged particles that decay within the 0.84 m radius of the central tracker is small. Further, the average transverse momentum of the muons produced by decays of this type is approximately 0.5 GeV/c. Since muons need an energy of at least 3 GeV/c to

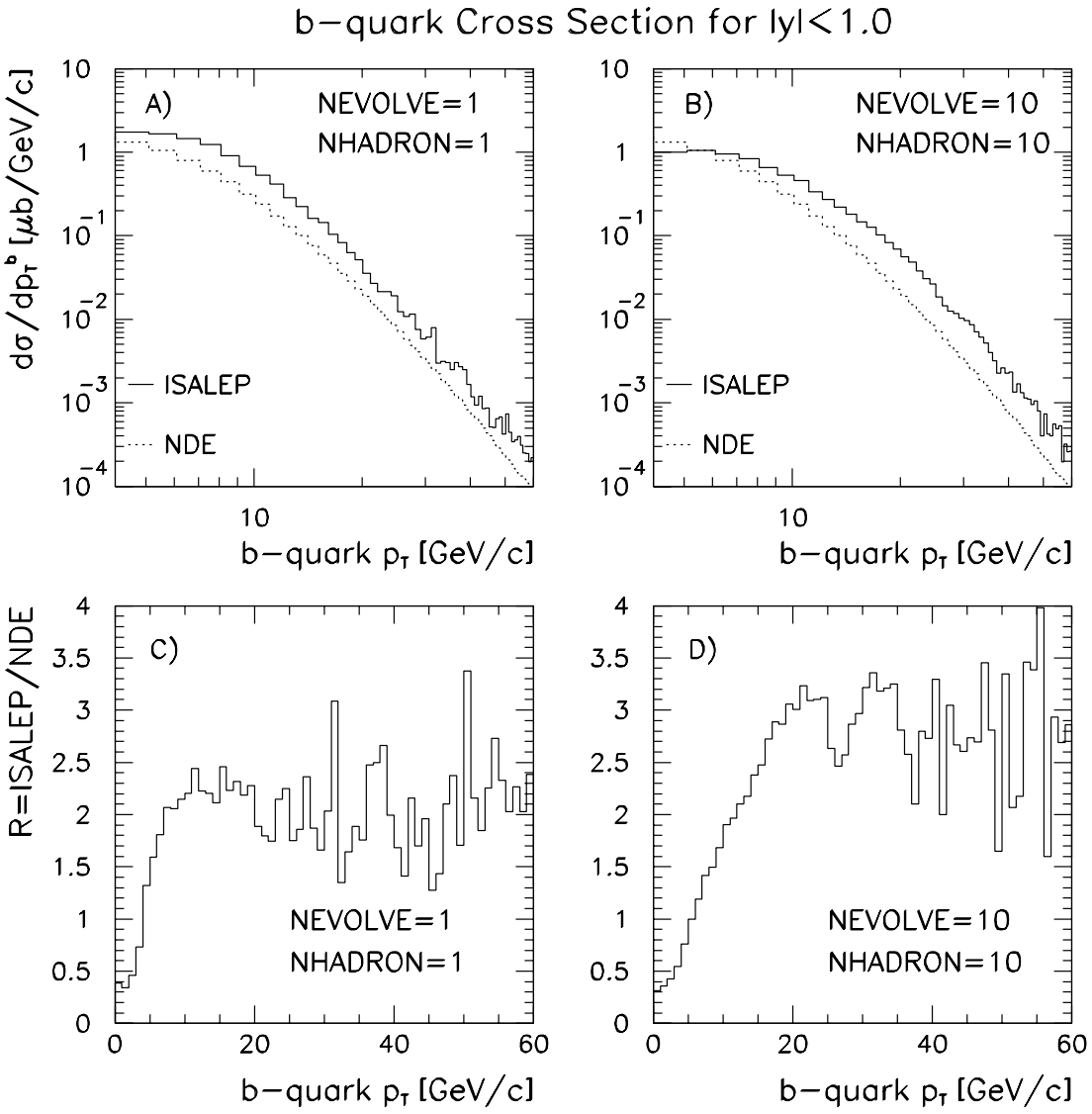


Figure 5-4: Comparison of the $b$-quark production cross section for $|y^b| < 1.0$ as given by ISALEP for two different sets of parameters NHADRON and NEVOLVE. A) and B) show the ISALEP cross section with the central NDE value, while C) and D) show the ratio, R $\equiv \frac{\text{ISALEP}}{\text{NDE}}$ for each set of ISALEP parameters.

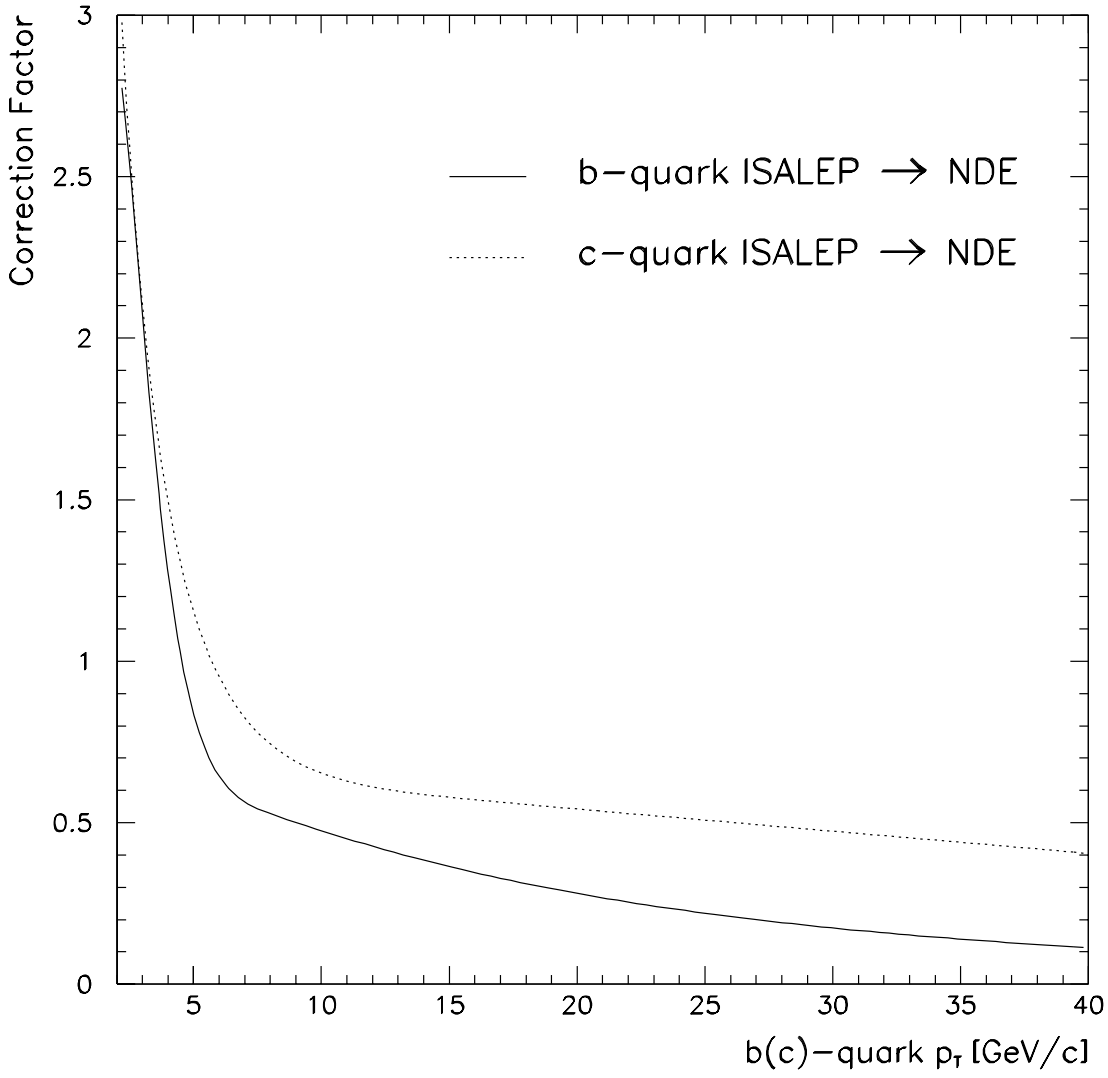


Figure 5-5: Correction factor for $b$ and $c$-quark production plotted as a function of the average $Q\overline{Q}$ $P_T$. This factor is used to normalize the ISALEP cross sections to the NLO calculations of NDE.

make it through the iron toroid, the fraction of muons from pion (and kaon) decays is further reduced. However, the branching fraction for the decay of charged pions and kaons into muons is large resulting in a non-negligible background contribution.

There are two important backgrounds that can contribute to the dimuon sample. The first involves events in which a prompt muon is produced from the decay of a heavy quark, and a second muon is produced from the decay of a pion or kaon. The second background consists of dimuon events in which both muons are the result of pion or kaon decays. A Monte Carlo event generator was written to determine the relative magnitude of the contribution from each of these processes. It was found that the events in which both muons are produced from the decay of charged pion or kaons (double decay events) was more than a factor of two smaller than the 'prompt plus decay' events, so the full Monte Carlo event simulation was restricted to the prompt plus decay events.

A decay package [59] was written to speed up the production of the prompt plus decay Monte Carlo sample. A sample of $b\overline{b}$ and $c\overline{c}$ events was created in which at least one prompt muon was produced. These events were then input into the decay package which created a list of possible decay candidates ($\pi^{\pm}$, $K^{\pm}$, $K^0_L$) that satisfied $P_T^{\pi,K} > 3.0$ GeV/c and $|\eta^{\pi,K}| < 0.9$. One of these particles was chosen at random and was forced to decay into a muon. The probability that this type of decay occurs is given by

$$P = \left(1 - e^{-\frac{R_{CD}}{c\tau}\frac{m_{\pi/K}}{E_{\pi/K}}}\right) \mathrm{BR}(\pi/K \to \mu), \tag{5.6}$$

where $R_{CD}$ is the radius of the central tracking volume, $c\tau$ is the particle decay length, and BR($\pi/K \to \mu$) is the appropriate branching fraction.

The weight assigned to each of these events is given by the product of the cross sectional weight for the ISAJET event, the probability that a pion or kaon decays, and the number of possible decay candidates. This calculation is further complicated by the fact that each event contains several pions and kaons that can possibly decay. The full details of how these effects are accounted for are discussed in reference [59]. This package was checked by comparing it with the results found from the more rigorous treatment of $\pi$/K decays by DØGEANT.

### 5.2.3 Drell-Yan Background

Drell-Yan production has been modeled with the ISAJET event generator. The DRELLYAN option within ISAJET models the LO process $q\overline{q} \to \gamma^* \to \mu^+\mu^-$ while using QCD radiative corrections to simulate NLO processes. These higher order processes are of the form

$$\begin{array}{l} q\overline{q} \to \gamma^* g \to \mu^+\mu^- g \\ q\overline{q} \to \gamma^* g \to \mu^+\mu^- g \end{array} \tag{5.7}$$

The NLO calculation of the Drell-Yan cross section diverges as $P_T \to 0$. ISAJET circumvents this difficulty by replacing the $1/P_T^2$ term in the cross section expression with a cutoff parameterization designed to produce the correct integrated cross

section. This parameterization is

$$\frac{1}{P_T^2} \rightarrow \frac{1}{\sqrt{P_T^4 + P_0^4}}, \tag{5.8}$$

where $P_0^2$ is defined as $M_{\gamma^*}$ (0.2 GeV/c$^2$).

The Drell-Yan Monte Carlo event sample was generated with the EHLQ structure functions. A mass range of 4–40 GeV/c$^2$ was selected for the $\gamma^*$. The cross sectional weight of the events in the sample were modified to match the measured cross section from data [60].

## 5.3 Monte Carlo Simulation of Data

In order for the generated Monte Carlo events to be truly useful, one must determine the detector response for each event. Various simulation packages exist which have been designed to modify the Monte Carlo so that the generated events better simulate the data. Each event is sent through the DØ detector geometry, DØGEANT, simulating the expected hits in the muon system and the expected calorimeter response. Next, the muon data is smeared to account for chamber inefficiencies and survey uncertainties. Finally, a trigger simulation package is used to simulate the Level 1, Level 1.5, and Level 2 trigger responses.

### 5.3.1 DØGEANT

The purpose of DØGEANT is to simulate the DØ detector. DØGEANT is actually a customized version of the CERN program library package GEANT [61]. GEANT takes each Monte Carlo event and simulates the interactions that the particles would have within the detector. GEANT uses various physics processes to simulate particle track evolution including: multiple Coulomb scattering, full electromagnetic and hadronic showering, electron and muon bremsstrahlung, and particle decays. GEANT then uses this tracking information to produce digital information analogous to the raw data taken by the detector.

In general, the DØ detector geometry has been modeled well. However, a balance must be achieved between detail and the CPU time required by the program. For example, electromagnetic showers are allowed to evolve only until the secondary particle energy reaches 200 MeV. Below this point the energies are determined through parameterization. DØGEANT assumes a muon resolution of

$$\left(\frac{\delta P}{P}\right)^2 = (0.18)^2 + (0.001P)^2 \tag{5.9}$$

### 5.3.2 MUSMEAR

DØGEANT does not simulate all of the inefficiencies in the muon system. The inefficiencies not simulated in DØGEANT include alignment uncertainties, drift time resolutions, and pad latch inefficiencies. Further, the true detector muon momentum resolutions are not as good as DØGEANT assumes. Since each of these inefficiencies

has a tendency to change over the course of the experiment, the MU_SMEAR package was created to simulate these changes. The advantage to this method is that one set of Monte Carlo can be quickly processed with several versions of MU_SMEAR. This gives one the ability to quickly simulate the efficiencies of the muon system during different time periods of the experiment.

### 5.3.3 VMS_FILTER

VMS_FILTER is the full DØ trigger simulator which is designed to simulate the Level 1 and Level 1.5 hardware trigger, and the Level 2 software trigger system. The Level 1 and Level 1.5 simulators are designed to exactly duplicate the trigger and trigger framework decisions made by the hardware. The Level 2 code in the simulator is essentially the same as the code used in the online software trigger.

The trigger simulator is flexible enough that it can be used with either data or Monte Carlo. In general, the simulator is slightly more efficient with Monte Carlo than with the data. Correction factors (see Section 6.1.3) must be applied to efficiencies obtained from the simulator when using Monte Carlo. Furthermore, some online triggering tools are not simulated such as the Scintillator Veto, and Multiple Interaction Veto tools. Monte Carlo events sent though the simulator pass these tools at 100%. Thus, these efficiencies must be determined in other ways (see Chapter 6).

# Chapter 6

# Efficiency Studies

The event selection cuts and trigger requirements described in Chapter 4 are designed to select quality events from the dimuon data sample while enhancing the $b\overline{b} \rightarrow \mu\mu X$ signal. These cuts ultimately affect the number of events seen in the final data sample. Therefore, the efficiencies of these selection requirements must be determined before a cross section measurement can be made. This chapter describes the methods used to determine each of these efficiencies.

ISAJET $b\overline{b} \rightarrow \mu\mu X$ and $c\bar{c} \rightarrow \mu\mu X$ Monte Carlo are used to simulate The Level 1 and Level 2 trigger efficiencies. This Monte Carlo sample has been processed by the methods described in Section 5.2 so that the Monte Carlo more accurately simulates the inefficiencies contained in the data. Whenever possible, the efficiencies obtained from the Monte Carlo are compared with efficiencies obtained from data. If a discrepancy is found, a correction factor is used to adjust the Monte Carlo efficiency

curve.

All of the uncertainties reported in this chapter represent 68.4% binomial confidence intervals. The value, 68.4%, is chosen by convention, because it represents a $1\sigma$ error in a Gaussian distribution. The details of the binomial error analysis used in this thesis are given in Appendix A.

## 6.1 Trigger Efficiencies

Processed Monte Carlo is used to determine the Level 1 and Level 2 muon trigger efficiencies. In theory, one should use data to determine these efficiencies. However, one often lacks the unbiased muon samples that are required to perform these measurements. Therefore, we are forced to rely on Monte Carlo simulations for these efficiencies. Whenever possible, comparisons between the efficiencies obtained from Monte Carlo are compared to efficiencies which are obtained from the data. If necessary, the normalization of the Monte Carlo efficiencies are adjusted to match the data.

Before the trigger efficiencies can be found, the following kinematic cuts must be applied to the Monte Carlo events

- $4 < P_T^{\mu} < 25$ GeV/c (Both Muons)
- $\mid \eta_{\mu} \mid < 0.8$ (Both Muons)
- $6 < M_{\mu\mu} < 35$ GeV/c$^2$

| Version | Filter | First Run | Last Run | Integrated Luminosity ($nb^{-1}$) |
|---|---|---|---|---|
| v7.08 | MU_2_LOW | 85277 | 88674 | 20200 |
| v7.12 | MU_2_CENT | 89299 | 90794 | 11500 |
| v7.15 | MU_2_CENT | 90795 | 93115 | 14500 |

Table 6-1: Table listing the different simulator versions and filters used in this analysis. Each combination represents a different running period for the detector. The integrated luminosity for each of these periods is also given.

Only events which satisfy these kinematic cuts are used in the measurement of the trigger efficiencies. The combined Level 1 and Level 2 efficiency is defined as the number of events satisfying the Level 1 and Level 2 requirements divided by the total number of Monte Carlo events. This efficiency is plotted as a function of the ISAJET (or real) variables: $P_T^{\mu}$(leading) and $\Delta\varphi_{\mu\mu}$. This is necessary, because these efficiencies will be applied to the data sample *after* the muon momentum resolutions have been unfolded (Chapter 8).

### 6.1.1 History Dependence of the Level 1 and Level 2 Trigger

The history of the Level 2 software and the Level 1 hardware triggers are detailed in Chapter 4. In this analysis there are three different running periods which must be simulated by the monte carlo. These running periods are listed in Table 6-1.

A trigger efficiency must be found for each of the time periods listed in Table 6-1, because it is expected that each will have slightly different efficiencies. It is also expected that each time period will be progressively more efficient than its predecessor.

Figs. 6-1, 6-2, and 6-3 show that this is indeed true, but within the statistics of the Monte Carlo Samples used here, the three efficiencies are nearly equal.

### 6.1.2 The Scintillator Veto Tool

As mentioned previously, VMS_FILTER does not simulate the Level 1 and Level 2 scintillator veto tools. Instead, the efficiencies for these tools must be extracted directly from the data. This efficiency is complicated by the fact that the number of octants used by the scintillator veto tools changed several times during the course of run 1B (see Tables 4-1 and 4-2).

Three different scintillator efficiencies must be determined: the Level 1 SCT efficiency, the Level 2 biased, and Level 2 unbiased efficiencies. When combined in the proper manner, these efficiencies can be used to measure the overall efficiency of the scintillator veto tools. The 'Level 1 SCT efficiency' is defined as the efficiency of finding a scintillator trigger in the same octant as a muon CCT trigger. The 'biased Level 2 efficiency' gives the likelihood that a muon will trigger a scintillator PDT given that a Level 1 SCT trigger was found in the same octant. The 'unbiased Level 2 efficiency' is similar to the biased efficiency except that no level 1 SCT requirement was made.

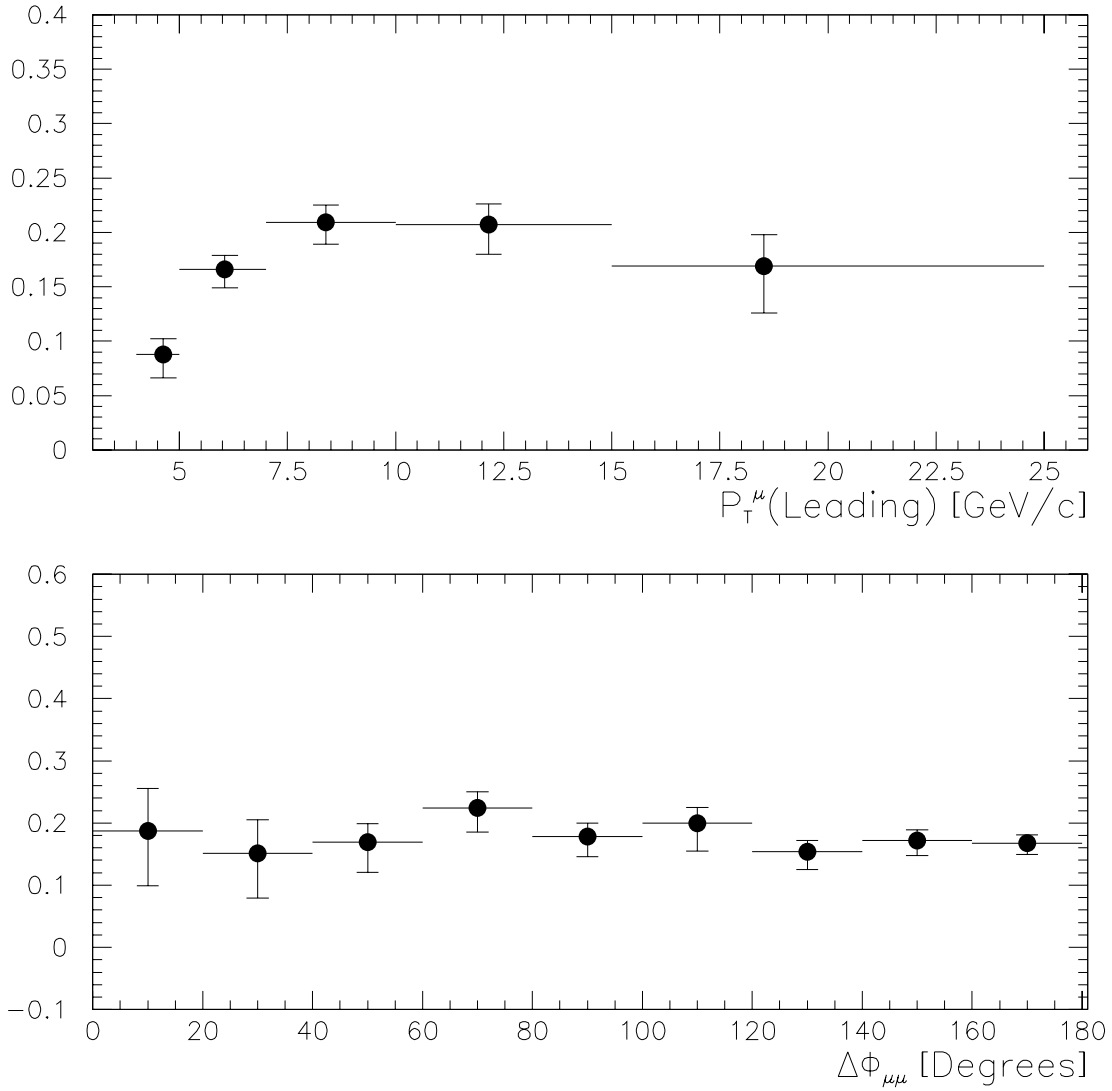


Figure 6-1: The combined Level 1 · Level 2 trigger efficiencies as a function of ISAJET (real) $P_T^{\mu}$ and $\Delta\varphi_{\mu\mu}$. These efficiencies represent the trigger conditions for runs 85277 through 88674.

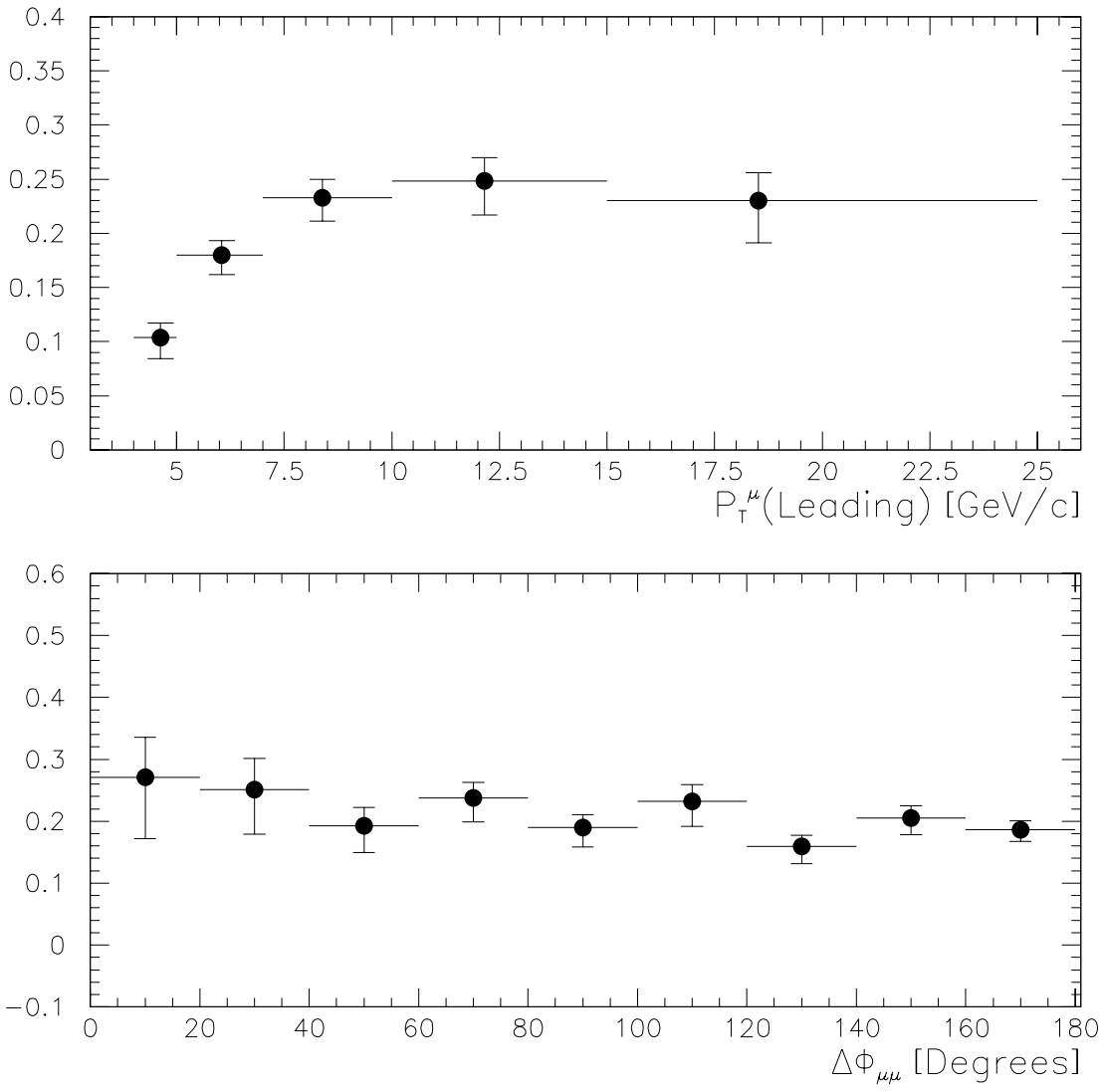


Figure 6-2: The combined Level 1 · Level 2 trigger efficiencies as a function of ISAJET (real) $P_T^{\mu}$ and $\Delta\varphi_{\mu\mu}$. These efficiencies represent the trigger conditions for runs 89299 through 90794.

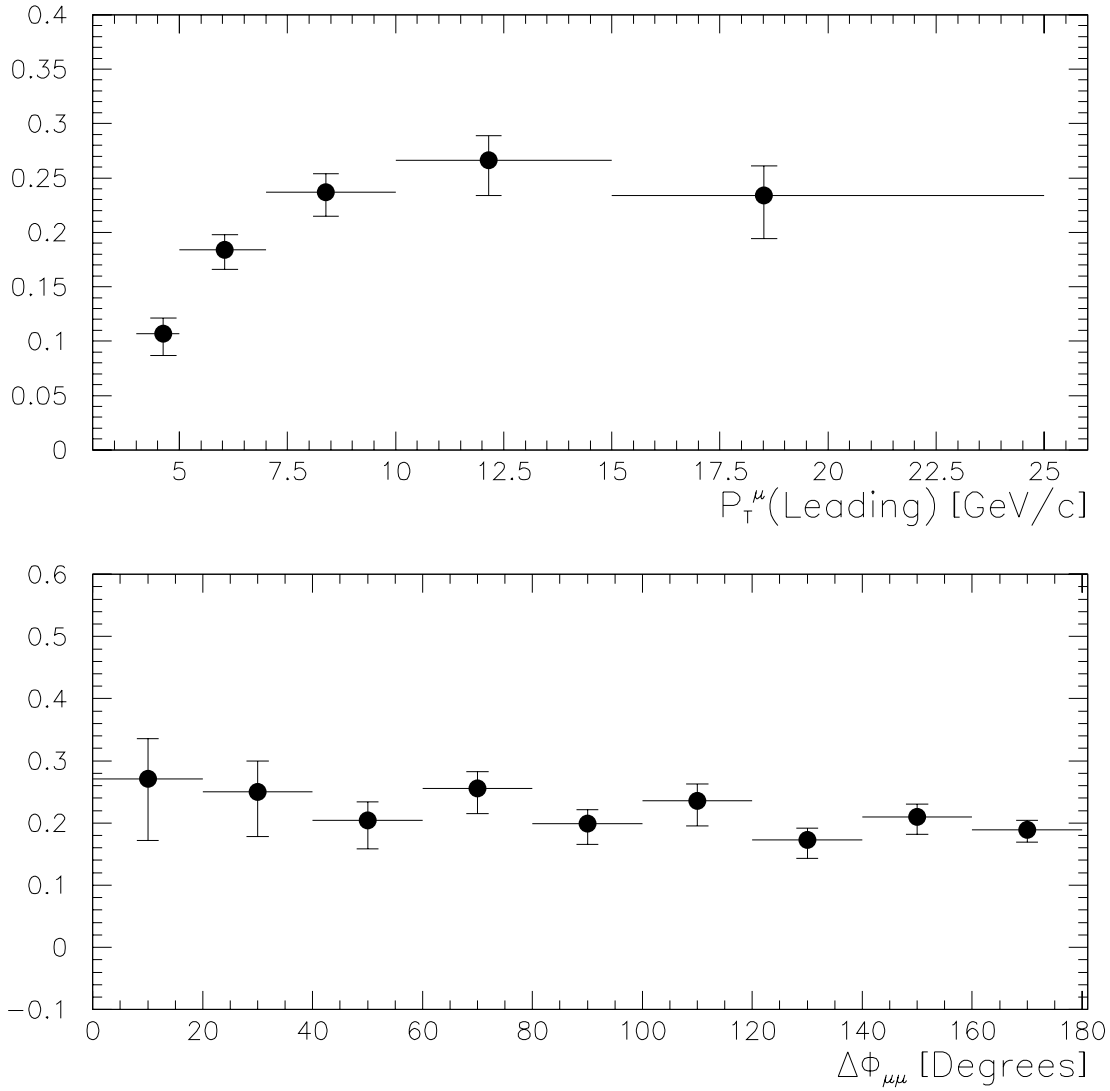


Figure 6-3: The combined Level 1 · Level 2 trigger efficiencies as a function of ISAJET (real) $P_T^{\mu}$ and $\Delta\varphi_{\mu\mu}$. These efficiencies represent the trigger conditions for runs 90795 through 93115.

**Level 1 Veto**

The Level 1 scintillator veto efficiency is found by combining the individual Level 1 SCT efficiencies according to the Level 1 scintillator veto logic (See Table 6-2). The Level 1 SCT efficiency is obtained from a set of 'scintillator unbiased' single muon events. These events are obtained from the data by requiring the Level 2 filter MU_1_LOW_NOSCINT. This filter is unique, because it does not use the Level 1 or Level 2 scintillator veto tools. The muon selection cuts listed in Tables 4-5 and 4-6 are applied to this sample with the exception that no associated jet or scintillator requirements were made. 195 such events were selected and scanned manually to eliminate poor quality muon tracks.

Recorded in this data sample is information about individual SCT triggers (AND/OR terms). Since the muons in this sample have all passed the level 1 CCT requirement, the SCT efficiency is simply the percentage of these tracks that have a matching Level 1 SCT. This efficiency was found to be $\epsilon_{SCT} = 95.0^{+1.3}_{-3.4}\%$. $\epsilon_{SCT}$ can now be used to correct the dimuon Monte Carlo which is used to determine the Level 1 trigger efficiencies. Each of the muons in the Monte Carlo that point to an octant with active scintillator coverage are assigned the probability, $\epsilon_{SCT}$, of triggering a level 1 SCT. The overall probability that an event passes the Level 1 scintillator tool depends upon the octants hit by the muons.

- Both muons miss octants with active scintillators. Since octants without scintillator coverage do not participate in the veto logic, these events are assigned

| | |
|---|---|
| Define CCTX as a muon CCT trigger in octant X | |
| Define SCTX as a SCT trigger in octant X | |
| Let SCT_CONFIRM | = TRUE if at least one CCTX·SCTX is found |
| Let SCINT_VETO | = TRUE if at least one CCTX·(not SCTX) is found |
| Let SCINT_REJECT | = not SCINT_CONFIRM and SCINT_VETO |

Table 6-2: The logic used to determine whether an event is rejected by the Level 1 scintillator veto tool. The event is reject if SCINT_REJECT is true.

a weight of 1.

- Only one of the two muons hits an octant with active scintillators. An event weight of $\epsilon_{SCT}$ is assigned.

- Both muons hit active SCT's. Since only one of the two SCT's must trigger for the event to be confirmed, an event weight of $\epsilon_{SCT}(2 - \epsilon_{SCT})$ is assigned.

This weighting is performed on an event by event basis with the dimuon ISAJET Monte Carlo being used to measure the Level 1 trigger efficiency. The net result is a Level 1 scintillator veto tool efficiency of $98 \pm 1\%$.

**Level 2 Veto**

Both the biased and unbiased level 2 scintillator efficiencies have been measured elsewhere [62] (see Table 6-3). These studies show that the Level 2 unbiased scintillator efficiency is $95.5 \pm 0.5\%$, while the biased efficiency is $99.5 \pm 0.3\%$. A weight is assigned to each of the Monte Carlo muons according to the following prescription.

- Tracks pointing to octants without active Level 2 scintillator coverage are assigned a weight of 1. These tracks do not participate in the Level 2 veto decision.
- Tracks pointing to octants with active Level 2 scintillator coverage that also participated in the Level 1 SCT decision are assigned the weight $\epsilon_{SCT} \cdot \epsilon_{biased}$.
- Tracks pointing to octants with active Level 2 scintillator coverage that did *not* participate in the Level 1 SCT decision are assigned the weight $\epsilon_{unbiased}$.

These weights reflect that probability that an individual muon will trigger a scintillator.

The Monte Carlo is adjusted by assigning one of these weights to each of the muons in every event. Since the scintillator tool requires that both muons satisfy the scintillator requirement, the Level 2 scintillator efficiency is found by multiplying the weights of both muons. After applying these weights to each of the events, the Monte Carlo can then be used to calculate the combined Level 1 $\cdot$ Level 2 scintillator efficiency. The resulting combined scintillator efficiency is measured as $93 \pm 2\%$. The Level 2 scintillator veto efficiency can then be determined by taking the ratio of the combined Level 1 $\cdot$ Level 2 scintillator efficiency with the Level 1 scintillator efficiency found in Section 6.1.2. This results in a Level 2 scintillator efficiency of $95 \pm 2\%$.

### 6.1.3 Corrections to the Trigger Efficiencies

Some differences exist between the processed Monte Carlo used to calculate the trigger efficiencies and the dimuon data sample. An example of this is the drift times which

| | |
|---|---|
| Level 1 SCT efficiency | $95.0^{+1.3}_{-3.4}\%$ |
| Unbiased Level 2 efficiency | $95.4 \pm 0.5\%$ |
| Biased Level 2 efficiency | $99.5 \pm 0.3\%$ |
| Level 1 Veto Efficiency | $98 \pm 1\%$ |
| Level 2 Veto Efficiency | $95 \pm 2\%$ |
| Combined Efficiency | $93 \pm 2\%$ |

Table 6-3: The Level 1 and Level 2 scintillator veto efficiencies.

are used to determine the position of hits within the muon chambers. The distribution of drift times in the data often have non-Gaussian tails which are due to occasional poor measurements by the hardware. These poorly measured hits are often rejected by the tracking and reconstruction code resulting in an increase in the track quality flag, IFW4.

It is necessary to calibrate the trigger efficiencies obtained from the Monte Carlo so that they accurately reflect the inefficiencies present in the data. This is accomplished be comparing efficiencies obtained from the Monte Carlo with the efficiencies obtained from data. When necessary, the Monte Carlo is adjusted so that its efficiencies match those found in the data.

### Level 1 Single Muon Efficiency

Single muon events are used to test the Level 1 muon tracking efficiency. The Monte Carlo sample was created with the ISAJET event generator by requiring that $b\overline{b}$ and $c\overline{c}$ events produce at least one muon. These Monte Carlo events were then processed with MU_SMEAR, VMS_FILTER, and the full DØ reconstruction program. The data

sample required that the events contain at least one reconstructed muon and that the event pass at least one non-muon Level 2 filter. The selection cuts listed in Table 6-4 were applied to both samples.

The Level 1 tracking efficiency is simply

$$\epsilon_{L1} = \frac{N_{L1}}{N_{unb}}, \tag{6.1}$$

where $N_{unb}$ is the number of unbiased muon events, and $N_{L1}$ is the number of unbiased muons passing the Level 1 trigger requirement. In the Monte Carlo, $N_{unb}$ is the number of events passing the selection cuts, and $N_{L1}$ is the number of these events which also pass the single muon trigger MU_1_LOW. The data sample is more difficult to handle, because the trigger MU_1_LOW was prescaled for the majority of run 1B. Therefore, an alternate method was used to determine whether a data event passes the Level 1 requirement. In this case, the track quality word IFW3 was used. Bit 16 of this flag word is set whenever a muon track has a matching CCT trigger. Thus, $N_{unb}$ consists of events passing the selection cuts and a non-muon Level 2 filter, and $N_{L1}$ is the number of these events which also have a matching CCT trigger (bit 16 of IFW3).

The Level 1 tracking efficiencies obtained from both the Monte Carlo and data are shown in Fig. 6-4. Both efficiencies agree extremely well; therefore, no corrections to the Monte Carlo are required.

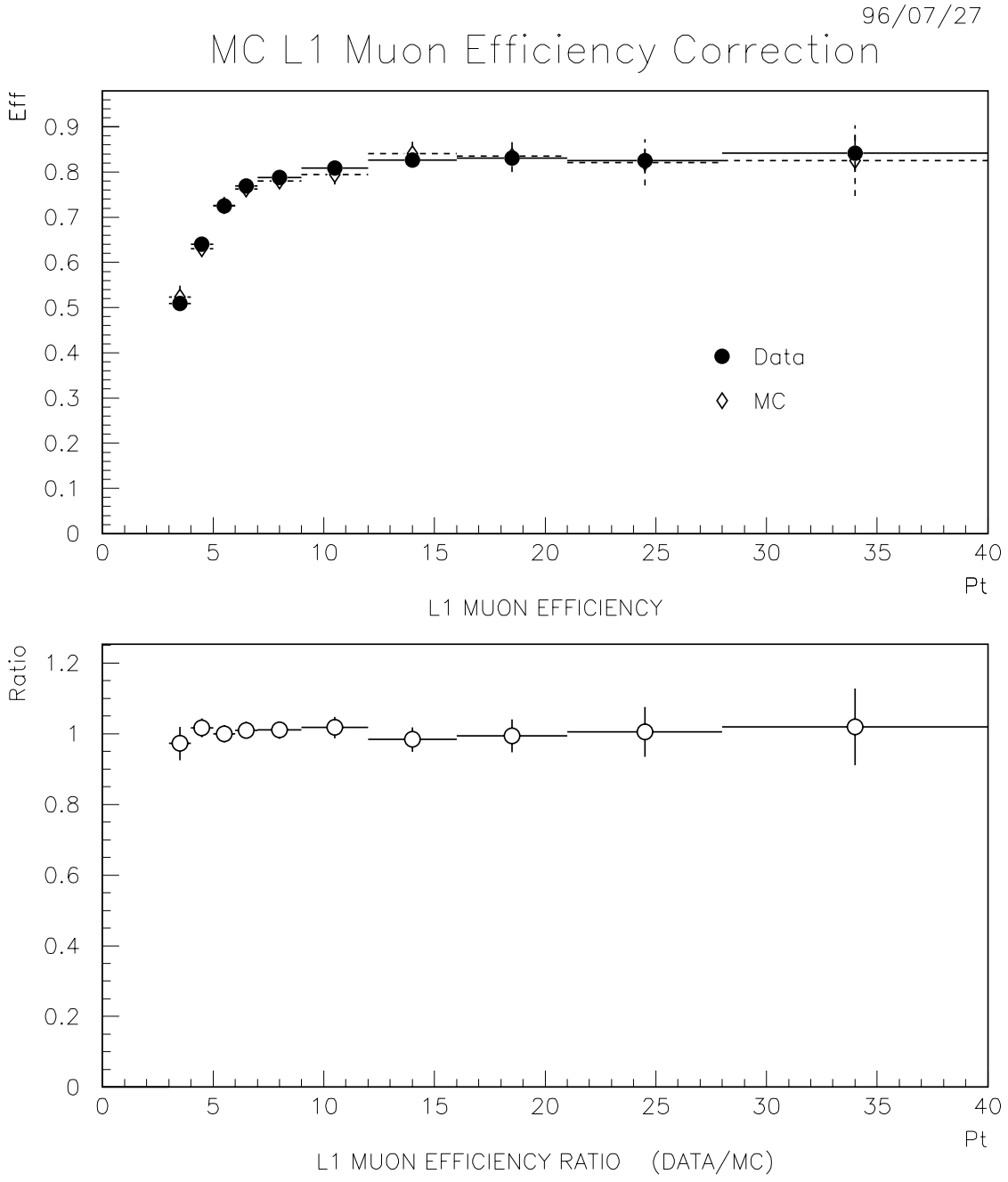


Figure 6-4: The Level 1 CCT efficiency found in the data (dark circles) and Monte Carlo (diamonds). The upper plot shows the actual efficiencies, while the lower plot shows the ratio of the two.

| | |
|---|---|
| Pseudorapidity Range | $\|\eta_\mu\| < 0.8$ |
| Energy in Calorimeter | $> 1$ GeV |
| Calorimeter Fraction | HFRACT $= 1$ |
| Central Detector Track Match | $\chi^2_\mu > 0$ |
| Good Momentum Resolution | $\int B \cdot dl > 0.5$ GeV |

Table 6-4: Single muon selection cuts. The events satisfying these criteria were used in the Level 1 efficiency comparison studies.

**Level 2 Calorimeter Confirmation Efficiency**

The $b\overline{b} \rightarrow \mu\mu X$ selection cuts given in Table 4-6 give an event sample consisting dimuons with associated jets. For these events, the Level 2 calorimeter confirmation tool is expected to have an efficiency near 100%. This can be demonstrated with events taken from an unbiased data sample and ISAJET Monte Carlo. The analysis cuts listed in Tables 4-5 and 4-6 are applied to both samples with some exceptions. First, the calorimeter quality cuts, ETRACK and HFRACT, are not made. Second, each of the muons in the data sample is required to have good scintillator timing information, $|\Delta tof| < 10$ ns.

The calorimeter confirmation tool sums the energy in the cells near the muon tracks and requires that this energy exceed 0.5 GeV. Unfortunately, this variable is not stored in the reconstructed data banks; but similar, more stringent, quantities are stored ($E^{1NN}_{cal}$). It was found that greater than 99% of the events in both the data and Monte Carlo samples passed the offline cut: $E^{1NN}_{cal} > 0.75$ GeV. This implies that the Level 2 calorimeter conformation tool is extremely efficient for the dimuon events

used in this analysis. Therefore, efficiency corrections for this tool are not required.

### Level 2 Single Muon Efficiency

There are two Level 2 efficiencies which must be tested. The first is the efficiency associated with the 'good' tracking condition. This condition is equivalent to the offline cut IFW4 = 1. Non-Gaussian tails in the drift time distributions cause some hits in the muon chambers to be measured inaccurately. Tracks which normally would have passed the 'good' condition may be reconstructed with IFW4 $\geq$ 2. Similarly, the 'best' tracking efficiency (IFW4 = 0) must also be tested. Information about the quality of the reconstructed Level 2 muon tracks is located in the events summary (ESUM) and filter (FILT) banks in the reconstructed data.

Dimuon data and Monte Carlo event samples are used to study the Level 2 tracking efficiencies. The quality cuts listed in Table 6-5 were used to select the events required for these studies. Each muon is required to have a matching CCT trigger. It is also required that the two muons be in different muon octants. This requirement is needed to insure that both muons trigger a Level 1 CCT. In addition, the events are required to have at least one, but no more that two, central Level 2 muon tracks.

Each event has at least one muon which passes a Level 2 single muon filter. This muon is the biased muon in the event, while the other muon is considered unbiased. The 'good' efficiency is given by

$$\epsilon_{good} = \frac{N_{good,unb}}{N_{unb}}, \tag{6.2}$$

| | |
|---|---|
| Number of Muons | Only 2 Muons |
| Pseudorapidity | $\|\eta_\mu\| < 0.8$ |
| Muon Transverse Momentum | $4 < P_T^\mu < 25$ GeV |
| Fiducial Cut | $\varphi < 80^\circ$ or $\varphi > 110^\circ$ |
| Associated Jet | $\Delta R_{\mu,jet} \leq 0.7$ |
| Jet Energy | $E_T^{jet} > 12$ GeV |
| Calorimeter Energy | ETRACK $> 0.5$ GeV |
| Calorimeter Layers | HFRACT $> 0.6$ |
| Number of Layers | 2 or 3 |
| Dimuon Invariant Mass | $6 \leq M_{\mu\mu} \leq 35$ GeV/c$^2$ |
| CCT Requirement | Both muons must trigger a CCT |
| Octants | Muons must be in different CCT octants |
| Number of Level 2 muons | 1 or 2 |
| Level 2 $\eta$ Requirement | $\|\eta_\mu^{L2}\| < 1$ |
| Level 2 Requirement | MU_1_LOW or MU_1_LO_JET or MU_1_MAX |

Table 6-5: The selection criteria used to select dimuon events for the Level 2 tracking efficiency studies.

where $N_{unb}$ is the number of unbiased muons, and $N_{good,unb}$ is the number of unbiased muons satisfying the 'good' tracking condition. Note that it is possible for both muons in the event to be used in this calculation, because both muons might satisfy the Level 2 filter requirement.

This calculation was performed with both the dimuon data and ISAJET Monte Carlo samples. Each of the resulting efficiencies is shown in Fig. 6-5. Some differences exist between the two efficiency curves, but no clear $P_T^\mu$ dependence can be found. An average of the ratio given in the lower plot in Fig. 6-5 will be taken as the 'good' efficiency correction factor. This correction factor, with its standard deviation, is

$$\epsilon_{good} = 94 \pm 4\%. \tag{6.3}$$

The 'best' efficiency is found by

$$\epsilon_{best} = \frac{N_{best,unb}}{N_{good,unb}}, \tag{6.4}$$

where $N_{best,unb}$ is the number of unbiased muons satisfying the best condition. The selection cuts listed in Table 6-5 are used again in this study. As before, one of the two muons is considered biased because it passes a single muon trigger while the other muon is unbiased. The results of this calculation (Fig. 6-6) show that the data and Monte Carlo 'best' efficiencies agree very well. Therefore, no correction is made for this efficiency.

Poorly measured drift times can also cause muon tracks to be reconstructed with track qualities of IFW4 $\geq 2$. Consequently, these tracks will be rejected by the Level 2 muon tracking code. This problem does not occur in the Monte Carlo, because the Monte Carlo assumes a Gaussian shape for the distribution of the drift times. Therefore, the Monte Carlo reconstruction efficiency is 100%.

The true reconstruction efficiency can be obtained directly from the data by looking at an event sample containing jets in octants with muon CCT triggers. A sample of these events were scanned manually to determine if the muon was actually present, and whether a muon was reconstructed [63]. It was found that the reconstruction efficiency is

$$\epsilon_{reco} = 95 \pm 3\%. \tag{6.5}$$

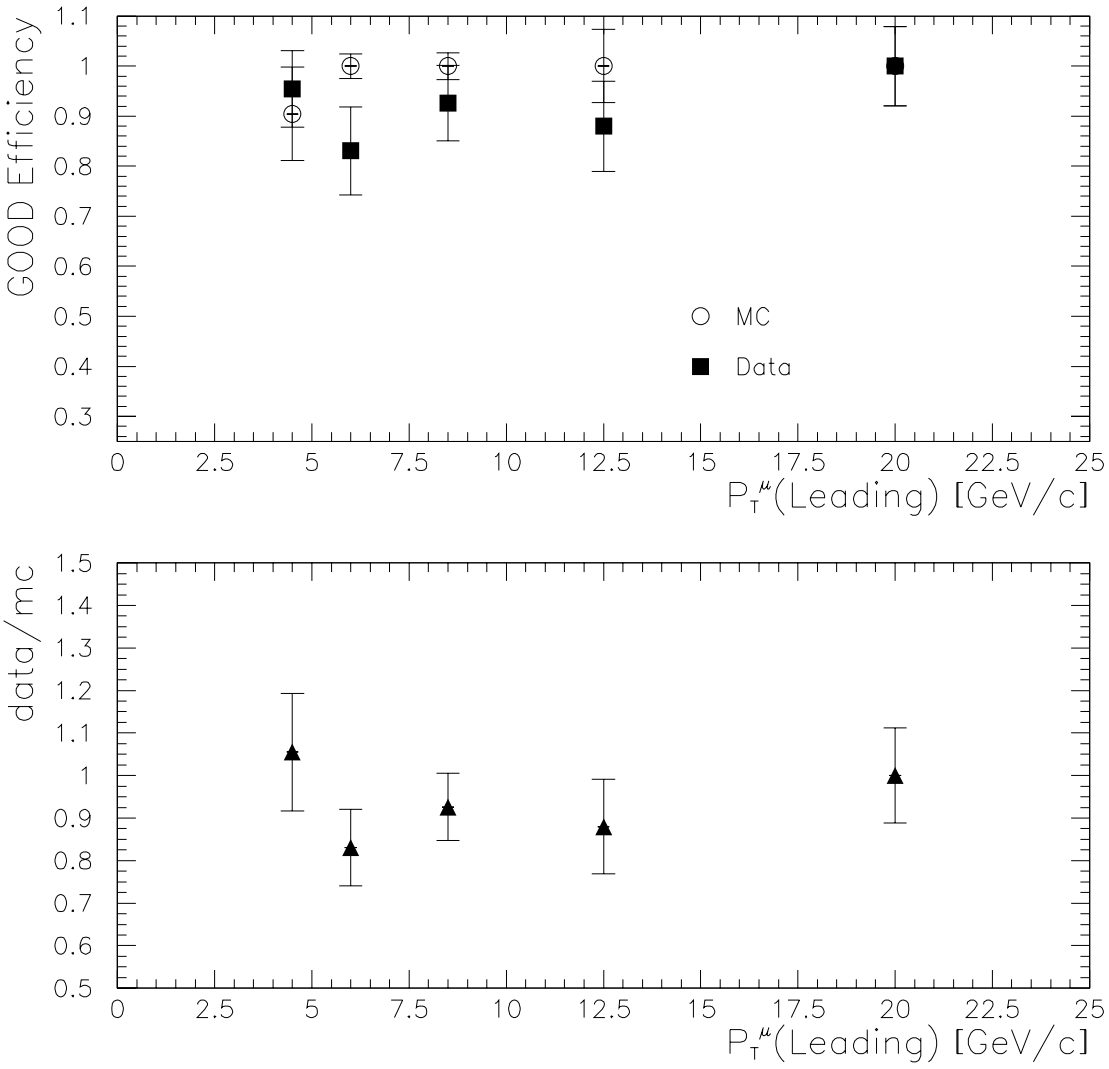


Figure 6-5: The 'good' tracking efficiency for single muons. The upper plot shows the efficiencies obtained from both the Monte Carlo and data samples. The lower plot shows the ratio of the two curves.

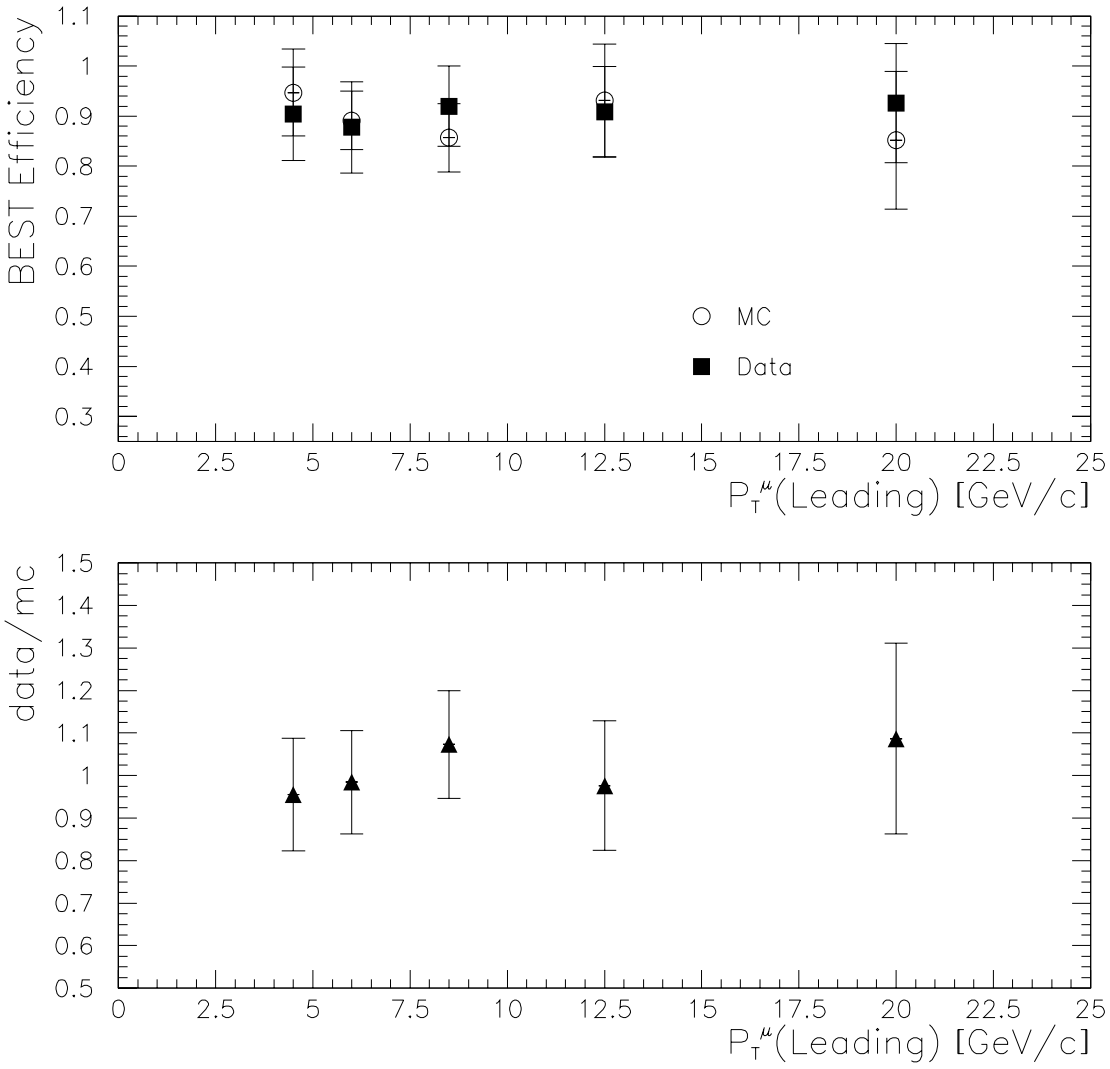


Figure 6-6: The 'best' tracking efficiency for single muons. The upper plot shows the efficiencies obtained from both the Monte Carlo and data samples. The lower plot shows the ratio of the two curves.

It is assumed that this efficiency is independent of $P_T^{\mu}$.

#### Corrections to the Dimuon Trigger Efficiencies

In general, good agreement has been found between the efficiencies found in the data and Monte Carlo. The primary differences were found with the 'good' efficiency, $\epsilon_{good}$, and the reconstruction efficiency, $\epsilon_{reco}$. Since the dimuon triggers used in this analysis require both muons to satisfy the 'good' requirement, a correction of

$$w_{corr} = \epsilon_g^2 \cdot \epsilon_{reco}^2 = 80 \pm 5\% \tag{6.6}$$

is applied to the Monte Carlo. This calibrates the Monte Carlo trigger efficiencies so that the Monte Carlo more accurately simulates the inefficiencies found in the data.

## 6.2 Selection Cut Efficiencies

The following section discusses the efficiencies associated with each of the selection cuts used in this analysis. A summary of these efficiencies can be found in Table 6-6.

### 6.2.1 Muon Track Quality, IFW4

The Level 2 trigger requirements used to select the dimuon data sample require that both muons satisfy the 'good' track quality condition. In addition, at least one muon must satisfy the 'best' condition. Since an identical cut is applied offline in this analysis, it is expected that this cut will be nearly 100% efficient. This has been

confirmed with a sample of reconstructed $b\overline{b} \rightarrow \mu\mu X$ Monte Carlo events which have been processed with the MU_SMEAR package. An efficiency of 100% with negligible uncertainty was found.

### 6.2.2 Calorimeter Energy Deposition

Two energy deposition cuts are used in this analysis: ETRACK $>$ 0.5 GeV and HFRACT $>$ 0.6. A sample of quality dimuon events is used to determine the efficiency of these cuts. This sample was obtained by applying all of the quality cuts described in Tables 4-5 and 4-6, with a few exceptions. First, the requirement on the track quality flag, IFW4, is tightened; Both muons are forced to satisfy IFW4 = 0. Second, the calorimeter energy deposition cuts are applied only to the biased muon in the event. These cuts are not applied to the second (unbiased) muon. Of the 1460 unbiased muons, 1433 pass the requirement ETRACK $>$ 0.5 GeV and HFRACT $>$ 0.6. Thus, the calorimeter energy deposition efficiency is

$$\epsilon_{MTC} = 98.2^{+0.2}_{-0.5}\% \tag{6.7}$$

### 6.2.3 Scintillator Time-of-Flight

Two scintillator efficiencies must be considered. The first is the efficiency of requiring that a muon hit and trigger an active scintillator. This efficiency is primarily a function of geometrical acceptance and scintillator PDT efficiency. This efficiency must be taken into account whenever an analysis rejects muons that do not have scintillator

timing information. However, in this analysis, muons without valid scintillator timing information are kept in the data sample. Therefore, the geometrical acceptance and PDT efficiencies need not be considered here.

The second scintillator efficiency which must be considered is the efficiency associated with the selection cut $|\Delta tof| < 10$ ns. This selection cut has been studied with a set of low momentum dimuon events [62]. Standard muon identification cuts were used to obtain a relatively clean dimuon event sample. A reduction in the cosmic ray backgrounds was obtained by requiring that the invariant mass of the dimuon pair be within 600 MeV/c$^2$ of the $J/\psi$ mass. The cut, $|\Delta tof| < 10$ ns, was found to be $97.4 \pm 0.6\%$ efficient. The systematic error is dominated by the 3% uncertainty associated with estimating the cosmic ray background in this sample.

### 6.2.4 Muon Fiducial Volume

The efficiency of the fiducial cut, $\varphi < 80^\circ$ or $\varphi > 110^\circ$, is determined from processed ISAJET Monte Carlo. Due to the non-uniform acceptance of the detector in $\varphi$, it is possible that this inefficiency will have functional dependencies on both $P_T^\mu$ and $\Delta\varphi_{\mu\mu}$. As can seen in Fig. 6-7, this variable was found to be nearly uniform in both variables.

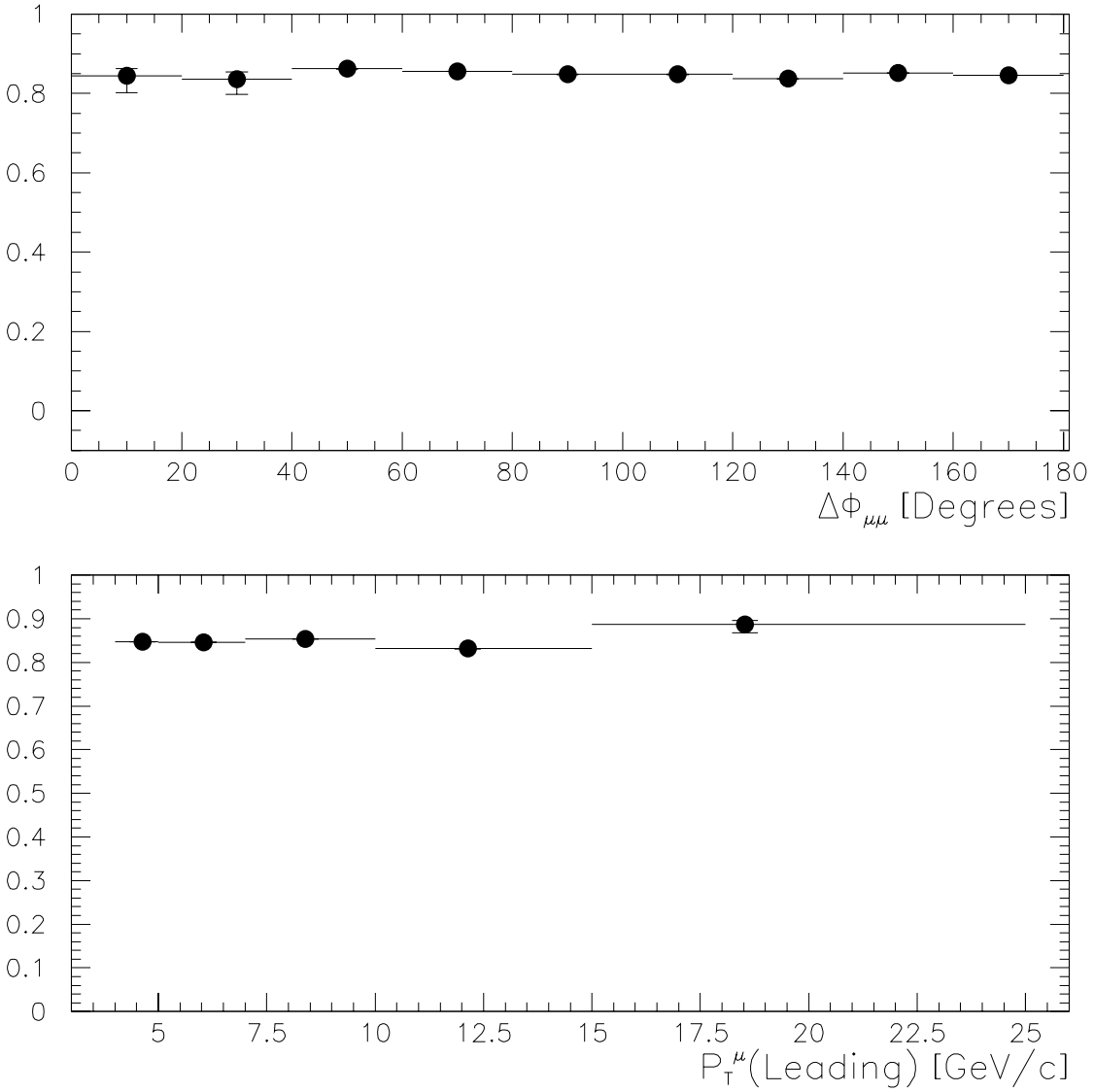


Figure 6-7: The efficiency of the $\varphi$ fiducial cut, $\varphi < 80°$ or $\varphi > 110°$, as given by ISAJET Monte Carlo. The efficiency is plotted as a function of ISAJET (real) variables.

### 6.2.5 Associated Jet Efficiency

Processed ISAJET ($b\overline{b} \rightarrow \mu\mu X$ and $c\bar{c} \rightarrow \mu\mu X$) Monte Carlo was used to determine the efficiency of requiring that a jet with $E_T > 12$ GeV be associated with each of the muons. Figure 6-8 shows the $\Delta R$ distribution between muons and jets as given by ISAJET. Since the 0.7 cone algorithm was used in the reconstruction of the jets, it is natural to require that the muons and their associated jets be within $\Delta R = 0.7$.

Since this efficiency will be applied to the data *after* the data is unfolded, this efficiency must be calculated in terms of ISAJET (real) $P_T^\mu$ and $\Delta\varphi_{\mu\mu}$. In measuring this efficiency, the $\eta_\mu$, $P_T^\mu$, and invariant mass cuts listed Table 4-6 are made on the two leading ISAJET muons. It was also required that the Monte Carlo events have at least two reconstructed muons within $|\eta_\mu| < 1$. One then looks to see if each of the reconstructed muons have a jet ($E_T > 12$ GeV) within $\Delta R = 0.7$.

It was found that the associated jet efficiencies were the same regardless of the type of muon trigger used to select the Monte Carlo events. The exceptions to this were muon plus jet triggers which bias the events so that they are more likely to satisfy the associated jet requirement. Therefore, in an attempt to increase the statistics of the Monte Carlo sample, it was required that the Monte Carlo events satisfy either MU_2_LOW or MU_1_LOW. The resulting efficiencies can be seen in Fig. 6-9.

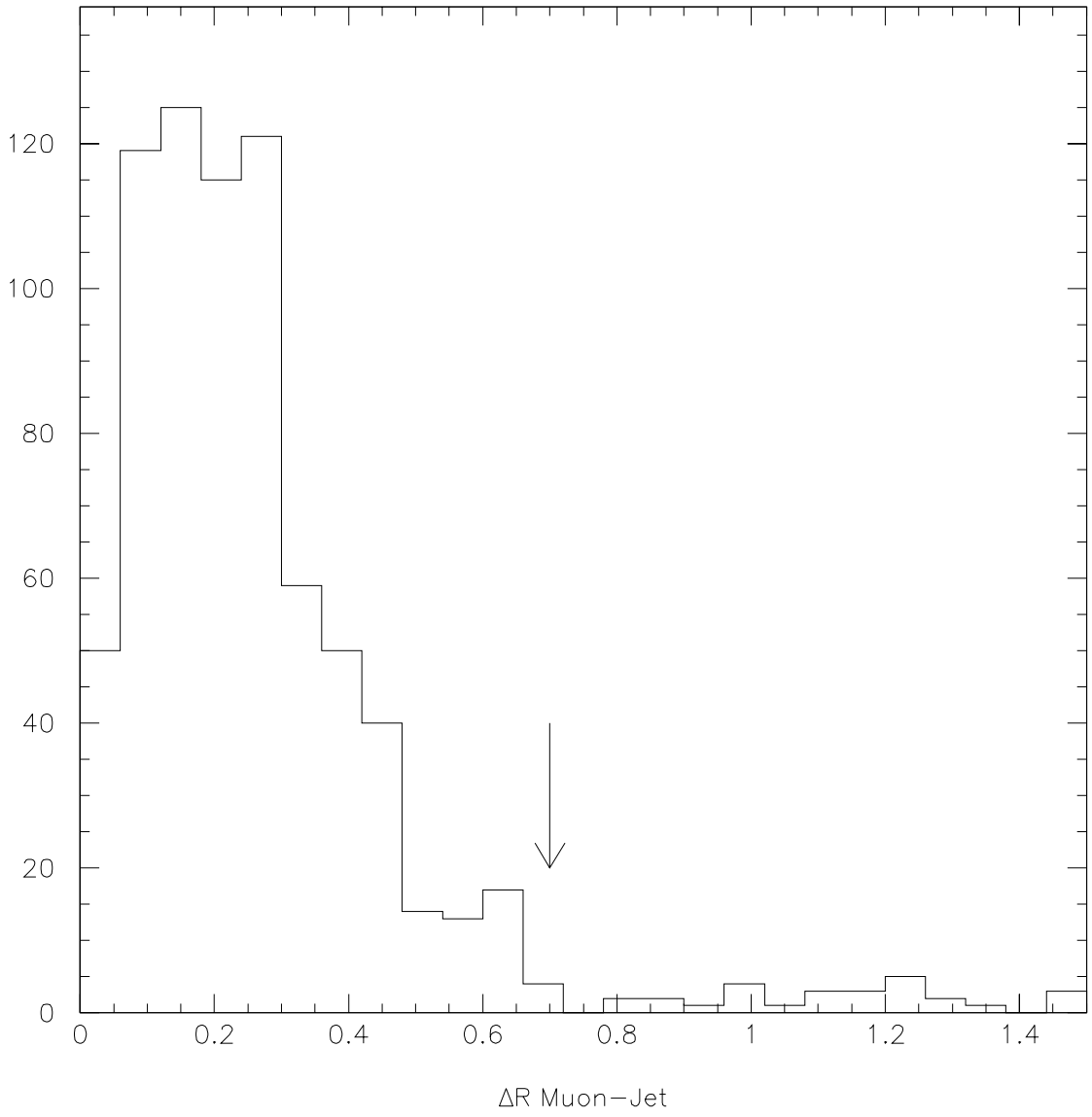


Figure 6-8: The $\Delta R = \sqrt{\Delta\varphi^2 + \Delta\eta^2}$ distribution between muons and jets as given by ISAJET Monte Carlo. A selection cut is made at $\Delta R = 0.7$ to insure that the jets are closely associated with the muons.

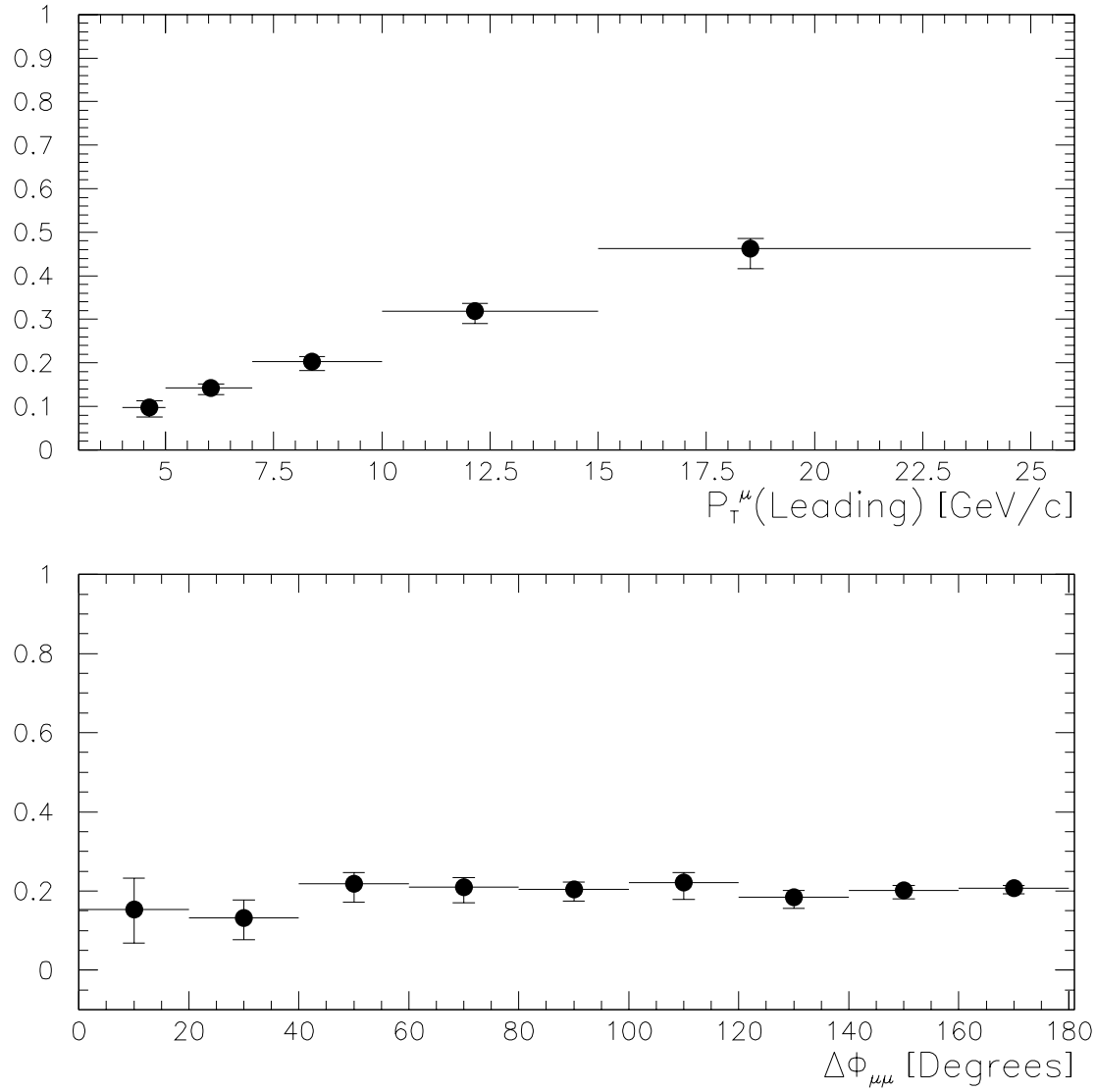


Figure 6-9: The associated jet efficiency as a function of ISAJET (real) $P_T^\mu$ and $\Delta\varphi_{\mu\mu}$. The jets are required to have $E_T > 12$ GeV.

| Selection Cut | Efficiency (%) |
|---|---|
| IFW4 $\leq 1$ | 100 |
| ETRACK $> 0.5$ GeV | |
| & HFRACT $> 0.6$ | $98.2\pm^{+0.2}_{-0.5}$ |
| $\|\Delta tof\| < 10$ ns | $97.4 \pm 0.6$ |
| $\varphi < 80^\circ$ or $\varphi > 110^\circ$ | $85.0 \pm 0.2$ |
| Total | $81.3\pm^{+0.7}_{-0.8}$ |

Table 6-6: A summary of the efficiencies of the dimuon selection cuts.

## 6.3 Total Efficiency

Obtaining the total efficiency for dimuon event selection is complicated by the fact that there are three separate trigger efficiency curves. Each trigger efficiency represents a different time period during the run, but they can be combined via the equation

$$\epsilon = \frac{\sum_{i=1}^{3} \epsilon_i \cdot \mathcal{L}_i}{\sum_{i=1}^{3} \mathcal{L}_i}, \tag{6.8}$$

where $\mathcal{L}_i$ is the integrated luminosity for each of the running periods given in Table 6-1, and $\epsilon_i$ is the trigger efficiency during that time period.

This trigger efficiency is then combined with the other efficiencies discussed in this chapter to obtain the total efficiency for finding dimuon events. This efficiency is shown in Fig. 6-10 as a function of $P_T^\mu$(leading) and $\Delta\varphi_{\mu\mu}$. These efficiencies are also listed in Tables B-7 and B-8, and are used in Chapter 9 to calculate the inclusive dimuon and $b\overline{b} \to \mu\mu X$ cross sections.

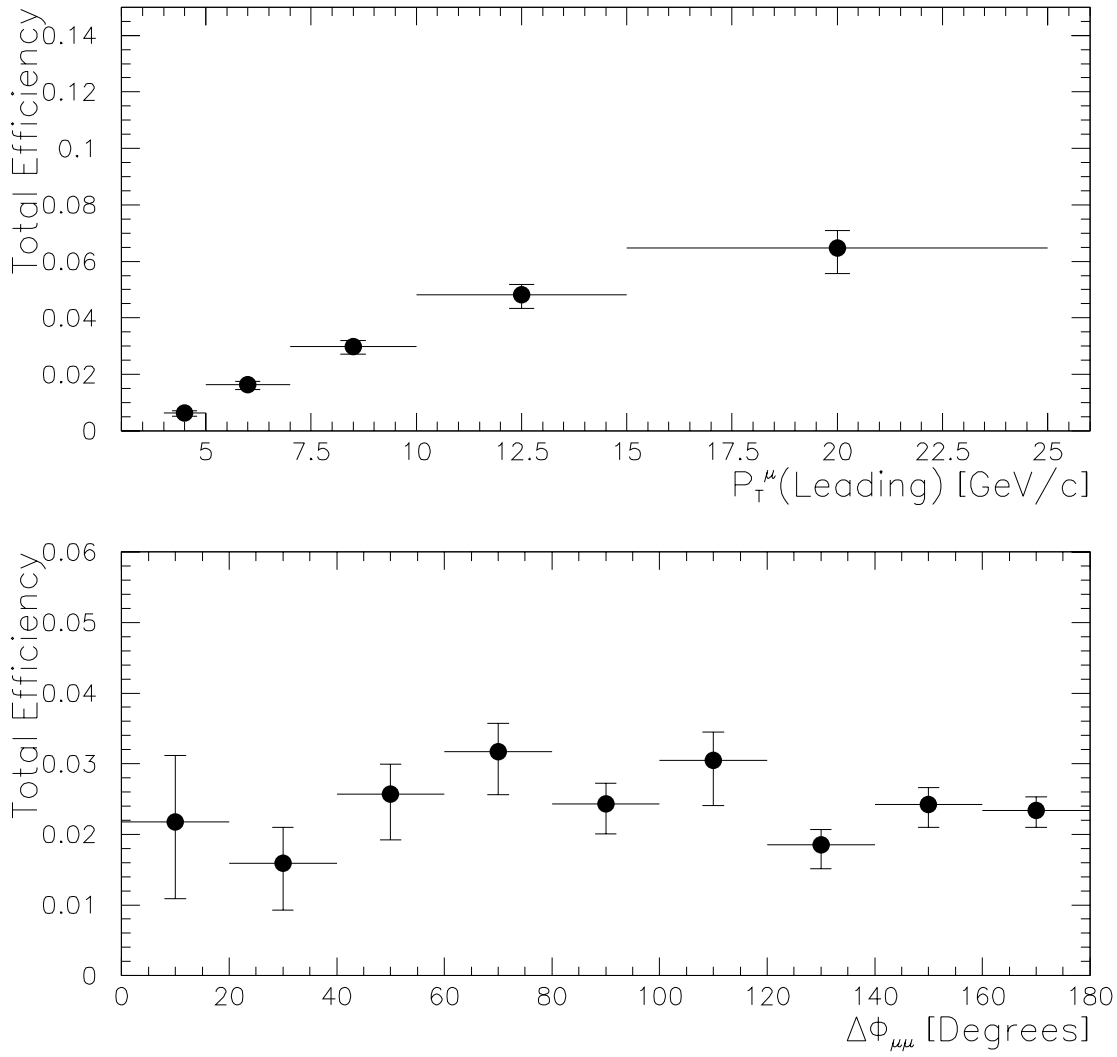


Figure 6-10: The total efficiency for detecting dimuon events.

# Chapter 7

# Signal and Background Determination

In $p\overline{p}$ collisions, many different processes contribute to the dimuon event sample. Given the selection cuts used in this analysis, there are only a few processes that contribute significantly. These processes include:

- The prompt decay of a $b$ and $\overline{b}$-quark pair into muons.
- The prompt decay of a $c$ and $\overline{c}$-quark pair into muons.
- The prompt decay of one heavy quark plus the in-flight decay of a pion or kaon into a muon.
- The decay-in-flight of two pions (or kaons).

In addition, fake dimuon events can be produced by cosmic ray muons which pass through the detector.

This chapter discusses the techniques used to separate the $b\overline{b} \rightarrow \mu\mu X$ signal from the background processes. Scintillator timing information and central detector tracks are used to determine the cosmic ray background, while a maximum log-likelihood fitting technique is used to differentiate the $b\overline{b} \rightarrow \mu\mu X$ signal from the remaining processes.

## 7.1 Scintillator $\Delta tof$ Fits

In this data sample, the largest source of background events not associated with $p\overline{p}$ collisions are muons produced by cosmic rays. Particles resulting from the cascade of cosmic rays are incident upon the earth with a flux of $1.8 \times 10^2 \mathrm{m}^{-2}\mathrm{s}^{-1}$ at sea level. Of these, approximately 75% are muons. Therefore, cosmic ray muons hit the DØ detector at an approximate rate of $4 \times 10^4$ Hz. This high rate, coupled with the fact that reconstructed muon tracks are constrained *only* along the z-axis of the muon system (along the beam pipe), means that the cosmic ray contamination is significant in the dimuon event sample.

To combat this, scintillator time-of-flight ($tof$) information is used to separate the cosmic ray muons from beam-produced muons. The reconstruction code determines the scintillator time-of-flight by projecting the muon tracks to the scintillators. The code then checks to see if the scintillator photomultiplier tubes (PMT) register a

| | |
|---|---|
| Trigger Requirement | MU_2_LOW or MU_2_CENT |
| Pseudorapidity | $\|\eta_\mu\| < 0.8$ |
| Transverse Momentum | $3.3 < P_T^\mu < 25$ GeV/c |
| Track Quality | IFW4 = 0 |
| Calorimeter Energy | ETRACK > 0.5 GeV |
| Hadronic Energy | HFRACT > 0.6 |
| A-Stubs | Rejected |
| Number of Muon Layers | 2 or 3 |
| Fiducial Cut | $\varphi < 80^\circ$ or $\varphi > 110^\circ$ |
| Dimuon Invariant Mass | $2 < M_{\mu\mu} < 4$ GeV/c$^2$ |
| Muon Signs | Opposite signed dimuons |
| Scintillator Timing | Must have a valid $tof$ |

Table 7-1: The trigger and selection cuts used to find J/$\psi$. Note that both muons are required to have a valid scintillator $tof$ so that the $\Delta tof$ distribution for these events may be studied.

signal above threshold. If a signal is found, the $tof$ is recorded in the data. This $tof$ is measured with respect to the center of the 50 ns gate in which the scintillators are active.

$\Delta tof$ is defined as the measured $tof$ minus the 'expected' $tof$. The expected $tof$ is simply the amount of time needed for a particle, traveling at the speed of light, to traverse the distance spanning the interaction region and the scintillators. The expected $tof$ for a muon is approximately 20 ns, but this varies somewhat depending upon the geometrical location of the hit scintillator. The $\Delta tof$ distribution for beam-produced muons is Gaussian in shape and has a width of $\sigma \sim 2.4$ ns. Figure 7-1(a) shows the $\Delta tof$ distribution for $J/\psi$ events. The cuts used to select these events are listed in Table. 7-1. This is a useful sample with which to study the $\Delta tof$ signal as the J/$\psi$ sample is expected to have very little cosmic contamination.

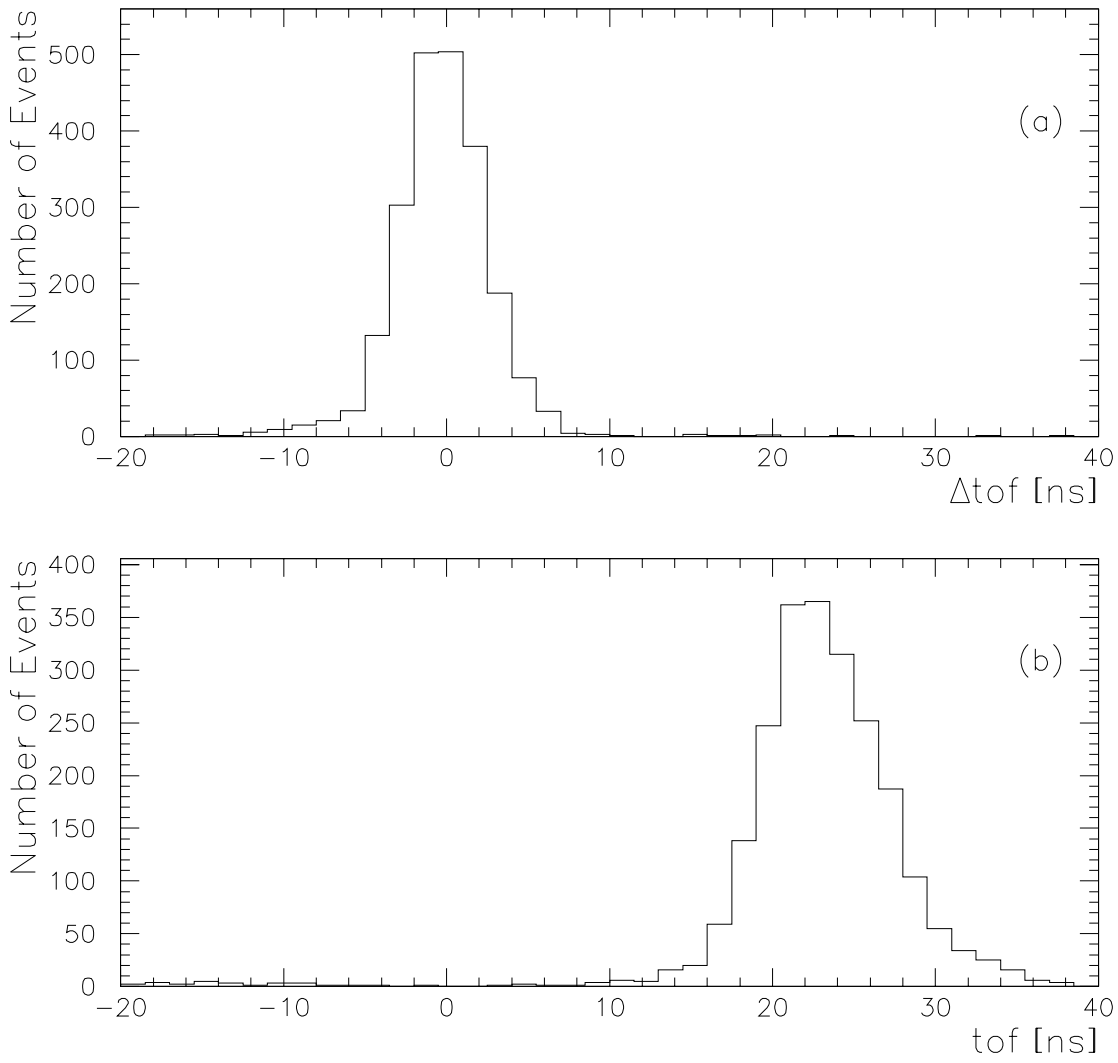


Figure 7-1: The $\Delta tof$ and $tof$ distributions for the leading muon in a J/$\psi$ dimuon sample. The shape of the distributions are Gaussian.

| | |
|---|---|
| Transverse Momentum | $4 < P_T^\mu < 25$ GeV/c |
| Pseudorapidity | $\|\eta_\mu\| < 1$ |
| Track Quality | IFW4 = 0 |
| Scintillator Timing | Must have a valid $tof$ |

Table 7-2: The quality cuts used to select events from cosmic ray special runs.

The $\Delta tof$ distribution for cosmic ray events is nearly flat between $-20 \leq \Delta tof \leq$ 20 ns. Outside of this range, the distribution begins to fall off. This is demonstrated in Fig. 7-2, where the $\Delta tof$ distribution is plotted for events taken from cosmic ray special runs. A set of loose selection cuts was applied to this sample which selected events in the same kinematic region as the dimuon event selection cuts used in this analysis. These selection cuts are listed in Table 7-2.

In this analysis, all muons triggering a scintillator PMT must satisfy the cut

$$|\Delta tof| < 10 \text{ ns}. \tag{7.1}$$

For muons hitting a scintillator, this cut has been shown to be 97.4±0.6% efficient [62]. However, not all muons hit a scintillator. Therefore, the data must be subdivided into three different categories. The first category contains those events in which both muons hit scintillators and have valid $tof$'s. The second category contains events in which only one of the two muons hits a scintillator, and the final category contains events in which neither muon hits a scintillator. This events in this last category are the most difficult to handle, because the lack of $tof$ information forces one to use alternative methods to measure the cosmic ray contamination.

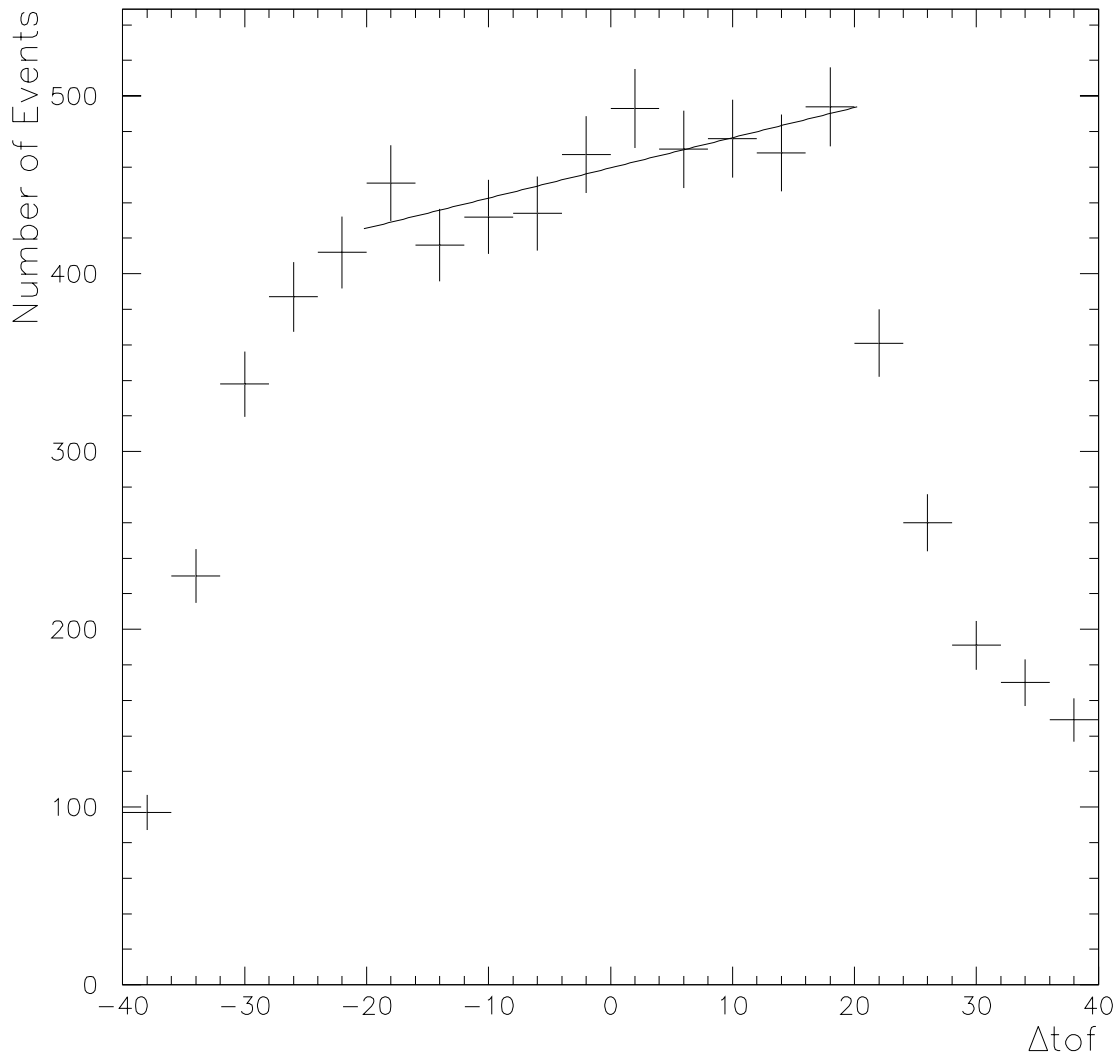


Figure 7-2: The $\Delta tof$ distribution for events taken from cosmic ray special runs. In the range $-20 \leq \Delta tof \leq 20$ ns the distribution is nearly flat. Outside of this range the spectrum falls off due to scintillator trigger biases.

### 7.1.1 Two Muons with $\Delta tof$ Information

For the case in which both muons hit scintillators, both muons are required to satisfy the cut $|\Delta tof| < 10$ ns. From the scintillator $tof$ distribution for J/$\psi$ events (Fig. 7-1(b)), we find that it typically takes 20 ns for a muon to traverse the distance between the interaction region and the muon scintillators. This means that it takes 40 ns for a cosmic ray to travel between scintillators in opposite octants. Thus, a reconstructed cosmic ray produces two muon tracks with $tof$'s which are approximately 40 ns apart. The selection cut given by Eq. 7.1 only allows the two muons to have $tof$'s which are less than 20 ns apart. Therefore, applying the $\Delta tof$ cuts on both muons is an effective way of eliminating cosmic ray events. For the purposes of this analysis, this cut will be taken as 100% effective; and in this data sample, there were 925 such events.

### 7.1.2 One Muon with $\Delta tof$ Information

In the second case only one of the two muon tracks hits a scintillator. The $\Delta tof$ distribution for the events satisfying this condition are shown in Fig. 7-3. Two distributions are shown. The first is the $\Delta tof$ distribution for the events in which only the leading muon hits a scintillator. Out of 1281 such events, 588 pass the $\Delta tof$ cut (Eq. 7.1). The second distribution shows those events in which only the trailing muon hits a scintillator. Out of 671 such events, 480 pass the $\Delta tof$ cut. In all, a total of 1068 events satisfy the requirement of Eq. 7.1.

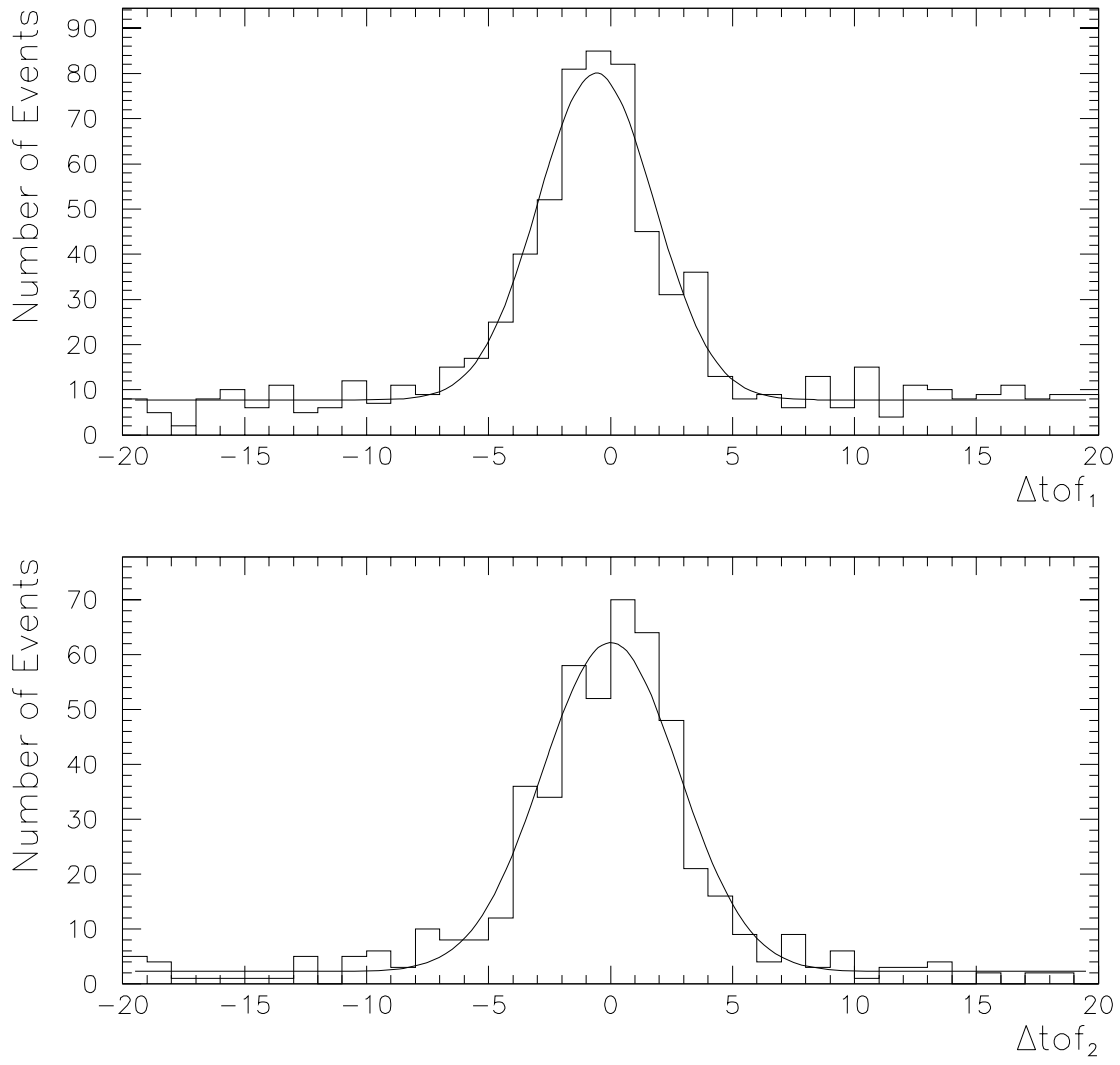


Figure 7-3: The $\Delta tof$ distribution for the events in which only one of the two muons 'hits' a scintillator. The top (bottom) plot contains events in which only the leading (trailing) muon hits. Also shown in the fit of a Gaussian and line to the data.

Fig. 7-3(a) shows a higher level of cosmic ray contamination than Fig. 7-3(b). This is readily explained by the fact that cosmic rays most often hit the top of the DØ detector first. The cosmic ray muons lose energy as they pass through detector; therefore, cosmic ray muons tend to reconstruct as a leading (trailing) muon which is located at the top (bottom) of the detector. Since the scintillator coverage is much less complete on the bottom half of the detector, it is less likely that a cosmic ray muon will reconstruct as a trailing muon which hits a scintillator. Conversely, cosmic rays muons are more likely to produce events in which the leading muon hits a scintillator. Thus, it is expected that Fig. 7-3(a) will show a higher cosmic ray contamination than Fig. 7-3(b).

A Gaussian and a line are fit to the bins within $-20 < \Delta tof < 20$ ns for each of the distributions in Fig. 7-3. From this fit, the amount of cosmic ray contamination in each sample can be determined by calculating the area under the line in the region $-10 \leq \Delta tof \leq 10$ ns. The errors of these fits are then used to calculate the systematic error associated with the cosmic ray background estimation. The fractional errors associated with Figs. 7-3(a) and (b) are found with

$$\sigma_{cos} = \frac{\sigma_{P0} \cdot w}{N}, \tag{7.2}$$

where $\sigma_{P0}$ is the error associated with the y-intercept of the fit line, $N$ is the number of events found within $-10 < \Delta tof < 10$ ns, and $w$ is the width of the interval (20 ns). This is done for both the leading and trailing muons; and in both cases,

the relative uncertainty was found to be 1.0%. This means that the total number of cosmics found in this case is $206 \pm 10$ events.

### 7.1.3 Muons without $\Delta tof$ Information

The third case to consider is when neither muon hits a scintillator. There were 103 such events which most often consist of muons exiting via the bottom of the detector. A small subset of these events have one muon exiting through the bottom of the detector while the second muon passes through cracks in the scintillator coverage.[1] Since these muon tracks do not have time-of-flight information, an alternate method must be used to determine cosmic ray contamination. Cosmic ray muons are much less likely to produce muon tracks that have matching tracks in the central detector (CD). Conversely, beam-produced muons are much more likely to have matching CD tracks. The variable that we shall use to distinguish between cosmics and beam-produced muons is $p_{CD}$ which is defined as the probability that either of the two reconstructed muons has a matching CD track. Out of the 103 events in this sample, $N_p = 82$ pass the CD match requirement and $N_f = 21$ fail. Once the CD match efficiency for both cosmic ray and beam-produced muons is known, the number of cosmics in the sample can be determined by solving the matrix equation

$$\begin{bmatrix} p_{CD}^{cosmic} & p_{CD}^{signal} \\ (1-p_{CD}^{cosmic}) & (1-p_{CD}^{signal}) \end{bmatrix} \begin{bmatrix} N_c \\ N_s \end{bmatrix} = \begin{bmatrix} N_p \\ N_f \end{bmatrix}, \tag{7.3}$$

[1] It is also possible for muons to hit scintillators yet not produce valid *tof* information. Such muons hit the scintillators outside of the 50 ns gate that the scintillators are active.

where $N_c$ is the number of cosmic ray events in the sample, and $N_s$ is the number of beam-produced events.

A set of 'golden' dimuon events is used to determine the CD match efficiency for cosmic ray and beam-produced muons. These golden events are described in Section 7.1.1 and consist of events in which both muons have scintillator time-of-flight information. Separating cosmic ray muons from beam-produced dimuons can be accomplished by cutting on the quantity $(tof_1 - tof_2)$. Beam-produced muons are expected to have $(tof_1 - tof_2)$ near zero. This can be seen in Fig. 7-4 as the central peak centered on $(tof_1 - tof_2) = 0$ ns. It takes 40 ns for a cosmic ray muon to traverse the distance between scintillators in opposite octants of the detector. This is readily seen in Fig. 7-4 as the peaks centered near approximately $\pm$40 ns. It is worth noting that the peak near approximately -40 ns is much larger than the peak near approximately 40 ns. This implies that $tof_2$ is preferentially larger than $tof_1$. This is expected as cosmic ray muons most often hit the top of the detector and exit through the bottom loosing energy as they pass through the iron toroid and calorimeter. Therefore, in a cosmic ray event, the reconstructed muon with the highest momentum will most often be the muon with the smallest $tof$.

Beam-produced events are selected from the golden sample by applying the cut $|tof_1 - tof_2| < 10$ ns, while cosmic ray events are selected by requiring $|tof_1 - tof_2| > 30$ ns. The number events satisfying the CD match requirement gives the efficiency for cosmic ray and beam-produced events (see Table 7-3). Equation 7.3 is then used

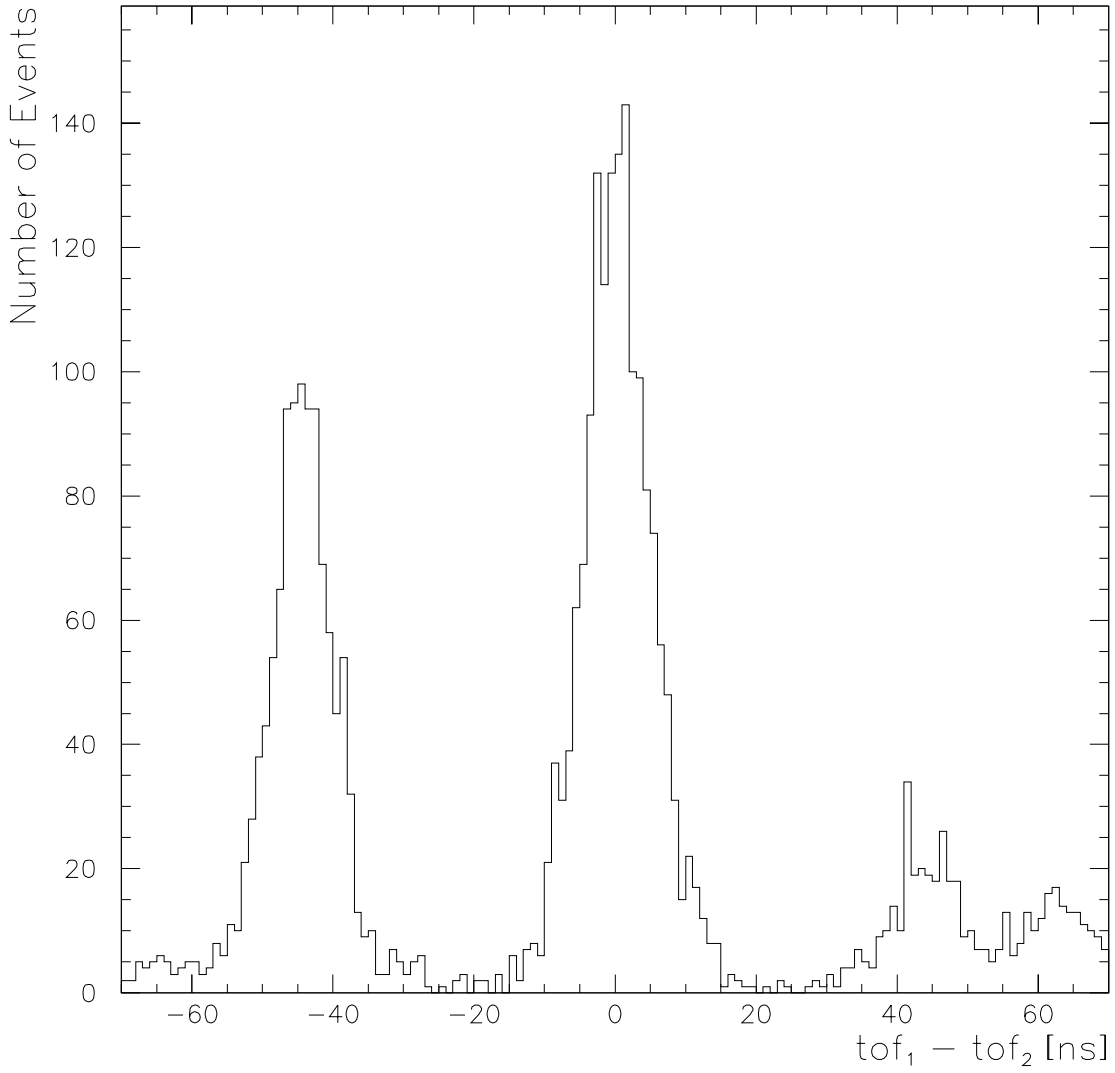


Figure 7-4: The $(tof_1 - tof_2)$ distribution for the golden dimuon sample described in Section 7.1.1.

| $\lvert tof_1 - tof_2 \rvert$ (ns) | $N_p$ | $N_f$ | $p_{CD}$ |
|---|---|---|---|
| $> 30$ (Cosmics) | 1097 | 551 | 66.6% |
| $< 10$ (Signal) | 1447 | 41 | 95.7% |
| $> 40$ (Cosmics) | 939 | 467 | 66.8% |
| $> 50$ (Cosmics) | 298 | 153 | 66.1% |
| $< 5$ (Signal) | 1058 | 40 | 96.4% |
| $< 2$ (Signal) | 508 | 16 | 96.9% |

Table 7-3: The efficiency of requiring that at least one of the two muon tracks have a matching track in the central detector. A cut on $(tof_1 - tof_2)$ is used to select cosmic ray and beam-produced events from a golden dimuon sample. The first two entries in the table are used in Eq. 7.3 to calculate the cosmic contamination ($N_c = 56.9$ events). The remaining entries are used to calculate the systematic uncertainty ($\pm 3.2$ events).

to estimate the number of cosmic ray events in the sample, $N_c = 56.9$.

The systematic uncertainty associated with the measurement of the cosmic contamination is found by varying the $(tof_1 - tof_2)$ cuts used to select the cosmic and beam-produced data samples. It is possible that some cosmic ray muons have made it into our beam-produced sample and that some beam-produced events may be present in the cosmic ray sample. Tightening and loosening the $tof_1 - tof_2$ cut gives a measure of this effect. Table 7-3 lists all of the variations on the $(tof_1 - tof_2)$ cut that were used along with the resulting CD match efficiencies, $p_{CD}$. These efficiencies are then used to recalculate the cosmic contamination. The difference between the new measurements of $N_c$ and the original are used as a measure of the systematic uncertainty. Consequently, the cosmic contamination of the 103 events in this data sample is reported as $N_c = 56.9 \pm 3.2$.

| Description | Total # | # of Cosmics | % Cosmics |
|---|---|---|---|
| 2 muons with *tof* | 921 | 0 | 0 |
| 1 muon with *tof* | 1068 | $200.6 \pm 10.2$ | $19.0 \pm 1.0$ |
| 0 muons with *tof* | 103 | $56.9 \pm 3.2$ | $55.2 \pm 3.1$ |
| Total data Sample | 2092 | $257.5 \pm 10.7$ | $12.3 \pm 0.5$ |

Table 7-4: A summary of the cosmic ray contamination for the dimuon data sample. The data has been divided into the three categories that are defined above. Different methods were used to determine the cosmic ray contamination in each category.

### 7.1.4 Total Cosmic Contamination

The results of the cosmic ray studies can now be combined to determine the total cosmic contamination of the data sample, $257.5 \pm 10.7$ events. This represent a $12.3 \pm 0.5\%$ contamination. These results are summarized in Table 7-4 and will be used later when performing the maximum likelihood fits.

## 7.2 The Maximum Likelihood Fit

A maximum log-likelihood fitting technique is used to extract the $b\overline{b} \rightarrow \mu\mu X$ signal from dimuons produced by background processes. This fit is performed on an event-by-event basis instead of with data that has been placed placed into $P_T^{\mu}$ or $\Delta\varphi_{\mu\mu}$ bins. Several processes must be accounted for in the fitting procedure. These include dimuon events produced by $b\overline{b}$ and $c\overline{c}$ quark pairs as well as events in which one or both muons are the result of a pion (or kaon) decay. The purpose of the likelihood fit is to find the fraction, $A_j$, of the dimuon data sample which has been produced by

each of the above processes.

It is necessary to maximize the log likelihood function

$$L = \ln \sum_{i=1}^{N} \mathcal{L}_i = \prod_{i=1}^{N} \ln \mathcal{L}_i, \tag{7.4}$$

where $N$ is the number of events in the data sample. The likelihood function, $\mathcal{L}_i$, is given by

$$\mathcal{L}_i = \sum_{j=1}^{N_p} \left[ A_j \prod_{k=1}^{N_v} p_k^j(x_k^i) \right], \tag{7.5}$$

where the summation in $j$ is over the $N_p$ physics processes ($b\overline{b} \rightarrow \mu\mu X$, $c\bar{c} \rightarrow \mu\mu X$, prompt plus $\pi$/K decay, and cosmic ray muons), and the product in $k$ is over the $N_v$ variables ($P_T^{rel}$ and $z$) which are represented by $x_k$ in the above equation. The variables $P_T^{rel}$ and $z$ will be defined in detail later. $A_j$ is the fraction of events attributed to process $j$. $p_k^j(x_k^i)$ is the probability density function which must be created for each of the $k$ processes as a function of each of the variables, $x_k$, and evaluated for each of the $i$ events.

Since an event must be produced by one of the $N_p$ processes, a normalization condition

$$\sum_{j=1}^{N_p} A_j = 1 \tag{7.6}$$

is applied. This condition is included in the likelihood function by transforming the $N_p$ variables, $A_j$, into a set of $N_{p-1}$ independent variables. For a fit to four physical

processes, this is given by

$$\begin{aligned} \alpha_0 &= A_0 \\ \alpha_1 &= \tfrac{A_1}{1-A_0} \\ \alpha_2 &= \tfrac{A_2}{1-A_0-A_1}, \;\; 0 \leq \alpha_i \leq 1. \end{aligned} \tag{7.7}$$

which is used in conjunction with the normalization condition, Eq. 7.6, to produce

$$\begin{aligned} A_0 &= \alpha_0 \\ A_1 &= (1-\alpha_0)\cdot\alpha_1 \\ A_2 &= (1-\alpha_0)\cdot(1-\alpha_1)\cdot\alpha_2 \\ A_3 &= (1-\alpha_0)\cdot(1-\alpha_1)\cdot(1-\alpha_2). \end{aligned} \tag{7.8}$$

The four processes represented by the $A_j$ are dimuons produced from the decay of $b\overline{b}$ quark pairs, $c\overline{c}$ quark pairs, $b$-quark plus $\pi$(K) decays, and cosmic rays. In this case the percentage of cosmic contamination, $A_0$, is known to be $12.3 \pm 0.5\%$ from the studies detailed in Section 7.1. Therefore, $A_0 = \alpha_0$ is held constant while the remaining $N_{p-2}$ variables are allowed to vary.

The maximum value of the log likelihood function is found by solving the equation

$$\frac{\delta(-2\cdot\ln\sum_i \mathcal{L})}{\delta\alpha_j} = 0, \;\; j = 1,\ldots,N_j - 1 \tag{7.9}$$

The CERNLIB package MINUIT [64] was used to perform this maximization. Note that the minus sign in Eq. 7.9 is included because MINUIT is designed to minimize functions, not maximize as we require. Also, the factor of two is included so that a change of $\Delta(-2\cdot\ln\mathcal{L}) = +1$ from the minimum of the function corresponds to a

$1\sigma$ Gaussian error on $\alpha_j$. The MINOS error analysis package was called from within MINUIT to find the contours in the $N_{p-1}$ dimensional space which corresponds to a $\Delta(-2\cdot\ln\mathcal{L}) = +1$ change from the minimum value. MINOS also determines the value of $\alpha_i$ that is required to produce this change. These contours in the $N_{p-1}$ dimensional space are not necessarily symmetric. Therefore, asymmetric upper and lower errors are produced.

## 7.3 Input Distributions

### 7.3.1 $P_T^{rel}$ Distributions

$P_T^{rel}$ is defined as the transverse momentum of a muon with respect to its associated jet axis, or

$$P_T^{rel} = |\vec{P}_\mu| \sin\theta^{rel}, \tag{7.10}$$

where $\theta^{rel}$ is the relative angle between the muon and jet axis. This definition is illustrated in Fig. 7-5. $P_T^{rel}$ was chosen because of its ability to distinguish between $b\bar{b} \to \mu\mu X$ events and the other backgrounds in the sample. $P_T^{rel}$ can distinguish between these processes, because the momentum transfer values, $Q^2$, in the reaction $b \to \mu X$ are large compared to the $Q^2$ found in the background processes.

The value of $P_T^{rel}$ depends upon how one chooses the jet definition. For this analysis, it is best to define the jet so that its $\eta$, $\varphi$, and $E_T$ reproduce the kinematics

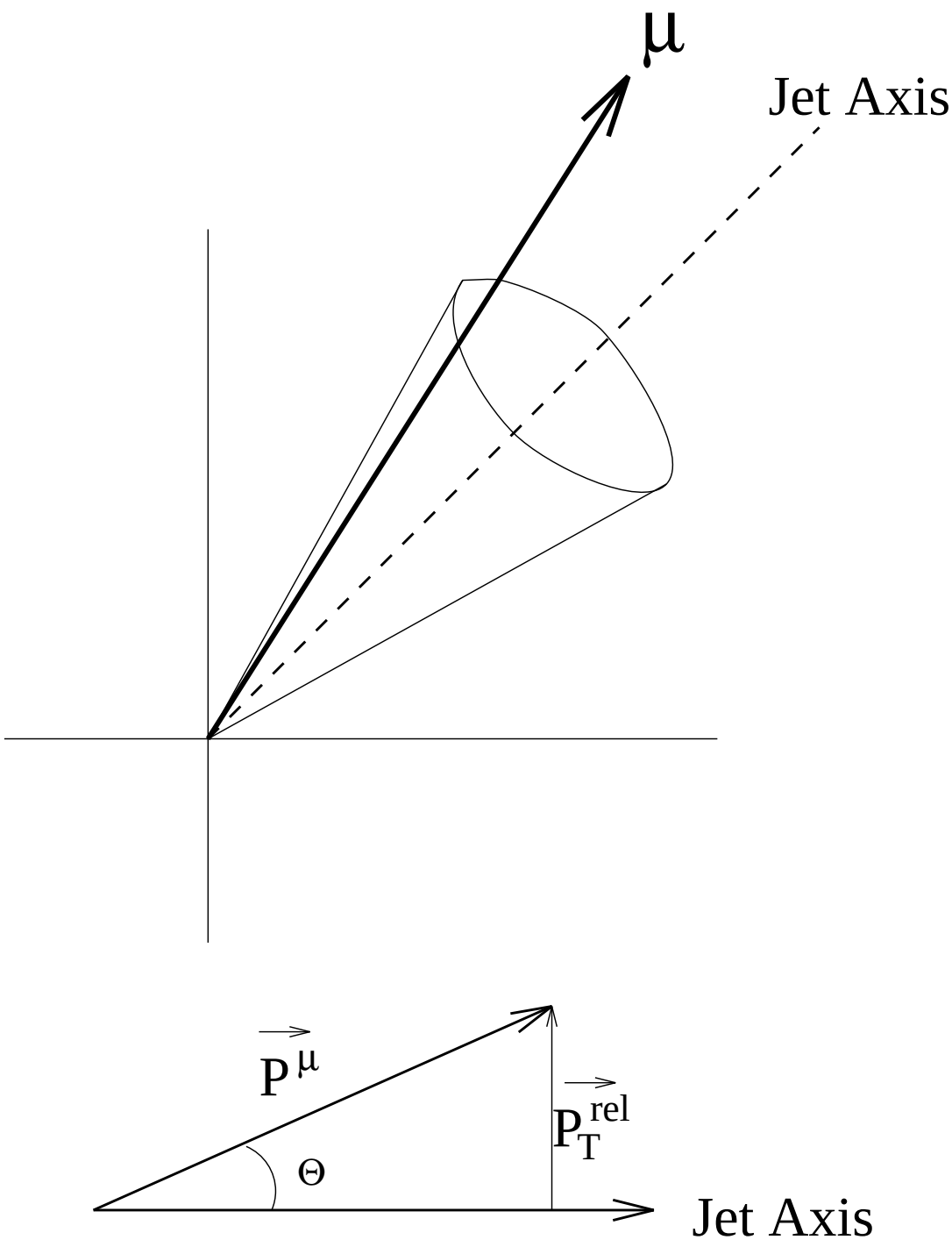


Figure 7-5: $P_T^{rel}$ is defined as the momentum of the muon which is transverse to the jet axis.

of the $b$-quark that produced the jet. Note that the standard jet definition given by the 0.7 cone algorithm reconstructs jets based solely upon the calorimeter cell energies (calorimeter jets). Any muons which may be associated with the jet are ignored except for the minimum ionizing energy deposited by the muon into the calorimeter. Since muons can carry away a significant fraction of the $b$-quark's energy, it is important to include these muons in the jet definition. Therefore, the muon and calorimeter jet momentum 4-vectors are added together to form the jets used in this analysis.

Before the 4-vectors can be added, the expected energy deposition by the muon into the calorimeter must be subtracted from the calorimeter jet energy. This is necessary so that this energy is not double counted when the calorimeter jet and muon momentum 4-vectors are added. The corrected calorimeter jet energy is given by

$$\vec{E}'_{cal} = \sum_{i=1}^{N_t} \vec{E}^i_{cal} - E_\mu \hat{P}_\mu, \tag{7.11}$$

where the summation is over the $N_t$ towers in the jet; $\vec{E}^i_{cal}$ is the energy vector for tower $i$ projected along the x, y, and z axes; $E_\mu$ is the expected deposition of energy into the calorimeter by the muon; and $\hat{P}_\mu$ is the unit vector in the direction of the muon momentum vector.

It is reasonable to assume that the corrected calorimeter jet is the result of the fragmentation of a $D^*$ meson. This Assumption allows one to use the mass of the $D^*$ meson (2 GeV/$c^2$) as the mass of the jet. This is then used to calculate the

calorimeter jet momentum.

$$|\vec{P}_{cal}|^2 = |\vec{E}'_{cal}|^2 - (2\ \mathrm{GeV/c^2})^2$$
$$\vec{P}_{cal} = |\vec{P}_{cal}|\hat{E}'_{cal} \tag{7.12}$$

Finally, the corrected calorimeter jet and muon momentum 4-vectors are added giving the corrected jet energy and momentum.

$$\begin{pmatrix} E_{jet} \\ \vec{P}_{jet} \end{pmatrix} = \begin{pmatrix} |\vec{E}'_{cal}| \\ \vec{P}_{cal} \end{pmatrix} + \begin{pmatrix} E_{\mu} \\ \vec{P}_{\mu} \end{pmatrix} \tag{7.13}$$

Fully processed Monte Carlo (Section 5.2.1) is used to determine the $P_T^{rel}$ distribution for dimuon events from $b\overline{b}$, $c\overline{c}$, and $b$-quark plus $\pi$/K decay events. It was found the $c$-quark plus decay events are indistinguishable from $c\overline{c}$ events. Similarly, events in which two $\pi$ (or K) decay into muons is also indistinguishable from the $c\overline{c}$ distribution. Therefore, the $c$-quark plus decay and double $\pi$/K decay events are not fit independently, but are included with the $c\overline{c}$ events.

In creating the $P_T^{rel}$ input distributions, all of the selection cuts that were applied to the data were applied to the Monte Carlo events. It was also required that the events pass either MU_2_LOW, MU_2_CENT, or the MU_1_LOW trigger. Even though MU_1_LOW was not used in the analysis of the data, it can be used here. The $P_T^{rel}$ distribution produced by events satisfying MU_1_LOW have the same shape as the distributions produced by events satisfying MU_2_LOW and MU_2_CENT.

The $P_T^{rel}$ distributions for the leading and trailing muons are then fit with the

function

$$f(x) = \begin{cases} p_3 \cdot x^4 + p_2 \cdot x^3 + p_1 \cdot x^2 - \alpha \cdot x, & x \leq p_5 \\ \beta \cdot e^{-p_4 \cdot x}, & x > p_5 \end{cases} \tag{7.14}$$

where the $p_i$ are free parameters and

$$\begin{aligned} \beta &= -\left[\tfrac{1}{1+p_4 p_5}\right](p_1 p_5^2 + 2p_2 p_5^3 + 3p_3 p_5^4) e^{p_4 p_5} \\ \alpha &= \beta p_4 e^{-p_4 p_5} + 2p_1 p_5 + 3p_2 p_5 + 4p_3 p_5 \end{aligned} \quad . \tag{7.15}$$

The variables $\alpha$ and $\beta$ are designed to constrain Eq. 7.14 so that $f(0) = 0$ and the polynomial and exponential join smoothly at $x = p_5$. A likelihood fit is used to fit this function to each of the Monte Carlo $P_T^{rel}$ distributions. After the fit, these functions are normalized to unit area so that they may be used as the input probability density functions for the log-likelihood fit.

The fits to the $P_T^{rel}$ distributions for dimuons from $b\overline{b}$ decays is shown in Fig. 7-6. Figures 7-7 and 7-8 show the analogous plots for $c\overline{c}$ and $b$-quark plus $\pi$/K decay events. The cosmic ray $P_T^{rel}$ distributions is obtained directly from the data. All of the analysis cuts listed in Tables 4-5 and 4-6 are applied to the data with the exception that anti-scintillator $\Delta tof$ cuts are made, $-40 < \Delta tof < -12$ or $12 < \Delta tof < 80$. This cut selects cosmic ray events from the data and is estimated to be 99% pure. The fits to the cosmic ray $P_T^{rel}$ distributions for the reconstructed dimuons are shown in Fig. 7-9.

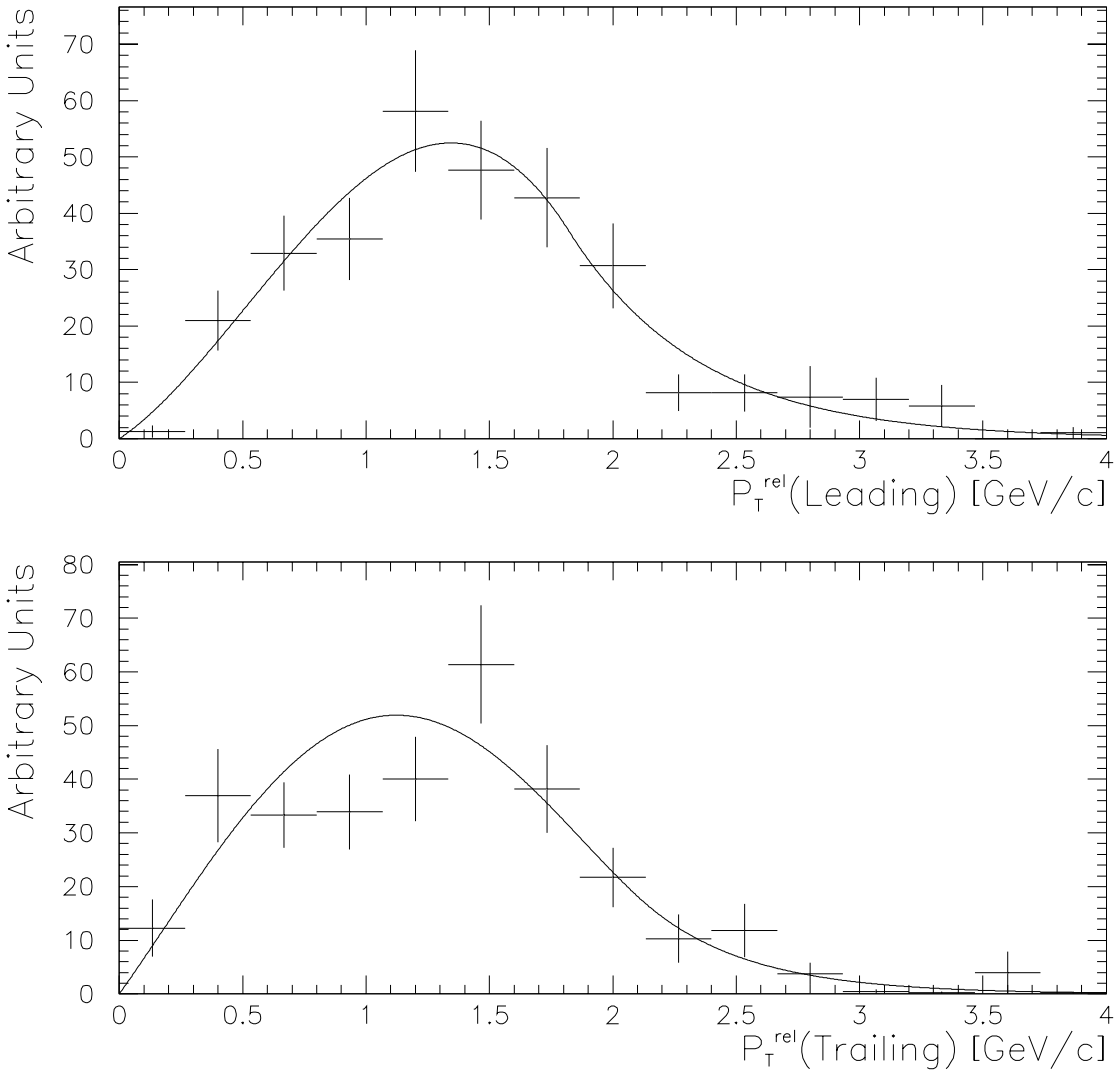


Figure 7-6: The fit to the processed Monte Carlo $P_T^{rel}$ distributions for $b\overline{b} \rightarrow \mu\mu X$ events.

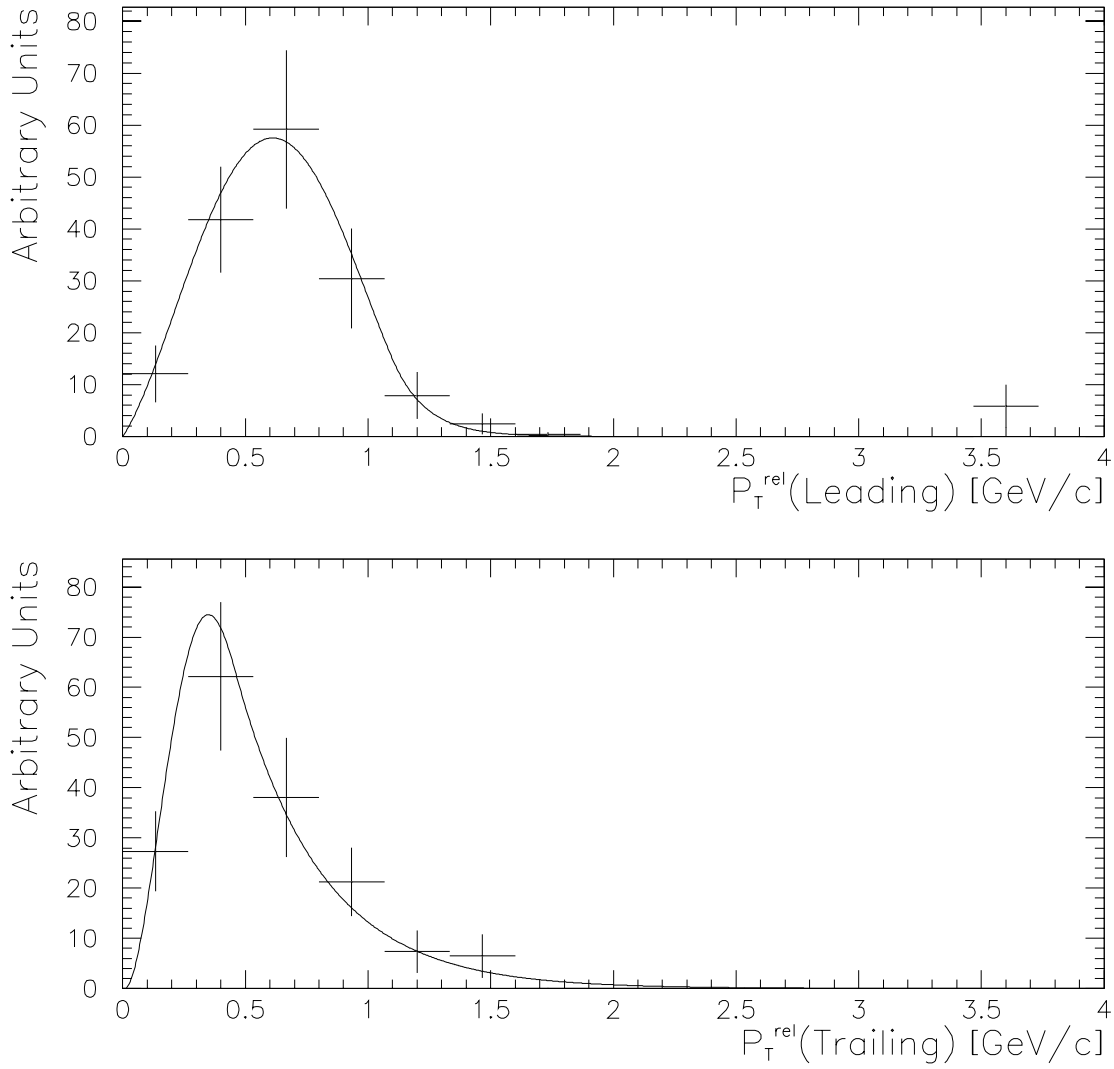


Figure 7-7: The fit to the processed Monte Carlo $P_T^{rel}$ distributions for $c\bar{c} \rightarrow \mu\mu X$ events.

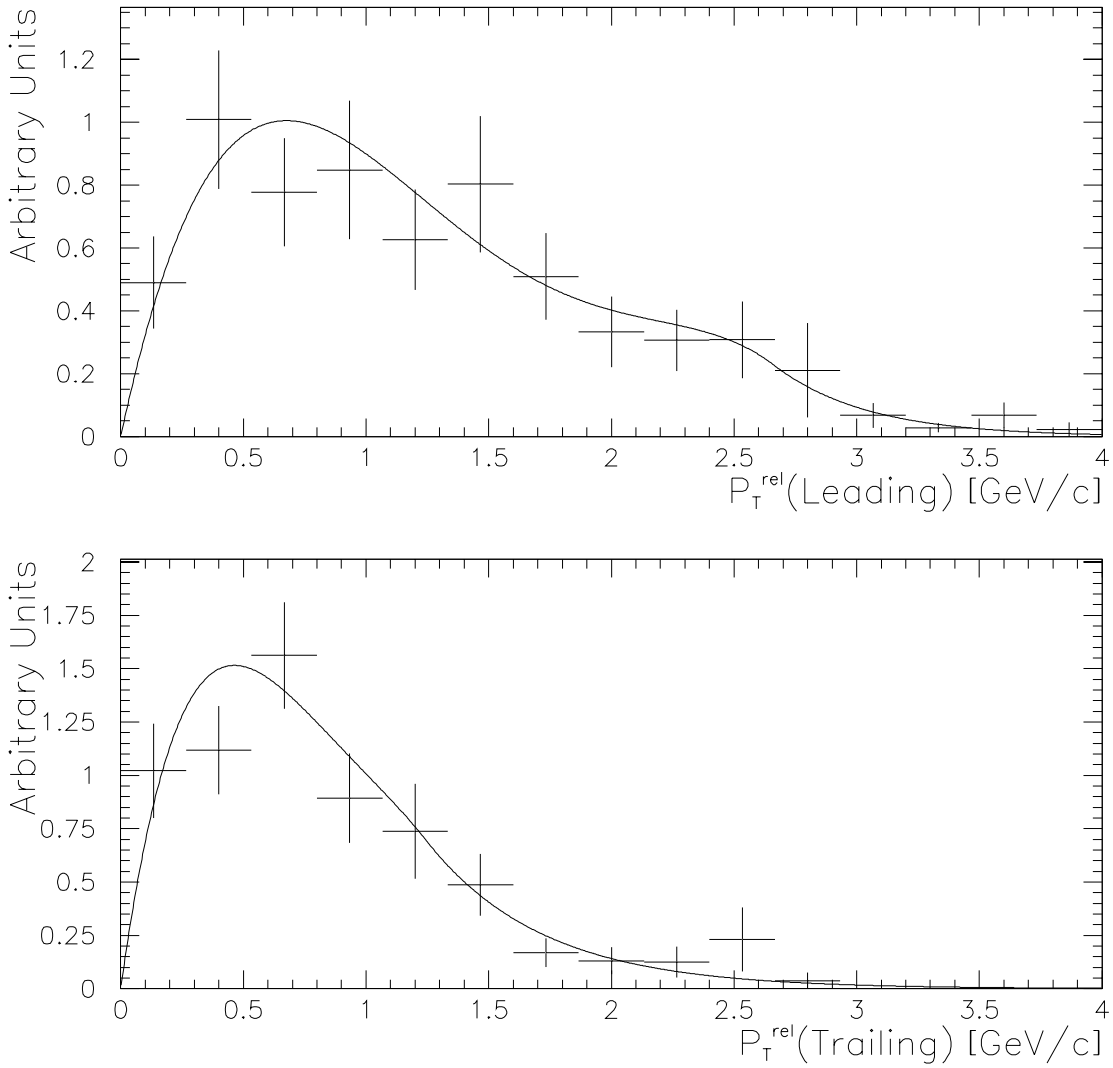


Figure 7-8: The fit to the Monte Carlo $P_T^{rel}$ distributions for events in which both a $b$-quark and a $\pi$ (or Kaon) decay into muons.

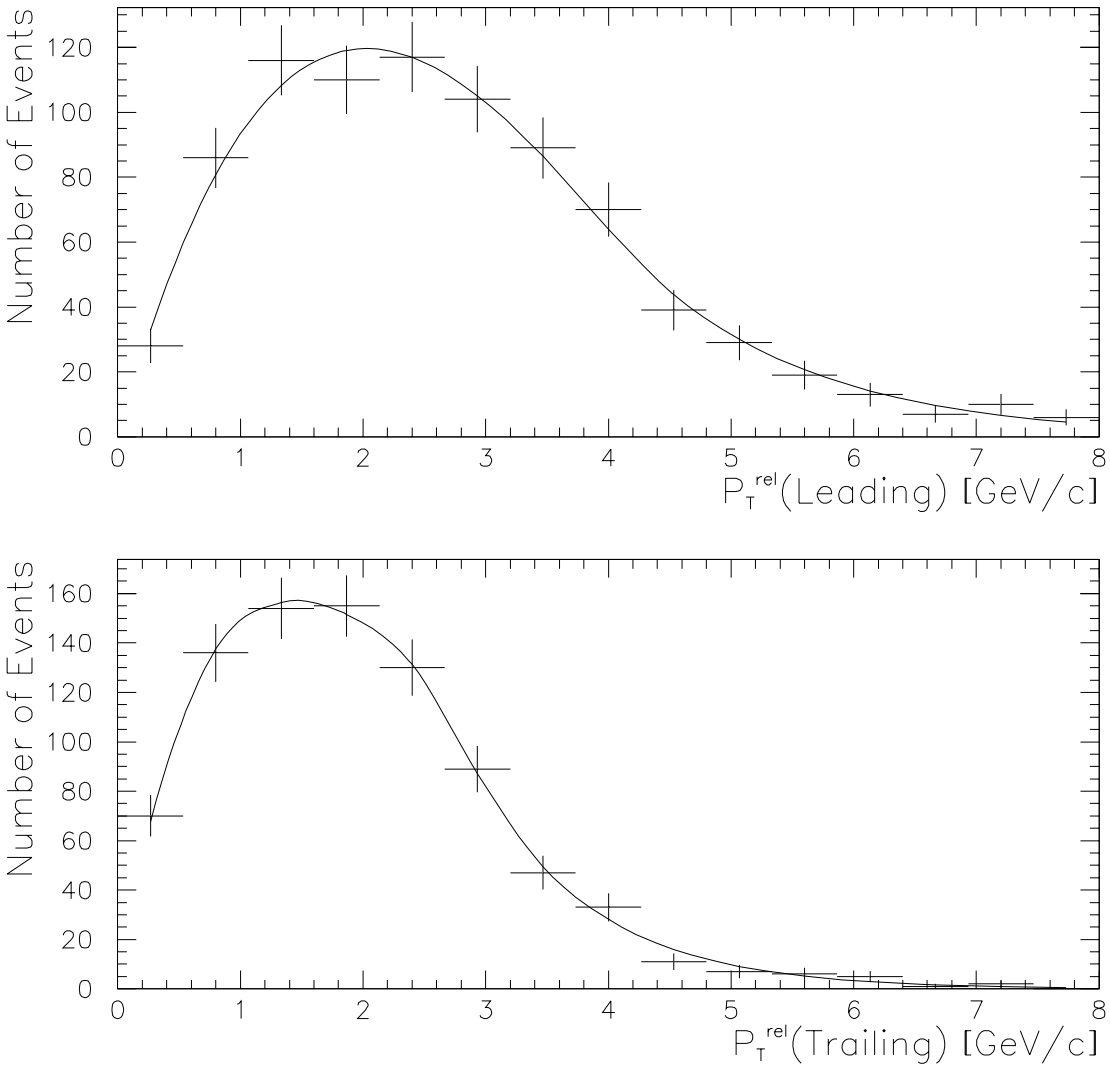


Figure 7-9: The fit to the cosmic ray $P_T^{rel}$ distributions.

### 7.3.2 $z$ Distributions

Another variable which is useful for distinguishing between the various processes that produce dimuon events is $z$. This variable is defined as the fraction of jet energy carried away by muon along the jet axis. More precisely

$$z = \frac{|\vec{P}_\mu| \cos\theta^{rel}}{|\vec{P}_{jet}|}. \tag{7.16}$$

Here, the jets are corrected by the methods described in Section 7.3.1. This implies that $|\vec{P}_\mu| < |\vec{P}_{jet}|$. Therefore, $z$ will always fall within the range $0 < z < 1$. As before, fully processed Monte Carlo is used to determine the $z$ distributions for the $b\overline{b}$, $c\overline{c}$, and $b$-quark plus decay processes. Also, the $c\overline{c}$, $c$-quark plus decay, and double $\pi$/K $z$ distributions are indistinguishable and are, therefore, not fit separately. The function used to fit the $z$ distribution is

$$f(x) = \begin{cases} p_1 e^{\left(-\frac{1}{2}[\frac{x-p_2}{p_4}]^2\right)}, & x \leq p_2 \\ p_1 e^{\left(-\frac{1}{2}[\frac{x-p_2}{p_3}]^2\right)}, & x > p_2 \end{cases} \tag{7.17}$$

which is simply an asymmetric Gaussian. The results of these fits can be seen in Figures 7-10, 7-11, and 7-12.

The cosmic ray $z$ distribution is obtained directly from the data by using the anti-scintillator cuts described in Section 7.3.1. The results of the fit to the cosmic ray $z$ distributions are shown in Fig. 7-13.

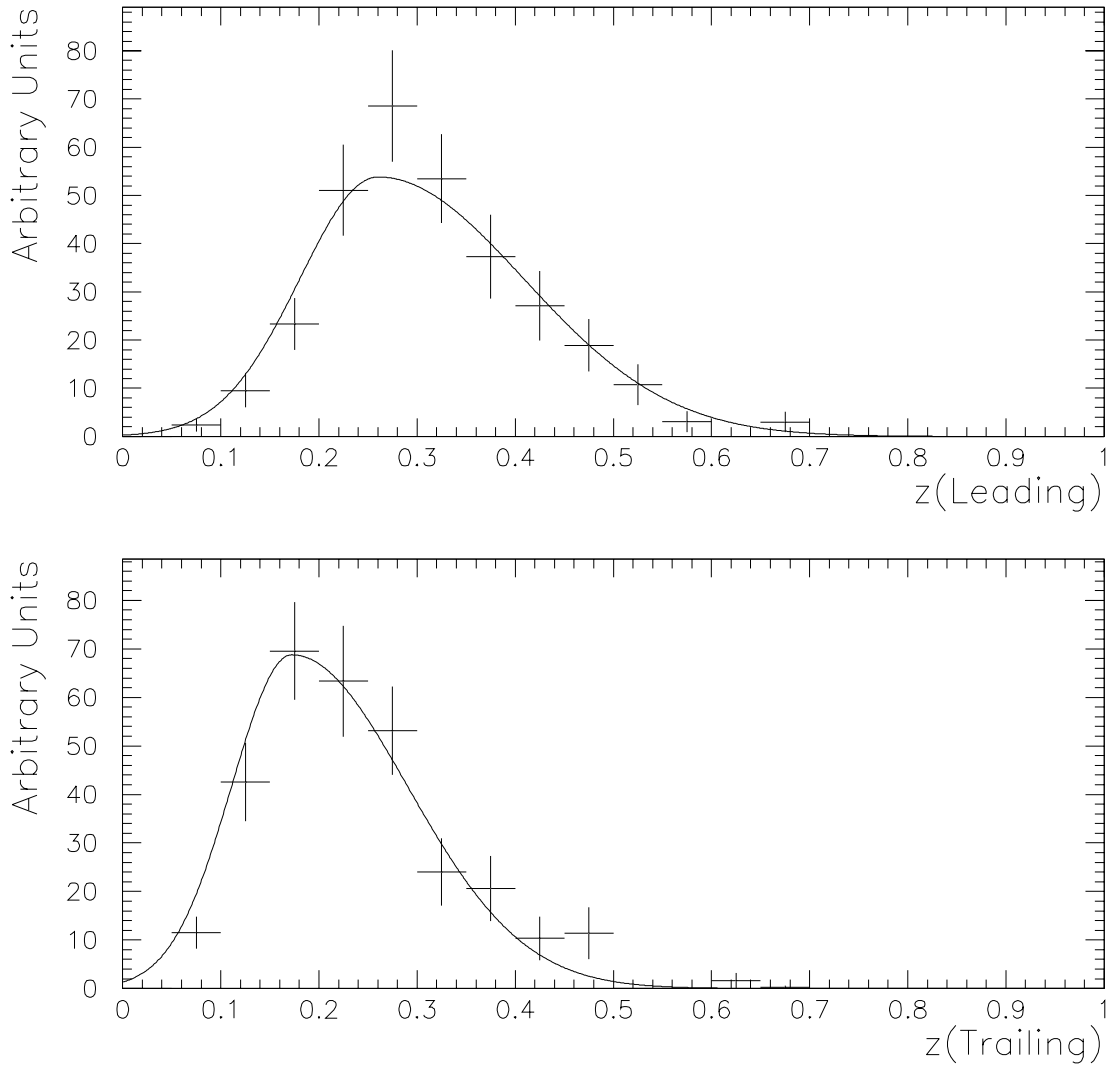


Figure 7-10: The fit to the processed Monte Carlo $z$ distributions for $b\overline{b} \to \mu\mu X$ events.

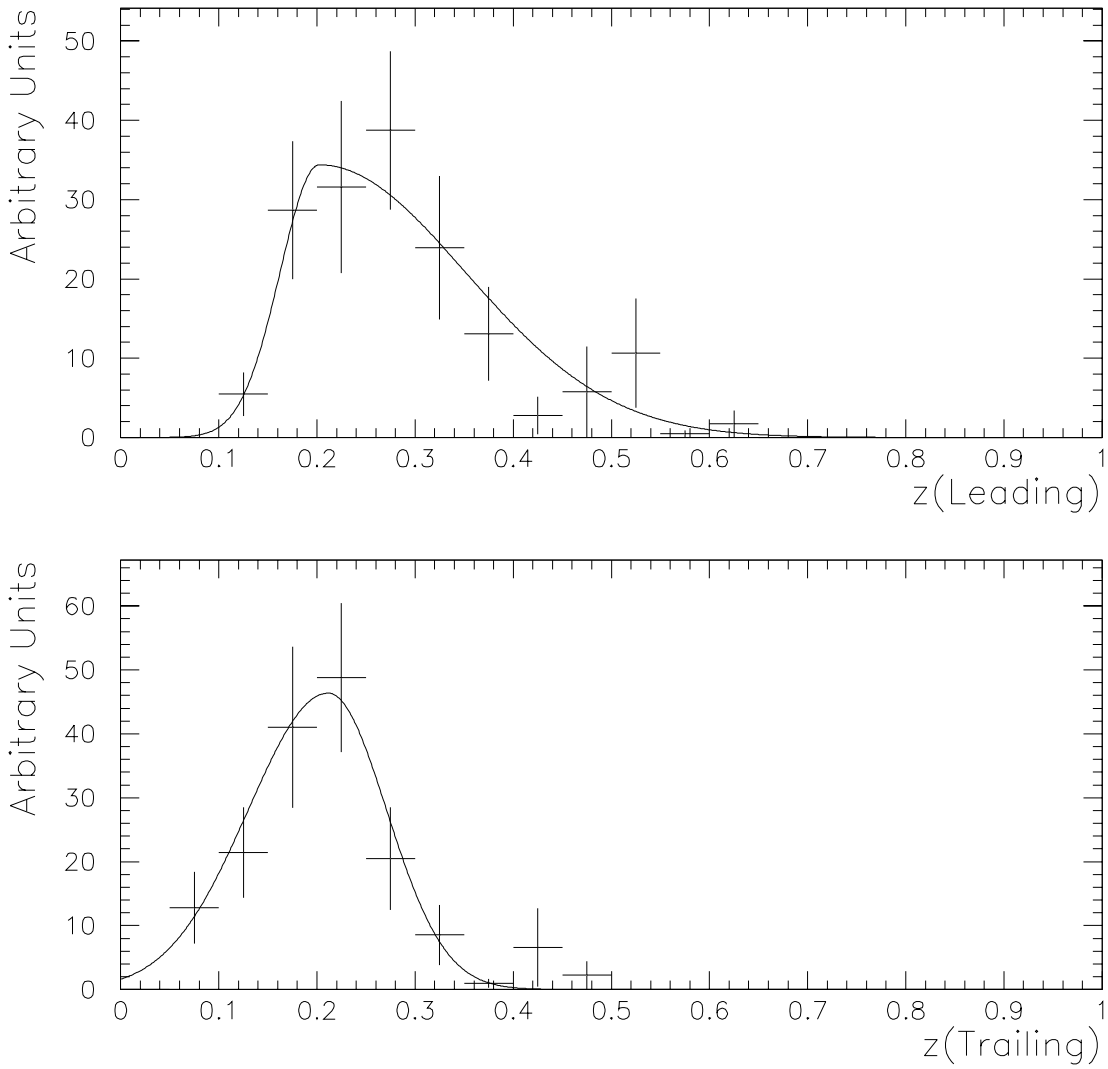


Figure 7-11: The fit to the processed Monte Carlo $z$ distributions for $c\bar{c} \rightarrow \mu\mu X$ events.

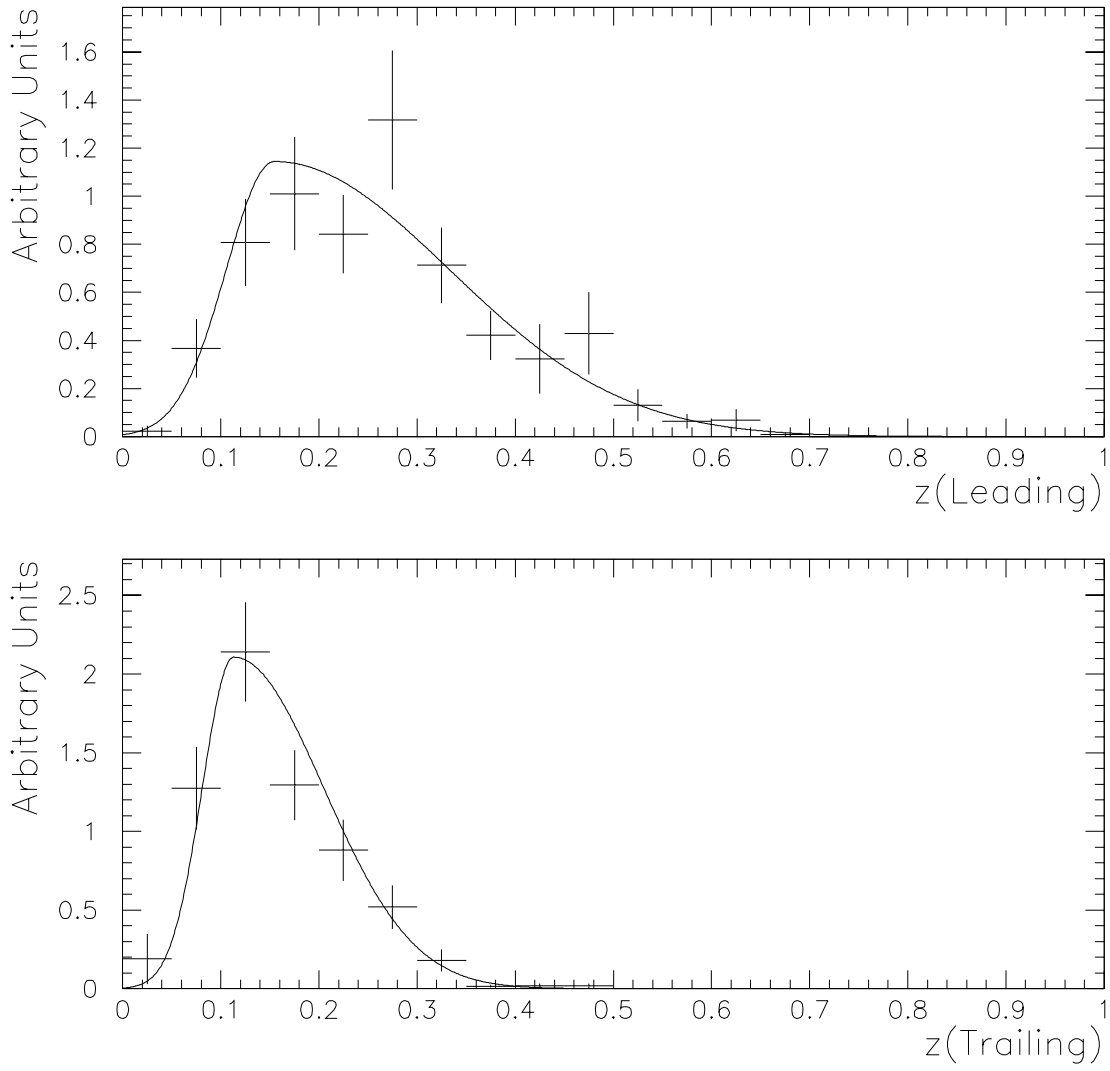


Figure 7-12: The fit to the processed Monte Carlo $z$ distributions for events in which both a $b$-quark and a $\pi$/K decay into muons.

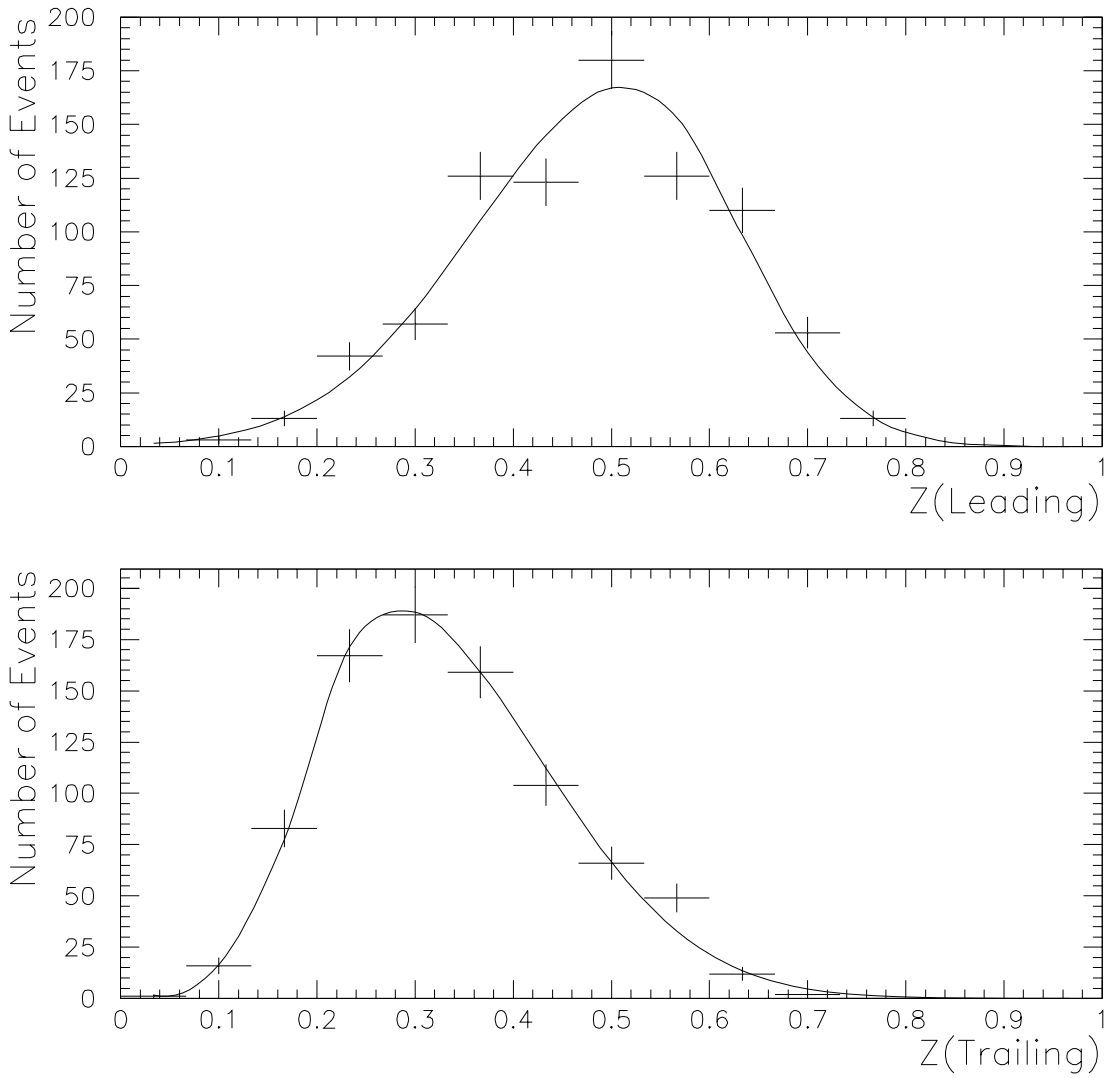


Figure 7-13: The fit to the cosmic ray $z$ distribution.

## 7.4 Results of the Fits

### 7.4.1 Fit to the Monte Carlo

The effectiveness of the fitting technique can be tested by fitting a Monte Carlo sample with a known mixture of processes. The likelihood fits are then used in an attempt to predict this composition. When performing these tests, slight modifications to the input distributions must be made. First, the Monte Carlo does not contain cosmic ray events. Therefore, the amount of cosmic ray contamination, $A_0$, was set to $0 \pm 0\%$. This ensures that this process does not contribute to the fit. Second, the Monte Carlo used to create the input distributions for these tests were not corrected as described in Chapter 5. When fitting the data, it is important to make these corrections. However, here it is unnecessary.

Two different event samples were created (see Table 7-5). Set A was chosen so that the proportions of $b\overline{b}$, $c\overline{c}$, and prompt plus decay approximates what is seen in the data. This set contains a total of 520 Monte Carlo events. The mixture in set B was chosen arbitrarily and contains a total of 723 events. In both cases, the Maximum Likelihood method does a good job of determining the percentage of $b\overline{b}$, $c\overline{c}$ and prompt plus decay processes contained in the Monte Carlo samples. This gives us confidence that the method works and is stable. Fig. 7-14 shows the resulting $P_T^{rel}$ distributions after the fit is performed on set B. Similarly, Fig. 7-15 shows the corresponding $z$ distributions.

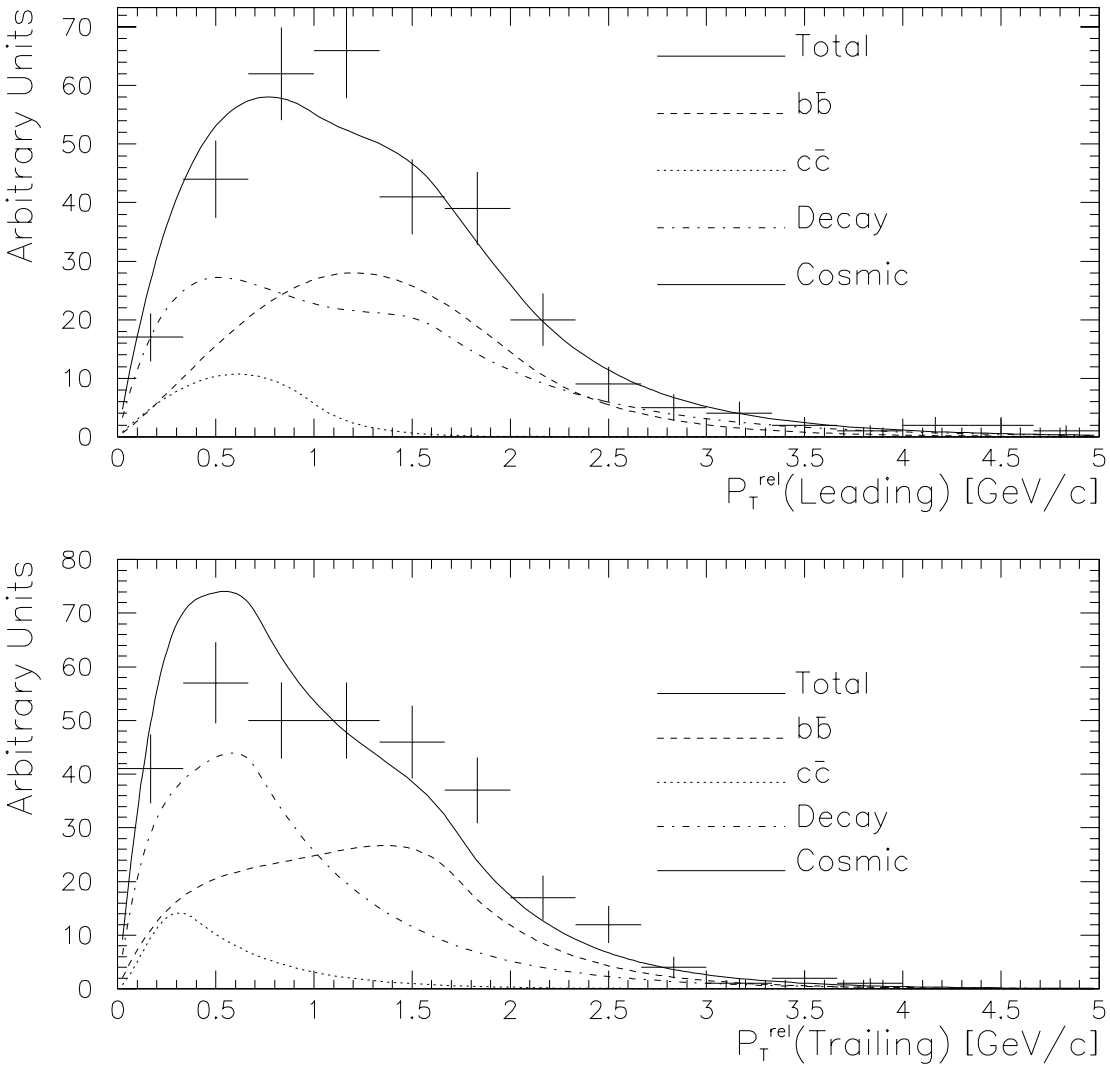


Figure 7-14: The $P_T^{rel}$ distributions fit to the events in set B (Table 7-5).

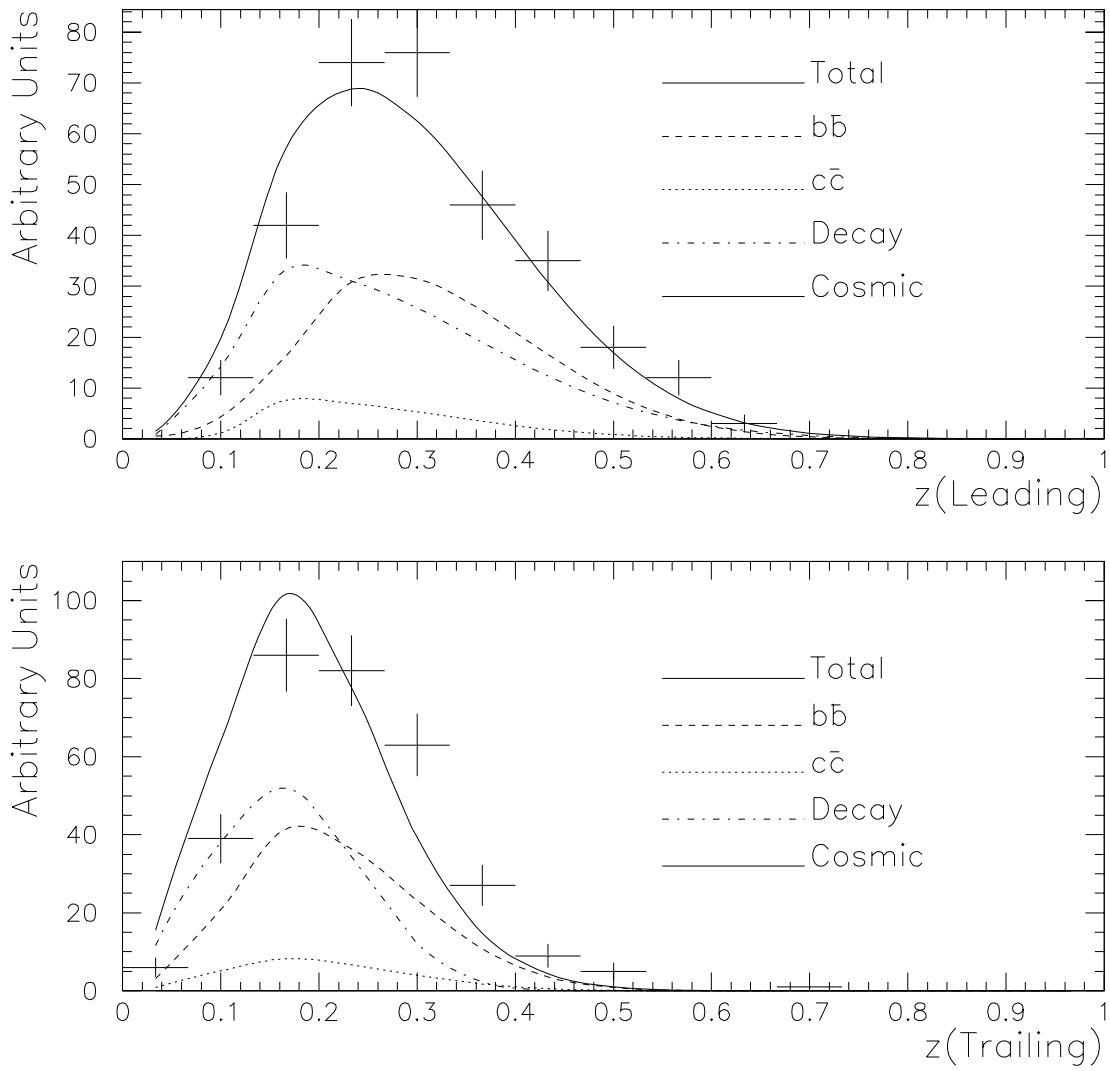


Figure 7-15: The $z$ distributions fit to the events in set B (Table 7-5).

| | % $b\overline{b}$ | % $c\overline{c}$ | % $b$-quark plus $\pi$/K decay |
|---|---|---|---|
| Set A | | | |
| Monte Carlo | 60.0 | 9.6 | 30.4 |
| Results of Fit | $58.4^{+4.4}_{-4.5}$ | $5.4^{+3.2}_{-2.9}$ | $36.2^{+4.8}_{-5.0}$ |
| Set B | | | |
| Monte Carlo | 43.2 | 11.8 | 45.0 |
| Result of Fit | $44.3 \pm 3.8$ | $8.6^{+2.9}_{-2.8}$ | $47.1^{+4.2}_{-4.3}$ |

Table 7-5: Two different Monte Carlo event samples were created. Set A was designed to approximate what is found in the data. Set B is a random mixture of processes. In both cases the maximum likelihood fit does a good job of determining the fractions.

| Process Name | Percentage |
|---|---|
| $b\overline{b}$ | $45.6 \pm 1.8$ |
| $c\overline{c}$ | $13.7 \pm 1.5$ |
| Prompt plus Decay | $28.3 \pm 1.8$ |
| Cosmics | $12.3 \pm 0.5$ |

Table 7-6: Results of the maximum log-likelihood fit to the data.

### 7.4.2 Fit to the Data

The results of the maximum likelihood fit to the data are summarized in Table 7-6. The percentage of cosmic contamination was determined using the methods described in Section 7.1 and was found to be $12.3 \pm 0.5\%$. This value was fixed during the fit, while the remaining processes were allowed to vary. The resulting fits can be seen in Fig. 7-16 ($P_T^{rel}$) and Fig. 7-17 ($z$).

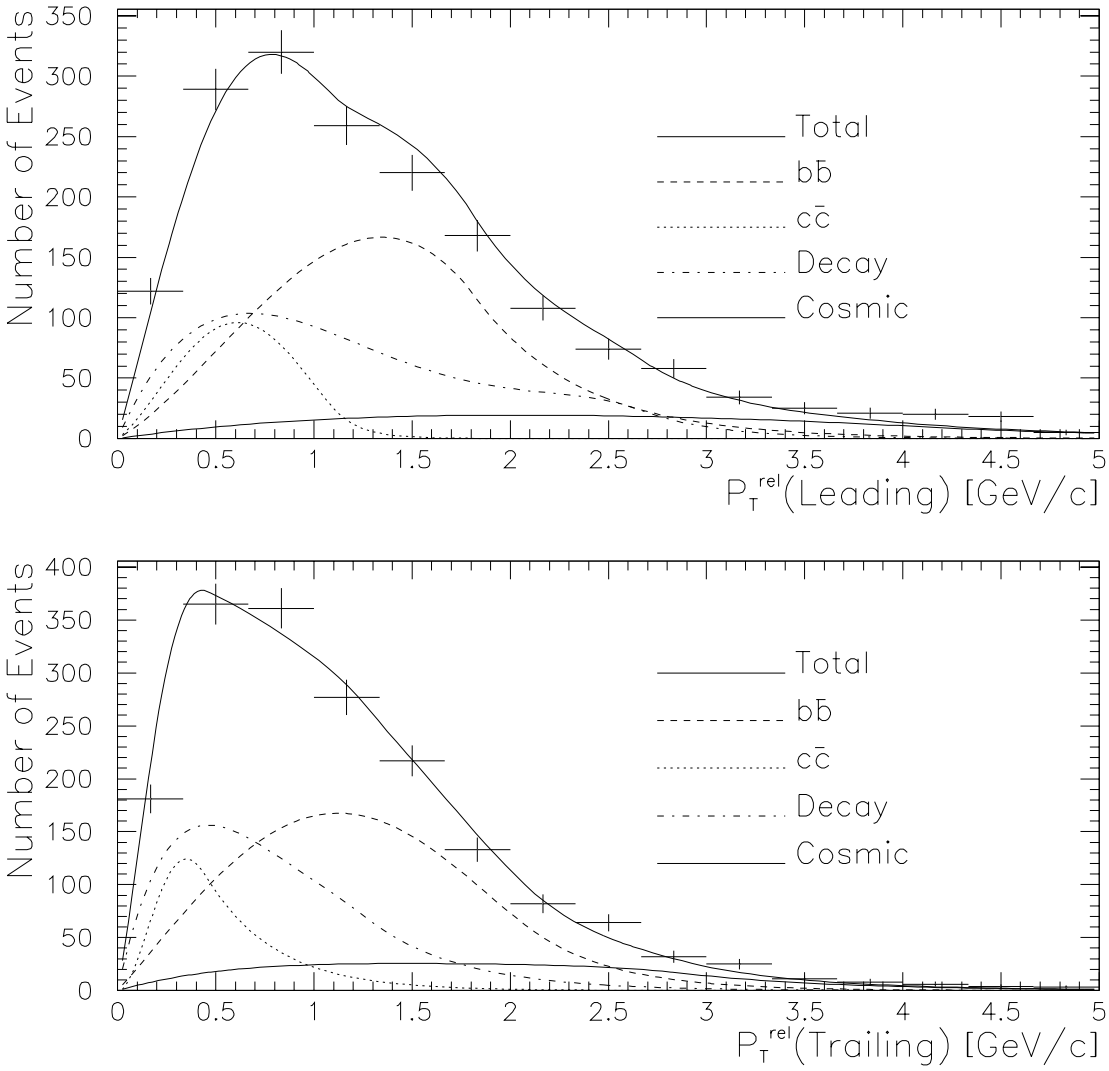


Figure 7-16: The $P_T^{rel}$ distributions that result from the maximum likelihood fit to the data.

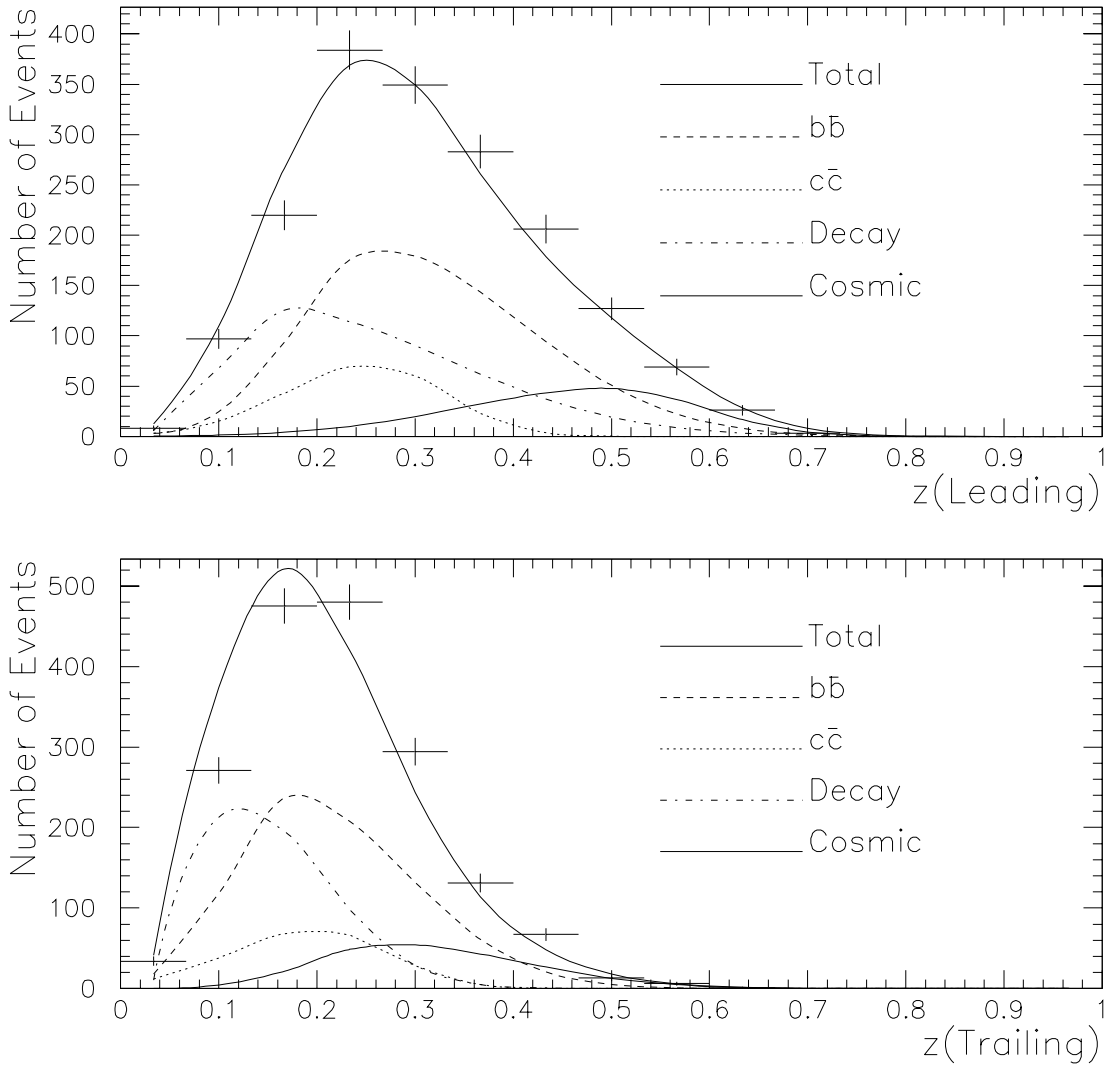


Figure 7-17: The $z$ distributions that result from the maximum likelihood fit to the data.

## 7.5 Systematic Uncertainties

Two types of systematic errors must be considered. The first is the uncertainty described in Section 7.2. This uncertainty gives information about the quality of the fit. For clarity, this uncertainty shall be referred to as the 'fitting uncertainty' and is determined by the MINOS error analysis program. The second error is the systematic uncertainty associated with our choice of input probability density functions for $P_T^{rel}$ and $z$ (the 'PDF uncertainty'). Differences between the Monte Carlo and data can lead to input distribution functions which differ from the true probability density functions required by the data. Uncertainties such as this can not be determined by the MINOS error analysis package. Instead, the PDF uncertainty must be determined through other means.

One measure of the PDF uncertainty can be obtained by using different Monte Carlo samples to create new input distribution functions. The maximum likelihood fit to the data is then repeated with each of the new sets of input functions. The difference between the new and original results (Table 7-7) will be taken as the PDF uncertainty. Three different sets of input distribution functions were used for this study. Each is described in detail below and is summarized in Table 7-7.

In the first set of test input functions, the sequential decay of $b$-quarks are handled differently. In the original set of input functions (Section 7.3), the $P_T^{rel}$ and $z$ distributions for the $b\bar{b} \to \mu\mu X$ process included the sequential decay of $b$-quarks. In other words, these input functions were created from Monte Carlo samples which in-

| Process Name | Prompt and Sequentials | 1/2 G.S. | No G.S. |
|---|---|---|---|
| $b\overline{b}$ | 2% | 4% | 3% |
| $c\overline{c}$ | 4% | 5% | 5% |
| Prompt plus Decay | 1% | 1% | 1% |
| Total Error | 5% | 6% | 6% |

Table 7-7: Systematic errors for the fits to the Monte Carlo.

cluded events in which one (or both) of the heavy quarks decay into a $c$-quark which subsequently decays into a muon. A test of the stability of the fit is to create a set of input distributions in which the sequential $b$-quark decays are fit independently of the prompt $b \rightarrow \mu$ decays. $P_T^{rel}$ and $z$ distributions were created separately for the prompt and sequential $b$-quark decays. These input functions were then used in the maximum likelihood fit. The results from this fit agree with the original method to within 5%. This shows relatively good agreement between the two methods.

Two more test were performed. In these tests, the amount of gluon splitting was altered in the Monte Carlo. In the first set the amount of gluon splitting was reduced by one half, and in the second set the gluon splitting was removed completely from the Monte Carlo sample. As will be seen later (Section 9.2.4) ISAJET tends to over-estimate the amount of gluon splitting present in the $b\overline{b} \rightarrow \mu\mu X$ sample. Therefore, altering the Monte Carlo in this manner presumably makes it more like the data. The results of this fit are shown in Table 7-7 and agree with the original method to within 6%. These results are summarized in Table 7-8.

All three of these tests agree with the original fit to within 6%. Therefore, the

| | |
|---|---|
| Fitting Uncertainty | $< 0.5\%$ |
| PDF Uncertainty: | |
| $P_T^\mu$ Distribution | 12% |
| $\Delta\varphi_{\mu\mu}$ Distribution | 10% |

Table 7-8: A summary of the systematic errors associated with the maximum log-likelihood fits. The fitting uncertainty is calculated be taking the errors listed in Table 7-6 and propagating them through Eq. 9.3. Note that the PDF uncertainty dominates.

relative PDF uncertainty for the likelihood fits will be taken as 6%. This uncertainty must now be translated into into an uncertainty in each $P_T^\mu$ (or $\Delta\varphi_{\mu\mu}$) bin. Simple error propagation gives the relation between the total systematic uncertainty and the uncertainty per bin.

$$\frac{\sigma_N}{N} = \frac{1}{N}\left[\sum_{i=1}^{n_b}\left(\frac{\sigma_{N_i}}{N_i}\right)^2\right]^{\frac{1}{2}}, \tag{7.18}$$

where $n_b$ in the total number of bins, $N$ is the total number of events, and $N_i$ is the number of events per bin. If it is assumed that the fractional uncertainty in each bin is approximately equal, then this expression can be written as

$$\left(\frac{\sigma_{N_i}}{N_i}\right) = \left(\frac{\sigma_N}{N}\right)\frac{N}{\left[\sum_{i=1}^{b} N_i^2\right]^{1/2}}. \tag{7.19}$$

This translates into a 12% relative uncertainty in each of the $P_T^\mu$ bins, and a 10% relative uncertainty in each $\Delta\varphi_{\mu\mu}$ bin (see Table 7-8).

## 7.6 Variable Correlations

The likelihood function (Equations 7.4 and 7.5) assumes that the variables being used in the fit are uncorrelated. This is not strictly true for $P_T^{rel}$ and $z$, because it can be shown that the two variables are somewhat correlated. To show this, we begin by defining the correlation between to random variables, $X$ and $Y$

$$\rho = \frac{\sigma_{XY}}{\sigma_X \cdot \sigma_Y}, \tag{7.20}$$

where $\sigma_{XY}$ is the covariance between $X$ and $Y$ given by

$$\sigma_{XY} = \overline{(X \cdot Y)} - \overline{X} \cdot \overline{Y}. \tag{7.21}$$

$\sigma_X$ is the square root of the variance for variable $X$, and $\overline{X}$ is the average value of the random variable $X$. The variance can be calculated by taking the difference between the average of $X^2$ and the square of the average of $X$,

$$\sigma_X^2 = \overline{(X^2)} - (\overline{X})^2. \tag{7.22}$$

The correlation, as defined by Eq. 7.20, is simply a normalized covariance which must have values within the interval $-1 \leq \rho \leq 1$. If $\rho = 1$, the variables are completely correlated. Conversely, if $\rho = -1$ the variable are anti-correlated. Ideally, the variables chosen for the log-likelihood fit should be uncorrelated ($\rho = 0$). However, Table 7-9 shows that this isn't the case. Instead, the correlation values are found to range from -0.250 to 0.382. Since the variables are correlated, the fitting uncertainty

| | $P_T^{rel,1}$ | $P_T^{rel,2}$ | $z^1$ | $z^2$ |
|---|---|---|---|---|
| $z^2$ | -0.143 | -0.246 | 0.382 | 1 |
| $z^1$ | -0.250 | -0.179 | 1 | |
| $P_T^{rel,2}$ | 0.168 | 1 | | |
| $P_T^{rel,1}$ | 1 | | | |

Table 7-9: The correlations between the variables used in the maximum log-likelihood fits. The correlation between the $P_T^{rel}$ and $z$ variables for both the leading(1) and trailing(2) muons are shown. Note that the variables are all loosely correlated.

is somewhat underestimated. Fortunately, the fitting uncertainty is small compared to the PDF uncertainty (see Table 7-8). Therefore, the correlation effects can be ignored.

# Chapter 8

# Data Unfolding Techniques

Finite detector resolutions can cause smearing effects in measured data samples. In this analysis, several variables must be simultaneously unfolded to account for these effects. These variables include the $P_T^\mu$ of both the leading and the trailing muons, the azimuthal opening angle between the two muons ($\Delta\varphi_{\mu\mu}$), and the dimuon invariant mass. Each of these variables must be unfolded before a true cross section can be measured.

Before beginning this discussion, some terms that are used later must be defined. Care must be taken to properly distinguish between the smeared and unsmeared distributions in both the Monte Carlo and data. To begin with, we must distinguish between a real and a measured variable. A 'real' variable is one that represents the true value of a physical quantity. In the data, the real variables are unobservable because of finite detector resolutions and other smearing effects. Instead, the best we

can do is observe the 'measured' variables which in this analysis are the reconstructed quantities. Monte Carlo is different than data in that we know both the real (ISAJET) and the measured (reconstructed) quantities.

Four different distributions will be used in this analysis. Each distribution is given a name to uniquely identify it in the following discussion. Two Monte Carlo distributions will be used:

- **Input Distribution**

  The distribution of ISAJET (real) quantities shall be referred to as the 'input distribution' . Several different input distributions will be used in this analysis including distributions in $P_T^{\mu}$ and $\Delta\varphi_{\mu\mu}$.

- **Smeared Distribution**

  A histogram of reconstructed Monte Carlo quantities shall be referred to as a 'smeared distribution'. These distributions simulate the measured quantities found in the data.

Analogously, two data distributions will be used which have also been given unique names.

- **Data Distribution**

  A 'data distribution' is simply a histogram of measured (reconstructed) data. The data distribution is the one that must be unfolded.

- **Unfolded Distribution**

The 'unfolded distribution' is the unfolded data distribution. If the unfolding is done correctly, the unfolded distribution will be the same as the true spectrum.

## 8.1 Bayesian Unfolding

A Bayesian method [65] is used to unfold the data. This technique unfolds binned data distributions by iteratively applying Bayes' theorem,

$$p(C_j|E_i) = \frac{p(E_i|C_j) \cdot p(C_j)}{\sum_{l=1}^{n_C} p(E_i|C_l) \cdot p(C_l)} \tag{8.1}$$

where $C_j$ represents the number of real (or causal) events falling into the $j^{th}$ bin, $E_i$ is the number of measured events found in the $i^{th}$ measured bin, and $n_C$ is the number of causal bins. $p(X)$ is the probability that X occurs, and $p(X|Y)$ is the probability that measurement X is made given causal event Y. For example, assume that we have a $P_T^{\mu}$ muon distribution measured in $i$ bins, $P_T^{data}[i]$, that we wish to unfold into $j$ causal bins, $P_T^{real}[j]$. Equation 8.1 tells us that the unfolding matrix is proportional to the probability that a real event occurred in bin $j$, $p(P_T^{real}[j])$, times the likelihood that this event produces measured event $i$, $p(P_T^{data}[i]|P_T^{real}[j])$.

At first glance, Bayes' theorem seems ineffective, because it is impossible to calculate the smearing matrix without first knowing the distribution of the real events. In other words, Bayes' theorem lets one calculate the the answer only if the correct answer has already been supplied. D'Agostini [65] successfully circumvents this difficulty by using the theorem in an iterative fashion. To begin with, one simply guesses

at the distribution of the real data, $p_{\circ}(C_i)$. If one is totally ignorant of the shape of the true distribution, then a uniform distribution can be chosen. Next, Monte Carlo is used to build the smearing matrix, $P(E_j \mid C_i)$. At this point, Bayes' theorem (Eq. 8.1) is used to produce an approximation for the unfolding matrix, $P(C_i \mid E_j)$. This approximate unfolding matrix can then be used to calculate an approximation of the unfolded distribution. This unfolded distribution, in turn, can then be used to calculate new values for $p(C_i)$. One proceeds iteratively by using the new $p(C_i)$ values to recalculate the unfolding matrix until the successive $p(C_i)$ values converge.

The Bayesian unfolding method has several advantages over other unfolding techniques. First, the unfolding is independent of the shape of the Monte Carlo used to build $P(E_j \mid C_i)$. Although our Monte Carlo does a reasonably good job of reproducing the data, it is not perfect. Therefore, it is important that this method give us the ability to unfold the data without biasing the results. Another advantage is that this method allows events migrate between bins. Thus, covariances between the bins in the unfolded distribution can be calculated [65].

## 8.2 Application of D'Agostini's Method

When using this unfolding technique, care must be taken to properly build the smearing matrix, $P(E_j \mid C_i)$. A few of the more pertinent considerations are detailed below.

### 8.2.1 Boundary Problems

Bayes' theorem allows events to migrate between bins during the unfolding process. One disadvantage of this migration is that events which pass kinematic cuts before the unfolding may fail these same cuts *after* the unfolding. In other words, a cut on a measured variable is not equivalent to making the same cut on the corresponding real variable. For example, in this analysis we wish to make a cut on the real $P_T$ of the muons so that $4 < P^{\mu}_{T,real} < 25$ GeV/c. Of course, this cut cannot be made until *after* the measured $P^{\mu}_{T}$ spectrum has been unfolded. Fig. 8-1 demonstrates that events satisfying $4 < P^{\mu}_{T,reco} < 25$ GeV/c do not necessarily satisfy $4 < P^{\mu}_{T,real} < 25$ GeV/c.

The unfolding must be done in a manner which allows one to apply cuts on real variables *after* the unfolding. This is accomplished by keeping additional bins that will later be removed after the unfolding is completed. Using Fig. 8-1 as our example, it is best to keep events that fall within the bins 3-4 GeV/c and 25-40 GeV/c in both the real and measured distributions. Keeping these bins allows events to properly migrate into (or out of) the spectrum during unfolding. After the unfolding is complete, these extraneous bins can be removed. By removing the bins after the unfolding one is effectively cutting on real variables.

### 8.2.2 Efficiency Dependence

Some efficiencies must be taken into consideration when building $P(E_j \mid C_i)$. Efficiencies that have real variable dependencies must be handled with care. For example,

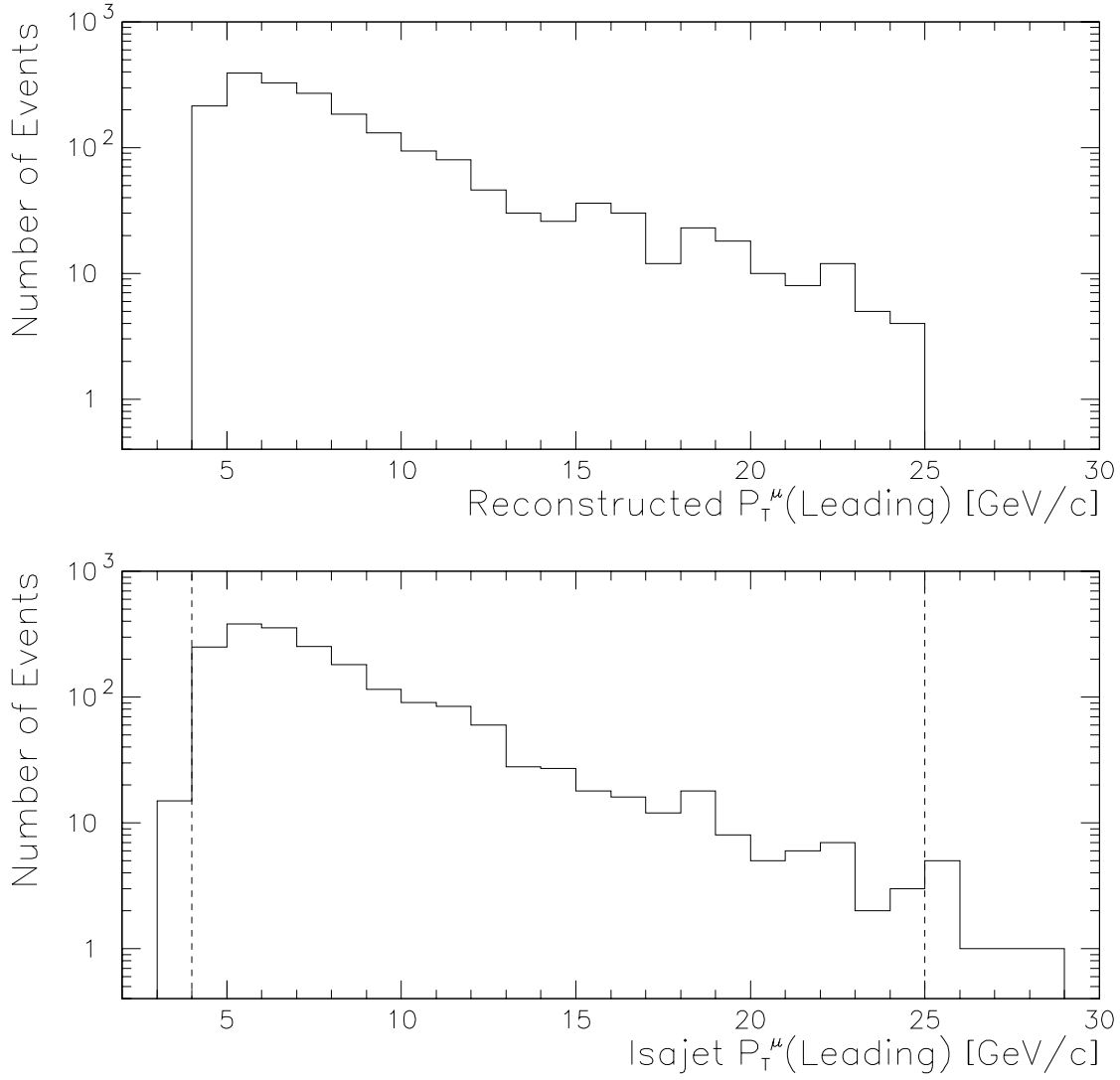


Figure 8-1: In both plots the requirement $4 < P^{\mu}_{T,reco} < 25$ GeV/c is applied to the ISAJET Monte Carlo events. This cut can be seen clearly in the upper plot which plots the reconstructed $P^{\mu}_{T}$(leading). The bottom plot shows the same events plotted as a function of ISAJET $P^{\mu}_{T}$(leading).

the Level 1 and Level 2 trigger efficiencies increase with increasing $P^{\mu}_{T,reco}$. In order for the unfolding method to work, the smearing matrix must accurately reflect the smearing that occurs in the data. A $P^{\mu}_{T,reco}$ dependent efficiency can alter the smearing matrix, because it biases the measured bins. This type of dependence changes the likelihood that a causal event will be seen in any particular measured bin.

These inefficiencies can be taken into account by properly building the smearing matrix. The data in this analysis was required to pass a dimuon trigger: MU_2_LOW or MU_2_CENT. Therefore, when using Monte Carlo events to build the smearing matrix, it is required that each of the Monte Carlo events pass either MU_2_LOW, MU_2_CENT, or MU_1_LOW. MU_1_LOW is included because it was found that it increased the number of events passing the trigger requirement without altering $P(E_j \mid C_i)$. This effectively builds into the smearing matrix knowledge of the trigger biases.

### 8.2.3 Multi-Variable Unfolding

The unfolding is further complicated by the fact that more than one variable be must simultaneously unfolded. In this analysis, we wish to plot the cross section as a function of $P^{\mu}_{T}$(leading) and $\Delta\varphi_{\mu\mu}$; therefore, both variables must be unfolded. In addition, the $P_T$ of the trailing muon and the invariant mass of the dimuon pair must be unfolded, because it is possible to gain or lose events depending upon how the these variables unfold.

| Bin Number | $P_T^\mu$(leading) (GeV/c) | | $P_T^\mu$(Trailing) (GeV/c) | | $M_{\mu\mu}$ (GeV/c$^2$) |
|---|---|---|---|---|---|
| 1 | 4-5 | and | 4-25 | and | 6-35 |
| 2 | 5-7 | and | 4-25 | and | 6-35 |
| 3 | 7-10 | and | 4-25 | and | 6-35 |
| 4 | 10-15 | and | 4-25 | and | 6-35 |
| 5 | 15-25 | and | 4-25 | and | 6-35 |
| 6 | 3-4 | or | 3-4 | or | 5-6 |
| 7 | 25-40 | or | 25-40 | or | 35-50 |
| 8 | Events failing a mixture of cuts.[1] | | | | |

Table 8-1: This table describes the definitions of the bins used for the $P_T^\mu$ distribution. After the unfolding is complete, only bins one through five will be kept. The remaining bins are used only during the unfolding so that events can migrate into (out of) the bins of interest.

The binning chosen for this analysis is shown in Table 8-1 for the $P_T^\mu$ spectrum and in Table 8-2 for the $\Delta\varphi_{\mu\mu}$ spectrum. This same binning is used in both the measured and the unfolded distributions. In general, one does not have to use the same binning in the two distributions, but for the sake of simplicity the same binning is used here.

Notice that the $P_T^\mu$ bins 3-4 GeV/c and 25-40 GeV/c, and the invariant mass bins 5-6 GeV/c$^2$ and 35-50 GeV/c$^2$ are included. In the end, the cross sections will be reported only for $4 < P_T^\mu < 25$ GeV/c and $6 < M_{\mu\mu} < 35$ GeV/c$^2$. Therefore, bins 6–8 in Table 8-1 and bins 10–12 in Table 8-2 are discarded after the unfolding is complete.

[1]Events in this bin satisfy the conditions given both by bins 6 and 7. As an example, an event with $P_T^\mu$(leading)$>$ 25 GeV/c and $P_T^\mu$(Trailing)$<$ 4 GeV/c would be placed into this bin. Very few events satisfy this condition.

[2]Events in this bin satisfy the conditions given by both bins 10 and 11.

| Bin Number | $\Delta\varphi_{\mu\mu}$ (Degrees) | | $P_T^{\mu}$(leading) (GeV/c) | | $P_T^{\mu}$(Trailing) (GeV/c) | | $M_{\mu\mu}$ (GeV/c$^2$) |
|---|---|---|---|---|---|---|---|
| 1 | 0-20 | and | 4-25 | and | 4-25 | and | 6-35 |
| 2 | 20-40 | and | 4-25 | and | 4-25 | and | 6-35 |
| 3 | 40-60 | and | 4-25 | and | 4-25 | and | 6-35 |
| 4 | 60-80 | and | 4-25 | and | 4-25 | and | 6-35 |
| 5 | 80-100 | and | 4-25 | and | 4-25 | and | 6-35 |
| 6 | 100-120 | and | 4-25 | and | 4-25 | and | 6-35 |
| 7 | 120-140 | and | 4-25 | and | 4-25 | and | 6-35 |
| 8 | 140-160 | and | 4-25 | and | 4-25 | and | 6-35 |
| 9 | 160-180 | and | 4-25 | and | 4-25 | and | 6-35 |
| 10 | 0-180 | and | 3-4 | or | 3-4 | or | 5-6 |
| 11 | 0-180 | and | 25-40 | or | 25-40 | or | 35-50 |
| 12 | Events failing a mixture of cuts.[2] | | | | | | |

Table 8-2: This table describes the definitions of the bins used for the $\Delta\varphi_{\mu\mu}$ distribution. After the unfolding is complete, only bins one through nine will be kept. The remaining bins are used only during the unfolding so that events can migrate into (out of) the bins of interest.

## 8.3 Testing the Unfolding

It is important to test the unfolding method as this gives us confidence that the method is working. These tests also give us a measure of the systematic uncertainties associated with the unfolding. Processed Monte Carlo (Section 5.2) was used for all of the subsequent tests. The Monte Carlo includes events from both the $b\overline{b} \rightarrow \mu\mu X$, $c\bar{c} \rightarrow \mu\mu X$, and 'prompt plus decay' ISAJET Monte Carlo samples (see Section 5.2.2). All of these samples may be used because the momentum smearing effects are independent of the physics process that produce the muon tracks. Further, this method is independent of the shape of the Monte Carlo input distribution, so the two samples, which may have slightly different shapes, can both be used. To test the effectiveness

of this method, one simply attempts to unfold the Monte Carlo smeared distribution to see if the unfolding method recovers the original input distribution.

### 8.3.1 Different Initial Guesses

As mentioned, an initial guess of the shape of the unfolded spectrum, $p_\circ(C_i)$, must be supplied. Each iteration of the method improves the $p(C_i)$ values until the 'correct' (or unfolded) values are converged upon. D'Agostini has shown [65] that his method is independent of the initial choice for $p(C_i)$. However, the statistics of the Monte Carlo samples that he used are much larger than the ones available for this analysis; therefore, it is important to verify that the method is still $p_\circ(C_i)$ independent.

When unfolding data, the best guess for the $p_\circ(C_i)$ values is given by the Monte Carlo input distribution:

$$P_\circ(C_i) = \frac{C_i}{\sum_{j=1}^{n} C_j}, \tag{8.2}$$

where $C_i$ represents the number of events falling into the i$^{th}$ bin in the input distribution, and the sum is over all of the bins listed in Tables 8-1 and 8-2. This represents our best guess of the shape of the real distribution. The results of the unfolding, using Eq. 8.2 as the initial guess, can be seen in Fig. 8-2. In this case the method converges in just one iteration, and the unfolded distribution perfectly reproduces the input distribution. However, this is expected, because the correct answer (Eq. 8.2) was supplied from the start.

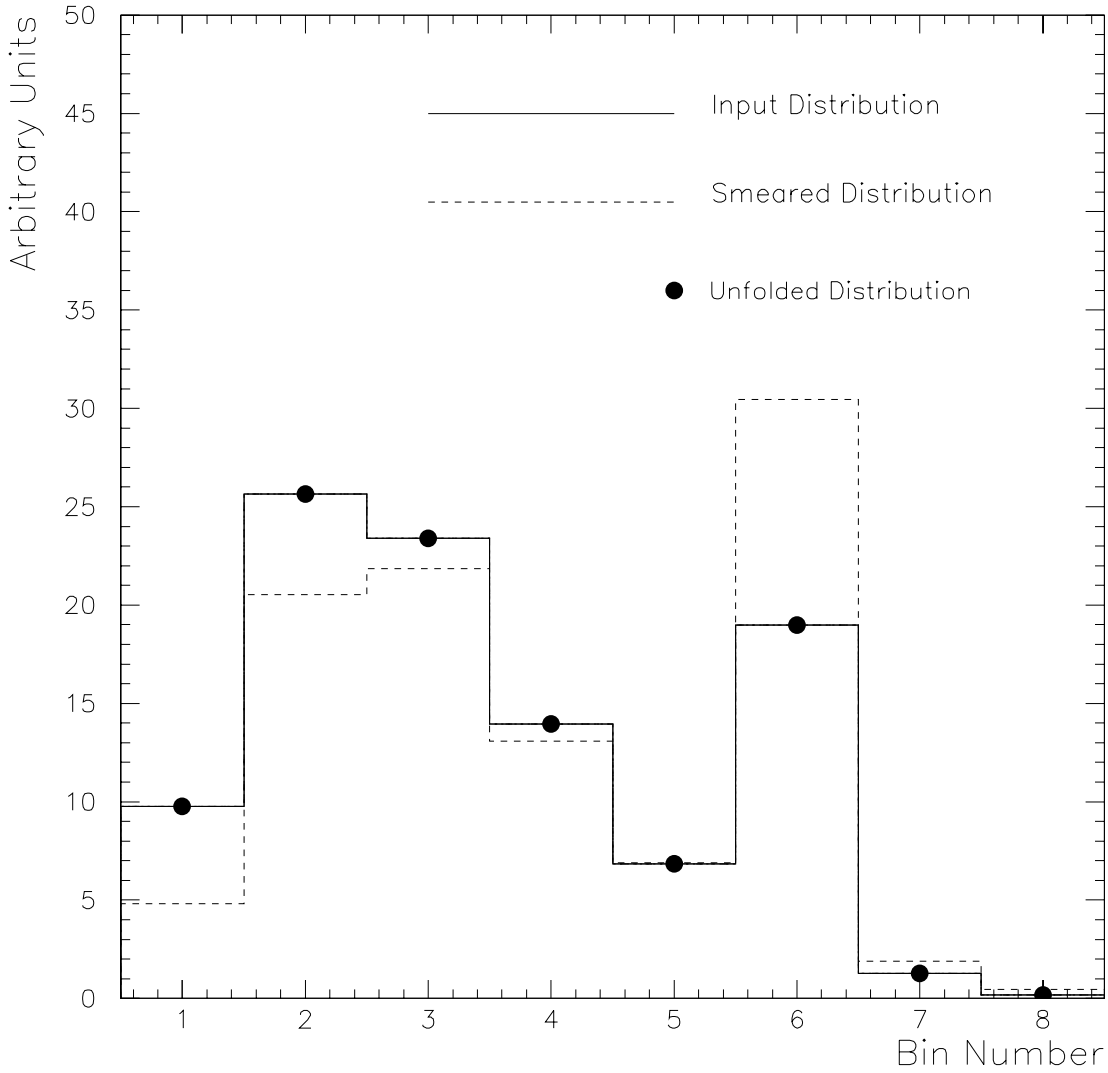


Figure 8-2: The Monte Carlo input (solid line) and smeared (dashed line) distributions are plotted according to the binning defined in Table 8-1. The unfolded spectrum (dark circles) exactly reproduces the original input distribution.

A more strenuous test of the unfolding method can be made by choosing $P_\circ(C_i) = 1/n$, where $n$ is the total number of bins. This initial guess assumes total ignorance of the shape of the real spectrum and assigns equal probabilities to each of the bins. The results of unfolding the smeared Monte Carlo distribution using this initial guess can be seen in Fig. 8-3. Here, the unfolded spectrum does not accurately reproduce the input distribution. This implies that the available Monte Carlo statistics cannot support such an unrealistic $p_\circ(C_i)$. If the $p_\circ(C_i)$ is very different than the true distribution, it takes many iterations ($\sim 200$) before the method converges. Excessive iterations tend to magnify the statistical fluctuations present in the Monte Carlo and data [65]. In this example, the method fails because of the limited Monte Carlo statistics used in creating the smearing matrix. Therefore, it is important that one choose reasonable values for $p_\circ(C_i)$.

### 8.3.2 Shape Independence

It has been shown that not all $p_\circ(C_i)$ can be used. Instead, a reasonable guess for $p_\circ(C_i)$ must be chosen. It then becomes necessary to show that this choice for $p_\circ(C_i)$ works well regardless of the shape of the distribution being unfolded. As mentioned above, the Monte Carlo input distribution is our best estimate of the true distribution. Therefore, Eq. 8.2 will be used for $p_\circ(C_i)$. The effectiveness of this choice can be demonstrated by attempting to unfold distorted Monte Carlo distributions. Weighting factors are applied to the Monte Carlo distorting shape of the distributions.

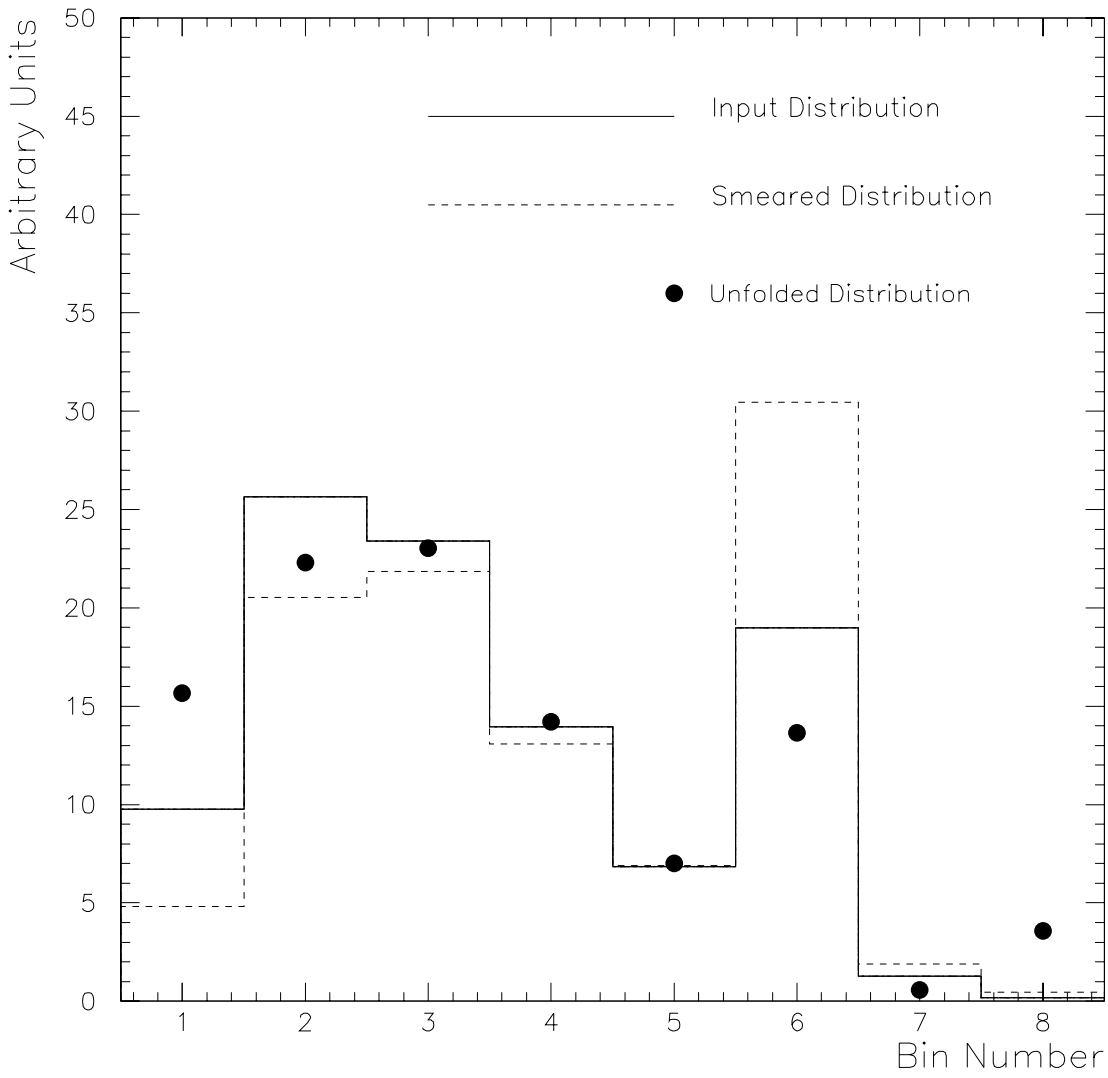


Figure 8-3: The Monte Carlo input (solid line) and smeared (dashed line) distributions are plotted according to the binning defined in Table 8-1. The unfolded spectrum (dark circles) does not accurately reproduce the original input distribution. A uniform $p_\circ(C_i)$ was chosen for this unfolding.

The unfolding method is then tested by attempting to unfold these new distributions.

Two different weighting factors were applied to the Monte Carlo. The first weighting factor is designed to make the input distribution fall less quickly with increasing $P_T^{\mu}$. This weighting factor was simply a straight line

$$Weight = 5\ \frac{\mathrm{c}}{\mathrm{GeV}} \times P_T^{\mu}(leading) \tag{8.3}$$

The second weighting factor is designed to make the input distribution more steep in $P_T^{\mu}$. In this case, the weight used is

$$Weight = -5\ \frac{\mathrm{c}}{\mathrm{GeV}} \times P_T^{\mu}(\mathrm{Leading}) + 130 \tag{8.4}$$

Both of the weighted input distributions were then unfolded. The results can be seen in Figures 8-4 and 8-5. In both cases the unfolded distributions are reasonably good reproductions of the weighted input distribution. These tests give us confidence that the unfolding method works even when the data has a different shape than the Monte Carlo.

The weighted Monte Carlo distributions were used to estimate the systematic uncertainty associated with the unfolding process. To do this, the relative error between the unfolded and input distributions was calculated. The relative errors in each bin were then averaged and found to be 7%. An average was taken because no clear $P_T^{\mu}$ or $\Delta\varphi_{\mu\mu}$ dependence could be found in the unfolding error. This 7% difference is then taken as the systematic error for the unfolding procedure employed in this analysis.

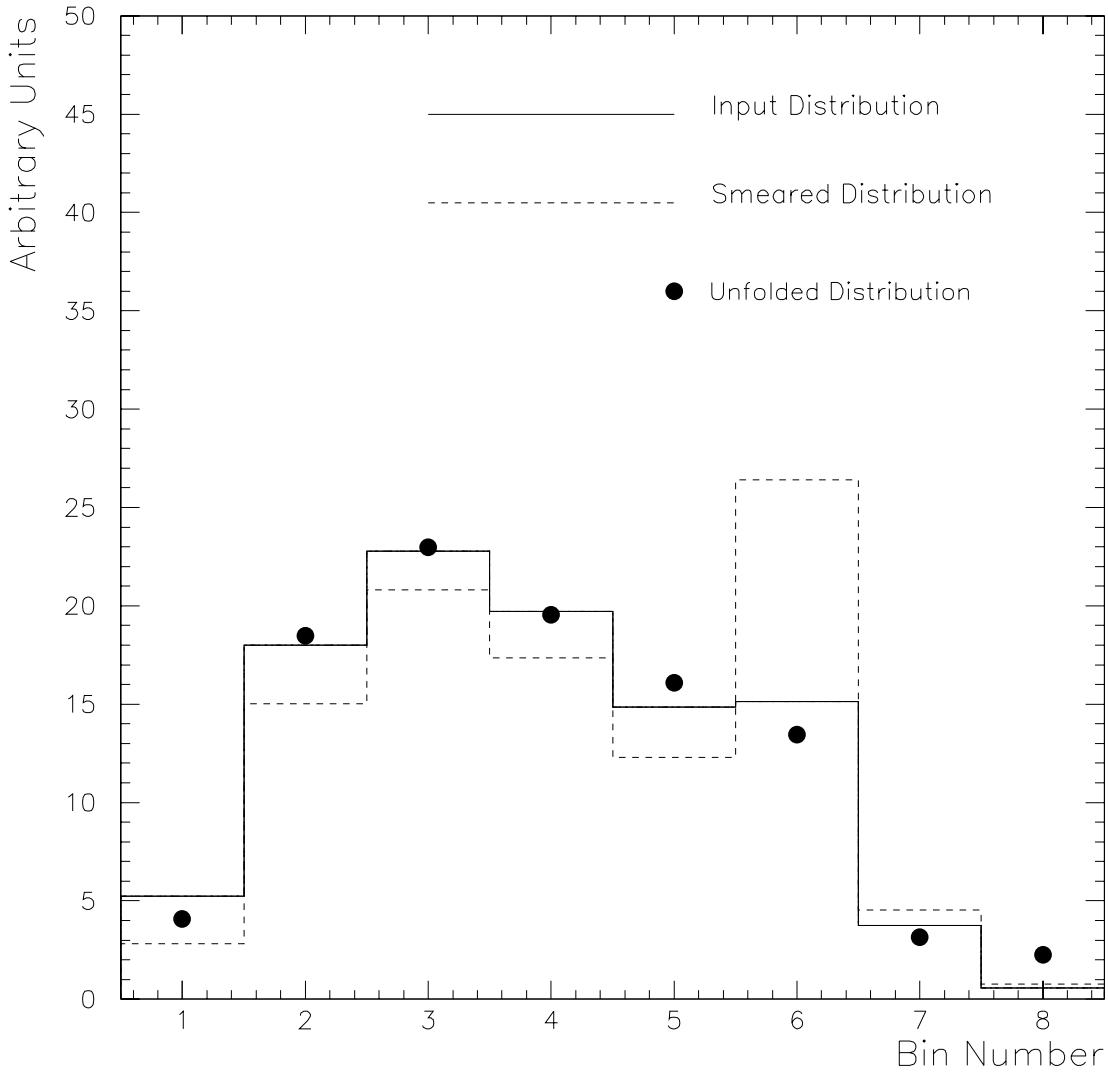


Figure 8-4: The Monte Carlo input (solid line) and smeared (dashed line) distributions are plotted according to the binning defined in Table 8-1. The unfolded spectrum (dark circles) reproduces the original input distribution reasonably well. In this test the input distributions was weighted by Eq. 8.3.

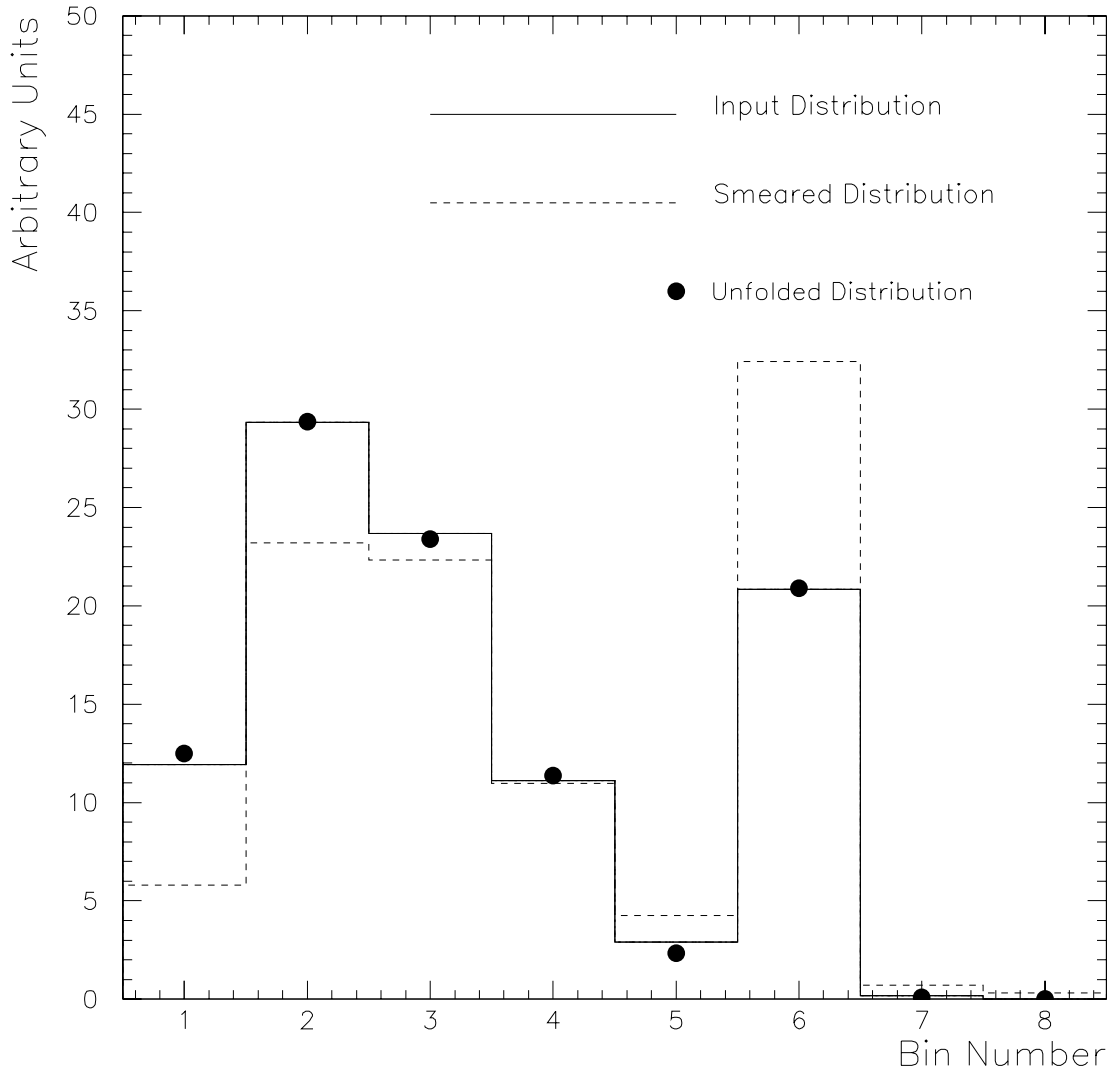


Figure 8-5: The Monte Carlo input (solid line) and smeared (dashed line) distributions are plotted according to the binning defined in Table 8-1. The unfolded spectrum (dark circles) reproduces the original input distribution reasonably well. In this test the input distributions was weighted by Eq. 8.4.

## 8.4 Unfolding the Data

At this point, the cosmic subtracted inclusive dimuon spectrum can be unfolded. Similarly, the $b\overline{b} \rightarrow \mu\mu X$ spectrum (Section 7.4) is also unfolded. After the unfolding is complete, bins six through eight in the $P_T^{\mu}$ distribution and bins ten through twelve in the $\Delta\varphi_{\mu\mu}$ distribution are discarded. The results are shown in Figures 8-6 and 8-7. In both figures the measured data is shown as histograms. The unfolded data points are plotted with error bars representing the 7% systematic uncertainty associated with the unfolding process.

An interesting feature in Figures 8-6 and 8-7 is bin 6 (10) in the $P_T^{\mu}$ ($\Delta\varphi_{\mu\mu}$) distributions. This bin shows the largest differences between the measured and unfolded distributions. This behavior was also observed when unfolding Monte Carlo test distributions (Figures. 8-2, 8-4, and 8-5). Events in this bin are those which fail one of the cuts $P_T^{\mu} < 4$ GeV/c or $M_{\mu\mu} < 6$ GeV/c$^2$. An excess of events in the measured spectrum implies that smearing effects are causing the reconstruction code to underestimate the $P_T$ and $M_{\mu\mu}$ values for events near the boundary $P_T^{\mu} = 4$ GeV/c and $M_{\mu\mu} = 6$ GeV/c$^2$.

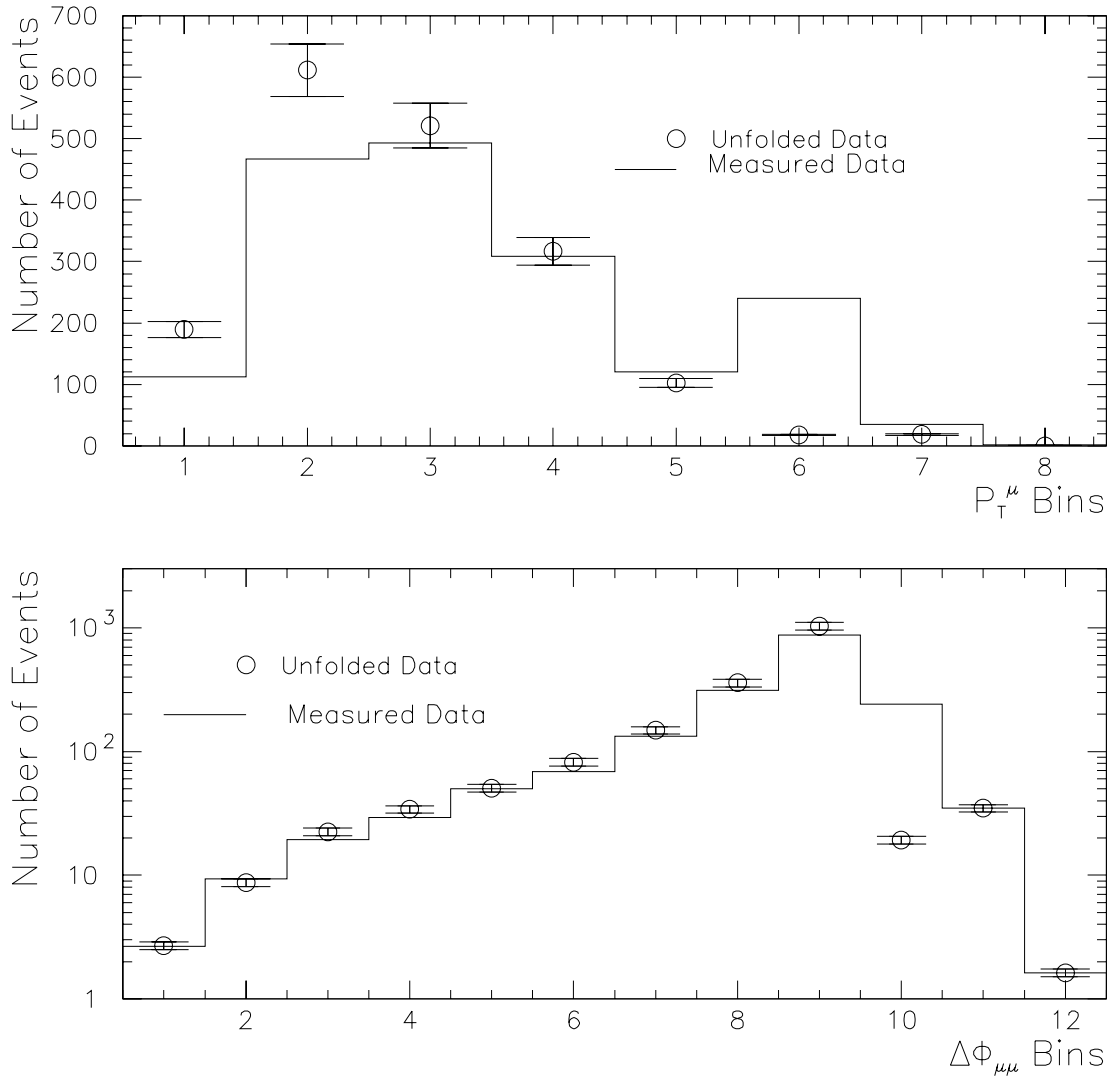


Figure 8-6: The measured and unfolded dimuon distributions. The errors shown represent the 7% systematic uncertainty associated with the unfolding.

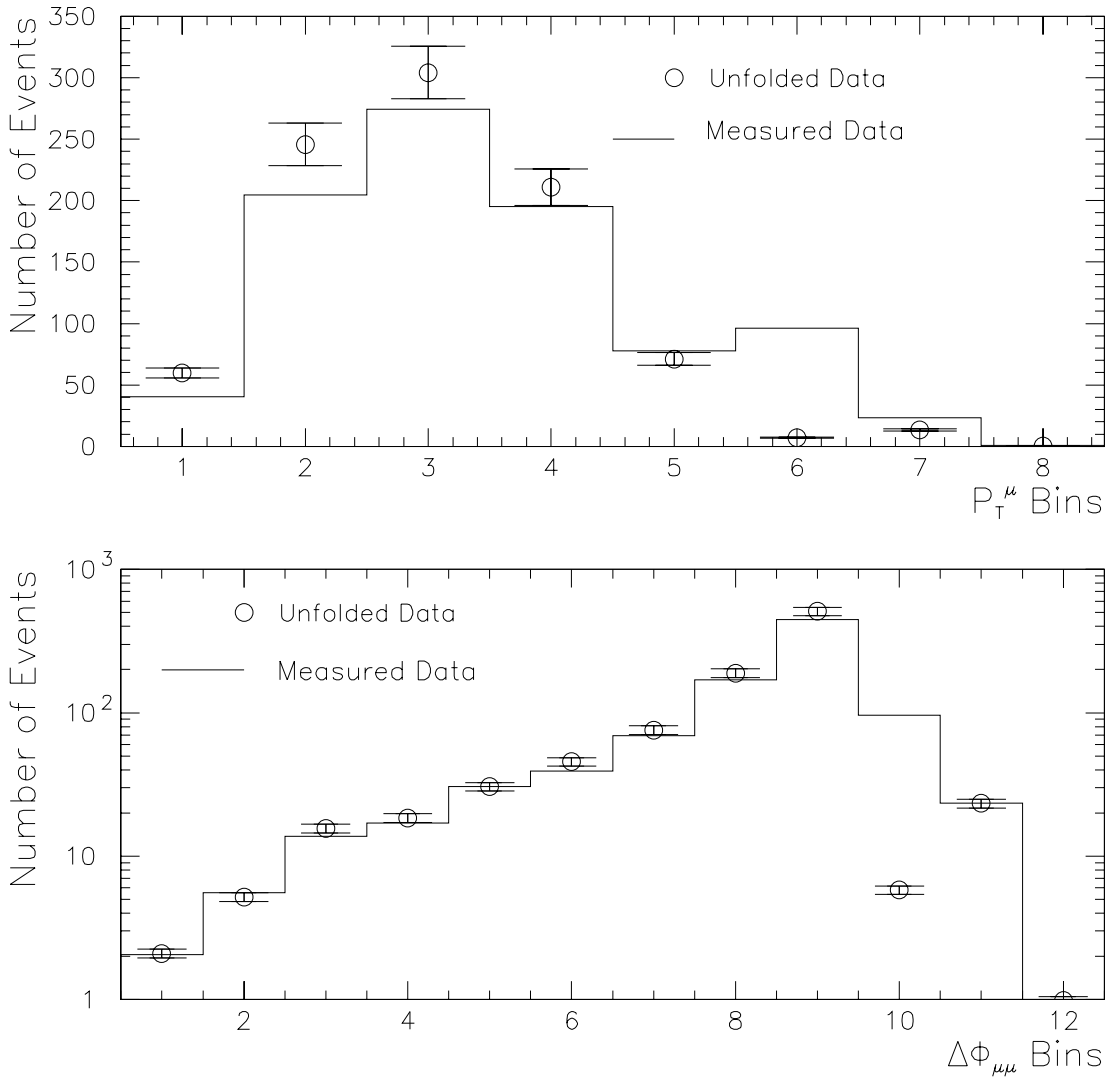


Figure 8-7: The measured and unfolded $b\bar{b} \rightarrow \mu\mu X$ distributions. The errors shown represent the 7% systematic uncertainty associated with the unfolding.

# Chapter 9

# Cross Sections and Correlations

## 9.1 Dimuon Production

The fundamental cross section in this analysis is the inclusive dimuon differential cross section. Since each muon is required to have an associated jet, this cross section measures dimuon production from processes which produce associated jets. These processes include $b\overline{b}$ and $c\overline{c}$ production, as well as events in which one or both muons are the products of a $\pi$ (or K) decay. Drell-Yan and $\Upsilon$ production is not expected to contribute to this cross section since these processes produce isolated dimuons. In addition, the cross section is only for dimuons which satisfy the following kinematic cuts:

- $4 \leq P_T^{\mu} \leq 25$ GeV/c (both muons)
- $|\eta_{\mu}| < 0.8$ (both muons)

- $6 < M_{\mu\mu} < 35$ GeV/c$^2$

The dimuon invariant mass cut excludes dimuon events produced by J/$\psi$ and $Z$, and greatly reduces contributions from sequential $b$-quark decays.

The differential cross sections are given by

$$\frac{d\sigma}{dP_T^\mu} = \frac{N - N_{cos}}{\epsilon_{Tot} \int \mathcal{L} dt \Delta P_T^\mu} \text{ and} \tag{9.1}$$

$$\frac{d\sigma}{d\Delta\varphi_{\mu\mu}} = \frac{N - N_{cos}}{\epsilon_{Tot} \int \mathcal{L} dt}, \tag{9.2}$$

where $\epsilon_{Tot}$ is the total efficiency for trigger and selection requirements, $\int \mathcal{L} dt$ is the total integrated luminosity for the sample, $N$ is the total number of unfolded events in each of the $P_T^\mu$ or $\Delta\varphi_{\mu\mu}$ bins, $N_{cos}$ is the cosmic ray contamination in each bin, and $\Delta P_T^\mu$ is the width of the $P_T^\mu$ bin. The $d\sigma/d\Delta\varphi_{\mu\mu}$ cross section is not divided by the $\Delta\varphi_{\mu\mu}$ bin widths, because this cross section is reported per 20° bins.

The background studies (described in Chapter 7) found the total cosmic contamination to be $12.3 \pm 0.5\%$ for the entire dimuon sample. This, in addition to the fractions given in Table 7-6, is used to calculate an event-by-event weighting factor, $w_{ij}$, which determines the probability that event $i$ was produced by process $j$. This weight is given by

$$w_{ij} = \frac{A_j \cdot \prod_{k=1}^{N_k} p_k^j(x_k^i)}{\sum_{l=1}^{N_j} \left[ A_l \cdot \prod_{k=1}^{N_k} p_k^l(x_k^i) \right]}. \tag{9.3}$$

$A_j$ is the fraction of process $j$ contained in the sample (taken from Table 7-6), and the $p_k^j(x_k^i)$ are the probability density functions described in Section 7.3. The number

of cosmics in each bin is calculated by

$$N_{cos} = \sum_{i=1}^{N_b} w_{i4}, \tag{9.4}$$

where process 4 is defined as cosmic ray dimuon production, and the summation is over the $N_b$ events in the bin of interest.

The data used in this analysis (Table 4-4) corresponds to a total integrated luminosity of 46.2 pb$^{-1}$. The trigger and selection cut requirements are given in Tables 4-5 and 4-6. The efficiency of the trigger requirements and selection cuts are described in Chapter 6 and are tabulated in Table 6-6. After cosmic ray subtraction, the data is unfolded with the methods described in Chapter 8.

The resulting cross sections are shown in Figures 9-1 and 9-2. For completeness, these cross sections are listed in Appendix B along with the inputs into the cross section calculations. The ISAJET predictions for $b\overline{b}$, $c\overline{c}$, and prompt plus decay production are also shown in these figures. As described in Section 5.2.1, the ISAJET cross sections for $b\overline{b}$ and $c\overline{c}$ production have been separately normalized to the NLO QCD predictions of Nason *et al.*. In both the $d\sigma/dP_T^{\mu}$ and $d\sigma/d\Delta\varphi_{\mu\mu}$ measurements, the ISAJET predictions lie below the data. There is good agreement with the shape of the ISAJET and data $P_T^{\mu}$ distributions; however the shape of the two $\Delta\varphi_{\mu\mu}$ distributions clearly disagree.

The systematic errors for the inclusive dimuon cross section are listed in Table 9-1. The methods by which these errors are estimated are given in Chapters 6, 7, and 8.

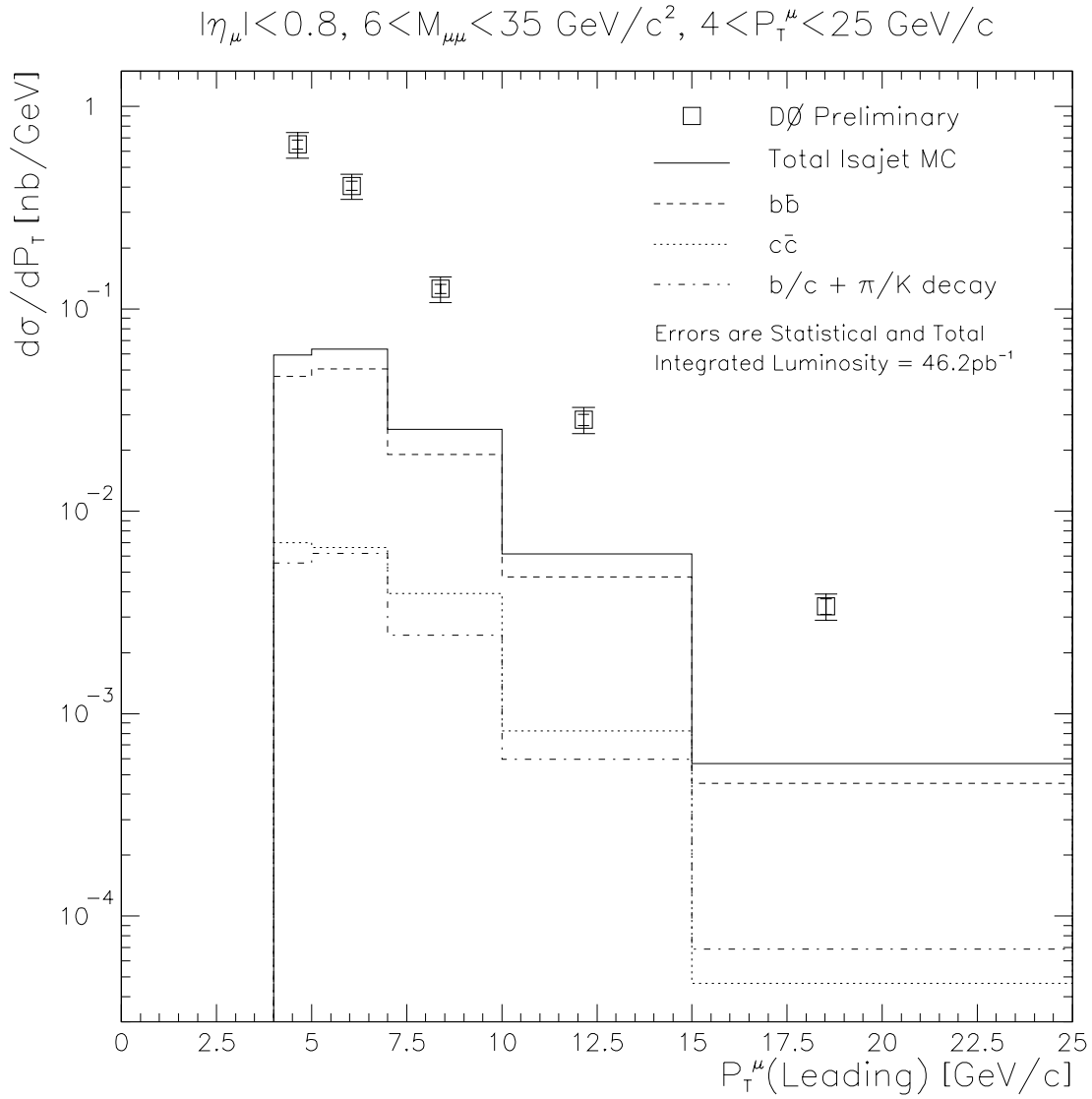


Figure 9-1: The measured inclusive dimuon differential cross section as a function of $P_T^\mu$. Also shown are the ISAJET predictions for $b\overline{b}$, $c\overline{c}$, and prompt plus $\pi$/K decay.

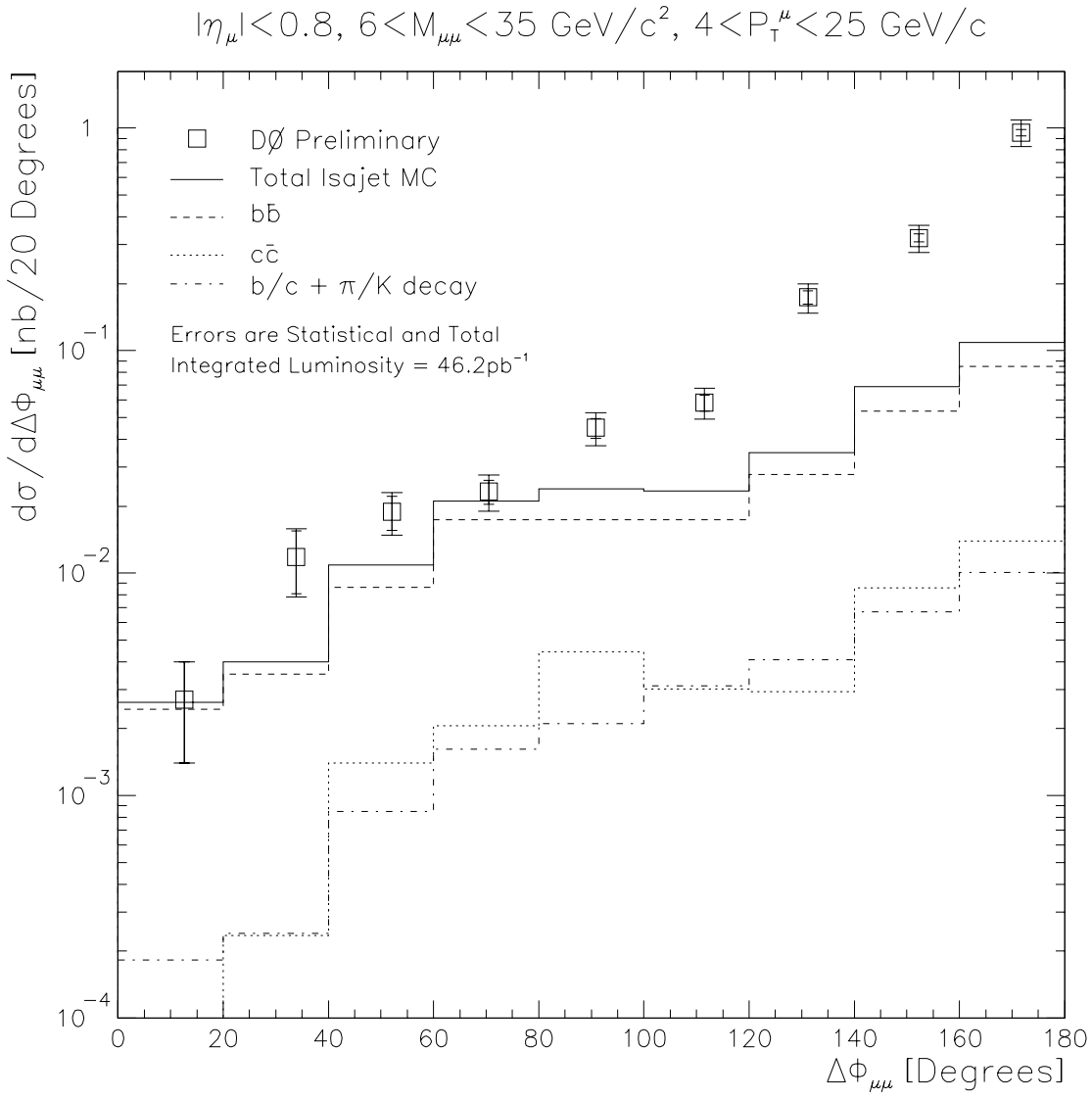


Figure 9-2: The measured inclusive dimuon differential cross section as a function of $\Delta\varphi_{\mu\mu}$. Also shown are the ISAJET predictions for $b\overline{b}$, $c\overline{c}$, and prompt plus $\pi$/K decay.

| Source | Relative Uncertainty $(d\sigma/dP_T^\mu)$ | $(d\sigma/d\Delta\varphi_{\mu\mu})$ |
|---|---|---|
| Cosmic Subtraction | 0.5% | 0.5% |
| Momentum Resolution | 10% | 10% |
| Efficiencies | 8-15% | 9-46% |
| Integrated Luminosity | 5% | 5% |
| Unfolding | 7% | 7% |
| Total [1] | 14-15% | 14-48% |

Table 9-1: The systematic uncertainties associated with measurement of the inclusive dimuon differential cross section. A range of values is given whenever an efficiency varies as a function of $P_T^\mu$ or $\Delta\varphi_{\mu\mu}$.

Only the systematic errors for the trigger and associated jet requirements are $P_T^\mu$ dependent. All other systematic errors are independent of $P_T^\mu$ and $\Delta\varphi_{\mu\mu}$. The outer error bars in Figures 9-1 and 9-2 show the total error which is the systematic and statistical uncertainties added in quadrature.

## 9.2 $b\overline{b} \to \mu\mu X$ Production

The methods used to obtain the $b\overline{b} \to \mu\mu X$ differential cross sections are very similar to those used to find the inclusive dimuon cross sections. In addition to subtracting the cosmic ray background from the sample, the $b\overline{b} \to \mu\mu X$ cross section requires that the events be weighted by the $b$-quark fraction, $f_b$. This fraction gives the probability that a dimuon event is produced by a $b\overline{b}$ quark pair.

[1] The total systematic uncertainty is calculated in several steps. First, the maximum likelihood fitting and PDF uncertainties are propagated through the unfolding matrix. Next, the efficiency, and integrated luminosity errors are propagated through Equations 9.1 and 9.2. The remaining uncertainties are then added in quadrature.

### 9.2.1 $b$-quark Fraction

It is useful to compare the measured $b$-quark fraction, obtained from the maximum likelihood fit, with the ISAJET prediction for $f_b$.

#### $f_b$ from ISAJET

The ISAJET Monte Carlo samples used to calculate $f_b$ are described in Chapter 5. Each has been processed with MU_SMEAR, VMS_FILTER, and the full DØ reconstruction program. The $b\overline{b}$ and $c\overline{c}$ cross sections are normalized to the prediction of Nason *et al.* (see Section 5.2.1). The fraction $f_b$ is determined by

$$f_b = \frac{\sigma_{b\overline{b}}}{\sigma_{b\overline{b}} + \sigma_{c\overline{c}} + \sigma_{Decay}}, \tag{9.5}$$

where $\sigma_{b\overline{b}}$, $\sigma_{c\overline{c}}$, and $\sigma_{Decay}$ are the binned cross sections for $b\overline{b}$, $c\overline{c}$, and prompt plus decay production respectively. The resulting $b$-quark fraction is shown in Fig. 9-3.

#### $f_b$ from Data

The weighting factors described in Equation 9.3 are again used to calculate the $b$-quark fraction. In this case, $f_b$ is determined by

$$f_b = \frac{\sum_{i=1}^{N} w_{i1}}{\sum_{j=1}^{N_{p-1}} \sum_{i=1}^{N} w_{ij}}, \tag{9.6}$$

where process 1 is defined as $b\overline{b}$ production, $N$ is the number of events, and $N_{p-1}$ are the number of processes excluding cosmic rays. Cosmic ray muons are not included in this calculation so that comparisons can be made with the Monte Carlo $f_b$ prediction.

The results of this calculation are plotted in Fig. 9-3. Within the statistics shown, the $b$-quark fraction extracted from data agrees with the predictions given by ISAJET Monte Carlo.

The $b$-quark fraction shown in Fig. 9-3 cannot be used with the dimuon data sample to calculate the $b\overline{b} \to \mu\mu X$ cross section because it ignores cosmic ray muons. Instead, this $b$-quark fraction is used only for comparison with Monte Carlo. This calculation is also useful in that it gives a measure of the $b$-quark content with respect to other physics processes.

When calculating the $b\overline{b} \to \mu\mu X$ cross section, one must measure an $f_b$ defined as

$$f_b = \frac{\sum_{i=1}^{N} w_{i1}}{\sum_{j=1}^{N_p} \sum_{i=1}^{N} w_{ij}}. \tag{9.7}$$

Here, the denominator includes all processes which produce dimuons including fake dimuon events produced by cosmic ray muons. The resulting $f_b$ is shown in Fig. 9-4.

### 9.2.2 $b\overline{b} \to \mu\mu X$ Cross Section

The $b\overline{b} \to \mu\mu X$ differential cross section is found by

$$\frac{d\sigma}{dP_T^{\mu}} = \frac{N_b}{\epsilon_{Tot} \int \mathcal{L} dt \Delta P_T^{\mu}}. \tag{9.8}$$

$$\frac{d\sigma}{d\Delta\varphi_{\mu\mu}} = \frac{N_b}{\epsilon_{Tot} \int \mathcal{L} dt}, \tag{9.9}$$

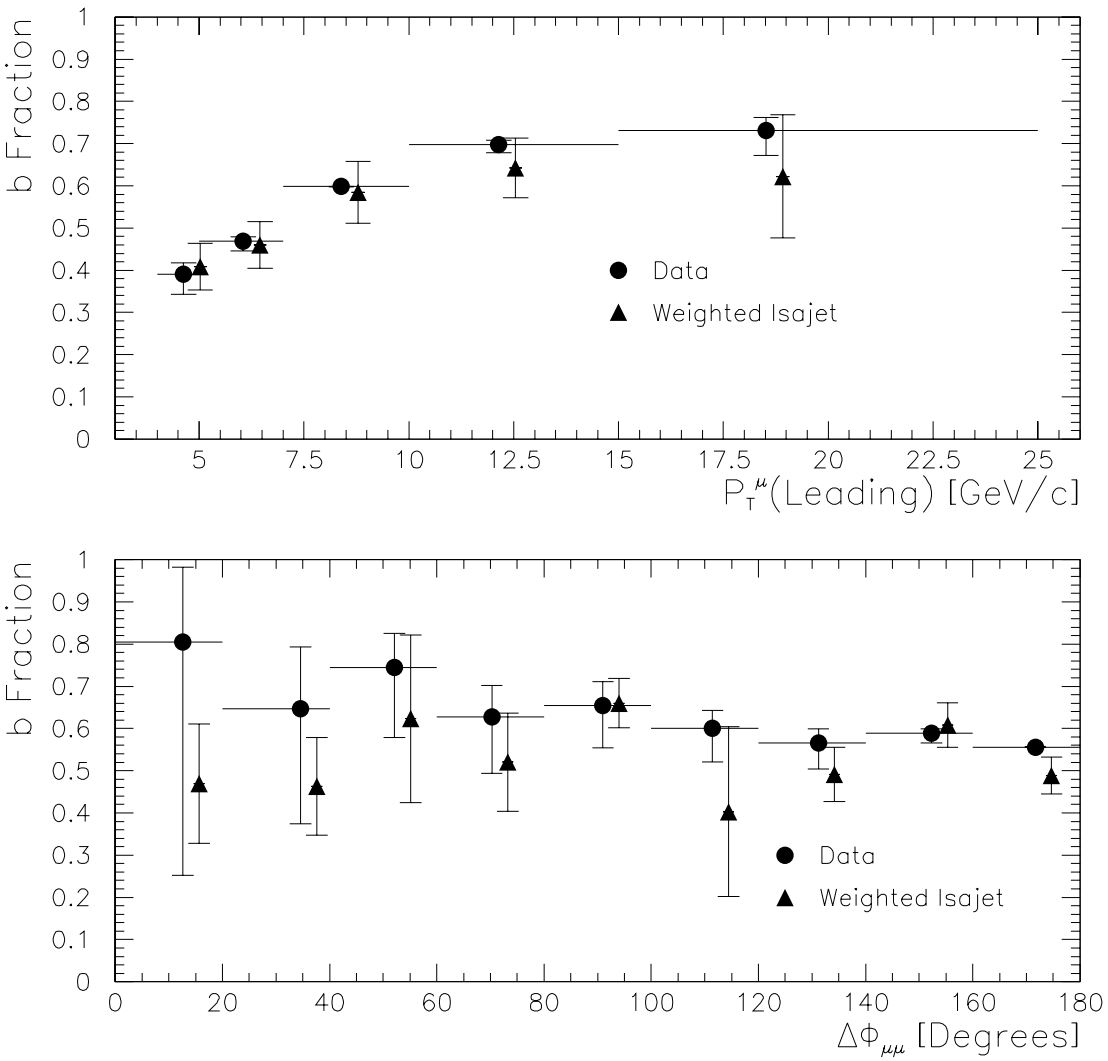


Figure 9-3: The $b$-quark content of the dimuon sample. The results from the maximum likelihood fit are shown along with the prediction given by ISAJET Monte Carlo. For clarity, the data and Monte Carlo have been offset from each other.

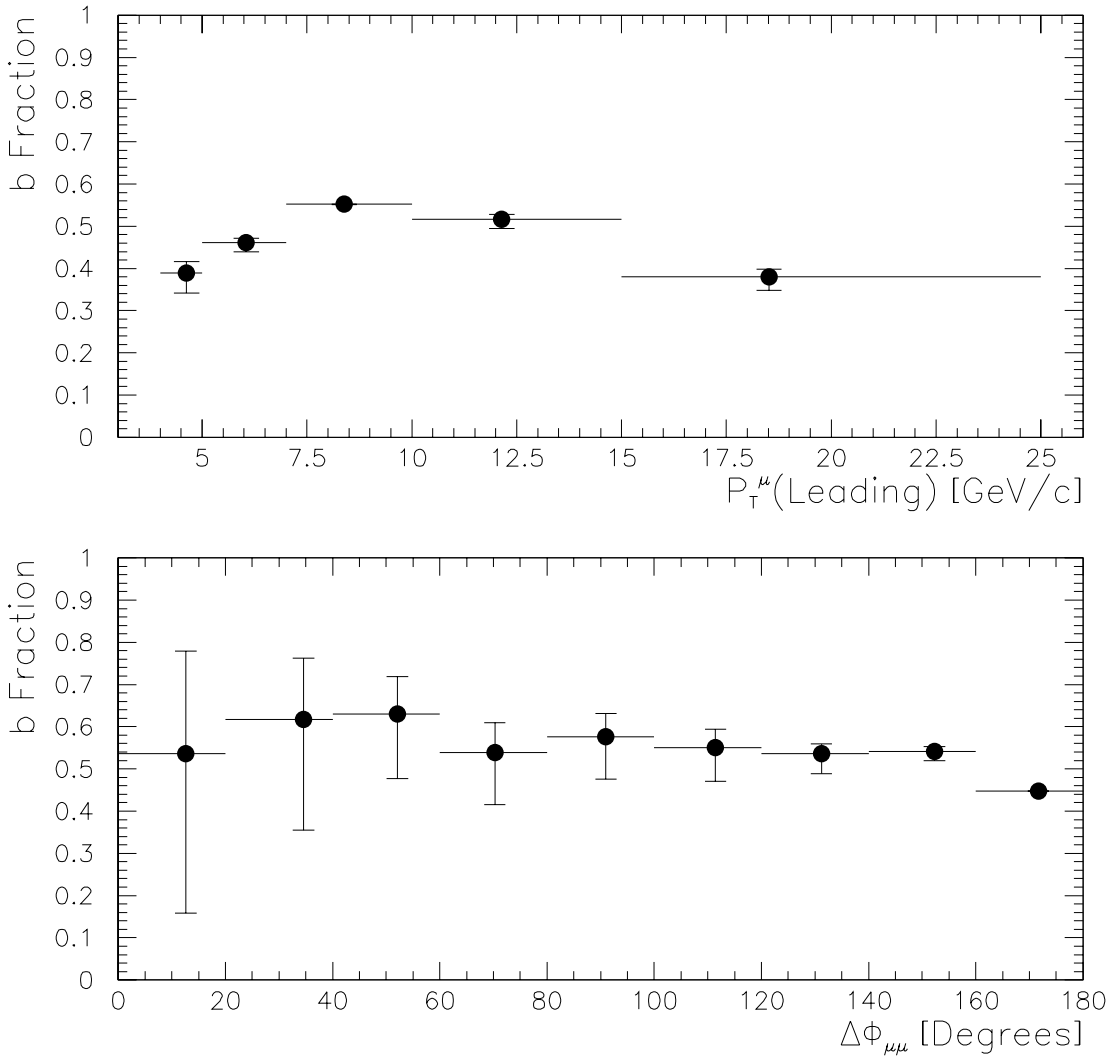


Figure 9-4: The $b$-quark fraction of the dimuon data sample. $f_b$ is calculated through Equation 9.7. This definition of $f_b$ includes cosmic ray events.

| Source | Relative Uncertainty $(d\sigma/dP_T^\mu)$ | $(d\sigma/d\Delta\varphi_{\mu\mu})$ |
|---|---|---|
| Likelihood fit | 0.5% | 0.5% |
| PDF Uncertainty | 12% | 10% |
| Momentum Resolution | 10% | 10% |
| Efficiencies | 8-15% | 9-46% |
| Integrated Luminosity | 5% | 5% |
| Unfolding | 7% | 7% |
| Total | 19-21% | 17-48% |

Table 9-2: The systematic uncertainties associated with measurement of the $b\overline{b} \to \mu\mu X$ differential cross section. A range of values is given whenever an efficiency varies as a function of $P_T^\mu$ or $\Delta\varphi_{\mu\mu}$.

where $N_b$ are the number of dimuon events per bin weighted by the $b$-quark fraction, Eq. 9.3.

The resulting inclusive $b\overline{b} \to \mu\mu X$ cross section is shown in Fig. 9-5. Also shown is the theoretical prediction given by HVQJET (Section 2.3.2). The results of the cross section calculation, as well as the inputs into the calculation, are tabulated in Appendix B. The systematic uncertainties associated with this calculation are listed in Table 9-2.

### 9.2.3 Inclusive $b$-quark Production Cross Section

Several factors must be taken into account before the integrated $b$-quark cross section, as a function of $b$-quark $P_T$, can be extracted from the differential $b\overline{b} \to \mu\mu X$ cross section. The kinematic cuts on the muons must be removed and the branching ratios must be taken into account. In addition, the $b$-quark kinematics, fragmentation, and

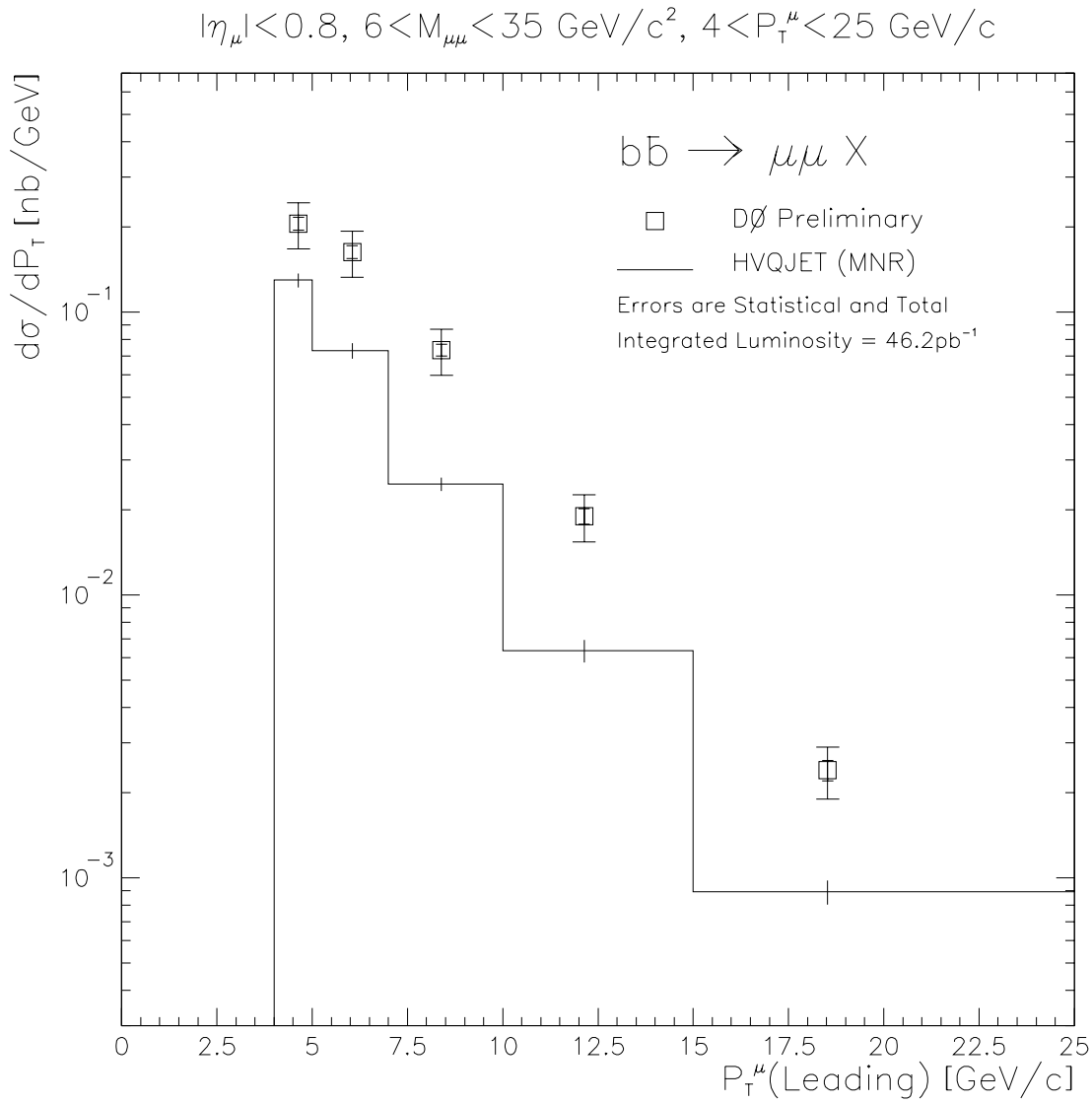


Figure 9-5: The $b\overline{b} \rightarrow \mu\mu X$ differential cross section as a function of $P_T^\mu$. Also shown is the prediction given by the HVQJET event generator (Section 2.3.2).

eventual decay of the quarks into muons must be modeled. A method for doing this was developed by UA1 [66, 67] and was subsequently used by CDF [68] and DØ [69]. This method will be used here and is described below.

Figure 9-6 is an illustration of how this method works. Monte Carlo samples are used to model $p\overline{p} \to \mu\mu X$ and $b\overline{b} \to \mu\mu X$ production as a function of $b$-quark $P_T$. The upper plot in Fig. 9-6 is the $p\overline{p} \to bX$ differential cross section. Here, all kinematic cuts have been removed with the exception of a requirement on the $b$-quark rapidity, $|y_b| < 1$. The lower plot in Fig. 9-6 is the $b\overline{b} \to \mu\mu X$ cross section prediction. In this cross section, the same muon kinematic cuts that were applied in the data analysis are applied to the $b\overline{b} \to \mu\mu X$ Monte Carlo sample. These kinematic cuts are

- $4 < P_T^{\mu} < 25$ GeV/c (Both Muons)
- $|\eta_{\mu}| < 0.8$ (Both Muons)
- $6 < M_{\mu\mu} < 35$ GeV/c$^2$

In this sample, no kinematic cuts are applied to the $b$-quarks. In this analysis, the NLO QCD theory of Mangano *et al.* is used to create the $p\overline{p} \to bX$ spectrum, while HVQJET is used to create the $b\overline{b} \to \mu\mu X$ distribution.

Since the transverse momentum of the muon is generally less than the transverse momentum of the parent $b$-quark, the muon kinematic cuts effectively impose a transverse momentum threshold on the accepted $b$-quark's. Therefore, it is useful to define some minimum $b$-quark transverse momentum, $P_T^{min}$, and report the integrated cross

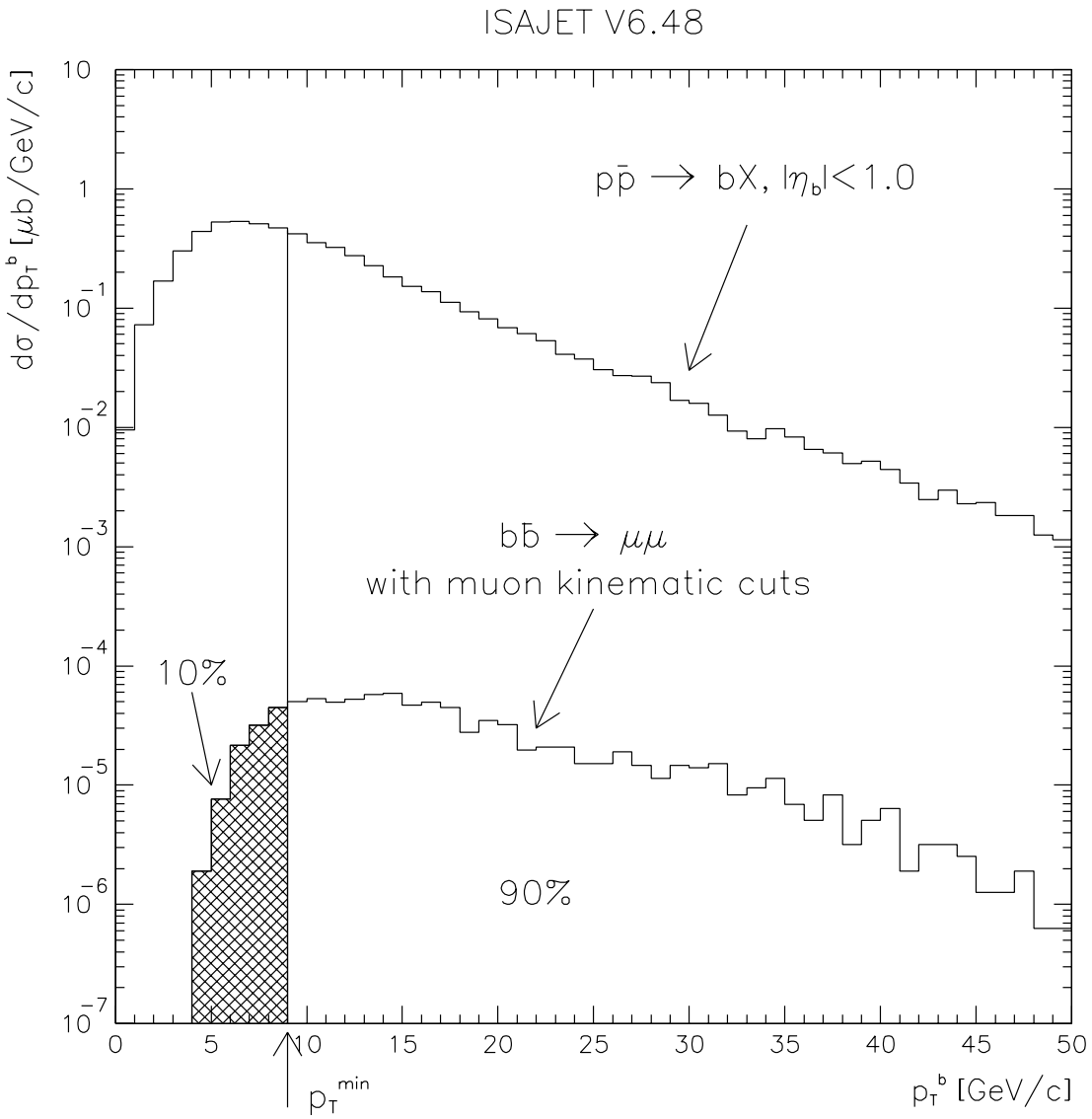


Figure 9-6: An illustration showing the Monte Carlo samples used to extract the $b$-quark production cross section. The upper curve is the $p\overline{p} \to bX$ cross section and the lower curve is the $b\overline{b} \to \mu\mu X$ cross section with muon kinematic cuts. The definition of $P_T^{min}$ is also shown.

section for all $P_T^b > P_T^{min}$. The variable $P_T^{min}$ is defined as the value of $P_T^b$ such that 90% of the Monte Carlo $b\overline{b} \to \mu\mu X$ cross section lies above this value

$$\int_{P_T^{min}}^{\infty} \frac{d\sigma_{b\overline{b}\to\mu\mu X}}{dP_T^b} dP_T^b \equiv (0.9)\sigma_{tot}, \tag{9.10}$$

where $d\sigma_{b\overline{b}\to\mu\mu X}/dP_T^b$ is the $b\overline{b} \to \mu\mu X$ differential cross section represented by the bottom curve in Fig. 9-6, and $\sigma_{tot}$ is the total $b\overline{b} \to \mu\mu X$ integrated cross section.

The integrated inclusive $b$-quark cross section is given by

$$\sigma_b(P_T^b > P_T^{min}, |y^b| < 1.0) = \sigma^{Data}_{b\overline{b}\to\mu\mu X} \cdot \frac{\sigma_b^{MC}}{\sigma^{MC}_{b\overline{b}\to\mu\mu X}}, \tag{9.11}$$

where $\sigma^{Data}_{b\overline{b}\to\mu\mu X}$ is the measured integrated $b\overline{b} \to \mu\mu X$ cross section, $\sigma_b^{MC}$ is the integrated $p\overline{p} \to bX$ cross section for $P_T^b > P_T^{min}$ from Monte Carlo, and $\sigma^{MC}_{b\overline{b}\to\mu\mu X}$ is the integrated cross section for $b\overline{b} \to \mu\mu X$ from Monte Carlo. This calculation is performed at several $P_T^{min}$ values. This is accomplished by altering the $P_T^{\mu}$(leading) cut in both $\sigma^{MC}_{b\overline{b}\to\mu\mu}$ and $\sigma^{Data}_{b\overline{b}\to\mu\mu}$. The results of these calculations are given in Table 9-3 and are plotted in Fig. 9-7. The measured cross section is plotted along with the NLO QCD prediction of Nason *et al.* [4]. The details of the generation of the theoretical curve and its uncertainties are given in Section 2.3.1.

There are several systematic errors which must be taken into consideration. The first is the systematic error associated with the measurement of the $b\overline{b} \to \mu\mu X$ cross section (Table 9-2). Additional uncertainties are due to the method used to extract the integrated inclusive $b$-quark cross section. This includes the uncertainty associated with the $b$-quark fragmentation. This uncertainty is estimated by varying the Peterson

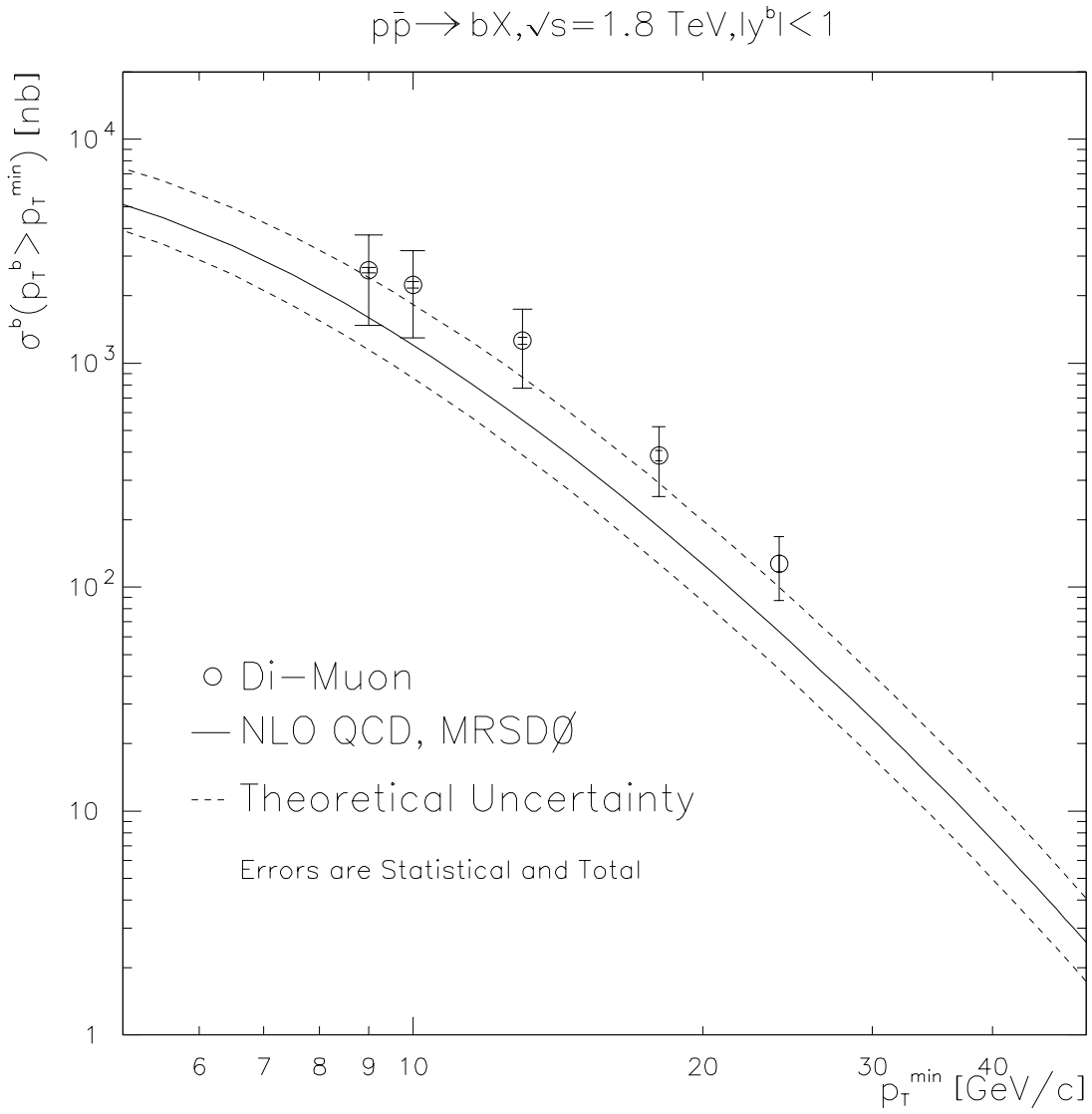


Figure 9-7: The integrated $b$-quark production cross section shown at various $P_T^{min}$. The theoretical curve is from NLO QCD theory (see Section 2.3.1).

| $P_T^{\mu_1}$ GeV/c | $P_T^{\mu_2}$ GeV/c | $P_T^{min}$ Gev/c | $\sigma_b(P_T^b > P_T^{min}, \|y^b\| < 1.0)$ $\mu$b |
|---|---|---|---|
| 4 | 4 | 9.0 | $2.61 \pm 1.13$ |
| 5 | 4 | 10.0 | $2.24 \pm 0.94$ |
| 7 | 4 | 13.0 | $1.26 \pm 0.49$ |
| 10 | 4 | 18.0 | $0.39 \pm 0.13$ |
| 15 | 4 | 24.0 | $0.13 \pm 0.04$ |

Table 9-3: Results of the $b$-quark production cross section measurement.

| Source | Relative Uncertainty |
|---|---|
| Fragmentation Parameterization (14%) | 20% |
| BR($b \to \mu X$) (3.5%) | 5% |
| Muon spectrum, $b \to \mu X$ (8%) | 11% |

Table 9-4: The systematic errors associated with the calculation of the $p\overline{p} \to bX$ cross section.

parameter by 50% and recalculating the ratio $\frac{\sigma_b^{MC}}{\sigma_{b\overline{b}\to\mu\mu X}^{MC}}$. This ratio changes by 14% for each muon [69]. Another uncertainty arises from the error in the inclusive branching ratio $b \to \mu X$. Using the error on the Particle Data Group value for the $b \to \mu X$ branching ratio, an uncertainty of 3.5% is assigned to each muon. A systematic error is also associated with the muon spectrum from B hadron decays which is assumed by HVQJET. This uncertainty is taken to be 8% [70]. Errors due to the structure functions will have little effect, because these errors affect $\sigma_b^{MC}$ and $\sigma_{b\overline{b}\to\mu\mu X}^{MC}$ approximately equally. All of these errors are summarized in Table 9-4.

### 9.2.4 $b\overline{b}$ Correlations

Correlations between the $b$ and $\overline{b}$-quarks are particularly interesting, because they give insights into the various mechanisms for $b\overline{b}$ production. Recall that the LO mechanism is flavor creation, Fig. 2-3. Conservation of transverse momentum implies that the $b$ and $\overline{b}$ will be produced approximately back-to-back in azimuthal angle. Higher order contributions to $b\overline{b}$ production produce smaller $\Delta\varphi_{b\overline{b}}$ values.

Whenever $P_T^b$ is more than a few GeV/c, $b$-quarks produce muons which travel in the same approximate direction as the parent $b$-quark. Thus, $\Delta\varphi_{\mu\mu}$ gives a good measure of $\Delta\varphi_{b\overline{b}}$. This is demonstrated in Figure 9-8 which uses ISAJET Monte Carlo to show that $\Delta\varphi_{\mu\mu}$ and $\Delta\varphi_{b\overline{b}}$ are strongly correlated. In Fig. 9-9 the measured $b\overline{b} \rightarrow \mu\mu X$ cross section is plotted as a function of $\Delta\varphi_{\mu\mu}$ along with the ISAJET prediction. The shape of the two distributions clearly disagree. It is not surprising that ISAJET cannot reproduce the shape of the data. A bug was recently discovered by the authors of ISAJET which causes it to overestimate the amount of gluon splitting in $Q\overline{Q}$ production. In Fig. 9-10 the $b\overline{b} \rightarrow \mu\mu X$ cross section is plotted along with the prediction from HVQJET (see Section 2.3.2). The shape of the HVQJET distribution agrees well with the shape of the measured $\Delta\varphi_{\mu\mu}$ distribution with some small differences in the lower $\Delta\varphi_{\mu\mu}$ bins.

ISAJET is a leading order event generator which uses a parton shower (gluon radiation) approach to approximate higher order processes. In this approach, all interference terms are ignored (Fig. 2-5(d)). Phenomenologically, the production mechanisms

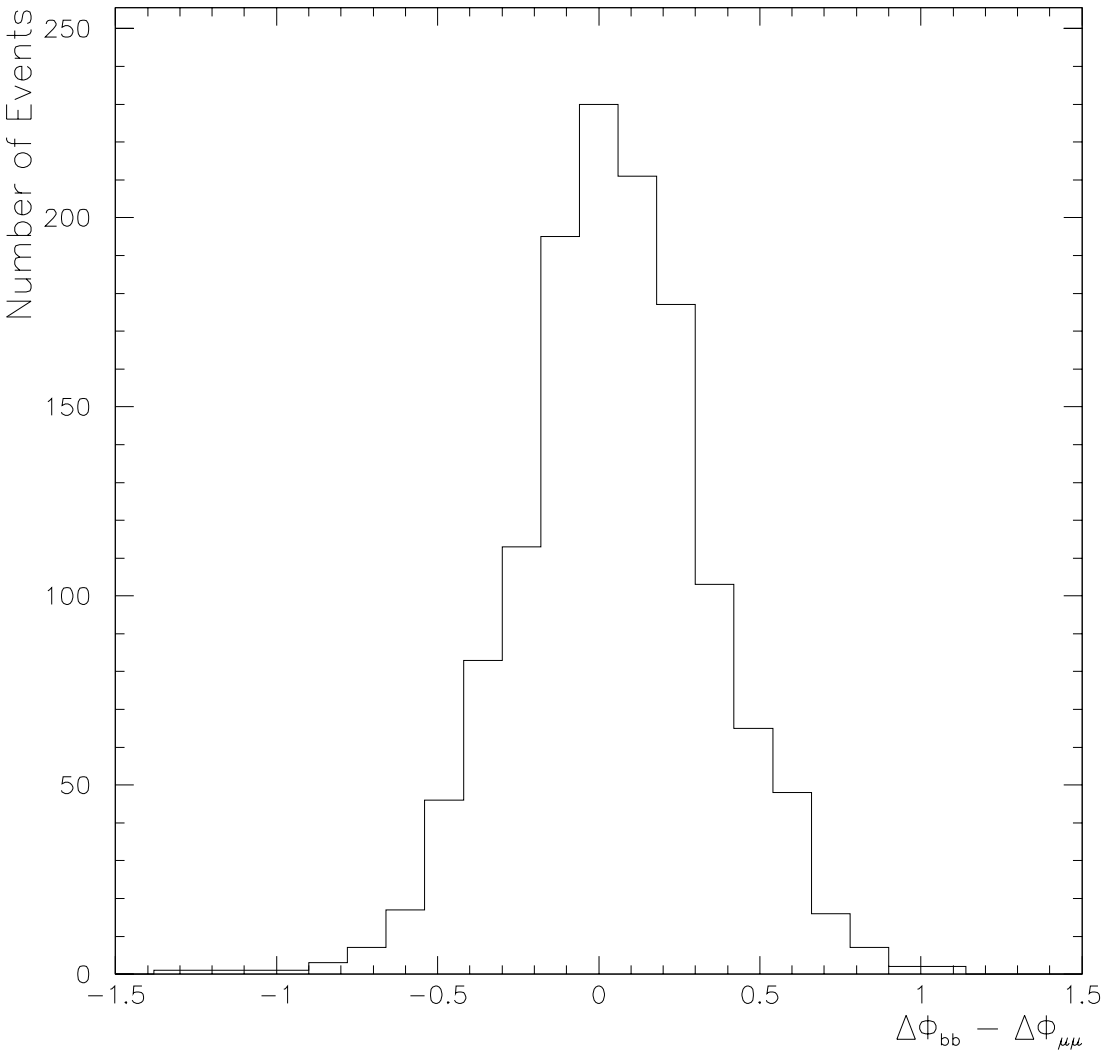


Figure 9-8: The difference between $\Delta\varphi_{b\bar{b}}$ and $\Delta\varphi_{\mu\mu}$ for ISAJET dimuon events. Since the muons travel in the same general direction as their parent $b$-quarks, $\Delta\varphi_{\mu\mu}$ and $\Delta\varphi_{b\bar{b}}$ are strongly correlated.

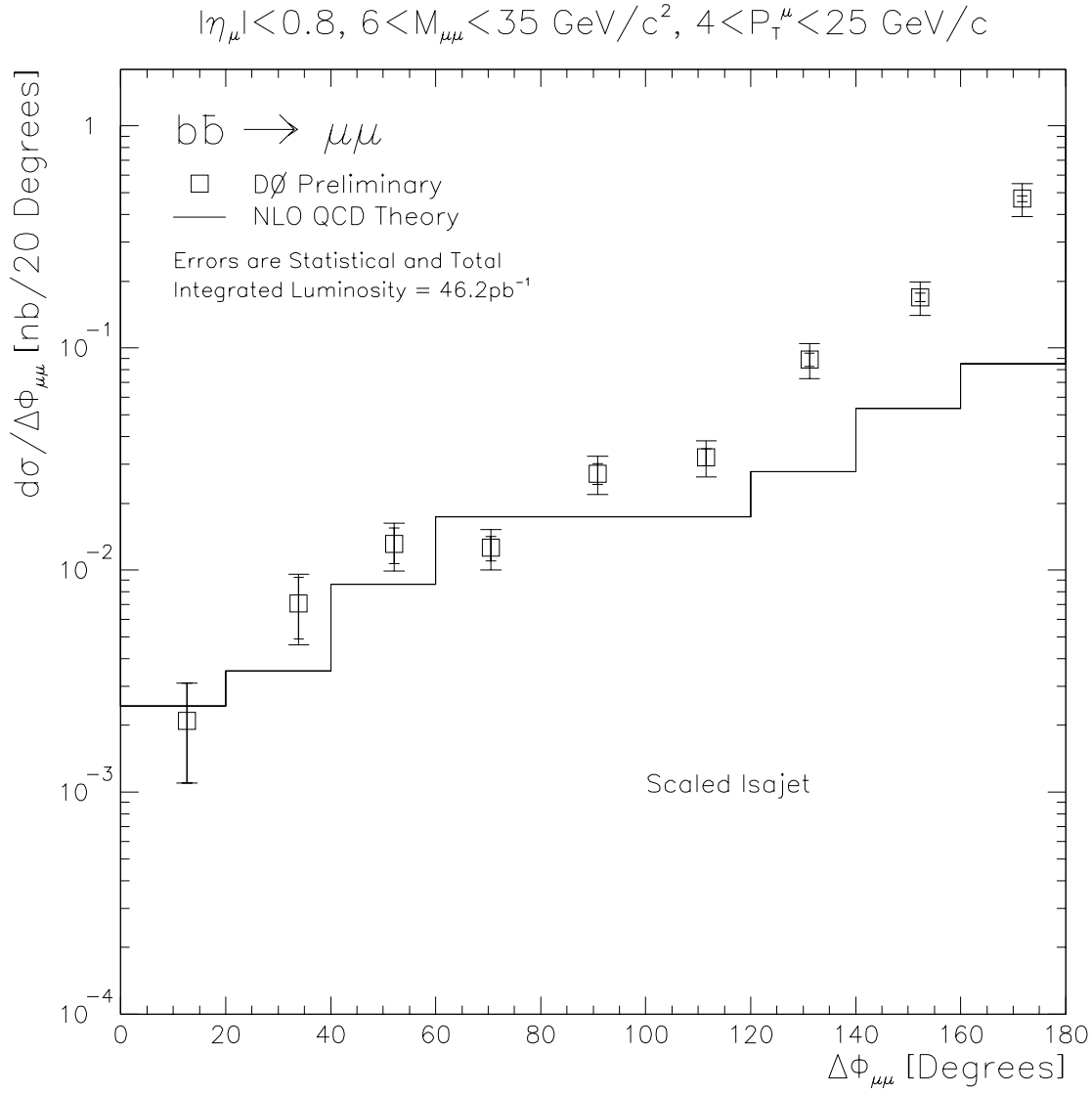


Figure 9-9: The measured $b\bar{b} \rightarrow \mu\mu X$ differential cross section plotted as a function of $\Delta\varphi_{\mu\mu}$. Also shown is the ISAJET prediction which has been scaled to the NLO QCD prediction of Nason *et al.*.

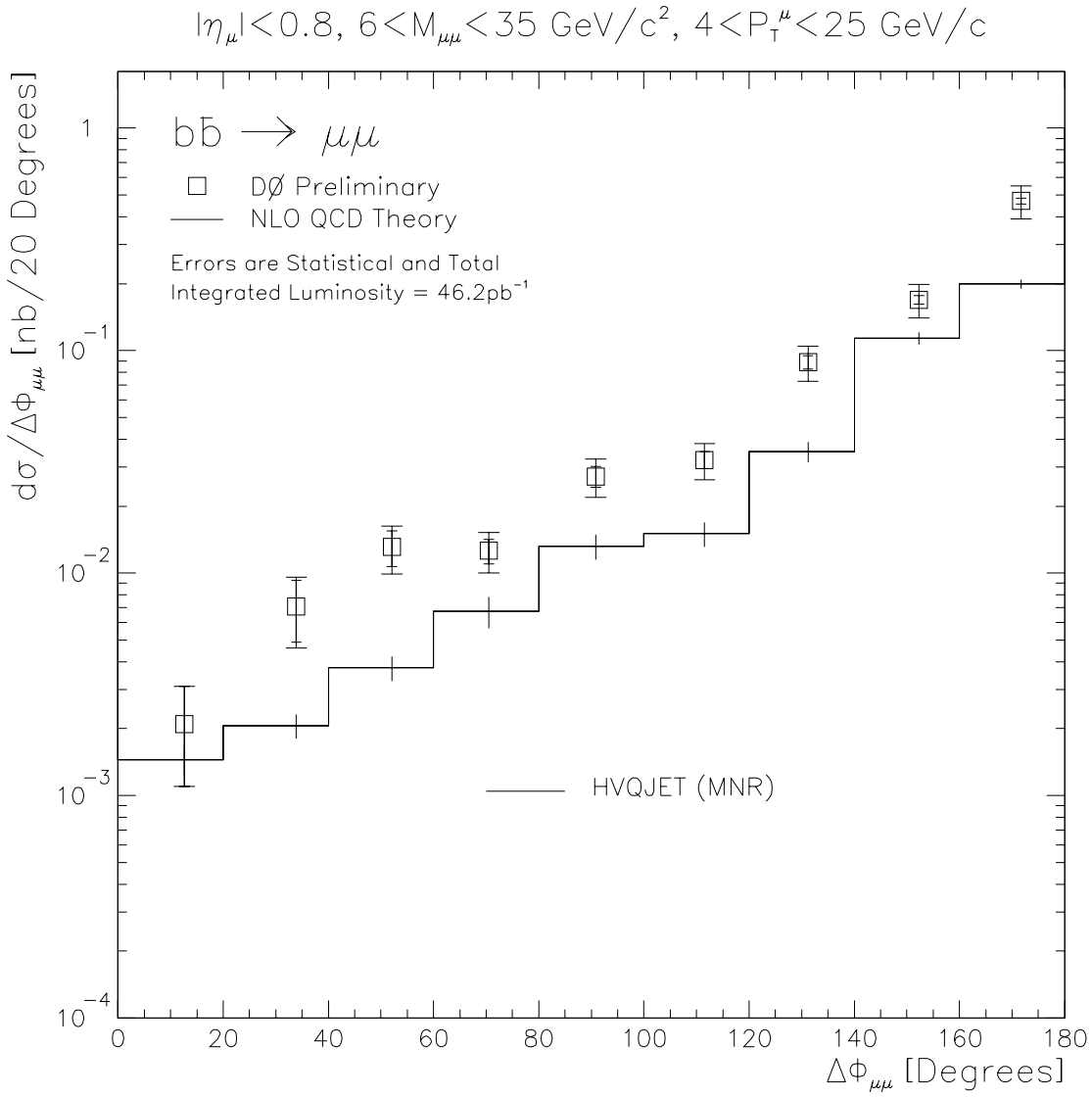


Figure 9-10: The measured $b\overline{b} \rightarrow \mu\mu X$ differential cross section as a function of $\Delta\varphi_{\mu\mu}$. Also shown is the prediction given by HVQJET which is an event generator based on the NLO QCD predictions of Mangano *et al.*.

| Process | Fit to Data | ISAJET Prediction |
|---|---|---|
| Gluon Splitting | $5.8 \pm 2.3\%$ | 20.3% |
| Flavor Excitation | $8.1 \pm 6.6\%$ | 16.0% |
| Flavor Creation | $86.1 \pm 6.6\%$ | 63.7% |

Table 9-5: Fraction of the $b\overline{b}$ production mechanisms found by fitting ISAJET distributions to the data. The uncertainties are from the fit only.

in ISAJET are flavor creation, flavor excitation, and gluon splitting (Figures 2-3 and 2-5). The $\Delta\varphi_{\mu\mu}$ distributions associated with each of these processes can be obtained from the Monte Carlo. Each distribution can then be fit to the data in order to determine the contributions from each process. The $\Delta\varphi_{\mu\mu}$ distributions, normalized to unit area, are shown in Fig. 9-11.

These three distributions can be fit to the data (see Fig. 9-12). The results of this fit are summarized in Table 9-5. It was found that approximately 80% of the $b\overline{b}$ production is from flavor creation, while flavor excitation and gluon splitting each contribute less than 10%. This is quite different than the predictions of ISAJET (Table 9-5). It is important to note that ISAJET flavor creation is not true leading order, because approximately 20% of the time the LO graphs are supplemented by gluon radiation terms. Further, it is somewhat artificial to separate $b$-quark production into these three classes, since this is only valid in the theoretical limit $m_b \to 0$. However, these classifications are useful in that they give a convenient way of comparing data and phenomenological models.

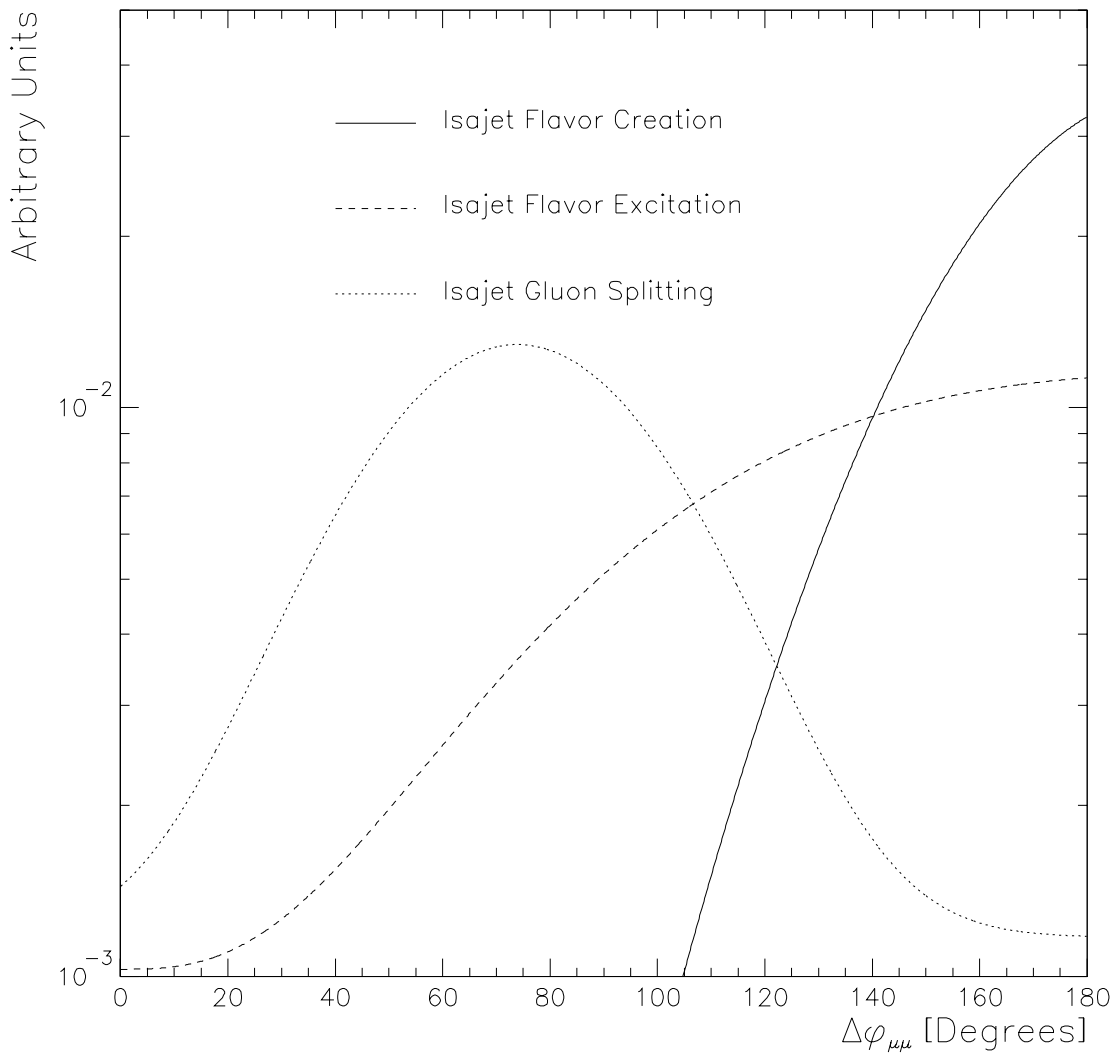


Figure 9-11: The $\Delta\varphi_{\mu\mu}$ distributions for leading order flavor creation, and the higher order processes: flavor excitation and gluon splitting. These distributions are obtained from ISAJET Monte Carlo.

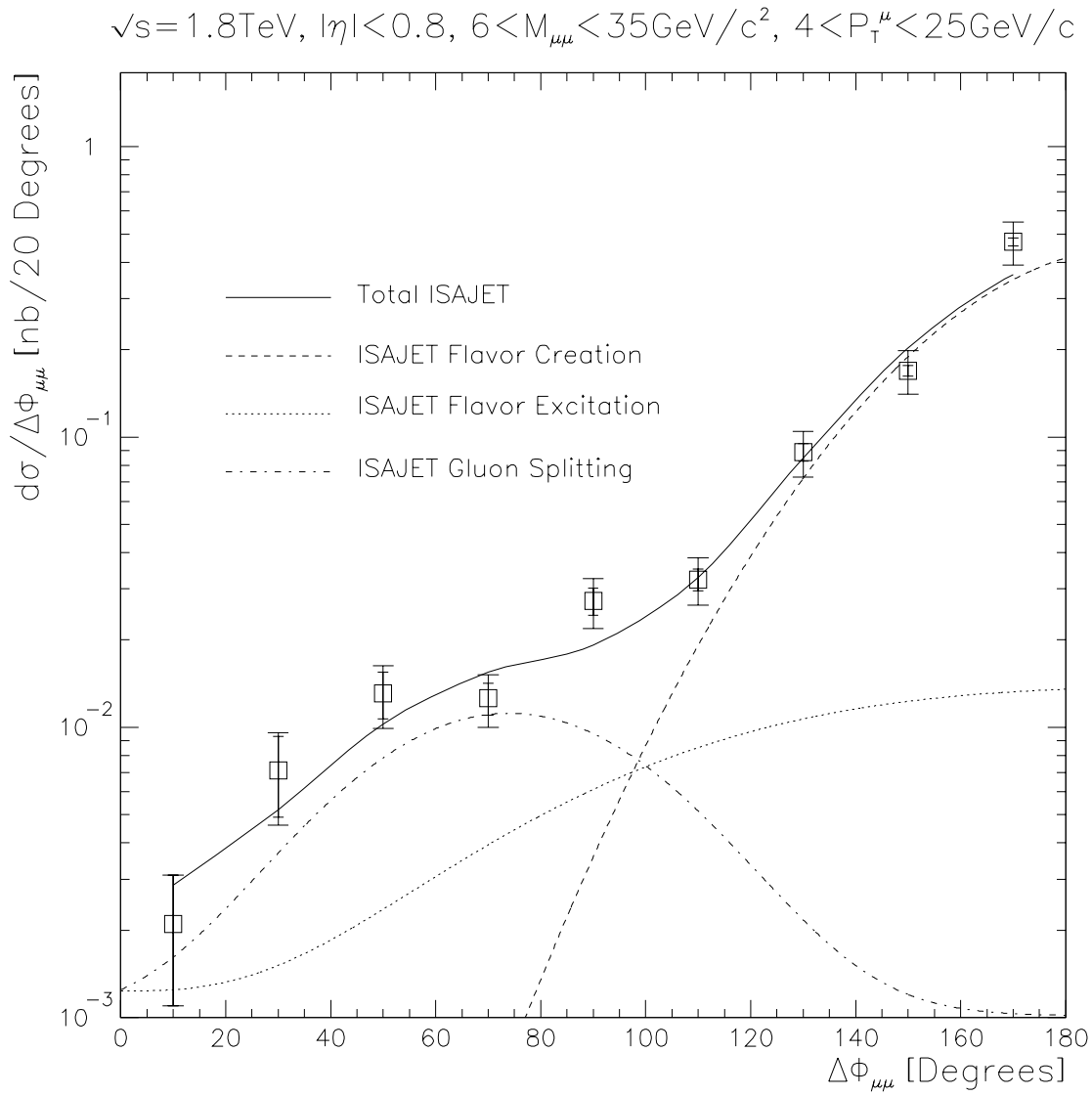


Figure 9-12: The three distributions shown in Fig. 9-11 are fit to the data. The results of the fit are summarized in Table 9-5.

# Chapter 10

# Discussion and Conclusions

## 10.1 Summary

This thesis describes the measurement of the $b$-quark production cross section and $b\overline{b}$ azimuthal angular correlations using dimuons. These measurements are interesting, because they can be directly compared to NLO QCD theory. The $b$-quark is uniquely suited for these comparisons because the theoretical predictions for $b$-quark production can be treated in a perturbative fashion. Also, the $b$-quark is light enough to be easily produced at Tevatron energies.

Two different measurements have been made. The first is the $b$-quark production cross section which has been compared with the NLO QCD prediction of Nason *et al.*. This cross section was first measured in 1989 by CDF resulting in a cross section that was approximately a factor three higher than NLO QCD predictions.

This motivated additional measurements of the $b$-quark cross section by CDF and DØ. Current measurements show that NLO QCD theory is still a factor of two below the measured cross section. This analysis presents the first measurement of the $b$-quark cross section using the higher statistics run 1B data sample taken at the DØ experiment. The $b$-quark production cross section presented in this thesis is consistent with previous measurements in that it lies along the upper boundary of the theoretical uncertainties (Fig. 9-7).

The measurement of the $b\overline{b} \rightarrow \mu\mu X$ inclusive differential cross section is shown in Figures 9-5 and 9-10. Of particular interest is the differential cross section $d\sigma/d\Delta\varphi_{\mu\mu}$ as it is sensitive to the various $b\overline{b}$ production mechanisms. Leading order mechanisms produce dimuons which are nearly back-to-back in azimuthal angle, while higher order mechanisms produce more complex topologies. Thus, the inclusive $b\overline{b} \rightarrow \mu\mu X$ differential cross section is interesting in that it gives us the ability to determine the amount of higher order contributions to the total $b\overline{b} \rightarrow \mu\mu X$ cross section.

The data for this analysis was selected from the run 1B collider run, 1994-1995, at the Tevatron. Only a subset of the total available runs were selected for the analysis, runs 85277 through 93115 . The details of why these particular runs were chosen are described in Chapter 4. The total integrated luminosity for this sample is 46.2 $\text{pb}^{-1}$.

Two triggers were used to select the data: MU_2_LOW and MU_2_CENT (Section 4.1). These triggers changed periodically throughout run 1B. These changes result in three different time periods which must be simulated by the DØ trigger sim-

ulator, VMS_FILTER (Section 4.1.3). The Level 1 and Level 2 scintillator veto tools are not simulated by VMS_FILTER. Therefore, the efficiency for these tools was determined separately (Section 6.1.2). Comparisons between efficiencies obtained from Monte Carlo and those taken directly from the data were made whenever possible. The details of this study, as well as the corrections that were subsequently applied to the trigger efficiencies, are described in Section 6.1.3.

ISAJET Monte Carlo was used to perform many of the efficiency studies discussed in this thesis. Two different correction factors were applied to this Monte Carlo. The first correction is used to transform the ISALEP generated events (NHADRON and NEVOLVE equal to 10) into the ISAJET equivalent (NHADRON and NEVOLVE equal to 1). An additional correction factor is applied to normalize the total $b$-quark and $c$-quark cross section given by ISAJET to the total cross section given by the NLO QCD predictions of Nason *et al.* [3, 4]. The correction factor for both $b\overline{b}$ and $c\overline{c}$ events are calculated separately and can be seen in Fig. 5-5.

The selection cuts, listed in Tables 4-5 and 4-6, each have inefficiencies which must be determined. Both data and fully processed ISAJET Monte Carlo were used to calculate the efficiencies and their systematic uncertainties (Section 6.2). The combined trigger and selection cut efficiencies can be seen in Fig. 6-10.

Several different processes contribute to the dimuon spectrum including $b\overline{b} \rightarrow \mu\mu X$, $c\bar{c} \rightarrow \mu\mu X$, cosmic rays, and the prompt decay of a $b$-quark (or $c$-quark) plus the decay of a $\pi$ (or K). The cosmic background was determined by using a combination

of the scintillator time-of-flight information (Sections 7.1.1 and 7.1.2) and matched central detector tracks (Section 7.1.3). The total cosmic contamination was found to be $12.3 \pm 0.5\%$.

A maximum log-likelihood fit was used to separate the remaining backgrounds from the $b\overline{b} \rightarrow \mu\mu X$ signal. Two variables, $P_T^{rel}$ and $z$, were used in this fit. These variables were chosen for their ability to distinguish between each of the dimuon production mechanisms. ISAJET Monte Carlo was used to create $P_T^{rel}$ and $z$ distributions for the $b\overline{b} \rightarrow \mu\mu X$, $c\bar{c} \rightarrow \mu\mu X$, and the 'prompt plus decay' processes. The $P_T^{rel}$ distributions can be seen in Figs. 7-6, 7-7, and 7-8 respectively. Similarly, the $z$ distributions are shown in Figs. 7-10, 7-11, and 7-12. A cosmic ray sample was obtained from the data by applying anti-scintillator cuts. The cosmic ray sample was then used to create $P_T^{rel}$ (Fig. 7-9) and $z$ distributions (Fig. 7-13).

The results of the maximum log-likelihood fit are given in Table 7-6. An event-by-event weighting scheme (Section 9.2.1) is then used to weight each event by the probability that it was produced by a $b\overline{b}$ quark pair. These weighted events can then be used to calculate the $b$-quark fraction for the data sample. This $b$-quark fraction is shown in Fig. 9-3 along with the fraction predicted by ISAJET Monte Carlo.

A Bayesian technique was used to unfold the muon momentum resolution (Chapter 8). This method was chosen because it is independent of the shape of the Monte Carlo distributions used by the method. Also, this technique allows one to perform the multi-variable unfolding that is required by this analysis. The $P_T^{\mu}$ and $\Delta\varphi_{\mu\mu}$ bin-

ning chosen for the data is described in Tables 8-1 and 8-2. These bins were chosen so that events may properly unfold into (or out of) the final $P_T^\mu$ and $\Delta\varphi_{\mu\mu}$ distributions. The unfolded $b\overline{b} \to \mu\mu X$ spectrum can be seen in Fig. 8-7.

## 10.2 Inclusive $b$-quark Cross Section

The $b\overline{b} \to \mu\mu X$ differential cross section is calculated using Eq. 9.8. This is simply the unfolded data weighted by the $b$-quark fraction and corrected for selection cuts, trigger efficiencies, integrated luminosity, and bin width. The resulting cross section, as a function of $P_T^\mu$, is shown in Fig. 9-5. This is plotted along with the NLO QCD predictions as given by HVQJET (Section 2.3.2).

A Monte Carlo technique (Section 9.2.3) is used to translate the differential cross section, with muon kinematic cuts, into the integrated inclusive $b$-quark production cross section for $|y_b| < 1$. The reported cross section is integrated over all $P_T^b$ above some minimum $b$-quark transverse momentum, $P_T^{min}$. The resulting integrated cross section is shown in Fig. 9-7 and is summarized in Table 9-3. The measurement is plotted along with the NLO QCD predictions of Nason *et al.* [3, 4]. The theoretical curve was created with the MRSD0 structure function using $\Lambda_4 = 215$ MeV and $\mu = \mu_0$ for the central value of the theory. The error bands were created by varying $\Lambda_4$ and $\mu$ to 280 MeV and $\mu_0/2$ for the upper uncertainty and 160 MeV and $2\mu_0$ for the lower curve.

It is useful to compare the $b$-quark cross section which has been extracted from

the dimuon plus jets sample with the cross sections extracted from the other DØ data samples. These other samples include single muons [71], single muons plus jets [69], and J/$\psi$ [72] events. These samples are approximately exclusive of the dimuon plus jets sample used in this analysis, and each sample contains different $b$-quark fractions, underlying $b\overline{b}$ production mechanisms, and systematic uncertainties. The extracted $b$-quark cross sections from each of these data sets, including the dimuon plus jets sample presented in this analysis, are plotted in Fig. 9-7. There is very good consistency among all the measurements both in shape and magnitude (Fig. 10-1). All of the measurements lie on the upper boundary of the theoretical uncertainty.

The CDF experiment [5] at Fermilab has also measured the integrated $b$-quark cross section at $\sqrt{s} = 1.8$ TeV. The integrated $b$-quark cross section using inclusive muons, electrons, J/$\psi$, and $\psi'$s [73, 74, 75, 76] data samples are shown in Fig. 10-2. These results are similar to those measured by DØ in that there is reasonable agreement between the data and the NLO QCD prediction, but the measured cross section is systematically higher than the central value of the NLO QCD theory. CDF has also measured the differential $b$-quark cross section using dimuons [68]. In this analysis, the silicon vertex detector is used to tag muons which decay from $b$-quark's. The resulting cross section is shown in Fig. 10-3. As before, the NLO QCD prediction is more than a factor of two below the measured $b$-quark cross section.

The integrated $b$-quark cross section has also been measured at $\sqrt{s} = 630$ GeV by UA1. Here the integrated $b$-quark cross section was for the rapidity range $|y_b| < 1.5$

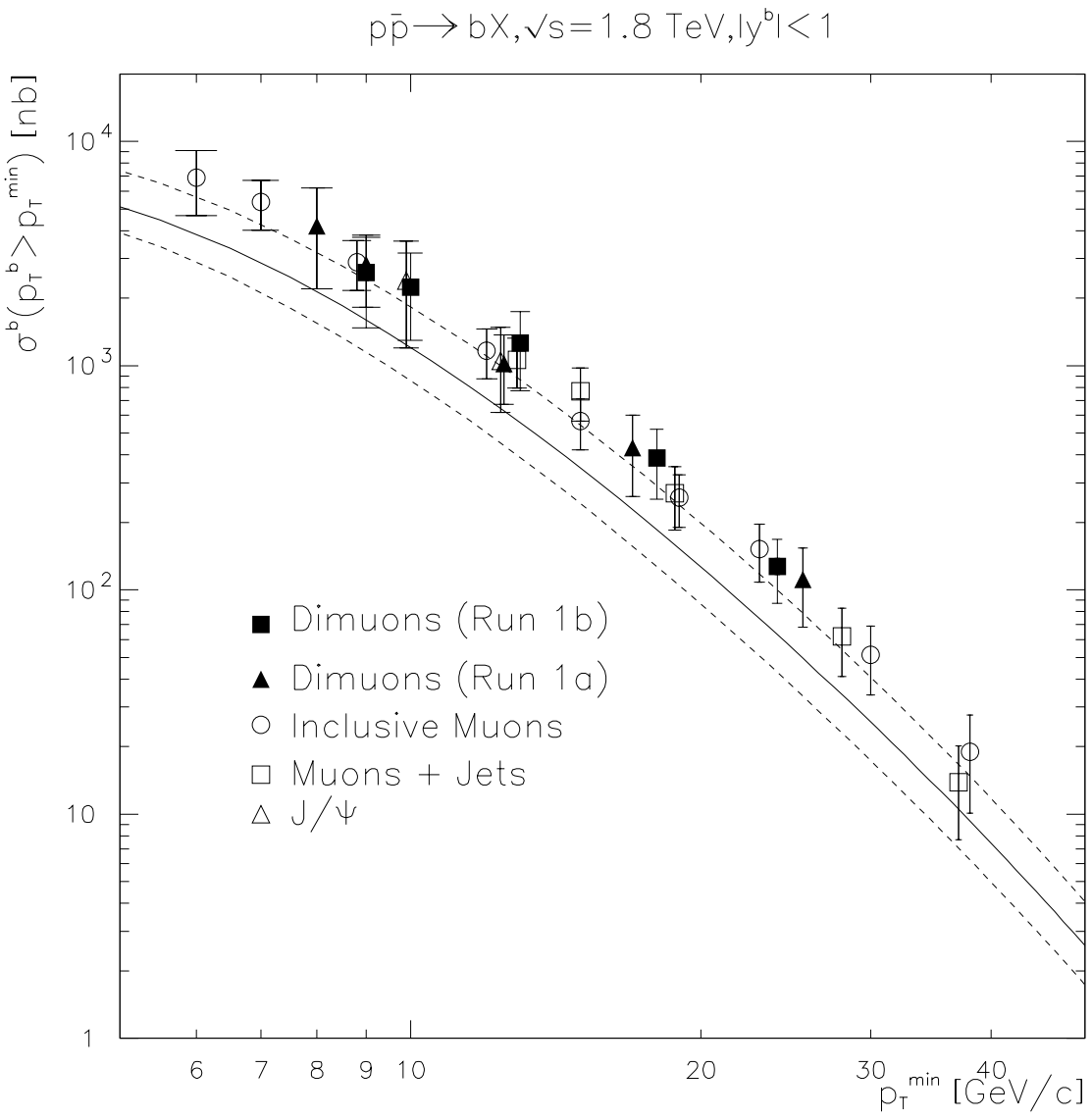


Figure 10-1: A comparison of all the DØ *b*-quark cross section measurements. All of the measurements are consistent with each other and lie on the upper boundary of the theoretical uncertainty. The error bars represent total errors.

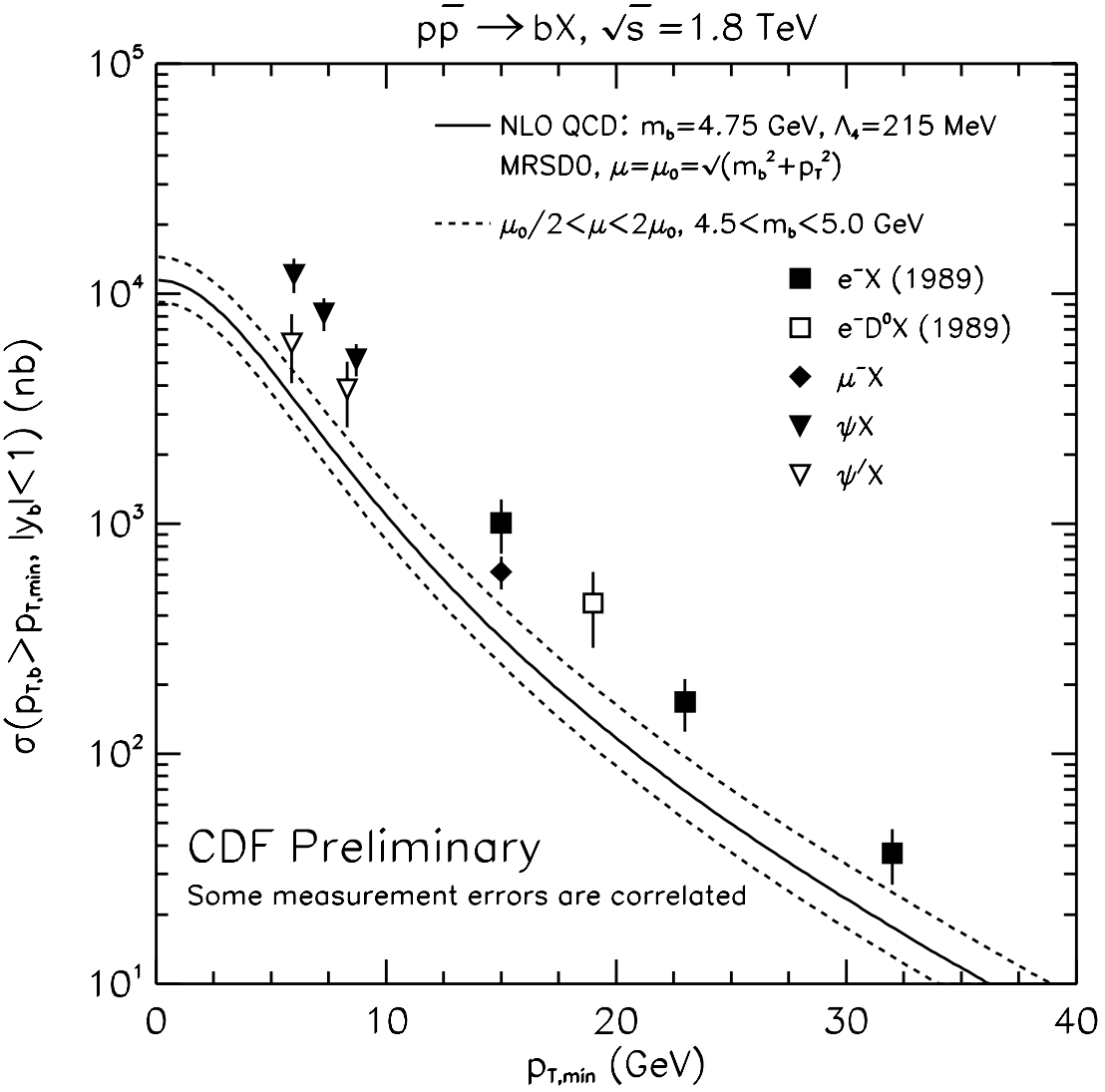


Figure 10-2: $b$-quark production cross section measurements made by the CDF experiment.

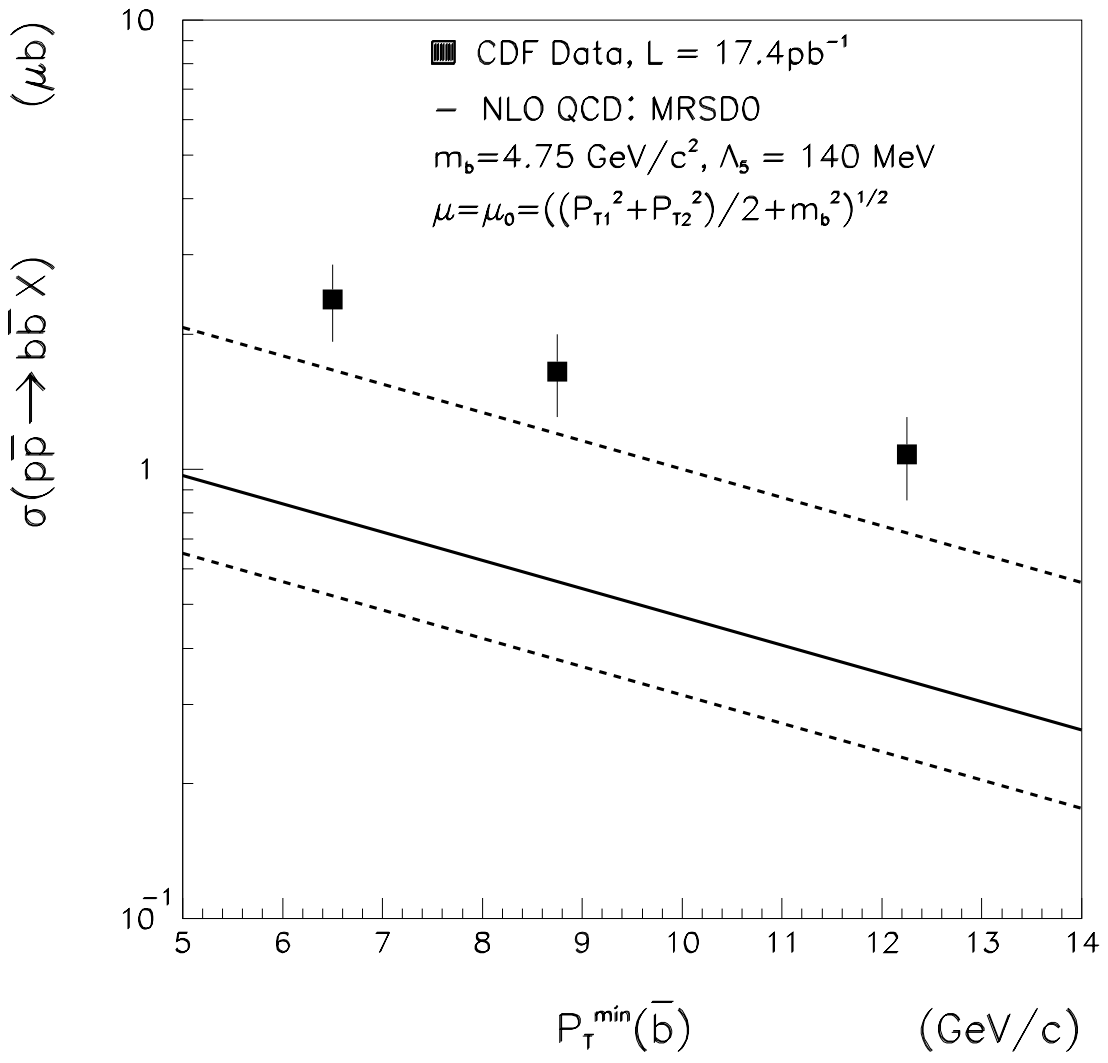


Figure 10-3: $b$-quark production cross section measurements made by the CDF experiment using dimuons.

was extracted. The data samples used to extract the $b$-quark cross section were inclusive dimuons [77] and single muons plus jets [66, 67]. The UA1 results are shown in Fig. 10-4. This measurement is compared to NLO QCD prediction of Nason *et al.* using the parameters $\mu = \sqrt{m_b^2 + P_T^2}$, $m_b = 4.75$ GeV, $\Lambda_4 = 260$ MeV, and the DFLM structure function.

The integrated $b$-quark cross sections measured at DØ and CDF are similar. Both cross sections are consistent with the NLO QCD prediction of Nason *et al.* within theoretical and experimental uncertainties. The mean value of the data, however, lies at the upper edge of the theoretical uncertainty. It is possible that new structure functions or different choices for the parameters, $\Lambda_4$ and $\mu$, may account for these differences. It has been shown that the parameters $m_b = 4.5$ GeV/c$^2$, $\mu = \mu_0/2$, $\Lambda_4 = 300$ MeV, and the MRSA structure function resolves this discrepancy [78] at both $\sqrt{s} = 630$ GeV and $\sqrt{s} = 1.8$ TeV. Note that these parameters are very similar to the parameters chosen to calculate the upper theoretical uncertainties for the predictions used in this analysis: $\mu = \mu_0/2$ and $\Lambda = 280$ MeV (see Fig. 9-7).

## 10.3 $b\bar{b}$ Correlations

Correlations between $b\bar{b}$ quark pairs are interesting, because it allows one to study the relative contributions of LO and NLO processes to the total $b\bar{b}$ cross section. In this analysis, the difference in azimuthal angle between the dimuons is used as the correlation variable. This variable is highly correlated with the difference in azimuthal

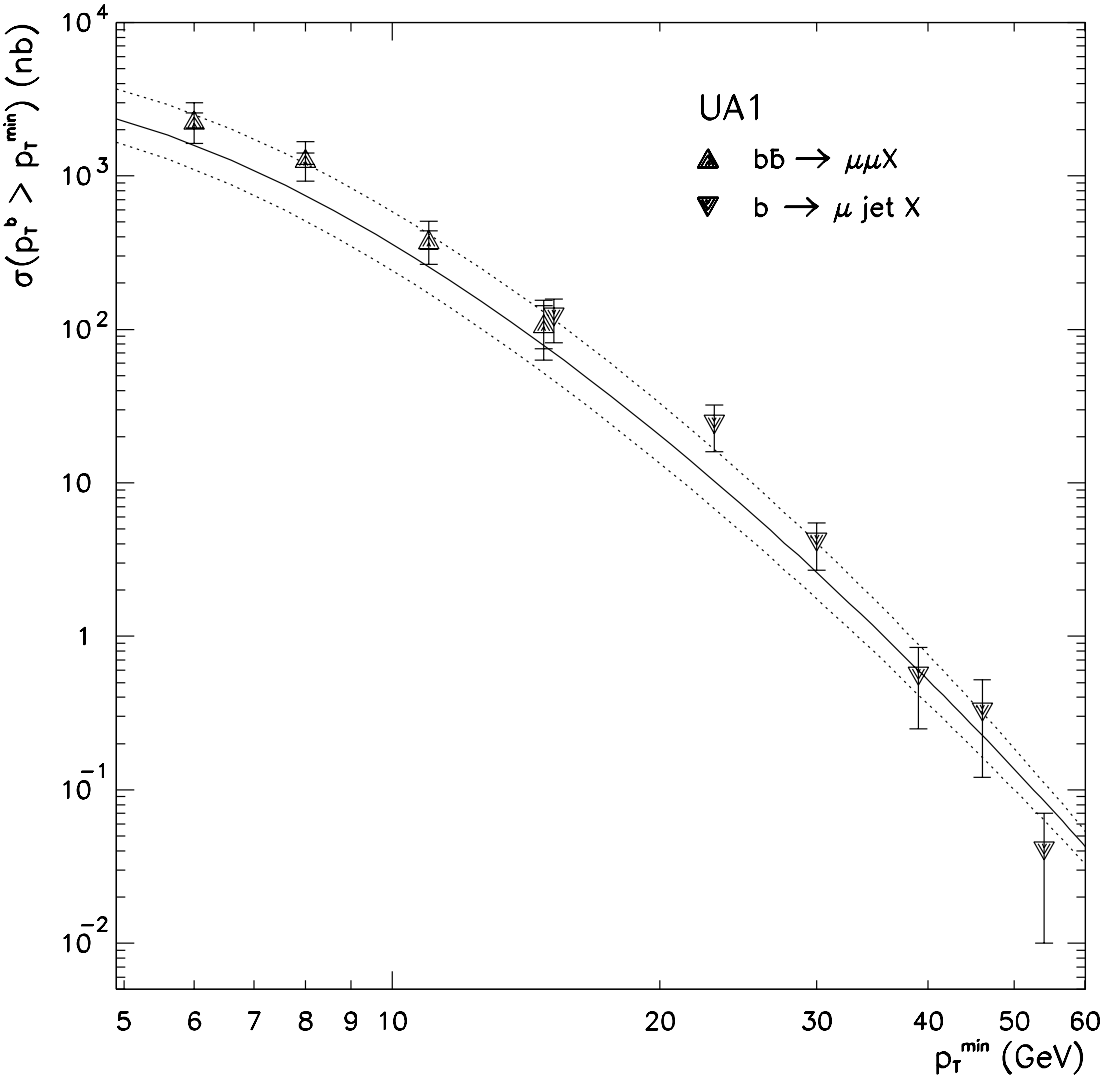


Figure 10-4: $b$-quark production cross section measurements made by the UA1 experiment. This data was taken at a center-of-mass energy of $\sqrt{s} = 630$ GeV. The theoretical curve is the prediction of Nason *et al.* using $\mu = \sqrt{m_b^2 + P_T^2}$, $m_b = 4.75$ GeV, $\Lambda_4 = 260$ MeV, and the DFLM structure function.

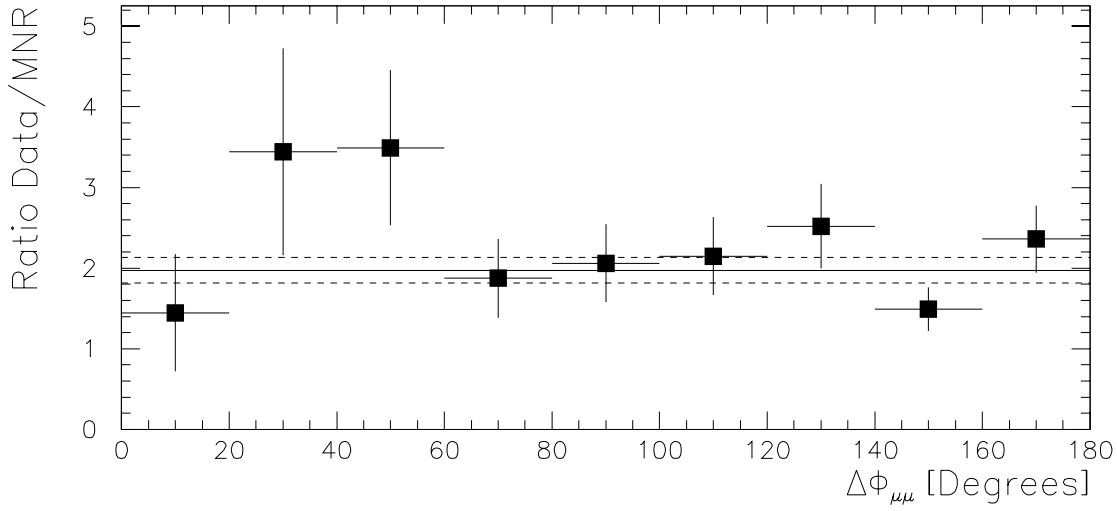


Figure 10-5: The ratio between the measured cross section and HVQJET as a function of $\Delta\varphi_{\mu\mu}$. A flat line is fit to the data and is plotted along with its error bar. The value of the fit is $2.0 \pm 0.2$.

angle between the $b$ and $\overline{b}$ as has been discussed in Section 9.2.4. In Figure 9-10, the differential cross section $d\sigma/d\Delta\varphi_{\mu\mu}$ for $b\overline{b} \rightarrow \mu\mu X$ production is plotted along with the NLO QCD prediction of HVQJET. The measurement agrees well with the shape of the NLO QCD prediction but on average lies a factor of $2.0 \pm 0.2$ (see Fig. 10-5) above the central value of the theory.

CDF has also studied $b\overline{b}$ correlations using dimuons [79]. Their analysis studies low momentum muons, $P_T^{\mu_1} > 3$ GeV/c, $3 < P_T^{\mu_2} < 7$ GeV/c, with a dimuon invariant mass of $M_{\mu\mu} > 5$ GeV/c$^2$. The silicon vertex detector is used to tag dimuons which have decayed from $b$-quark's. The results are shown in Fig. 10-6 along with NLO QCD predictions. Again, the data and theory agree well in shape but disagree in the overall normalization.

CDF has also made correlation measurements using their muon plus $b$-jet data

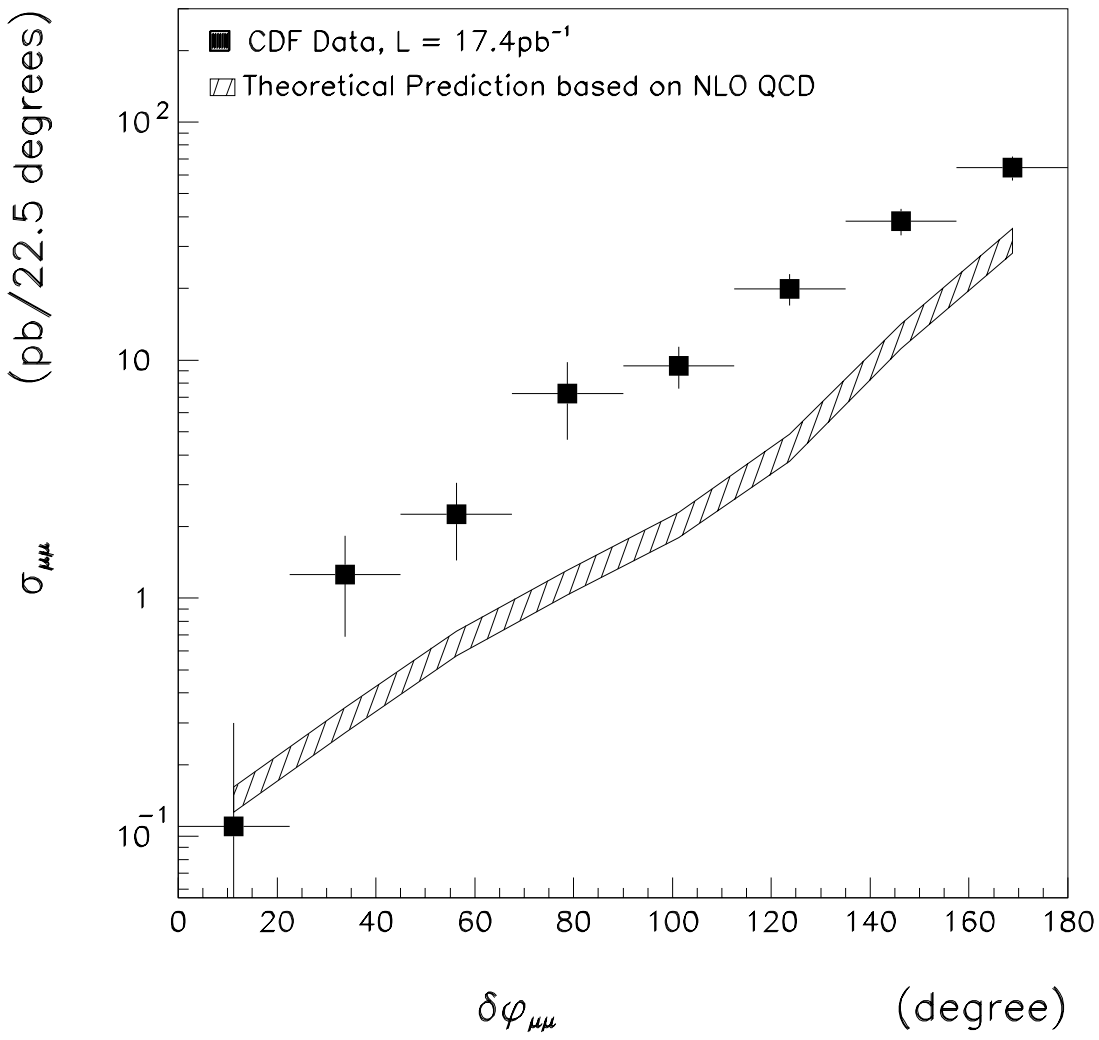


Figure 10-6: The $\Delta\varphi_{\mu\mu}$ correlation measurement made by the CDF experiment. The theoretical uncertainties are due to uncertainties in the efficiencies, branching ratio of $B \to \mu X$, and the $b$-quark fragmentation.

sample [80]. Here, the silicon vertex detector is used to tag the $b \rightarrow \mu X$ decay along with a recoiling $\overline{b}$-jet. The muon is required to have $P_T^{\mu} > 9$ GeV/c and $|\eta_{\mu}| \leq 0.6$, and the jet is required to have $E_T > 10$ GeV and $|\eta^b| < 1.5$. The results are shown in Fig. 10-7 along with the NLO QCD calculation given by Mangano *et al.*. The MRSD0 structure function is used along with $\mu_0 = \sqrt{m_b^2 + (P_T^{b^2} + P_T^{\overline{b}^2})/2}$ and a Peterson parameter of $\epsilon = 0.006$. The resulting B-hadrons were decayed by the CLEO Monte Carlo package [81]. Again, the shape of the data agrees well with the shape of the theory, but the data lies above the theoretical predictions.

A similar measurement has also been made at $\sqrt{s} = 630$ GeV by the UA1 collaboration. High mass, non-isolated muons pairs from the semileptonic decay of $b\overline{b}$ pairs [77] are shown in Fig. 10-8. The theoretical prediction uses the DFLM [82] structure function along with $\Lambda_4 = 260$ MeV. Again, the theory is systematically above the data.

In all, we see a consistent picture at both $\sqrt{s} = 630$ GeV and $\sqrt{s} = 1.8$ TeV. The shape of the $\Delta\varphi_{\mu\mu}$ distributions agree well in shape with the NLO QCD predictions but are approximately a factor of 2 higher in normalization.

## 10.4 Future Prospects

There are a number of interesting extensions to the analysis presented in this thesis. These include the measurement of the differential $b$-quark cross section, reconstruction of $b$-quark kinematics using muon corrected jets, and the use of complementary data

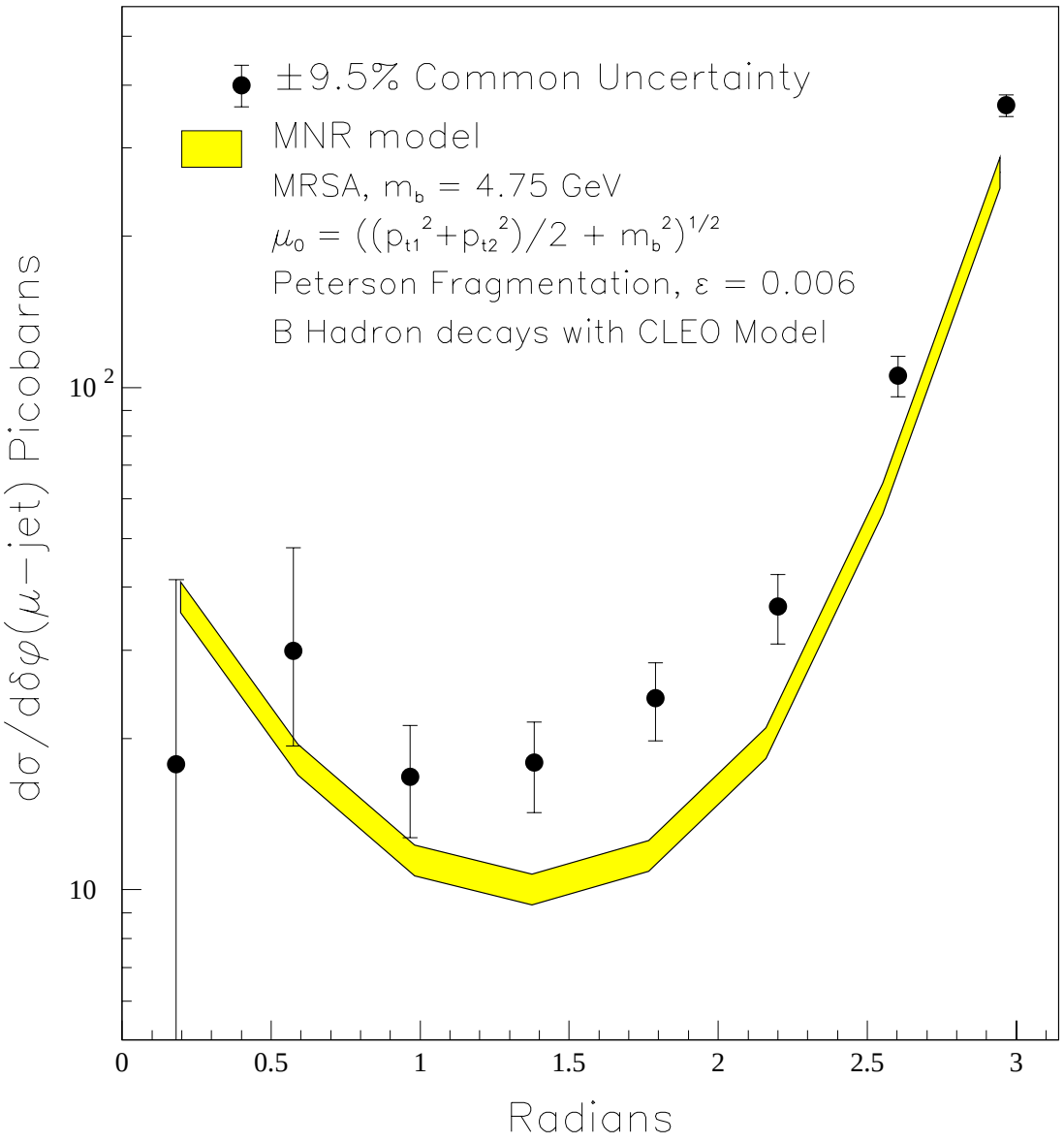


Figure 10-7: The CDF measurement of the muon plus b-jet cross section. The uncertainty in the theoretical curve is due to the branching ratio of $B \to \mu X$, and the $b$-quark fragmentation.

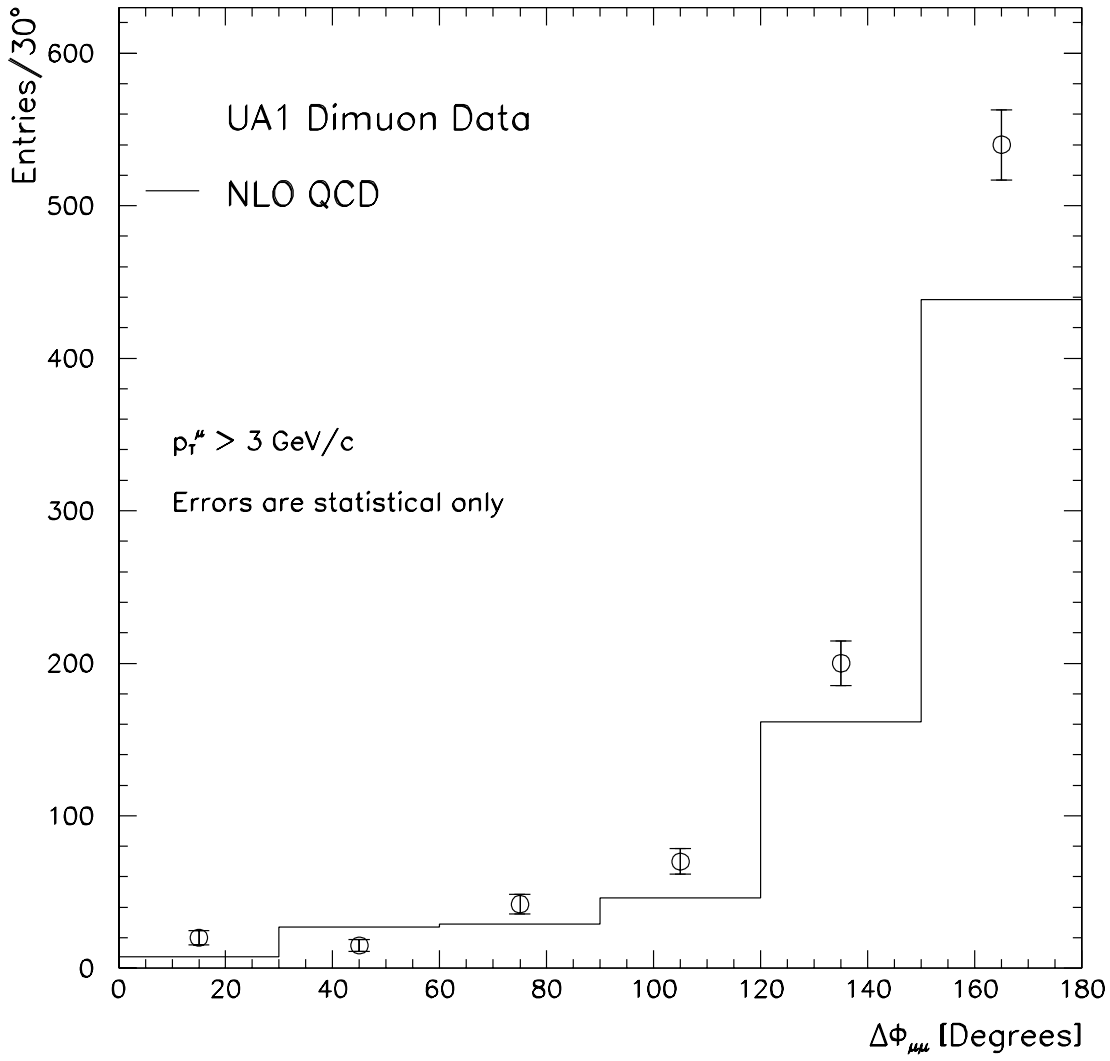


Figure 10-8: The $\Delta\varphi_{\mu\mu}$ correlation measurement made by the UA1 experiment at $\sqrt{s} = 630$ GeV. The theoretical curve is from the predictions of Nason *et al.*, $\Lambda_4 = 260$ MeV, $\mu = \sqrt{m_b^2 + P_T^2}$, and DFLM structure function.

samples. The purpose of these extensions is to further constrain NLO QCD theory and give additional measures of the higher order $b\overline{b}$ production mechanisms.

The current technique for extracting the $b$-quark production cross section uses Monte Carlo to estimate and model $b$-quark kinematics, fragmentation of the $b$-quark's into muons, and the effect of imposing muon kinematic cuts. Preliminary studies suggest that it may be possible to use Bayesian unfolding techniques (Chapter 8) to transform the $b\overline{b} \to \mu\mu X$ differential cross section, $d\sigma/dP_T^{\mu}$, into the inclusive $b$-quark differential cross section, $d\sigma/dP_T^{b}$. This technique essentially involves using the Monte Carlo to build a 'smearing matrix' which transforms the $p\overline{p} \to bX$ cross section (binned in $P_T^b$) into the $b\overline{b} \to \mu\mu X$ cross section (binned in $P_T^{\mu}$). The smearing matrix is then used in the iterative process described in Chapter 8 to build the 'unfolding matrix'. Work is currently in progress testing the feasibility of this technique.

In the analysis presented in this thesis, dimuons were used to extract information about $b$-quark kinematics. A better representation of the $b$-quark kinematics are the muon corrected jets described in Section 7.3.1. With the exception of the missing neutrino energy, the muon corrected jets contain all of the original $b$-quark's energy and momentum[1]. The difference in azimuthal angles between the corrected jets and the dijet invariant mass can be measured. Both are interesting as they are sensitive to the various $b$-quark production mechanisms.

[1]The jet cone size has been defined as $\Delta R = \sqrt{\Delta\eta^2 + \Delta\varphi^2} = 0.7$. There is no reason to expect $b$-quark jets to be this size. Therefore, calorimeter jets are not expected to exactly reproduce the energy of the hadronic shower produced in the semileptonic decay of $b$-quark's.

The dimuon plus dijet cross section measurement may also give insight into the single muon plus dijet sample. This sample consists of a single muon (plus associated jet) along with a recoiling hadronic jet. If the dijet invariant mass or azimuthal angle difference between dijets proves to be a successful $b\overline{b}$ correlation variable in the dimuon plus associated jets sample, then these same variables could be used in the much higher statistics single muon plus associated jets sample. Use of the single muon sample would give a much more detailed measurement of the higher order $b\overline{b}$ processes than can be achieved with the kinematically restricted dimuon sample.

The forward muon system (SAMUS) can also be used to study $b\overline{b}$ production. This sample consists of two muons, where one is within $|\eta_\mu| < 1.0$ and the second muon is within $2.2 < |\eta_\mu| < 3.3$. The three dimensional opening angle for these dimuons ranges from approximately 45° to 130°. This opening angle restriction tends to suppress the leading order production mechanism. Thus, the central plus forward dimuon sample is rich in dimuons produced from higher order production mechanisms. Correlation measurements with this sample will provide a unique test of NLO QCD.

Finally, like-sign dimuons can be studied. The dimuon sample used in this analysis was simplified by imposing a dimuon invariant mass cut. This cut eliminated dimuon production from J/$\psi$ events as well as dimuons from sequential $b$-quark decays. The price paid for this cut was a reduction in dimuon events with smaller opening angles where higher order processes contribute most. By choosing a sample of like-sign only dimuons, one does not have contributions from $c\overline{c}$ production, J/$\psi$ production, or

sequential decays. Thus, the lower bound on the invariant mass cut can be relaxed. This allows more dimuon events with smaller opening angles into the sample. Consequently, this increases the contributions from higher order production mechanisms. Following the analysis techniques detailed in this thesis, measurements of the $b$-quark cross section and $b\overline{b}$ correlations for like-sign dimuons could be made.

# Appendix A

# Error Propagation

## A.1 Statistics Models

In particle physics, the statistical model most widely used is the Poisson distribution. It is not possible to prove that this is the 'best' model. In fact, it is impossible to show this for *any* statistical model. Instead, Poisson statistics is chosen by convention. However, the underlying assumptions of this statistical model seem to make it a reasonable choice. These assumptions are

1. During a sufficiently short time, $\triangle t$, only 0 or 1 events can occur.

2. The probability of exactly one event occurring during the time interval, $\triangle t$, is proportional to this time interval.

3. Any non-overlapping intervals of length $\triangle t$ are independent Bernoulli trials.

These are all reasonable assumptions for an experiment of this type. Thus, the statistical error for the data will be taken as

$$\sigma_N = \sqrt{N}, \tag{A.1}$$

where N is the measured number of data points. For low statistics samples, this expression tends to underestimate the error. Fortunately, the statistics of this data sample are high enough for this effect to be ignored.

An efficiency, then, is simply the ratio of two numbers which individually obey Poisson statistics, $\epsilon = N/M$. Given this, it is easy to show that the efficiency, $\epsilon$, obeys binomial statistics.

**Theorem A.1** *Let $E$ represent a repeatable experiment which results in $N$ events that individually pass or fail a given condition. Also, let the number of events passing the condition, $N_p$, and the number of events failing the condition, $N_f$, each obey the Poisson statistical model. Then, the error associated with the random variable $\epsilon = \frac{N_p}{N}$ obeys the binomial statistical model.*

**Proof:** *Clearly, $N$ and $N_p$ are correlated variables. Thus it is more convenient to study the problem in terms of $N_p$ and $N_f$ which are uncorrelated. Using $N_p$ and $N_f$ to propagate the errors yields*

$$\begin{aligned}
\sigma_\epsilon^2 &= \left[\left(\frac{\delta\epsilon}{\delta N_p}\right)^2 \sigma_{Np}^2\right] + \left[\left(\frac{\delta\epsilon}{\delta N_f}\right)^2 \sigma_{Nf}^2\right] \\
&= \left[\left(\frac{1}{N_p + N_f} - \frac{N_p}{(N_p + N_f)^2}\right)^2 N_p\right] + \left[\left(\frac{N_p}{(N_p + N_f)^2}\right)^2 N_f\right]
\end{aligned}$$

$$= \frac{N_f^2 N_p + N_p^2 N_f}{N^4} = \frac{N_p N_f}{N^3}$$
$$= \frac{N_p(N - N_p)}{N^3} = \frac{\frac{N_p}{N}(1 - \frac{N_p}{N})}{N} \equiv \frac{\epsilon(1-\epsilon)}{N}$$

*This is just the expression for the binomial standard deviation divided by the total number of events, $N$.*

$$\sigma_\epsilon = \sqrt{\frac{\epsilon(1-\epsilon)}{N}}. \tag{A.2}$$

This expression is valid only when the statistics of the sample is relatively high. In probability theory, the expression $\epsilon = n_p/n$ is referred to as a point estimator. Eq. A.2 is known as the interval estimator.

## A.2 Confidence Intervals

In some of the samples used to determine efficiencies in this analysis, the statistics are low enough that an alternative to Eq. A.2 must be considered. The best classical alternative is the binomial confidence interval. A confidence interval can be defined in the following manner.

**Definition A.1** *Given an ensemble containing an infinite number of identical experiments in which each experiment produces a measurement $X_i$, the $100\gamma\%$ confidence interval represents the range of values, $(X_{low}, X_{high})$, such that each $X_i$ has a $100\gamma\%$ probability of falling within the range $X_{low} < X_i < X_{high}$.*

For the binomial distribution, the following theorem delimits the confidence interval.

**Theorem A.2 ([83])** *Let $Y$ be a binomial random variable with parameters $n$ and $p$ and let $p_1$ and $p_2$ be such that*

$$\begin{aligned} \sum_{j=0}^{y} \left( \begin{array}{c} n \\ \\ j \end{array} \right) p_2^j (1-p_2)^{n-j} &= \frac{\alpha}{2} \\ \sum_{j=y}^{n} \left( \begin{array}{c} n \\ \\ j \end{array} \right) p_1^j (1-p_1)^{n-j} &= \frac{\alpha}{2} \end{aligned} \tag{A.3}$$

*for any given observed value $y$. Then $(p_1, p_2)$ is a $100(1-\alpha)\%$ confidence interval for $p$.*

In practice, however, it is somewhat difficult to use this definition. To do so would require one to solve two coupled linear equations with a large number of terms.

A simpler approach [84] involves using the F distribution to approximate the binomial distribution. The F distribution is described in the following theorem.

**Theorem A.3 ([83])** *Let $U$ be a $\chi^2$ random variable with $d_1$ degrees of freedom, and let $V$ be an independent $\chi^2$ random variable with $d_2$ degrees of freedom. Then the random variable*

$$F = \frac{U/d_1}{V/d_2} \tag{A.4}$$

*has the density function*

$$f(x) = \frac{,\ ((d_1+d_2)/2}{,\ (d_1/2),\ (d_2/2)} \cdot \frac{(d_1/d_2)^{d_1/2} x^{(d_1/2)-1}}{(1+(d_1 x/d_2))(d_1+d_2)/2},\ x>0. \tag{A.5}$$

*This is called the F density function with $d_1$ and $d_2$ degrees of freedom (or defines the F probability law with $d_1$ and $d_2$ degrees of freedom).*

This distribution is similar to the binomial distribution in that it involves the ratio of two random variable, of which, only one is independent. Ostle *et al.* use this to come up with the following approximation to the $100\gamma\%$ binomial confidence interval.

$$L = \frac{X \cdot F_{[(1-\gamma)/2],[2X,2(n-X+1)]}}{(n-X+1)+X \cdot F_{[(1-\gamma)/2],[2X,2(n-X+1)]}} \tag{A.6}$$

$$U = \frac{(X+1) \cdot F_{[(1+\gamma)/2],[2(X+1),2(n-X)]}}{(n-X)+(X+1) \cdot F_{[(1+\gamma)/2],[2(X+1),2(n-X)]}}, \tag{A.7}$$

where $\epsilon = \frac{X}{n}$ is the efficiency, and $F_{[p],[\nu 1,\nu 2]}$ is the cumulative F distribution. The cumulative F distribution is tabulated in many different sources [83, 84]. By convention we choose $\gamma = .648$. This is a 64.8% confidence interval which represents a one sigma effect in Gaussian statistics.

In general, confidence intervals give larger errors than those given by the interval estimator, Eq. A.2. This is particularly true for low statistics and for efficiencies near 0 or 1. This is demonstrated in Fig. A-1. Also, the confidence interval is generally asymmetric about the expectation value. Conversely, the binomial interval estimator always gives symmetric errors.

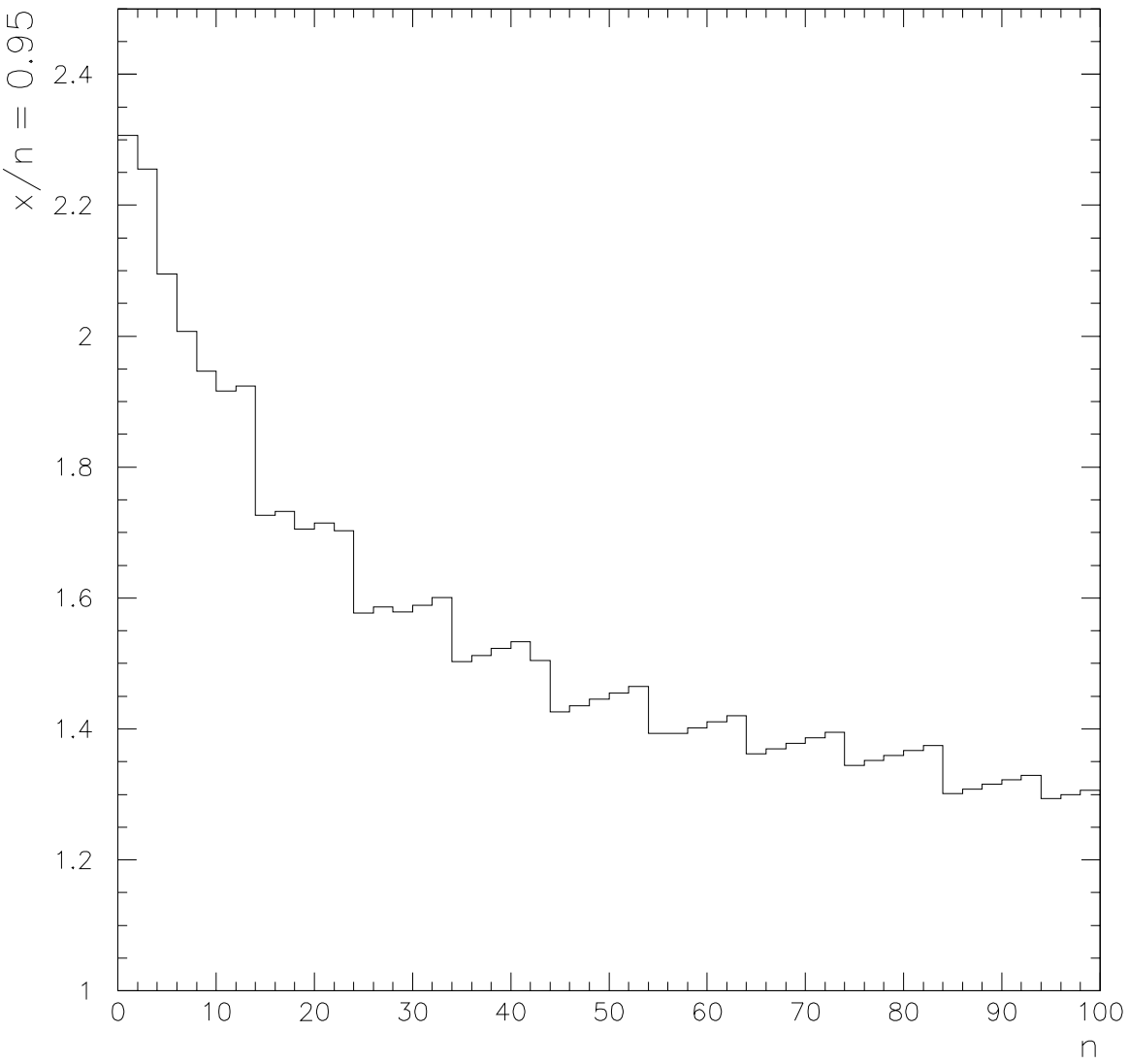


Figure A-1: The ratio of the width of the binomial confidence interval to the width given by the binomial interval estimator. An efficiency of $x/n = 95\%$ is held constant throughout the plot, while the total number of events, n, is allowed to vary. For low statistics, the interval estimator underestimates the error. The 'stair step' feature in the graph is due to the fact that a table lookup is used to determine the cumulative $F$ distribution.

In this thesis, Eq. A.1 is used to calculate the statistical errors of all data samples. This method is chosen due to the relatively high statistics of the data sample. Equations A.6 and A.7 are used whenever the statistical error for an efficiency is calculated. This is a conservative choice that is made to help insure that reasonable estimates of the 'true' errors are made even with low statistics.

# Appendix B

# Inputs to the $b\overline{b} \to \mu\mu X$ Cross Section

The tables given here list all of the inputs into the inclusive dimuon and $b\overline{b} \to \mu\mu X$ cross sections. Tables B-1 and B-2 define the $P_T^{\mu}$ and $\Delta\varphi_{\mu\mu}$ bins used in this analysis. Tables B-3 and B-4 show the raw dimuon, cosmic subtracted dimuon, and $b\overline{b} \to \mu\mu X$ spectrums.

The inclusive dimuon and $b\overline{b} \to \mu\mu X$ spectrums are unfolded via the methods described in Chapter 8 resulting in the unfolding matrices listed in Tables B-5 and B-6. These matrices unfold the data by

$$\vec{u} = M \cdot \vec{v}, \tag{B.1}$$

where $\vec{v}$ is the raw dimuon or $b\overline{b} \to \mu\mu X$ spectrum, $M$ is the unfolding matrix, and $\vec{u}$

is the unfolded spectrum. It should be noted that $u$ and $v$ are column vectors of the form

$$\vec{x} = \begin{bmatrix} x_1 \\ x_2 \\ \vdots \\ x_i \end{bmatrix}, \tag{B.2}$$

where the $x_i$ are the values of the dimuon or $b\overline{b} \rightarrow \mu\mu X$ spectrum in the $i^{th}$ bin. The unfolded cross sections are listed in Tables B-7 and B-8.

[1]Events in this bin satisfy the conditions given both by bins 6 and 7. As an example, an event with $P_T^{\mu}$(leading)$>$ 25 GeV/c and $P_T^{\mu}$(Trailing)$<$ 4 GeV/c would be placed into this bin. Very few events satisfy this condition.

[2]Events in this bin satisfy the conditions given by both bins 10 and 11.

| Bin Number | $P_T^\mu$(leading) (GeV/c) | | $P_T^\mu$(Trailing) (GeV/c) | | $M_{\mu\mu}$ (GeV/c$^2$) |
|---|---|---|---|---|---|
| 1 | 4-5 | and | 4-25 | and | 6-35 |
| 2 | 5-7 | and | 4-25 | and | 6-35 |
| 3 | 7-10 | and | 4-25 | and | 6-35 |
| 4 | 10-15 | and | 4-25 | and | 6-35 |
| 5 | 15-25 | and | 4-25 | and | 6-35 |
| 6 | 3-4 | or | 3-4 | or | 5-6 |
| 7 | 25-40 | or | 25-40 | or | 35-50 |
| 8 | Events failing a mixture of cuts.[1] | | | | |

Table B-1: This table describes the definitions of the bins used for the $P_T^\mu$ distribution. After the unfolding is complete, only bins one through five will be kept. The remaining bins are used only during the unfolding so that events can migrate into (out of) the bins of interest.

| Bin Number | $\Delta\varphi_{\mu\mu}$ (Degrees) | | $P_T^\mu$(leading) (GeV/c) | | $P_T^\mu$(Trailing) (GeV/c) | | $M_{\mu\mu}$ (GeV/c$^2$) |
|---|---|---|---|---|---|---|---|
| 1 | 0-20 | and | 4-25 | and | 4-25 | and | 6-35 |
| 2 | 20-40 | and | 4-25 | and | 4-25 | and | 6-35 |
| 3 | 40-60 | and | 4-25 | and | 4-25 | and | 6-35 |
| 4 | 60-80 | and | 4-25 | and | 4-25 | and | 6-35 |
| 5 | 80-100 | and | 4-25 | and | 4-25 | and | 6-35 |
| 6 | 100-120 | and | 4-25 | and | 4-25 | and | 6-35 |
| 7 | 120-140 | and | 4-25 | and | 4-25 | and | 6-35 |
| 8 | 140-160 | and | 4-25 | and | 4-25 | and | 6-35 |
| 9 | 160-180 | and | 4-25 | and | 4-25 | and | 6-35 |
| 10 | 0-180 | and | 3-4 | or | 3-4 | or | 5-6 |
| 11 | 0-180 | and | 25-40 | or | 25-40 | or | 35-50 |
| 12 | Events failing a mixture of cuts.[2] | | | | | | |

Table B-2: This table describes the definitions of the bins used for the $\Delta\varphi_{\mu\mu}$ distribution. After the unfolding is complete, only bins one through nine will be kept. The remaining bins are used only during the unfolding so that events can migrate into (out of) the bins of interest.

| Variable | Value | | | |
|---|---|---|---|---|
| $P_T^\mu$ Bin | 1 | 2 | 3 | 4 |
| $N_{Data}$ | 113 | 474 | 535 | 417 |
| $N_{\mu\mu}$ | $112.54 \pm 0.01$ | $466.81 \pm 0.03$ | $493.0 \pm 0.1$ | $308.1 \pm 0.1$ |
| $N_{b\bar{b}}$ | $40.36 \pm 0.16$ | $204.60 \pm 0.31$ | $274.12 \pm 0.32$ | $195.34 \pm 0.27$ |

| $P_T^\mu$ Bin | 5 | 6 | 7 | 8 |
|---|---|---|---|---|
| $N_{Data}$ | 233 | 247 | 89 | 2 |
| $N_{\mu\mu}$ | $120.3 \pm 0.1$ | $240.35 \pm 0.04$ | $34.79 \pm 0.07$ | $1.63 \pm 0.01$ |
| $N_{b\bar{b}}$ | $77.75 \pm 0.17$ | $96.13 \pm 0.22$ | $23.33 \pm 0.10$ | $0.98 \pm 0.02$ |

Table B-3: The $P_T^\mu$ bin numbers are defined in Table B-1. $N_{Data}$ is the raw dimuon data. The cosmic subtracted dimuon spectrum is given by $N_{\mu\mu}$, and $N_{b\bar{b}}$ represents the dimuon data after the $b$-quark fraction (Fig. 9-4) has been applied. The errors shown are the systematic uncertainties due to the maximum likelihood fits.

| Variable | Value | | | |
|---|---|---|---|---|
| $\Delta\varphi_{\mu\mu}$ Bin | 1 | 2 | 3 | 4 |
| $N_{Data}$ | 4 | 10 | 23 | 34 |
| $N_{\mu\mu}$ | $2.66 \pm 0.01$ | $9.31 \pm 0.02$ | $19.47 \pm 0.03$ | $29.29 \pm 0.03$ |
| $N_{b\bar{b}}$ | $2.06 \pm 0.02$ | $5.58 \pm 0.04$ | $13.76 \pm 0.06$ | $17.02 \pm 0.08$ |

| $\Delta\varphi_{\mu\mu}$ Bin | 5 | 6 | 7 | 8 |
|---|---|---|---|---|
| $N_{Data}$ | 57 | 75 | 140 | 339 |
| $N_{\mu\mu}$ | $50.28 \pm 0.04$ | $68.57 \pm 0.03$ | $132.76 \pm 0.04$ | $311.13 \pm 0.09$ |
| $N_{b\bar{b}}$ | $30.69 \pm 0.10$ | $39.28 \pm 0.12$ | $68.89 \pm 0.17$ | $168.94 \pm 0.25$ |

| $\Delta\varphi_{\mu\mu}$ Bin | 9 | 10 | 11 | 12 |
|---|---|---|---|---|
| $N_{Data}$ | 1090 | 247 | 89 | 2 |
| $N_{\mu\mu}$ | $877.27 \pm 0.17$ | $240.35 \pm 0.04$ | $34.79 \pm 0.07$ | $1.63 \pm 0.01$ |
| $N_{b\bar{b}}$ | $445.93 \pm 0.44$ | $96.13 \pm 0.22$ | $23.33 \pm 0.10$ | $0.98 \pm 0.02$ |

Table B-4: The $\Delta\varphi_{\mu\mu}$ bin numbers are defined in Table B-1. $N_{Data}$ is the raw dimuon data. The cosmic subtracted dimuon spectrum is given by $N_{\mu\mu}$, and $N_{b\bar{b}}$ represents the dimuon data after the $b$-quark fraction (Fig. 9-4) has been applied. The errors shown are the systematic uncertainties due to the maximum likelihood fits.

$$\begin{bmatrix}
0.457 & 0.096 & 0.030 & 0.013 & 0.009 & 0.108 & 0.000 & 0.000 \\
0.502 & 0.677 & 0.162 & 0.055 & 0.041 & 0.290 & 0.028 & 0.115 \\
0.000 & 0.206 & 0.636 & 0.243 & 0.102 & 0.307 & 0.114 & 0.000 \\
0.027 & 0.005 & 0.160 & 0.582 & 0.374 & 0.195 & 0.132 & 0.362 \\
0.000 & 0.010 & 0.010 & 0.102 & 0.435 & 0.056 & 0.313 & 0.129 \\
0.014 & 0.006 & 0.002 & 0.001 & 0.002 & 0.045 & 0.003 & 0.007 \\
0.000 & 0.000 & 0.000 & 0.004 & 0.038 & 0.000 & 0.407 & 0.387 \\
0.000 & 0.000 & 0.000 & 0.000 & 0.000 & 0.001 & 0.003 & 0.000
\end{bmatrix}$$

Table B-5: The unfolded dimuon $P_T^{\mu}$ unfolding matrix. Equation B.2 describes how this matrix is applied to the measured data distribution.

$$\begin{bmatrix}
1.000 & 0.000 & 0.000 & 0.000 & 0.000 & 0.000 & 0.000 & 0.000 & 0.000 & 0.000 & 0.000 & 0.000 \\
0.000 & 0.929 & 0.000 & 0.000 & 0.000 & 0.000 & 0.000 & 0.000 & 0.000 & 0.000 & 0.000 & 0.000 \\
0.000 & 0.066 & 0.964 & 0.024 & 0.000 & 0.000 & 0.000 & 0.000 & 0.000 & 0.016 & 0.000 & 0.000 \\
0.000 & 0.000 & 0.034 & 0.811 & 0.085 & 0.000 & 0.000 & 0.000 & 0.000 & 0.017 & 0.000 & 0.000 \\
0.000 & 0.000 & 0.000 & 0.058 & 0.788 & 0.044 & 0.000 & 0.000 & 0.000 & 0.030 & 0.029 & 0.062 \\
0.000 & 0.000 & 0.000 & 0.000 & 0.092 & 0.860 & 0.039 & 0.000 & 0.000 & 0.060 & 0.020 & 0.000 \\
0.000 & 0.000 & 0.000 & 0.000 & 0.000 & 0.095 & 0.879 & 0.031 & 0.000 & 0.048 & 0.066 & 0.096 \\
0.000 & 0.000 & 0.000 & 0.000 & 0.000 & 0.000 & 0.077 & 0.833 & 0.040 & 0.236 & 0.121 & 0.000 \\
0.000 & 0.000 & 0.000 & 0.000 & 0.000 & 0.000 & 0.000 & 0.124 & 0.957 & 0.557 & 0.307 & 0.382 \\
0.000 & 0.005 & 0.002 & 0.014 & 0.009 & 0.002 & 0.006 & 0.002 & 0.002 & 0.036 & 0.003 & 0.006 \\
0.000 & 0.000 & 0.000 & 0.093 & 0.026 & 0.000 & 0.000 & 0.010 & 0.002 & 0.000 & 0.451 & 0.454 \\
0.000 & 0.000 & 0.000 & 0.000 & 0.000 & 0.000 & 0.000 & 0.000 & 0.000 & 0.001 & 0.003 & 0.000
\end{bmatrix}$$

Table B-6: The unfolded dimuon $\Delta\varphi_{\mu\mu}$ unfolding matrix. Equation B.2 describes how this matrix is applied to the measured data distribution.

| Variable | Value | | | | |
|---|---|---|---|---|---|
| $P_T^\mu$ Bin | 1 | 2 | 3 | 4 | 5 |
| $P_T^\mu$ [GeV/c] | 4.64 | 6.05 | 8.39 | 12.14 | 18.53 |
| Unfolded $N_{\mu\mu}$ | 189.4 | 611.3 | 521.0 | 316.6 | 102.4 |
| $\pm$ Statistical | 10.0 | 31.2 | 26.1 | 19.5 | 7.7 |
| $\pm$ Systematic | 13.2 | 42.8 | 36.5 | 22.1 | 7.1 |
| Unfolded $N_{b\bar{b}}$ | 59.8 | 245.7 | 304.2 | 211.0 | 71.2 |
| $\pm$ Statistical | 3.2 | 12.8 | 15.0 | 13.0 | 5.2 |
| $\pm$ Systematic | 4.2 | 17.3 | 21.4 | 14.8 | 5.0 |
| Total Efficiency[%] | $0.63 \pm 0.12$ | $1.63 \pm 0.16$ | $2.99 \pm 0.28$ | $4.82 \pm 0.40$ | $6.47 \pm 0.80$ |
| $\Delta p_T^\mu$ [GeV/c] | 1 | 2 | 3 | 5 | 10 |
| $\int \mathcal{L} dt$ [pb$^{-1}$] | | | 46.2$\pm$2.5 | | |
| $\sigma_{\mu\mu}$ [pb/(GeV/c)] | 650.7 | 405.9 | 125.7 | 28.4 | 3.4 |
| $\pm$ Statistical | 34.4 | 20.7 | 6.3 | 1.8 | 0.3 |
| $\pm$ Systematic | 86.8 | 54.2 | 16.8 | 3.8 | 0.4 |
| $\sigma_{b\bar{b}\to\mu\mu}$ [pb/(GeV/c)] | 205.5 | 163.1 | 73.4 | 19.0 | 2.4 |
| $\pm$ Statistical | 11.0 | 8.5 | 3.6 | 1.2 | 0.2 |
| $\pm$ Systematic | 36.7 | 29.1 | 13.1 | 3.4 | 0.5 |

Table B-7: Input values into the cross section calculation for the $P_T^\mu$ spectrum. Note that these calculations are performed *after* the unfolding is complete.

| Variable | Value | | | | |
|---|---|---|---|---|---|
| $\Delta\varphi_{\mu\mu}$ Bin | 1 | 2 | 3 | 4 | 5 |
| $\Delta\varphi_{\mu\mu}$ [deg] | 12.64 | 33.92 | 52.11 | 70.49 | 90.85 |
| Unfolded $N_{\mu\mu}$ | 2.7 | 8.7 | 22.4 | 34.1 | 50.5 |
| $\pm$ Statistical | 1.3 | 2.7 | 3.9 | 4.3 | 5.2 |
| $\pm$ Systematic | 0.5 | 0.7 | 1.6 | 2.3 | 3.6 |
| Unfolded $N_{b\bar{b}}$ | 2.1 | 5.2 | 15.6 | 18.5 | 30.5 |
| $\pm$ Statistical | 1.0 | 1.6 | 2.8 | 2.4 | 3.2 |
| $\pm$ Systematic | 0.4 | 0.6 | 1.1 | 1.2 | 2.2 |
| Total Efficiency[%] | $2.18 \pm 1.09$ | $1.59 \pm 0.66$ | $2.57 \pm 0.65$ | $3.17 \pm 0.61$ | $2.43 \pm 0.42$ |
| $\int \mathcal{L}dt$ [pb$^{-1}$] | | | 46.2$\pm$2.5 | | |
| $\sigma_{\mu\mu}$ [pb/(GeV/c)] | 2.7 | 11.8 | 18.9 | 23.3 | 45.0 |
| $\pm$ Statistical | 1.3 | 3.7 | 3.3 | 2.9 | 4.6 |
| $\pm$ Systematic | 0.5 | 0.2 | 0.2 | 0.3 | 0.6 |
| $\sigma_{b\bar{b}\to\mu\mu}$ [pb/(GeV/c)] | 2.1 | 7.1 | 13.1 | 12.6 | 27.2 |
| $\pm$ Statistical | 1.0 | 2.2 | 2.4 | 1.6 | 2.9 |
| $\pm$ Systematic | 0.4 | 1.2 | 2.1 | 2.0 | 4.4 |

| $\Delta\varphi_{\mu\mu}$ Bin | 6 | 7 | 8 | 9 |
|---|---|---|---|---|
| $\Delta\varphi_{\mu\mu}$ [deg] | 111.55 | 131.20 | 152.31 | 171.71 |
| Unfolded $N_{\mu\mu}$ | 82.3 | 148.3 | 359.0 | 1034.2 |
| $\pm$ Statistical | 6.8 | 10.1 | 14.8 | 34.4 |
| $\pm$ Systematic | 5.7 | 10.4 | 25.3 | 72.3 |
| Unfolded $N_{b\bar{b}}$ | 45.5 | 75.8 | 189.2 | 508.6 |
| $\pm$ Statistical | 3.9 | 5.2 | 8.1 | 16.4 |
| $\pm$ Systematic | 3.3 | 5.3 | 13.2 | 35.6 |
| Total Efficiency[%] | $3.05 \pm 0.64$ | $1.85 \pm 0.34$ | $2.42 \pm 0.32$ | $2.34 \pm 0.24$ |
| $\int \mathcal{L}dt$ [pb$^{-1}$] | | | 46.2$\pm$2.5 | |
| $\sigma_{\mu\mu}$ [pb/(GeV/c)] | 58.4 | 173.5 | 321.1 | 956.6 |
| $\pm$ Statistical | 4.8 | 11.8 | 13.2 | 31.8 |
| $\pm$ Systematic | 0.8 | 2.3 | 4.3 | 12.8 |
| $\sigma_{b\bar{b}\to\mu\mu}$ [pb/(GeV/c)] | 32.3 | 88.7 | 169.2 | 470.5 |
| $\pm$ Statistical | 2.8 | 6.1 | 7.2 | 15.2 |
| $\pm$ Systematic | 5.3 | 14.6 | 27.9 | 77.6 |

Table B-8: Input values into the cross section calculation for the $\Delta\varphi_{\mu\mu}$ spectrum. Note that these calculations are performed *after* the unfolding is complete.

# REFERENCES


[1] P. W. Higgs, Phys. Lett. **12** 132 (1964).

[2] M. Mangano, P. Nason, and G. Ridolfi, Nucl. Phys. **B 373** 295 (1992).

[3] P. Nason, S. Dawson, and R. Ellis, Nucl. Phys. **B 303** 607 (1988).

[4] P. Nason, S. Dawson, and R. Ellis, Nucl. Phys. **B 327** 49 (1989).

[5] F. Abe et al. (CDF Collaboration), Nucl. Instr. Meth. **A 271** 387 (1988).

[6] D. Fein, PhD thesis, University of Arizona, (1995).

[7] LEP collaborations: ALEPH, DELPHI, L3, and OPAL, Phys. Lett. **B 276** 247 (1992).

[8] S. Abachi et al. (DØ Collaboration), Phys. Rev. Lett. **74** 2632 (1995).

[9] F. Abe et al. (CDF Collaboration), Phys. Rev. Lett. **74** 2626 (1995).

[10] S. L. Glashow, Nucl. Phys. **B 10** 107 (1959).

[11] S. L. Glashow, Nucl. Phys. **B 22** 579 (1961).

[12] S. Weinberg, Phys. Rev. Lett. **19** 1264 (1967).

[13] A. Salam and J. C. Ward, Nuovo Cimento **11** 568 (1959).

[14] A. Salam, 8th Nobel Symposium, Aspenäsgarden, Sweden **367** (1968).

[15] M. Gell-Mann, Acta Phys. Austriaca Suppl. **IX** 733 (1972).

[16] H. Fritzsch, M. Gell-Mann, and H. Leutwyler, Phys. Lett. **B 47** 365 (1973).

[17] H. Fritzsch and M. Gell-Mann, XVIth International Conference on High Energy Physics 135 (1972).

[18] N. Deshpande et al., hep-ph **9604236** (1996). (preprint).

[19] Z. Kakushadze and S.-H. Tye, hep-th **9605221** (1996). (preprint).

[20] N. Cabibbo, Phys. Lett. **10** 531 (1963).

[21] M. Kobayashi and T. Maskawa, Progr. Th. Phys. **49** 652 (1973).

[22] L.-L. Chau and W.-Y. Keung, Phys. Rev. Lett. **53** 1802 (1984).

[23] J. H. Christenson et al., Phys. Rev. Lett. **13** 138 (1964).

[24] R. D. Field, *Applications of Perturbative QCD*, Addison-Wesley, New York, (1989).

[25] W. Bardeen et al., Phys. Rev. **D 18** 3998 (1978).

[26] R. K. Ellis and W. J. Stirling, Fermilab-Conf **90/164-T** (1990).

[27] J. D. Bjorken and S. S. Drell, *Relativistic Quantum Fields*, McGraw Hill, New York, (1964).

[28] C. Itsykson and K. Zuber, *Quantum Field Theory*, McGraw Hill, New York, (1964).

[29] W. Beenakker, DESY **90-064, ITP-SB-90-46** (1990).

[30] W. Beenakker et al., Phys. Rev. **D 40** (1989).

[31] G. Altarelli and G. Parisi, Nucl. Phys. **B 126** 298 (1977).

[32] C. Curci et al., Nucl. Phys. **B 126** 437 (1980).

[33] E. Eichten et al., Rev. Mod. Phys. **56** 579 (1984).

[34] E. Eichten et al., Rev. Mod. Phys. **58** 1065 (1986).

[35] J. Botts et al., Phys. Lett. **B 304** 159 (1993).

[36] A. Martin et al., Phys. Rev. **D 37** 1161 (1988).

[37] H. Plothow-Besch,. *PDFLIB: Structure Functions and $\alpha_s$ Calculations User's Manual, Version 3.00*, (1992). Program Library Entry W5051.

[38] F. Paige and S. Protopopesco, Fermilab Computing Division **PM0059** (1992).

[39] M. Baarmand, DØ Internal Note **2517** (1995).

[40] J. Thompson, DØ Internal Note **2367** (1994).

[41] B. Webber, Fermi National Accelerator Operations Bulletin **719** (1979).

[42] S. Abachi et al. (DØ Collaboration), Nucl. Instr. Meth. **A 338** 185 (1994).

[43] NVF company, P.O. Box 6096, Broadview, Ill 60153.

[44] Hedin, DØ Internal Note **1738** (1993).

[45] N. Grossman, DØ Internal Note **1527** (1992).

[46] Bicron Corporation, 12345 Kinsman Road, Newbury, OH 44065-9677.

[47] Luminosity Utilities, DØ LIBRARY Program.

[48] P. Quintas and D. Vititoe, DØ Internal Note **2680** (1995).

[49] FNALD0::TOP_DOC$HROOT:[GENERAL_INFO.RUN1B]BAD_RUN.RCP.

[50] CAFIX DØ LIBRARY Program Package.

[51] MUFIX DØ LIBRARY Program Package.

[52] R. Astur, DØ Internal Note **1662** (1993).

[53] A. Milder, PhD thesis, University of Arizona, (1993).

[54] R. Astur, DØ Internal Note **1763** (1993).

[55] G. Fox and S. Wolfram, Nucl. Phys. **B 168** 285 (1980).

[56] R. Field and R. Feynman, Nucl. Phys. **B 136** 1 (1978).

[57] C. Peterson, Phys. Rev. **D 27** 105 (1983).

[58] S. Squarcia, CERN **PPE/94-69** (1994).

[59] E. James, PhD thesis, University of Arizona, (1995).

[60] A. Smith, PhD thesis, University of Arizona, (1995).

[61] GEANT DØLIBRARY Program Package.

[62] D. Hedin, DØ Internal Note **2967** (1996).

[63] D. Hedin, "Eye-scanning for unbiased events",
FNALD0::USR$ROOT3:[HEDIN]SCANXXX.DOC.

[64] MINUIT, CERN LINBRARY Program.

[65] G. D'Agostini, DESY **94-099** (1994).

[66] C. Albajar et al. (UA1 Collaboration), Phys. Lett. **B 213** 405 (1988).

[67] C. Albajar et al. (UA1 Collaboration), Phys. Lett. **B 256** 121 (1991).

[68] F. Abe et al. (CDF Collaboration), FERMILAB-PUB **96/216-E** (1996).

[69] T. Huehn, PhD thesis, University of California, Riverdale, (1995).

[70] K. Bazizi, DØ Internal Note **2593** (1995).

[71] S. Abachi et al. (DØ Collaboration), Phys. Rev. Lett. **74** 3548 (1995).

[72] S. Abachi et al. (DØ Collaboration), Fermilab-Conf **96/03-E** (1996).

[73] F. Abe et al. (CDF Collaboration), Phys. Rev. Lett. **68** 3403 (1992).

[74] F. Abe et al. (CDF Collaboration), Phys. Rev. Lett. **69** 3704 (1992).

[75] F. Abe et al. (CDF Collaboration), Phys. Rev. Lett. **71** 500 (1993).

[76] F. Abe et al. (CDF Collaboration), Phys. Rev. **D 50** 4258 (1994).

[77] A. Geiser, PhD thesis, University of Aachen, Germany, (1992).

[78] A. Martin, R. Roberts, and W. Stirling, Phys. Rev. **D 50** 6734 (1994).

[79] F. Abe et al. (CDF Collaboration), Fermilab-CONF **95/289-E** (1995).

[80] F. Abe et al. (CDF Collaboration), Fermilab-PUB **95/289-E** (1995).

[81] P. Avery et al., Cornell Internal Note **CSN-212** (1985).

[82] M. Diemoz, F. Ferroni, E. Longo, and G. Martinelli, Z. Phys. **C 39** 21 (1988).

[83] H. J. Larson, *Introduction to Probablility Theory and Statistical Inference*, John Wiley & Sons, New York, (1982).

[84] B. Ostle and Malon, *Statistics in Research*, Iowa State Univ. Press, Ames, Iowa, (1988).